

NORTHWESTERN UNIVERSITY

The Search for the Higgs Boson and New Resonances Decaying to a Z
Boson and a Photon

A DISSERTATION

SUBMITTED TO THE GRADUATE SCHOOL
IN PARTIAL FULFILLMENT OF THE REQUIREMENTS

for the degree

DOCTOR OF PHILOSOPHY

Field of Physics and Astronomy

By

Brian Pollack

EVANSTON, ILLINOIS

June 2015

UMI Number: 3705342

All rights reserved

INFORMATION TO ALL USERS

The quality of this reproduction is dependent upon the quality of the copy submitted.

In the unlikely event that the author did not send a complete manuscript and there are missing pages, these will be noted. Also, if material had to be removed, a note will indicate the deletion.



UMI 3705342

Published by ProQuest LLC (2015). Copyright in the Dissertation held by the Author.

Microform Edition © ProQuest LLC.

All rights reserved. This work is protected against unauthorized copying under Title 17, United States Code



ProQuest LLC.
789 East Eisenhower Parkway
P.O. Box 1346
Ann Arbor, MI 48106 - 1346

© Copyright by Brian Pollack 2015

All Rights Reserved

ABSTRACT

The Search for the Higgs Boson and New Resonances Decaying to a Z Boson and a Photon

Brian Pollack

The Large Hadron Collider collected its first full sets of proton-proton collision data in 2011 and 2012. Using the Compact Muon Solenoid detector, two analyses were performed that searched for potential new physics with Z boson plus photon final states. The first analysis is a Higgs boson search, which looks for an enhancement of the recently discovered 125 GeV Higgs boson in the $H \rightarrow Z\gamma \rightarrow \ell\ell\gamma$ decay mode. The disintegration of the Higgs to a Z boson and a photon is expected to be at the per mil level, and any enhancement in this decay channel would be indirect evidence of new physics that would contribute to the loop diagrams responsible for the decay. The second analysis is a model independent search that looks for any potential $A \rightarrow Z\gamma \rightarrow \ell\ell\gamma$ signal, where A is any new resonance, in the mass range of 200 GeV or higher. The discovery of a signal in this channel would be direct evidence of physics beyond the standard model, and especially relevant for composite Higgs models that predict high sensitivity to the $Z\gamma$ decay mode. Both searches employ data driven background estimation methods and optimized event

selection to maximum signal sensitivity. The results of the low mass Higgs boson search show agreement with the standard model of particle physics, with expected exclusion limits at about 10 times the standard model, and observed exclusion limits at about 9.5 times the standard model. The results of the $A \rightarrow Z\gamma \rightarrow \ell\ell\gamma$ search exclude the presence of this resonance and decay mode in excess of about 1 fb for 200 GeV and higher. The sensitivity of this channel is found to be stronger than all other diboson channels. These results place strong limits on new physics models, and will guide the next generation of searches at the LHC for Run 2.

Acknowledgements

I'd like to thank my advisor, Mayda, for supporting me, mentoring me, and putting up with me in general for the last six years. I must also thank Michael, Kristian and Ming, and to Kevin, Andy, Andrew, Nate, and even Andrey, who all aided me time and time again.

To my parents, who encouraged me to pursue my passions whatever they may be, and selflessly supported me through all of my life. In many ways, I could not have come this far without you two. To my sister and the rest of my family for the love and encouragement that they constantly provide. And to my friends from high school, college, and graduate school, for keeping me relatively sane for all these years.

Thank you all.

Table of Contents

ABSTRACT	3
Acknowledgements	5
List of Tables	9
List of Figures	26
Chapter 1. Introduction	36
Chapter 2. Theory	38
2.1. Electroweak Symmetry Breaking	38
2.2. Higgs Production	41
2.3. Higgs Decay	42
2.4. Physics Beyond the Standard Model	44
Chapter 3. Experimental Apparatus	46
3.1. LHC	46
3.2. The Compact Muon Solenoid (CMS)	48
Chapter 4. Analysis	59
Chapter 5. Data and Simulation	62
5.1. Data Samples	62

5.2. Simulation Samples	63
Chapter 6. Object and Event Selection	68
6.1. Object Selection	68
6.2. Event Selection and Categorization	105
Chapter 7. Parametric Modeling	116
7.1. Background Modeling	116
7.2. Signal Modeling	131
Chapter 8. Systematic Uncertainties	135
8.1. Muon	136
8.2. Electron	136
8.3. Photon	137
8.4. Jets	138
8.5. PU, Acceptance, Branching Ratios, Cross Sections	142
8.6. Systematic Uncertainty Summary	142
Chapter 9. Results and Interpretation	145
9.1. $H \rightarrow Z\gamma \rightarrow \ell\ell\gamma$	145
9.2. $A \rightarrow Z\gamma \rightarrow \ell\ell\gamma$	148
References	151
Appendix A. Electron ID and Iso Fits	156
Appendix B. Bias Studies	163
B.1. $H \rightarrow Z\gamma$ Bias Studies	163

B.2. $A \rightarrow Z\gamma$ Bias Studies	182
Appendix C. $H \rightarrow Z\gamma$ Signal Fits	185

List of Tables

3.1	A short list of relevant LHC design parameters.	47
3.2	A short list of relevant LHC parameters for the 2011 and 2012 data taking runs.	48
5.1	Summary of 2011 and 2012 data samples.	63
5.2	Summary of MC signal and BG samples.	65
5.3	Expected signal yields for a 125 GeV SM Higgs boson for each production process.	65
6.1	2011 Election Selection Criteria.	75
6.2	Muon selection criteria	81
6.3	Photon Selection Criteria for $H \rightarrow Z\gamma$ Analysis.	85
6.4	The scale factors for photon selection without electron veto for 2011.	86
6.5	The scale factors for photon selection without electron veto for 2012.	87
6.6	The scale factors for electron veto selection. The efficiencies are around 99% in the barrel and 97-98% in the endcap.	87
6.7	The scale factors for electron veto selection. The efficiencies are around 99% in the barrel and 97-98% in the endcap.	88

6.8	Photon MVA Pre-Selection.	88
6.9	Photon MVA Scale Factors.	90
6.10	A summary of the measured photon energy scale and resolution for the data and MC. Values are given for 2011 and 2012 separately as well as in two categories of R_9 in EB.	92
6.11	Definition of the four untagged event classes, the fraction of selected events for a signal with $m_H = 125$ GeV produced by gluon-gluon fusion at 8 TeV and data in a narrow bin centered at 125 GeV. The expected mass resolution on the signal is also shown.	114
8.1	Summary of the variation of the $Z\gamma$ selection efficiency w.r.t. the default UE tune, Z2star.	139
8.2	Summary of the variation of the $Z\gamma$ plus dijet selection efficiency w.r.t. to the default UE tune, Z2star.	140
8.3	Summary of the variation of the dijet selection efficiency w.r.t. the default UE tune, Z2star.	140
8.4	Summary of additional systematic uncertainties on the dijet tagged event class.	140
8.5	Summary of the event migration systematic uncertainties on each untagged category for signal events produced via vector boson fusion.	142
8.6	Separate sources of systematic uncertainties accounted for in the $H \rightarrow Z\gamma$ analysis of the 7 and 8 TeV data set. The magnitude of the variation of the source that has been applied to the signal model is	

shown. GGH stands for Gluon-gluon fusion cross section, VBF Vector boson fusion cross section, VH vector boson associate production and ttH top pair associate production.

143

8.7 Separate sources of systematic uncertainties accounted for in the $A \rightarrow Z\gamma$ analysis. The magnitude of the variation of the source that has been applied to the signal model is shown.

144

B.1 4-Category Signal Yield Pulls, $m_H=120$, Gaussian turn-on for fit. Columns show results for the various background models used in combined signal+background fits to background-only toys. The four numbers given for each background fit model correspond to toys generated from either an gauss \times exponential, gauss \times power-law, sech \times exponential, or sech \times power-law truth model. Boldface is used to indicate the lowest-order polynomial that satisfies the “low-bias” pull criteria: $|\mu(nS/\sigma(nS))| \leq 0.2$

163

B.2 4-Category Signal Yield Pulls, $m_H=120$, Sech turn-on. Columns show results for the various background models used in combined signal+background fits to background-only toys. The four numbers given for each background fit model correspond to toys generated from either an gauss \times exponential, gauss \times power-law, sech \times exponential, or sech \times power-law truth model. Boldface is used to indicate the lowest-order polynomial that satisfies the “low-bias” pull criteria:
 $|\mu(nS/\sigma(nS))| \leq 0.2$

164

B.3 4-Category Type-A Criteria, $m_H=120$, Gaussian turn-on. Columns show results for the various background models used in combined signal+background fits to background-only toys. The four numbers given for each background fit model correspond to toys generated from either a gauss×exponential, gauss×power-law, sech×exponential, or sech×power-law truth model. Boldface is used to indicate the lowest-order polynomial that satisfies the “low-bias” type-A criteria:

$$|\mu(nS/\sigma(nB))| \leq 0.2 \quad 165$$

B.4 4-Category Type-A Criteria, $m_H=120$, Sech turn-on. Columns show results for the various background models used in combined signal+background fits to background-only toys. The four numbers given for each background fit model correspond to toys generated from either a gauss×exponential, gauss×power-law, sech×exponential, or sech×power-law truth model. Boldface is used to indicate the lowest-order polynomial that satisfies the “low-bias” type-A criteria:

$$|\mu(nS/\sigma(nB))| \leq 0.2 \quad 165$$

B.5 4-Category Signal Yield Pulls, $m_H=125$, Gaussian turn-on for fit. Columns show results for the various background models used in combined signal+background fits to background-only toys. The four numbers given for each background fit model correspond to toys generated from either an gauss×exponential, gauss×power-law, sech×exponential, or sech×power-law truth model. Boldface is used

to indicate the lowest-order polynomial that satisfies the “low-bias” pull criteria: $|\mu(nS/\sigma(nS))| <= 0.2$ 166

B.6 4-Category Signal Yield Pulls, $m_H=125$, Sech turn-on. Columns show results for the various background models used in combined signal+background fits to background-only toys. The four numbers given for each background fit model correspond to toys generated from either an gauss \times exponential, gauss \times power-law, sech \times exponential, or sech \times power-law truth model. Boldface is used to indicate the lowest-order polynomial that satisfies the “low-bias” pull criteria:

$$|\mu(nS/\sigma(nS))| <= 0.2 \quad 166$$

B.7 4-Category Type-A Criteria, $m_H=125$, Gaussian turn-on. Columns show results for the various background models used in combined signal+background fits to background-only toys. The four numbers given for each background fit model correspond to toys generated from either a gauss \times exponential, gauss \times power-law, sech \times exponential, or sech \times power-law truth model. Boldface is used to indicate the lowest-order polynomial that satisfies the “low-bias” type-A criteria:

$$|\mu(nS/\sigma(nB))| <= 0.2 \quad 167$$

B.8 4-Category Type-A Criteria, $m_H=125$, Sech turn-on. Columns show results for the various background models used in combined signal+background fits to background-only toys. The four numbers given for each background fit model correspond to toys generated from either a gauss \times exponential, gauss \times power-law, sech \times exponential,

or $\text{sech} \times \text{power-law}$ truth model. Boldface is used to indicate the lowest-order polynomial that satisfies the “low-bias” type-A criteria:

$$|\mu(nS/\sigma(nB))| \leq 0.2 \quad 167$$

- B.9 4-Category Signal Yield Pulls, $m_H=130$, Gaussian turn-on for fit. Columns show results for the various background models used in combined signal+background fits to background-only toys. The four numbers given for each background fit model correspond to toys generated from either an $\text{gauss} \times \text{exponential}$, $\text{gauss} \times \text{power-law}$, $\text{sech} \times \text{exponential}$, or $\text{sech} \times \text{power-law}$ truth model. Boldface is used to indicate the lowest-order polynomial that satisfies the “low-bias” pull criteria: $|\mu(nS/\sigma(nS))| \leq 0.2$

$$168$$

- B.10 4-Category Signal Yield Pulls, $m_H=130$, Sech turn-on. Columns show results for the various background models used in combined signal+background fits to background-only toys. The four numbers given for each background fit model correspond to toys generated from either an $\text{gauss} \times \text{exponential}$, $\text{gauss} \times \text{power-law}$, $\text{sech} \times \text{exponential}$, or $\text{sech} \times \text{power-law}$ truth model. Boldface is used to indicate the lowest-order polynomial that satisfies the “low-bias” pull criteria:

$$|\mu(nS/\sigma(nS))| \leq 0.2 \quad 168$$

- B.11 4-Category Type-A Criteria, $m_H=130$, Gaussian turn-on. Columns show results for the various background models used in combined signal+background fits to background-only toys. The four numbers given for each background fit model correspond to toys generated from

either a gauss \times exponential, gauss \times power-law, sech \times exponential, or sech \times power-law truth model. Boldface is used to indicate the lowest-order polynomial that satisfies the “low-bias” type-A criteria:

$$|\mu(nS/\sigma(nB))| <= 0.2 \quad 169$$

B.12 4-Category Type-A Criteria, $m_H=130$, Sech turn-on. Columns show results for the various background models used in combined signal+background fits to background-only toys. The four numbers given for each background fit model correspond to toys generated from either a gauss \times exponential, gauss \times power-law, sech \times exponential, or sech \times power-law truth model. Boldface is used to indicate the lowest-order polynomial that satisfies the “low-bias” type-A criteria:

$$|\mu(nS/\sigma(nB))| <= 0.2 \quad 169$$

B.13 4-Category Signal Yield Pulls, $m_H=135$, Gaussian turn-on for fit.
 Columns show results for the various background models used in combined signal+background fits to background-only toys. The four numbers given for each background fit model correspond to toys generated from either an gauss \times exponential, gauss \times power-law, sech \times exponential, or sech \times power-law truth model. Boldface is used to indicate the lowest-order polynomial that satisfies the “low-bias” pull criteria: $|\mu(nS/\sigma(nS))| \leq 0.2$

B.14 4-Category Signal Yield Pulls, $m_H=135$, Sech turn-on. Columns show results for the various background models used in combined signal+background fits to background-only toys. The four numbers

given for each background fit model correspond to toys generated from either an gauss \times exponential, gauss \times power-law, sech \times exponential, or sech \times power-law truth model. Boldface is used to indicate the lowest-order polynomial that satisfies the “low-bias” pull criteria:

$$|\mu(nS/\sigma(nS))| \leq 0.2 \quad 170$$

- B.15 4-Category Type-A Criteria, $m_H=135$, Gaussian turn-on. Columns show results for the various background models used in combined signal+background fits to background-only toys. The four numbers given for each background fit model correspond to toys generated from either a gauss \times exponential, gauss \times power-law, sech \times exponential, or sech \times power-law truth model. Boldface is used to indicate the lowest-order polynomial that satisfies the “low-bias” type-A criteria:

$$|\mu(nS/\sigma(nB))| \leq 0.2 \quad 171$$

- B.16 4-Category Type-A Criteria, $m_H=135$, Sech turn-on. Columns show results for the various background models used in combined signal+background fits to background-only toys. The four numbers given for each background fit model correspond to toys generated from either a gauss \times exponential, gauss \times power-law, sech \times exponential, or sech \times power-law truth model. Boldface is used to indicate the lowest-order polynomial that satisfies the “low-bias” type-A criteria:

$$|\mu(nS/\sigma(nB))| \leq 0.2 \quad 171$$

- B.17 4-Category Signal Yield Pulls, $m_H=140$, Gaussian turn-on for fit. Columns show results for the various background models used in

combined signal+background fits to background-only toys. The four numbers given for each background fit model correspond to toys generated from either an gauss \times exponential, gauss \times power-law, sech \times exponential, or sech \times power-law truth model. Boldface is used to indicate the lowest-order polynomial that satisfies the “low-bias” pull criteria: $|\mu(nS/\sigma(nS))| \leq 0.2$

172

B.18 4-Category Signal Yield Pulls, $m_H=140$, Sech turn-on. Columns show results for the various background models used in combined signal+background fits to background-only toys. The four numbers given for each background fit model correspond to toys generated from either an gauss \times exponential, gauss \times power-law, sech \times exponential, or sech \times power-law truth model. Boldface is used to indicate the lowest-order polynomial that satisfies the “low-bias” pull criteria:

$$|\mu(nS/\sigma(nS))| \leq 0.2 \quad 172$$

B.19 4-Category Type-A Criteria, $m_H=140$, Gaussian turn-on. Columns show results for the various background models used in combined signal+background fits to background-only toys. The four numbers given for each background fit model correspond to toys generated from either a gauss \times exponential, gauss \times power-law, sech \times exponential, or sech \times power-law truth model. Boldface is used to indicate the lowest-order polynomial that satisfies the “low-bias” type-A criteria:

$$|\mu(nS/\sigma(nB))| \leq 0.2 \quad 173$$

B.20 4-Category Type-A Criteria, $m_H=140$, Sech turn-on. Columns show results for the various background models used in combined signal+background fits to background-only toys. The four numbers given for each background fit model correspond to toys generated from either a gauss×exponential, gauss×power-law, sech×exponential, or sech×power-law truth model. Boldface is used to indicate the lowest-order polynomial that satisfies the “low-bias” type-A criteria:

$$|\mu(nS/\sigma(nB))| \leq 0.2 \quad 173$$

B.21 4-Category Signal Yield Pulls, $m_H=145$, Sech turn-on. Columns show results for the various background models used in combined signal+background fits to background-only toys. The four numbers given for each background fit model correspond to toys generated from either an gauss×exponential, gauss×power-law, sech×exponential, or sech×power-law truth model. Boldface is used to indicate the lowest-order polynomial that satisfies the “low-bias” pull criteria:

$$|\mu(nS/\sigma(nS))| \leq 0.2 \quad 174$$

B.22 4-Category Type-A Criteria, $m_H=145$, Gaussian turn-on. Columns show results for the various background models used in combined signal+background fits to background-only toys. The four numbers given for each background fit model correspond to toys generated from either a gauss×exponential, gauss×power-law, sech×exponential, or sech×power-law truth model. Boldface is used to indicate the

lowest-order polynomial that satisfies the “low-bias” type-A criteria:

$$|\mu(nS/\sigma(nB))| \leq 0.2 \quad 175$$

B.23 4-Category Type-A Criteria, $m_H=145$, Sech turn-on. Columns show results for the various background models used in combined signal+background fits to background-only toys. The four numbers given for each background fit model correspond to toys generated from either a gauss×exponential, gauss×power-law, sech×exponential, or sech×power-law truth model. Boldface is used to indicate the lowest-order polynomial that satisfies the “low-bias” type-A criteria:

$$|\mu(nS/\sigma(nB))| \leq 0.2 \quad 175$$

B.24 4-Category Signal Yield Pulls, $m_H=150$, Gaussian turn-on for fit. Columns show results for the various background models used in combined signal+background fits to background-only toys. The four numbers given for each background fit model correspond to toys generated from either an gauss×exponential, gauss×power-law, sech×exponential, or sech×power-law truth model. Boldface is used to indicate the lowest-order polynomial that satisfies the “low-bias” pull criteria: $|\mu(nS/\sigma(nS))| \leq 0.2$ 176

B.25 4-Category Signal Yield Pulls, $m_H=150$, Sech turn-on. Columns show results for the various background models used in combined signal+background fits to background-only toys. The four numbers given for each background fit model correspond to toys generated from either an gauss×exponential, gauss×power-law, sech×exponential,

or $\text{sech} \times \text{power-law}$ truth model. Boldface is used to indicate the lowest-order polynomial that satisfies the “low-bias” pull criteria:

$$|\mu(nS/\sigma(nS))| \leq 0.2 \quad 176$$

- B.26 4-Category Type-A Criteria, $m_H=150$, Gaussian turn-on. Columns show results for the various background models used in combined signal+background fits to background-only toys. The four numbers given for each background fit model correspond to toys generated from either a $\text{gauss} \times \text{exponential}$, $\text{gauss} \times \text{power-law}$, $\text{sech} \times \text{exponential}$, or $\text{sech} \times \text{power-law}$ truth model. Boldface is used to indicate the lowest-order polynomial that satisfies the “low-bias” type-A criteria:

$$|\mu(nS/\sigma(nB))| \leq 0.2 \quad 177$$

- B.27 4-Category Type-A Criteria, $m_H=150$, Sech turn-on. Columns show results for the various background models used in combined signal+background fits to background-only toys. The four numbers given for each background fit model correspond to toys generated from either a $\text{gauss} \times \text{exponential}$, $\text{gauss} \times \text{power-law}$, $\text{sech} \times \text{exponential}$, or $\text{sech} \times \text{power-law}$ truth model. Boldface is used to indicate the lowest-order polynomial that satisfies the “low-bias” type-A criteria:

$$|\mu(nS/\sigma(nB))| \leq 0.2 \quad 177$$

- B.28 VBF BG Yield Pulls, $m_H=120$ for fit models. Columns show results for the various background models used in combined signal+background fits to background-only toys. The two numbers given for each background fit model correspond to toys generated from

either an exponential or a power-law. Boldface is used to indicate the lowest-order polynomial that satisfies the “low-bias” pull criteria:

$$|\mu(nBG)/\sigma(nBG))| \leq 0.2 \quad 178$$

- B.29 VBF BG Yield Pulls, $m_H=125$ for fit models. Columns show results for the various background models used in combined signal+background fits to background-only toys. The two numbers given for each background fit model correspond to toys generated from either an exponential or a power-law. Boldface is used to indicate the lowest-order polynomial that satisfies the “low-bias” pull criteria:

$$|\mu(nBG)/\sigma(nBG))| \leq 0.2 \quad 178$$

- B.30 VBF BG Yield Pulls, $m_H=130$ for fit models. Columns show results for the various background models used in combined signal+background fits to background-only toys. The two numbers given for each background fit model correspond to toys generated from either an exponential or a power-law. Boldface is used to indicate the lowest-order polynomial that satisfies the “low-bias” pull criteria:

$$|\mu(nBG)/\sigma(nBG))| \leq 0.2 \quad 179$$

- B.31 VBF BG Yield Pulls, $m_H=135$ for fit models. Columns show results for the various background models used in combined signal+background fits to background-only toys. The two numbers given for each background fit model correspond to toys generated from either an exponential or a power-law. Boldface is used to indicate

the lowest-order polynomial that satisfies the “low-bias” pull criteria:

$$|\mu(nBG)/\sigma(nBG))| <= 0.2 \quad 179$$

- B.32 VBF BG Yield Pulls, $m_H=140$ for fit models. Columns show results for the various background models used in combined signal+background fits to background-only toys. The two numbers given for each background fit model correspond to toys generated from either an exponential or a power-law. Boldface is used to indicate the lowest-order polynomial that satisfies the “low-bias” pull criteria:

$$|\mu(nBG)/\sigma(nBG))| <= 0.2 \quad 180$$

- B.33 VBF BG Yield Pulls, $m_H=145$ for fit models. Columns show results for the various background models used in combined signal+background fits to background-only toys. The two numbers given for each background fit model correspond to toys generated from either an exponential or a power-law. Boldface is used to indicate the lowest-order polynomial that satisfies the “low-bias” pull criteria:

$$|\mu(nBG)/\sigma(nBG))| <= 0.2 \quad 180$$

- B.34 VBF BG Yield Pulls, $m_H=150$ for fit models. Columns show results for the various background models used in combined signal+background fits to background-only toys. The two numbers given for each background fit model correspond to toys generated from either an exponential or a power-law. Boldface is used to indicate the lowest-order polynomial that satisfies the “low-bias” pull criteria:

$$|\mu(nBG)/\sigma(nBG))| <= 0.2 \quad 181$$

B.35	typeA Bias, 200. Columns show results for the various background models used in combined signal+background fits to background-only toys. The three numbers given for each background fit model correspond to toys generated from either a power law, Laurent polynomial, or exponential-like truth model. Boldface and yellow highlight is used to indicate the lowest-order functional form that satisfies the “low-bias” criterion: $ \mu(nS/\sigma(nBG)) \leq 0.2$	182
B.36	typeA Bias, 250. Columns show results for the various background models used in combined signal+background fits to background-only toys. The three numbers given for each background fit model correspond to toys generated from either a power law, Laurent polynomial, or exponential-like truth model. Boldface and yellow highlight is used to indicate the lowest-order functional form that satisfies the “low-bias” criterion: $ \mu(nS/\sigma(nBG)) \leq 0.2$	182
B.37	typeA Bias, 300. Columns show results for the various background models used in combined signal+background fits to background-only toys. The three numbers given for each background fit model correspond to toys generated from either a power law, Laurent polynomial, or exponential-like truth model. Boldface and yellow highlight is used to indicate the lowest-order functional form that satisfies the “low-bias” criterion: $ \mu(nS/\sigma(nBG)) \leq 0.2$	183
B.38	typeA Bias, 350. Columns show results for the various background models used in combined signal+background fits to background-only	

- toys. The three numbers given for each background fit model correspond to toys generated from either a power law, Laurent polynomial, or exponential-like truth model. Boldface and yellow highlight is used to indicate the lowest-order functional form that satisfies the “low-bias” criterion: $|\mu(nS/\sigma(nBG))| \leq 0.2$ 183
- B.39 typeA Bias, 400. Columns show results for the various background models used in combined signal+background fits to background-only toys. The three numbers given for each background fit model correspond to toys generated from either a power law, Laurent polynomial, or exponential-like truth model. Boldface and yellow highlight is used to indicate the lowest-order functional form that satisfies the “low-bias” criterion: $|\mu(nS/\sigma(nBG))| \leq 0.2$ 183
- B.40 typeA Bias, 450. Columns show results for the various background models used in combined signal+background fits to background-only toys. The three numbers given for each background fit model correspond to toys generated from either a power law, Laurent polynomial, or exponential-like truth model. Boldface and yellow highlight is used to indicate the lowest-order functional form that satisfies the “low-bias” criterion: $|\mu(nS/\sigma(nBG))| \leq 0.2$ 184
- B.41 typeA Bias, 500. Columns show results for the various background models used in combined signal+background fits to background-only toys. The three numbers given for each background fit model correspond to toys generated from either a power law, Laurent

polynomial, or exponential-like truth model. Boldface and yellow highlight is used to indicate the lowest-order functional form that satisfies the “low-bias” criterion: $|\mu(nS/\sigma(nBG))| \leq 0.2$ 184

List of Figures

2.1	The symmetry-breaking ‘‘Mexican Hat Potential’’. There is no minimum at $\phi = 0$, which leads to a nonzero VEV.	39
2.2	Feynman diagrams for leading order Higgs production at the LHC.	42
2.3	Higgs production cross sections for $\sqrt{s} = 8$ TeV. Error bands are from theoretical uncertainties.	42
2.4	Higgs branching fractions for the most common decay modes.	43
2.5	Feynman diagrams for $H \rightarrow Z\gamma$.	44
2.6	Production cross sections as a function of m_η at the LHC Run II with $\sqrt{s} = 13$ TeV.	45
2.7	Branching ratios for the η particle as a function of θ and m_η , for $m_h = 125$ GeV.	45
3.1	General layout of the LHC experiments, as well as the accelerator complex which supplies them with collisions.	47
3.2	Schematic view of the CMS detector showing the various sub-detectors.	49
3.3	Schematic side-view of the CMS silicon tracker.	50

3.4	CMS tracker resolution performance as a function of η for three different charged particle momenta. Resolution for transverse momentum (left), transverse vertex resolution (center), and longitudinal vertex resolution (right) are shown.	51
3.5	Schematic of the CMS ECAL.	52
3.6	Electron energy resolution as a function of η in $Z \rightarrow ee$ events. The top two plots are of electrons that have a large footprint inside the ECAL. The bottom two plots represent electrons that have a much smaller footprint.	53
3.7	Photon energy resolution as a function of η in simulation. The top two plots are of photons that have a large footprint inside the ECAL, most likely due to showering within the tracker. The bottom two plots have a much smaller footprint, as they do not start to shower until entering the ECAL.	54
3.8	Schematic side-view of the CMS HCAL.	55
3.9	Schematic side-view of the CMS Muon detectors.	56
3.10	Muon resolution as a function of the transverse momentum.	57
5.1	Distribution of the number of vertices in the 2012 data sample and simulation.	67
6.1	Plots of electron trigger efficiencies for the 2011 run.	70

6.2	Plots of electron trigger efficiencies, binned in p_T and η . Top: Trailing trigger leg (10-20 GeV). Bottom: Trailing trigger leg (20+ GeV). Left: Data. Right: MC.	71
6.3	Plots of electron trigger efficiencies, binned in p_T and η . Top: Leading trigger leg (10-20 GeV). Bottom: Leading trigger leg (20+ GeV). Left: Data. Right: MC.	72
6.4	Scale factors for 2012 muon trigger, $ \eta $ of Muon 1 vs $ \eta $ of Muon 2. Left: Muon1 has $10 < pT < 20$ GeV, Muon2 has $pT > 20$ GeV. Right: Muon1 and Muon2 have $pT > 20$ GeV.	73
6.5	Performances of electron MVA-based ID in three different η bins: $ \eta < 0.8$ (left), $ \eta < 1.479$ (middle) and $ \eta > 1.479$ (right) $p_T > 20$ GeV.	76
6.6	Performances of electron MVA-based ID in three different η bins: $ \eta < 0.8$ (left), $ \eta < 1.479$ (middle) and $ \eta > 1.479$ (right) for $10 < p_T < 20$ GeV.	76
6.7	Tag and probe example fits to data for electron ID. Left: Passing probes, Right: Failing probes.	77
6.8	Tag and probe example fits to data for electron isolation. Left: Passing probes, Right: Failing probes.	78
6.9	Plots of electron ID efficiencies, binned in p_T and η . Top: ID (10-20 GeV). Bottom: ID (20+ GeV). Left: Data. Right: MC.	78
6.10	Plots of electron isolation efficiencies, binned in p_T and η . Top: Iso (10-20 GeV). Bottom: Iso (20+ GeV). Left: Data. Right: MC.	79

6.11	Muon ID scale factors per leg, broken into four eta bins.	83
6.12	Muon Iso scale factors per leg, broken into four eta bins.	84
6.13	Photon identification efficiency at 8 TeV (A+B) for (a) the barrel and the (b) the endcap. The "Medium" working point is used in this analysis. Similar performance is observed in 7 TeV data.	93
6.14	Tag-and-probe distributions used in the estimation of the photon efficiencies.	94
6.15	Electron veto efficiency for data and MC.	95
6.16	Training output and performances of the photon MVA ID. Red point on right plots represents medium WP cut-based photon ID. Top: Barrel, Bottom: Endcap.	96
6.17	Validation plots of Photon MVA ID with $Z \rightarrow \mu\mu\gamma$ MC. Left: Barrel. Right: Endcap.	97
6.18	Comparison of the fits on the $Z \rightarrow \mu\mu\gamma$ invariant mass distribution for data for 2012 AB and 2012 CD. Results for the barrel as well as for high and low R_9 are shown separately. Only the corrections at high E_T are relevant as the photon is required to have $p_T > 15$ GeV.	98
6.19	Comparison of the fits on the $Z \rightarrow \mu\mu\gamma$ invariant mass distribution for data for 2012 AB and 2012 CD. Results for the barrel as well as for high and low R_9 are shown separately. Only the corrections at high E_T are relevant as the photon is required to have $p_T > 15$ GeV.	99

6.20	Raw jet transverse momentum distribution for data and simulated signal events.	102
6.21	Jet rapidity gap distribution for data and signal events after the minimum transverse momentum on the jets is required.	102
6.22	Zeppenfeld distribution for data and signal events after requiring a minimum transverse momentum on the jets and the jet rapidity gap are required.	103
6.23	Dijet invariant mass for data and signal events after requiring a minimum transverse momentum on the jets, a jet rapidity gap and a maximum value on the Zeppenfeld variable.	103
6.24	Difference in azimuthal angle for data and signal events after requiring a minimum transverse momentum on the jets, a jet rapidity gap, a maximum value on the Zeppenfeld variable and the minimum value in the dijet invariant mass.	104
6.25	Final three-body mass distributions for the four datasets are reported for data and the main backgrounds (SM $Z\gamma$ and DYJets). Top plot is relative to 2011 $ee\gamma$, top right is for 2012 $ee\gamma$, bottom left is for 2011 $\mu\mu\gamma$ and bottom right is for 2012 $\mu\mu\gamma$.	107
6.26	Transverse momenta of final state particles in the $H \rightarrow Z\gamma$ analysis.	108
6.27	Mass distributions of $m_{ee\gamma}$ events in the four categories, before and after the $m_{\ell\ell} + m_{\ell\ell\gamma} > 185$ GeV cut.	108

6.28	Mass distributions of $m_{\mu\mu\gamma}$ events in the four categories, before and after the $m_{\ell\ell} + m_{\ell\ell\gamma} > 185$ GeV cut.	109
6.29	Mass distribution of $\mu\mu\gamma$ events vs. invariant mass distribution of $\mu\mu$ events from Z decay. The red line represents the mass-sum ($m_{\ell\ell} + m_{\ell\ell\gamma} > 185$) cut.	109
6.30	Mass distribution of $\mu\mu\gamma$ events vs. invariant mass distribution of $\mu\mu$ events from Z decay after applying the mass-sum requirement in data and simulated events for $m_H = 120$ GeV.	110
6.31	Acceptance X Efficiency as a function of signal mass for the $H \rightarrow Z\gamma$ analysis.	110
6.32	Three-body invariant mass for 2012 data for in $A \rightarrow Z\gamma$ analysis in the $\mu\mu\gamma$ (left) $ee\gamma$ (right) channel after the full analysis selection. Errors on data distributions are poissonian.	111
6.33	Transverse momentum distributions for the final state particles for the $A \rightarrow Z\gamma$ analysis. Top: dielectron channel. Bottom: dimuon channel.	111
6.34	$\gamma_{pT}/\ell\ell\gamma_m$ for signal (M200 and M500) and background. Left: Muon, Right: Electron.	112
6.35	Acceptance \times Efficiency as a function of signal mass for the $A \rightarrow Z\gamma$ analysis. Top: wide width. Bottom: narrow width. Left: dielectron channel. Right: dimuon channel.	112
6.36	The 2D dilepton distributions for the topological categories.	115

7.1	Three-body invariant mass for 2011 data in the ee γ channel after the application of the $m_{\ell\ell}+m_{\ell\ell\gamma}$ cut. Errors on data distributions are poissonian.	120
7.2	Three-body invariant mass for 2012 data in the ee γ channel after the application of the $m_{\ell\ell}+m_{\ell\ell\gamma}$ cut. Errors on data distributions are poissonian.	120
7.3	Three-body invariant mass for 2011 data in the $\mu\mu\gamma$ channel after the application of the $m_{\ell\ell}+m_{\ell\ell\gamma}$ cut. Errors on data distributions are poissonian.	121
7.4	Three-body invariant mass for 2012 data in the $\mu\mu\gamma$ channel after the application of the $m_{\ell\ell}+m_{\ell\ell\gamma}$ cut. Errors on data distributions are poissonian.	121
7.5	Three-body invariant mass for 2012 data in the $\mu\mu\gamma$ (right) and ee γ (left) channel. Errors on data distributions are poissonian.	122
7.6	Sample toy distributions for events in the ee γ channel. Truth model Gauss*pow shown, mH = 135 GeV, electron cat 4.	122
7.7	Example of mean bias (pull) distributions for events in the ee γ channel. Truth model Gauss*pow shown, mH = 135 GeV, cat 4.	122
7.8	Example of mean bias (Type-A) distributions for events in the ee γ channel. Truth model Gauss*pow shown, mH = 135 GeV, cat 4.	123
7.9	Mean signal yield for events in the ee γ channel. Truth model Gauss*pow shown, mH = 135 GeV, cat 4.	123

7.10	Background model fit to the $m_{ee\gamma}$ distribution for all event classes for the two data samples at 7 and 8 TeV. The statistical uncertainty bands shown are computed from the data fit.	124
7.11	Background model fit to the $m_{\mu\mu\gamma}$ distribution for all event classes for the two data samples at 7 and 8 TeV. The statistical uncertainty bands shown are computed from the data fit.	125
7.12	Mass distribution for the electron and the muon channels for the events in the dijet class at 8 TeV. The data is fitted to a polynomial of the third order.	126
7.13	Mass distribution for the electron and the muon channels combined for the events in the dijet class at 7 TeV. The data is fitted to a polynomial of the third order.	126
7.14	Three-body invariant mass for 2012 data in the $\mu\mu\gamma$ (left) $ee\gamma$ (right) channel with initial truth and test function fits. Errors on data distributions are poissonian.	129
7.15	Sample fits to MC toys. Left: $\mu\mu\gamma$, exp truth function, 200 GeV signal. Right: $ee\gamma$, pow truth function, 250 GeV signal.	130
7.16	Example of average signal distribution (left) and background yield (right) after 10k toys. $\mu\mu\gamma$ channel, Hill truth function, 500 GeV signal.	130
7.17	Example of bias metric distribution after 10k toys. $\mu\mu\gamma$ channel, Hill truth function, 500 GeV signal.	131

7.18	Background model fit to the $m_{\ell\ell\gamma}$ distribution for muon (left) and electron (right) channels at 8 TeV. The statistical uncertainty bands shown are computed from the data fit.	131
7.19	Crystal Ball + Crystal Ball fits in the $\mu\mu\gamma$ (left) $ee\gamma$ (right) channel for $m_H = 250$ GeV, wide signal width.	133
7.20	Crystal Ball + Gaussian fits in the $\mu\mu\gamma$ (left) $ee\gamma$ (right) channel for $m_H = 250$ GeV, narrow signal width.	133
7.21	Interpolated signals for the broad resonance signal models. Muon channel (left) and electron channel (right).	134
7.22	Interpolated signals for the narrow resonance signal models. Muon channel (left) and electron channel (right).	134
8.1	Effect of electron systematic uncertainties on expected limit for wide signal $A \rightarrow Z\gamma$ analysis. Left: Broad, Right: Narrow	137
9.1	(a) The exclusion limit on the cross section times the branching fraction of a Higgs boson decaying into a Z boson and a photon divided by the SM value. (b) Exclusion limit on the inclusive cross section alone, where the theoretical uncertainties on the cross section have been excluded in the limit setting.	147
9.2	Expected exclusion limit at 95% CL on the cross section times branching ratio for broad generated signal widths.	149

9.3 Expected exclusion limit at 95% CL on the cross section times
branching ratio for narrow generated signal widths. 150

CHAPTER 1

Introduction

The standard model of particle physics (SM) predicts all details and facets of subatomic particles: their production and decay, their charges and couplings, the interplay of matter and fields that are directly responsible for the physical universe as we know it. The search for the Higgs boson was one of the primary motivating factors for the construction of the LHC, as the Higgs was the last missing piece of the SM and had eluded experimental physicists for decades. Its discovery further confirmed the SM, which has met incredible success with respect to both its predictive power and its robustness in the face of countless experiments since its inception. While the Higgs has been discovered, it has not yet been subject to the full scientific rigour that may expose insufficiencies in the theory and lead scientists toward an even grander fundamental theory. The SM is incomplete; it does not account for observed phenomena like gravitational attraction, dark matter and energy, and the matter/anti-matter asymmetry in the observable universe. As long as there are experimentally confirmed phenomena that defy current understanding, scientists will push theories to their breaking point with ingenious experiments and analysis.

This manuscript will detail the search for the SM Higgs boson in the $H \rightarrow Z\gamma \rightarrow \ell\ell\gamma$ decay channel, and the search for a model independent, high mass resonance in the $A \rightarrow Z\gamma \rightarrow \ell\ell\gamma$ decay channel. Section 2 briefly describes the theoretical motivation for the existence of the Higgs boson, and current BSM theories that would give rise to a high mass resonance that couples to $Z\gamma$. The LHC experiment and the CMS detector are outlined in

3. Sections 4–9 describe the search for the Higgs boson and high mass resonances in the $Z\gamma$ decay mode, including the data sets used, the object reconstruction, the parametric modeling, the statistical methods employed, and the results and interpretations of those searches.

CHAPTER 2

Theory

2.1. Electroweak Symmetry Breaking

Prior to the proposal of the Higgs Mechanism, there was no widely accepted theoretical motivation for the existence of massive weak bosons. Even before the discovery of the W^\pm and Z bosons, experimentally observed short-range weak interactions implied that the weak bosons were very massive, and interacted with electromagnetic fields. However, the introduction of a simple mass term to the electromagnetic Lagrangian violates $U(1)$ gauge invariance. The following is a brief overview of the birth of the Higgs field in order to account for the mass asymmetry between the photon and the weak bosons [1, 2]. If a single complex scalar field is added to a simplified electromagnetic Lagrangian, we obtain equation 2.1:

$$(2.1) \quad \mathcal{L} = -\frac{1}{4}F_{\mu\nu}F^{\mu\nu} + |D_\mu\phi|^2 - V(\phi),$$

where

$$(2.2) \quad \begin{aligned} D_\mu &= \partial_\mu - ieA_\mu, \\ V(\phi) &= \mu^2|\phi|^2 + \lambda(|\phi|^2)^2. \end{aligned}$$

$V(\phi)$ is the most general renormalizable potential, and the Lagrangian is invariant under $U(1)$ rotations:

$$(2.3) \quad \begin{aligned} A_\mu(x) &\rightarrow A_\mu(x) - \partial_\mu \eta(x), \\ \phi(x) &\rightarrow e^{-ie\eta(x)} \phi(x), \\ \phi &\rightarrow e^{i\theta} \phi. \end{aligned}$$

If the μ^2 term in 2.2 is greater than 0, than the symmetries of the Lagrangian are preserved, and this simply describes QED with a massless photon and a single massive charged scalar. However, if $\mu^2 < 0$, then we obtain what is commonly known as the Mexican hat potential (Eq. 2.4, Fig. 2.1),

$$(2.4) \quad V(\phi) = -|\mu^2||\phi|^2 + \lambda(|\phi|^2)^2.$$

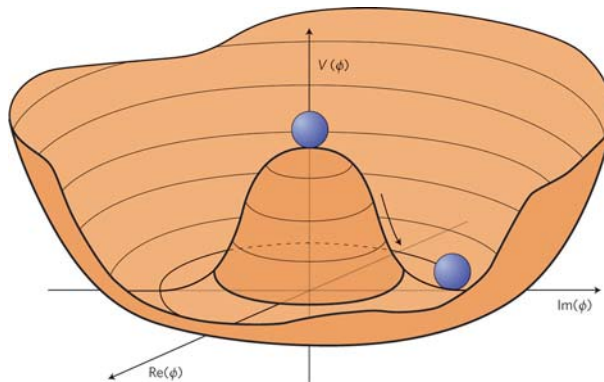


Figure 2.1. The symmetry-breaking ‘Mexican Hat Potential’. There is no minimum at $\phi = 0$, which leads to a nonzero VEV.

In this case, the minimum energy state is unstable at $\phi = 0$, and instead occurs at

$$(2.5) \quad \langle\phi\rangle = \sqrt{-\frac{\mu^2}{2\lambda}} \equiv \frac{v}{\sqrt{2}},$$

where $\langle\phi\rangle$ is the vacuum expectation value (VEV) of ϕ .

The Weinberg-Salam model of electroweak interactions can now be obtained evaluating an $SU(2)_L \times U(1)_Y$ gauge theory with complex scalar Φ and scalar potential $V(\Phi)$:

$$(2.6) \quad \begin{aligned} \Phi &= \begin{pmatrix} \phi^\dagger \\ \phi^0 \end{pmatrix}, \\ V(\Phi) &= -|\mu^2||\Phi^\dagger\Phi| + \lambda(|\Phi^\dagger\Phi|)^2. \end{aligned}$$

This complex scalar field has can be rewritten in terms of its VEV and the Higgs scalar, which arises from rewriting Φ in the unitary gauge (Eq. 2.7):

$$(2.7) \quad \begin{aligned} \langle\Phi\rangle &= \frac{1}{\sqrt{2}} \begin{pmatrix} 0 \\ v \end{pmatrix}, \\ \Phi &= \frac{1}{\sqrt{2}} \begin{pmatrix} 0 \\ v + h \end{pmatrix}. \end{aligned}$$

This choice of gauge allows Φ to be real everywhere without loss of generality. As a consequence, one of the two fields forming the initial complex scalar was “gauged away”, but its associated degrees of freedom are not lost. They are instead “eaten” by the gauge boson and form the longitudinal components of the vector field A_μ . This is known as the Higgs Mechanism, in which 3 of the degrees of freedom of Φ contribute to the mass terms of the W^\pm and Z bosons, and the fourth becomes the Higgs Field.

If we look at the Φ contribution to EW Lagragian of the form

$$(2.8) \quad \begin{aligned} \mathcal{L} &= (D^\mu \Phi)^\dagger (D_\mu \Phi) - V(\Phi), \\ D_\mu &= \partial_\mu + i\frac{g}{2}\tau W_\mu + i\frac{g'}{2}B_\mu Y, \end{aligned}$$

we can obtain the physical gauge fields corresponding to the W^\pm , Z , and photon. Equation 2.9 shows the definitions of the electroweak bosons and their masses.

$$(2.9) \quad \begin{aligned} A_\mu &= \frac{gB_\mu + g'W_\mu^3}{\sqrt{g^2 + g'^2}} \quad : M_A = 0, \\ W_\mu^\pm &= \frac{1}{\sqrt{2}}(W_\mu^1 \mp iW_\mu^2) \quad : M_W = \frac{1}{2}gv, \\ Z_\mu &= \frac{-g'B_\mu + gW_\mu^3}{\sqrt{g^2 + g'^2}} \quad : M_Z = \frac{v}{2}\sqrt{g^2 + g'^2}. \end{aligned}$$

2.2. Higgs Production

There are five main production methods that are considered in the $H \rightarrow Z\gamma$ analysis, which correspond to the five dominate methods for a 125 GeV Higgs. The leading method, which is about 10 times more prominent than the other four methods combined, is gluon-gluon fusion (ggH), which is primarily mediated by a top quark loop. Vector boson fusion (VBF), associated production with a vector boson (WH , ZH), and associated production with a top quark pair (tth) follow in decreasing likelihood. Figure 2.2 shows the relevant Feynman diagrams, and Figure 2.3 shows the various production methods for $\sqrt{s} = 8$ TeV.

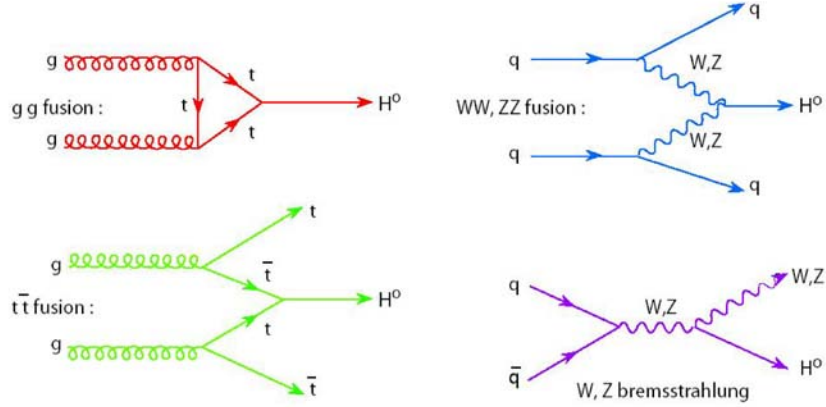


Figure 2.2. Feynman diagrams for leading order Higgs production at the LHC.

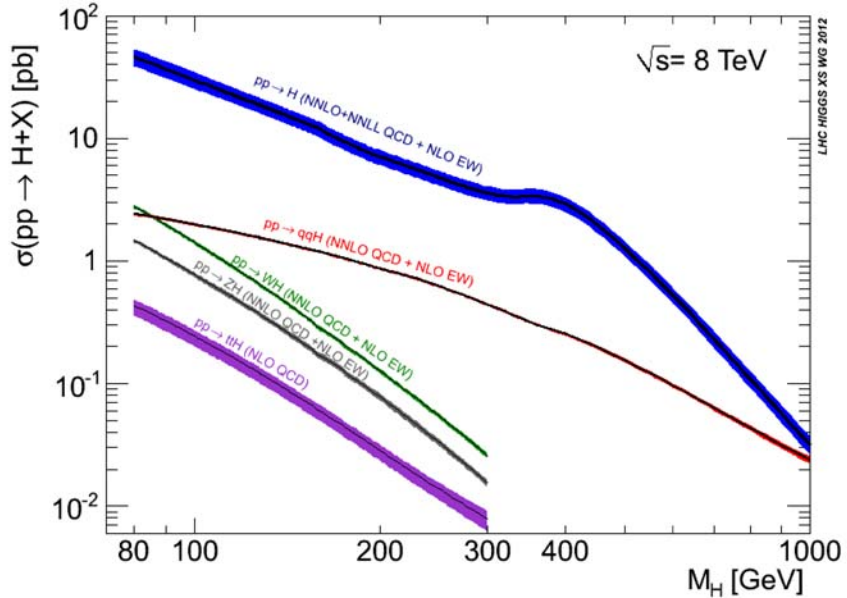


Figure 2.3. Higgs production cross sections for $\sqrt{s} = 8$ TeV. Error bands are from theoretical uncertainties.

2.3. Higgs Decay

The Higgs boson decays rapidly due to its mass, and therefore cannot be directly detected. Instead, it must be reconstructed by identifying the more stable daughter particles that are created from its decay. As it is both massive and couples to mass, the

Higgs decays tends to favor other massive bosons and fermions, as shown in Fig. 2.4. The $Z\gamma$ decay mode is not tree-level, as the photon has no mass and cannot couple directly to the Higgs boson. Instead, the $Z\gamma$ decay mode is loop-mediated at lowest order, which suppresses its decay width (Fig. 2.5).

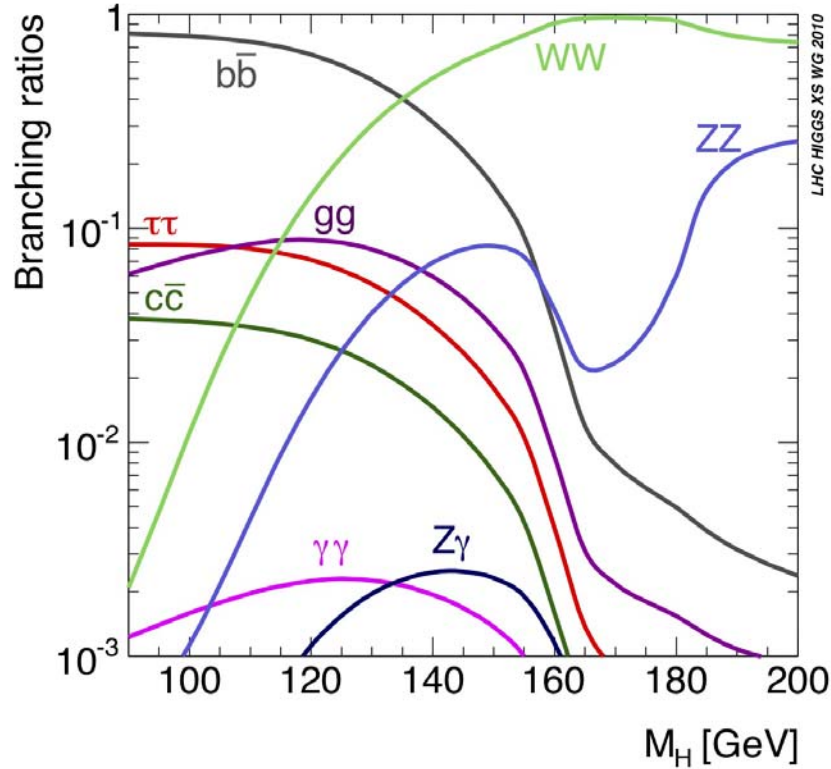


Figure 2.4. Higgs branching fractions for the most common decay modes.

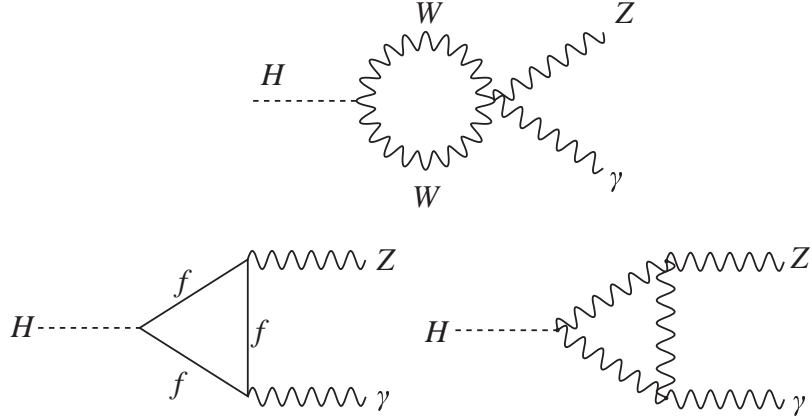


Figure 2.5. Feynman diagrams for $H \rightarrow Z\gamma$.

2.4. Physics Beyond the Standard Model

The discovery of the Higgs boson places experimental constraints on composite Higgs models, which are strong candidates for new physics that could shed light on the dark sector and the hierarchy problem. The following is a brief overview of a light, promising composite higgs model candidate that may couple to the Z boson and photon, and thus may be discoverable at the LHC.

In many common composite Higgs models, the Higgs boson similar to that of the SM model emerges as a pseudo-Nambu Goldstone Boson (pNGB), or as a composite scalar fluctuation relating to Technicolor (TC) theories [3, 4]. A particularly interesting light singlet, A , arises from an $SU(4)$ to $Sp(4)$ chiral symmetry breaking model. This scalar couples linearly to a Z boson and photon of the form:

$$(2.10) \quad g_{AZ\gamma} = \frac{gg' s_\theta c_\theta}{16\sqrt{2}\pi^2 v},$$

where θ is a free parameter. A light (less than twice the top mass) A particle would be particularly sensitive to $Z\gamma$, as it is greater than 10% of the branching fraction. It is also of interest to note that a signal would not be expected in the $\gamma\gamma$ channel, as the $A\gamma\gamma$ coupling vanishes at leading order because of the SU(4) symmetry. The production cross sections and branching fractions for A (labeled as η in the figures) are shown in Figs. 2.6 and 2.7.

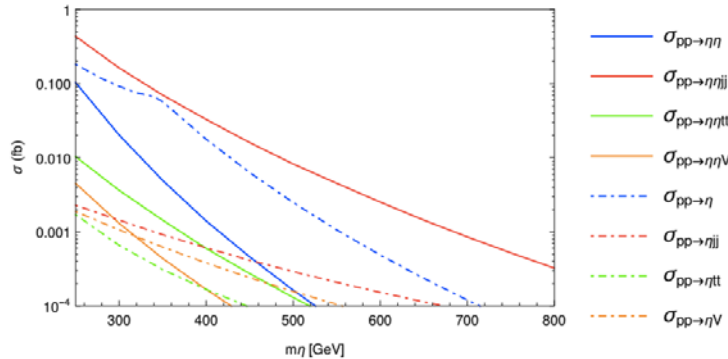


Figure 2.6. Production cross sections as a function of m_η at the LHC Run II with $\sqrt{s} = 13$ TeV.

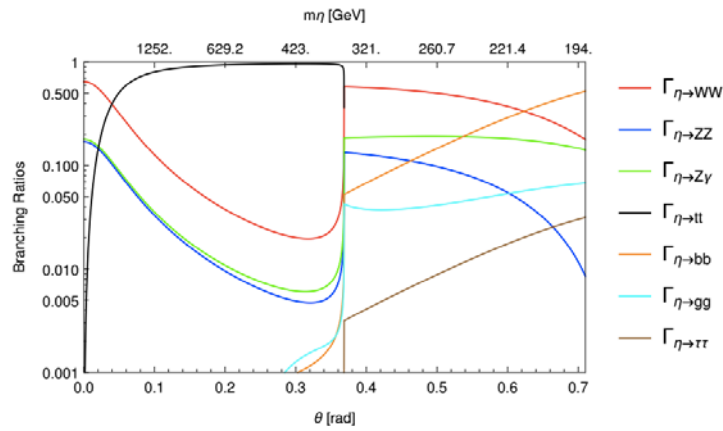


Figure 2.7. Branching ratios for the η particle as a function of θ and m_η , for $m_h = 125$ GeV.

CHAPTER 3

Experimental Apparatus

3.1. LHC

The LHC [5] is the largest and most powerful particle accelerator and collider that has ever been constructed. It is located at the European Organization for Nuclear Research (CERN) facility near Geneva, Switzerland, 50-175 meters below ground, and straddles the French-Swiss boarder. Its 27 km circumference is dotted with roughly 9300 bending, focusing and correcting magnets, and 16 RF cavities, all of which work in tandem to ensure that high energy proton-proton collisions occur up to 1 billion times per second. The peak design specifications are for a proton-proton center of mass energy of $\sqrt{s} = 14 \text{ TeV}$, at a luminosity of $\mathcal{L} = 10^{34} \text{ cm}^{-2}\text{s}^{-1}$.

In order to reach the maximum energy of 7 TeV per beam, the protons must flow through a series of smaller accelerators before finally being injected into the LHC. They start innocently enough as ionized hydrogen gas, are then passed through a linear accelerator (LINAC2), and then into three progressively larger synchrotrons (the PSB, PS, and SPS). Finally, at an energy of 450 GeV, the protons enter the LHC and are ramped up to their maximum energy before colliding with an opposing beam at one of the four interaction points (Fig. 3.1).

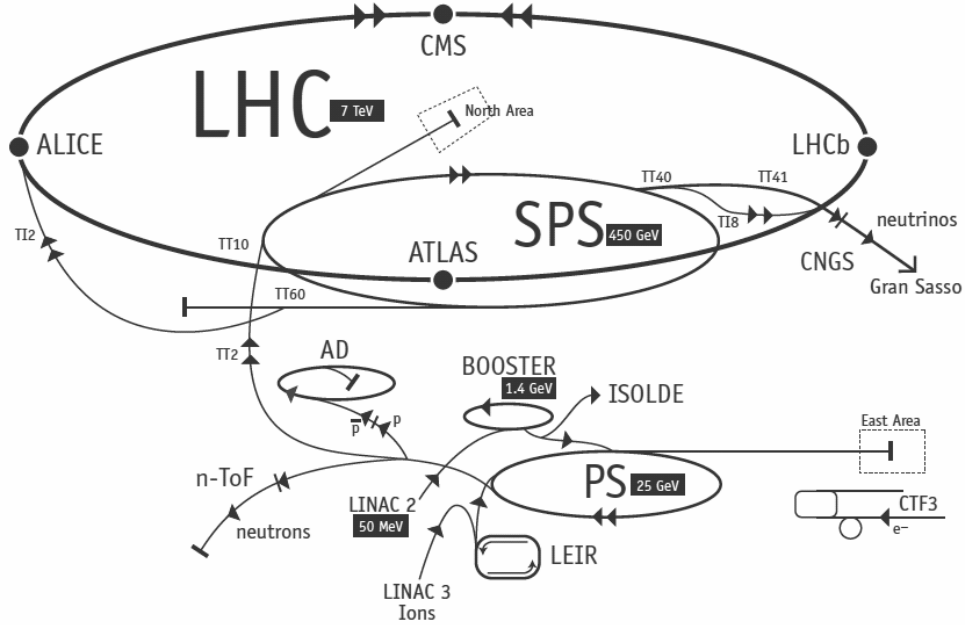


Figure 3.1. General layout of the LHC experiments, as well as the accelerator complex which supplies them with collisions.

Table 3.1 gives a summary of the relevant design parameters that characterize the LHC, while table 3.2 lists the relevant parameters that differ from design for the 2011 and 2012 data-taking period.

Requirement	
Energy per Proton	7 <i>TeV</i>
Dipole Mag. Field	8.33 <i>Tesla</i>
Design Lumi.	$10^{34} \text{ cm}^{-2}\text{s}^{-1}$
Bunch Separation	25 <i>ns</i>
Num. of Bunches	2808
Num of Protons/bunch	1.15×10^{11}
β^* at Inter. point	0.55 <i>m</i>
RMS beam radius at Inter. point	167 μm
Luminosity lifetime	15 <i>hr</i>
Number of collisions/crossing	≈ 20

Table 3.1. A short list of relevant LHC design parameters.

Requirement	2011	2012
Energy per Proton	3.5 TeV	4 TeV
Bunch Separation	50 ns	50 ns
Num. of Bunches	1380	1380
Num of Protons/bunch	1.0×10^{11}	1.65×10^{11}
Number of collisions/crossing	≈ 10	≈ 30

Table 3.2. A short list of relevant LHC parameters for the 2011 and 2012 data taking runs.

3.2. The Compact Muon Solenoid (CMS)

The Compact Muon Solenoid (CMS) [6] is one of two general purpose detectors at the LHC. It is a cylindrical, almost fully hermetically sealed detector, measuring 21.6 m long, 14.6 m in diameter, and 12500 tonnes (Fig. 3.2). The detector is designed around a large, high field, superconducting solenoid, which is necessary for accurately measuring the momenta of charged particles. A high granularity silicon-based tracking system along with electromagnetic (ECAL) and hadronic (HCAL) calorimetry is located within the solenoid, while a multi-detector muon system surrounds the outside of the magnet. Another hadronic calorimeter for forward jet detection resides near the beam line, directly after the muon system endcaps. A more detailed description of the various sub-systems can be found in the following sections.

3.2.1. Superconducting Magnet

CMS is designed around a superconducting solenoidal magnet with a length of 12.5 m, diameter of 6.3 m, and approximate mass of 220 tons. This magnet is necessary for accurate measurements of the momentum of high energy charged particles (especially muons, as they do not deposit significant amounts of energy into the calorimeters). The

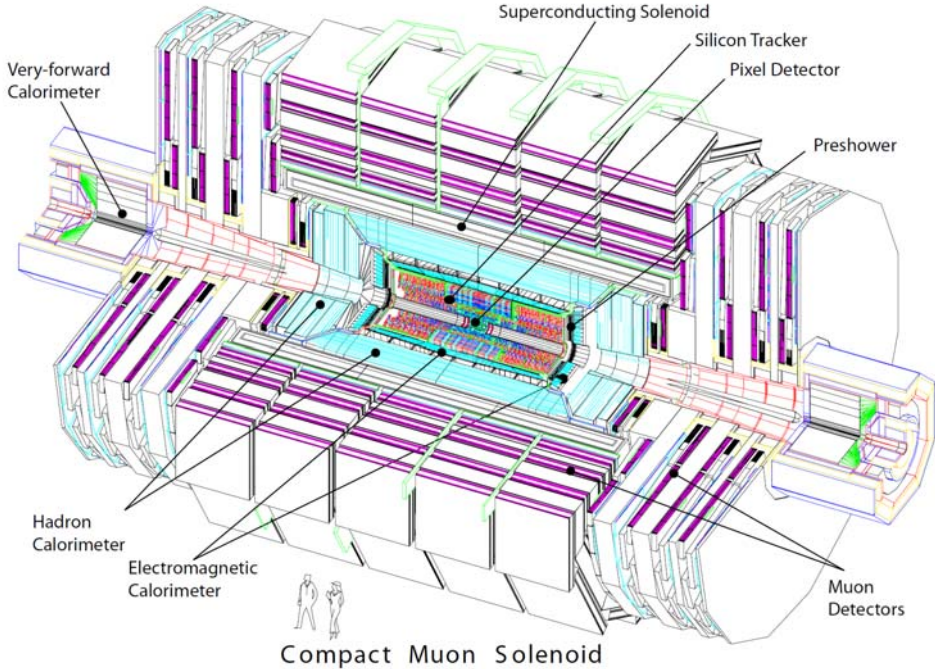


Figure 3.2. Schematic view of the CMS detector showing the various sub-detectors.

magnet is designed to supply the experiment with a 4 T magnetic field within the solenoid itself, however the working field strength of CMS is 3.8 T (a decision made to prolong the life of the magnet). The active bulk of the magnet is composed of NbTi, which is cooled to 4.5 K using liquid He. The silicon tracking system, the electromagnetic calorimeter, and the majority of the hadronic calorimeter are housed within the interior of the magnet.

3.2.2. Inner Tracking System

The inner tracking system (Fig. 3.3), located immediately outside of the beam pipe and extending to a radius of 1.25 m, consists of 1440 silicon pixel and 15148 silicon strip detector modules. This system was designed to measure the momentum of charged tracks, identify decay vertices, and identify photons which convert to e^+e^- pairs before depositing

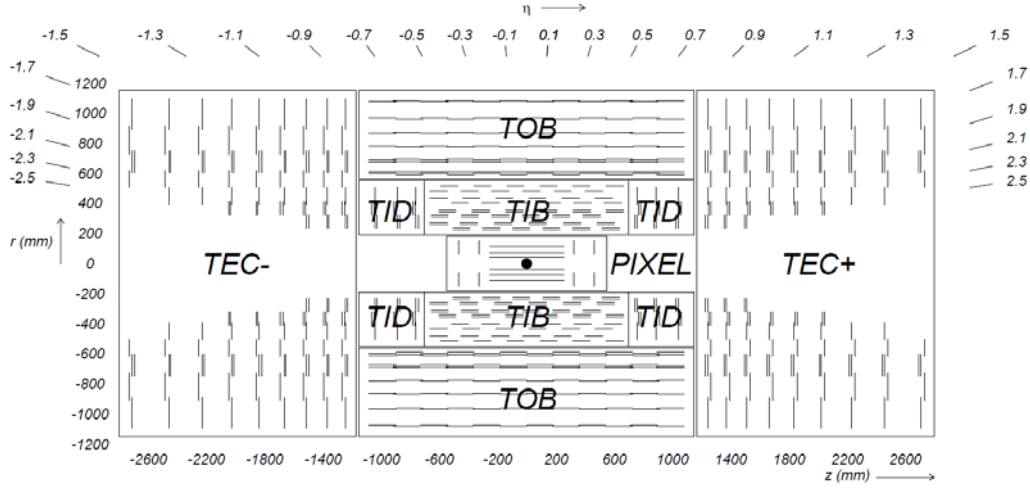


Figure 3.3. Schematic side-view of the CMS silicon tracker.

energy into the electromagnetic calorimeter. The need for a precise, high granularity, high speed, radiation hard tracking system motivated the decision to construct the largest silicon tracker to date.

The pixel system is located closest to the interaction point. There are 66 million $100 \times 150 \mu\text{m}^2$ silicon pixels, arranged in three barrel layers and two endcap disks, resulting in an active area of $\approx 1 \text{ m}^2$. The strip detector modules are located directly adjacent to the pixel system. The innermost strips consist of 4 barrel layers and 3 endcap disks, where each strip is $320 \mu\text{m}$ thick. The outer strip system surrounds the inner, and consists of 6 barrel layers of $500 \mu\text{m}$ thick strips, and the outer endcaps consist of 9 disks, with strip thickness of $320 \mu\text{m}$ and $500 \mu\text{m}$ for the inner and outer disks, respectively. All tracker systems cover a range in pseudorapidity of $|\eta| < 2.5$.

The tracker provides a momentum resolution ranging from $\approx 0.6\text{--}6\%$, depending on the transverse momentum and pseudorapidity of a given charged particle. Figure 3.4 shows

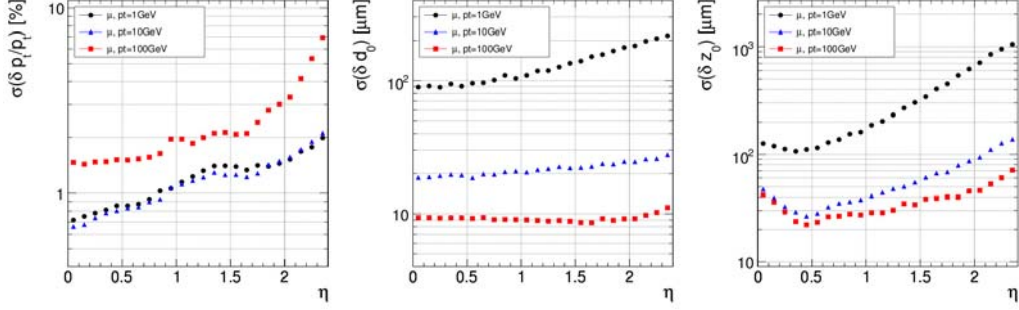


Figure 3.4. CMS tracker resolution performance as a function of η for three different charged particle momenta. Resolution for transverse momentum (left), transverse vertex resolution (center), and longitudinal vertex resolution (right) are shown.

the performance of the CMS tracker with regards to momentum and vertex resolution measurements.

3.2.3. Electromagnetic Calorimeter

The CMS ECAL (Fig. 3.5) boasts fine granularity, short radiation length, and high hermeticity and homogeneity, all of which lead to good energy resolution for high energy electromagnetic particles. These design decisions were driven, in part, to facilitate the discovery of the Higgs boson diphoton decay mode, but benefit any analysis that uses electrons or photons. The ECAL consists of Lead Tungstate ($PbWO_4$) crystals, 61200 of which are located in the barrel ($|\eta| < 1.5$), and 14846 of which are located in the endcap ($1.5 < |\eta| < 3.0$).

The crystals that compose the barrel (endcap) region measure $26 \times 26 \text{ mm}^2$ ($30 \times 30 \text{ mm}^2$) on the rear surface and smoothly taper to $22 \times 22 \text{ mm}^2$ ($28.62 \times 28.62 \text{ mm}^2$) on the front surface, and each have a length of 230 mm (220 mm). The crystal length for the barrel and endcap correspond to a radiation length of $25.8 X_0$ and $24.7 X_0$, respectively.

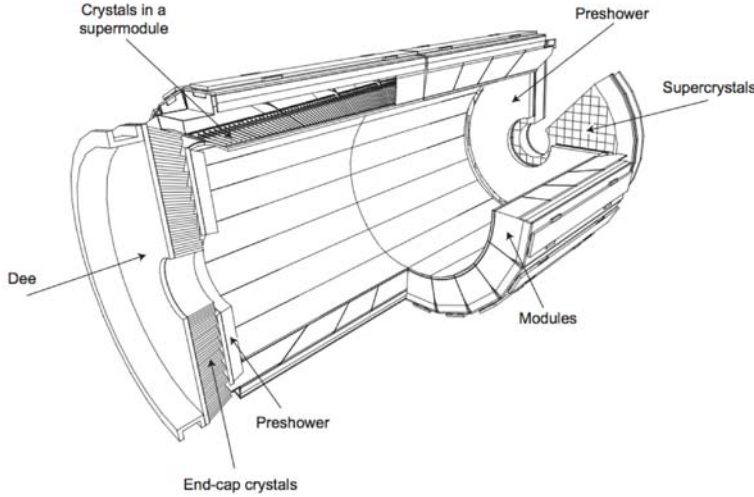


Figure 3.5. Schematic of the CMS ECAL.

To improve particle identification and position determination, the Preshower detector is located in front of the crystals in the endcap region. The Preshower is a two layer sampling calorimeter made of lead and silicon, with a total radiation length of $\approx 3 X_0$. This causes roughly 95% of single incident photons to start showering before reaching the second layer. This feature allows discrimination between photons and neutral pions in the endcap, and discrimination between electrons and other minimally ionizing particles (MIPs).

The energy resolution of the ECAL is dependent on the energy of the incident photon/electron, and is parameterized as

$$(3.1) \quad \left(\frac{\sigma}{E}\right)^2 = \left(\frac{S}{\sqrt{E}}\right)^2 + \left(\frac{N}{E}\right)^2 + C,$$

where the S, N, and C correspond to the stochastic, noise and constant terms respectively, which were determined to be $S = 2.8\%$, $N = 12\%$, and $C = 0.3\%$ during test beam

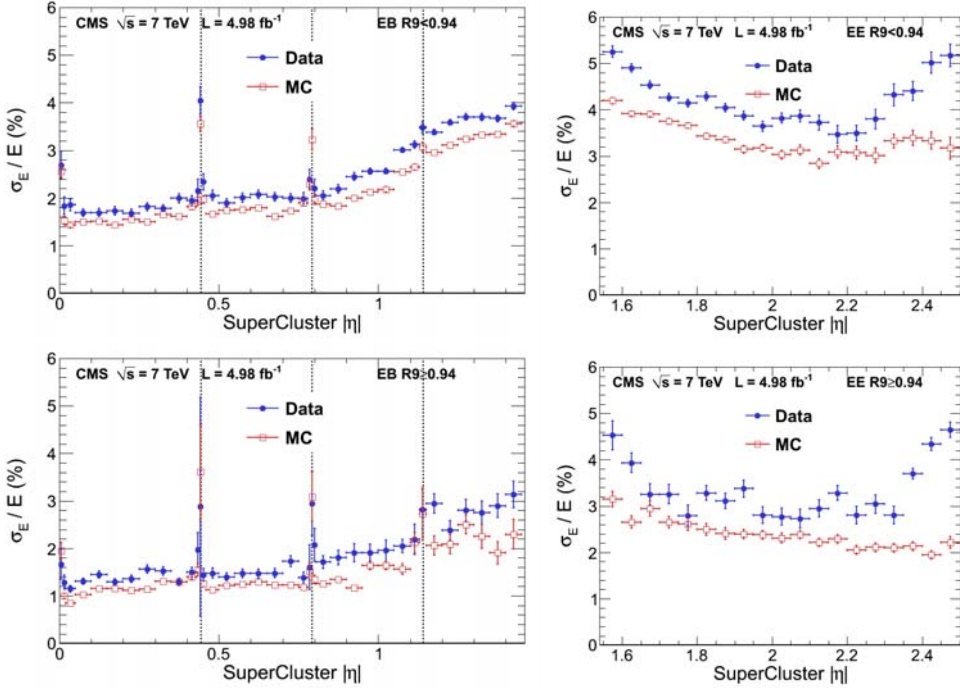


Figure 3.6. Electron energy resolution as a function of η in $Z \rightarrow ee$ events. The top two plots are of electrons that have a large footprint inside the ECAL. The bottom two plots represent electrons that have a much smaller footprint.

operations [7]. A plot of the resolution performance of electrons from the 2011 data period is shown in Fig. 3.6. A subsequent study of photon resolution using $H \rightarrow \gamma\gamma$ simulation is shown in Fig. 3.7 [8].

3.2.4. Hadronic Calorimeter

The accurate measurement of hadronic final states is crucial for a wide range of analyses at CMS. The CMS HCAL (Fig. 3.8) is mainly a brass and plastic sampling calorimeter designed to provide measurements of the position and momenta of hadronic jets. The majority of the HCAL is situated just outside of the ECAL, but still within the bore of

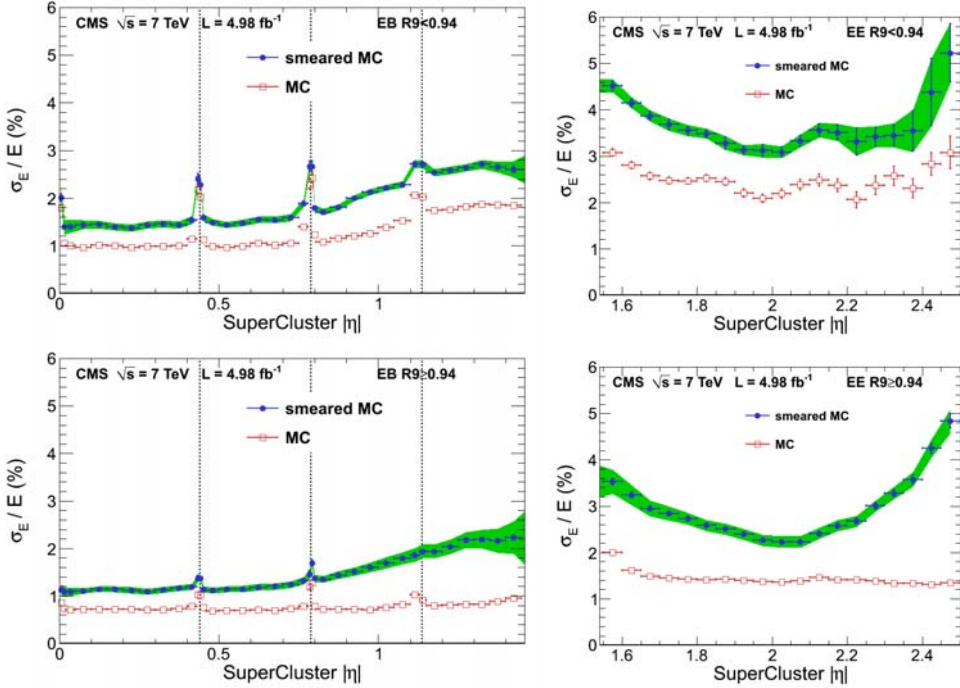


Figure 3.7. Photon energy resolution as a function of η in simulation. The top two plots are of photons that have a large footprint inside the ECAL, most likely due to showering within the tracker. The bottom two plots have a much smaller footprint, as they do not start to shower until entering the ECAL.

the magnet. It consists of four main subdetectors: the inner barrel (HB) and the outer barrel (HO) that cover $|\eta| < 1.3$, the endcaps (HE) that cover $1.3 < |\eta| < 3.0$ (HE), and the very forward (HF) that covers $3.0 < |\eta| < 5.0$. The HB is contained within the bore of the magnet, but it is radially restricted by the physical dimensions of the magnet and thus cannot fully absorb a high energy hadronic shower. To combat this issue, the HO is located directly outside the magnet, and acts as a tail catcher for hadronic showers that punch through the HB and magnet. Like the HB, the HE is also contained within the magnet bore, but the HF is situated outside of the magnet and the muon system.



Figure 3.8. Schematic side-view of the CMS HCAL.

The HB, HE, and HO are constructed of plastic scintillator tiles sandwiched between brass absorber plates to induce hadronic showers. The total amount of energy deposited into the brass plates cannot be directly measured, and must be inferred from the scintillator outputs. The HB (HE) absorber plates are 50.5–56.5 mm (79 mm) thick, while the scintillator panels are 3.7 mm (9 mm) thick.

The HF differs in construction and technology due to the high radiation environment in which it resides. It consists of quartz fibers and steel plate absorbers as opposed to plastic scintillators and brass. The fibers run lengthwise through the detector, and are composed of two types: long fibers which run the whole length of the detector and short fibers which only start at a depth of 22 cm away from the interaction point. The difference in fibre length allows HF to discriminate between electromagnetic and hadronic showers, as electromagnetic showers tend to initiate and deposit more quickly than their hadronic counterparts.

3.2.5. Muon Detectors

Muons are ideal final state particles; they deposit minimal energy into detector material but leave clear signatures in tracking systems, and thus can be accurately reconstructed without significant contamination from other high energy particles. The muon detectors are located outside of the calorimeters and the magnet, which both suppresses hadronic contamination and allows for a large track length when combined with measurements from the inner tracking system. The muon system consists of three different subdetectors: Drift tubes (DTs), which cover the barrel region of the detector, cathode strip chambers (CSCs), which cover the endcaps, and resistive plate chambers (RPCs), which overlap the other systems and provide redundant position and triggering functionality. A schematic diagram of the muon system is shown in Fig. 3.9. The muon resolution as a function of transverse momentum is shown in Fig 3.10.

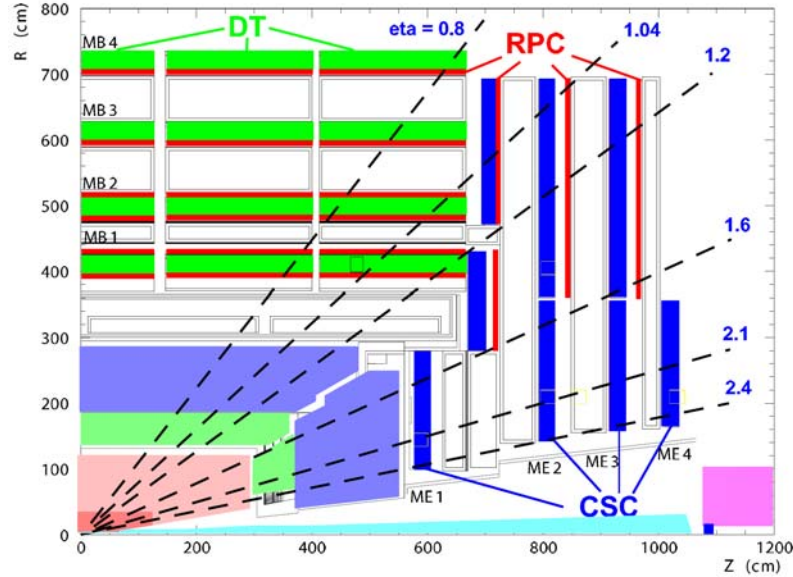


Figure 3.9. Schematic side-view of the CMS Muon detectors.

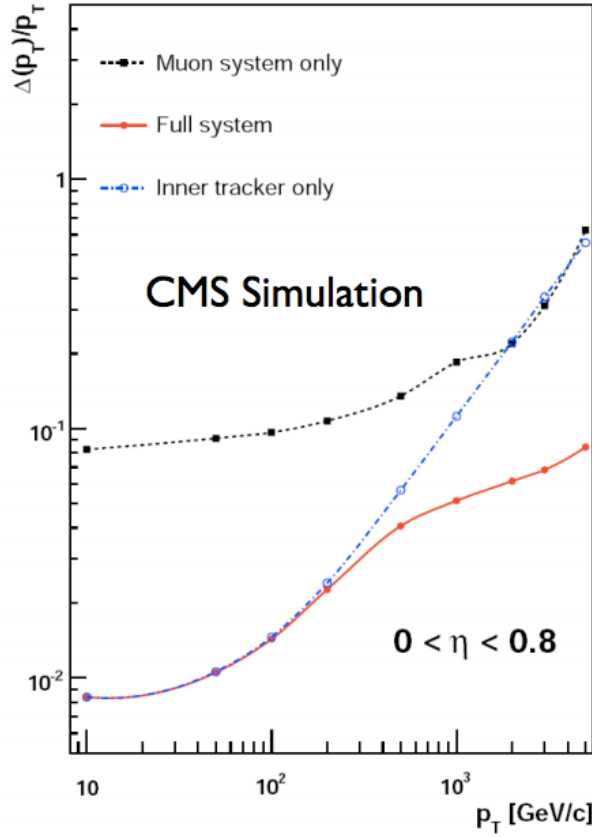


Figure 3.10. Muon resolution as a function of the transverse momentum.

3.2.6. Trigger

The LHC collides protons at a rate of 20-40 MHz (50 or 25 ns bunch spacing), which would be entirely too much data to write out if each event were recorded. To handle this exorbitant data rate, CMS uses a two-tier trigger system. The first tier, the Level - 1 Trigger (L1T), is a hardware-based system that incorporates the outputs of all the subdetectors. Rough measurements of particle momenta and energy are computed and passed to the global trigger system. The L1T reduces the event rate down to about 100 kHz, but further reduction is necessary in order to write out all interesting events.

The second tier is the High-Level Trigger (HLT). It is seeded by the L1T, but is software based, and uses full or close to full physics object reconstruction. This reduces the total event rate down to about 100 Hz, which can be recorded and written to disk. There are many HLTs, which trigger on various physics objects, and write out to different data streams. Of particular importance to the analyses in this document are the Double Muon and Double Electron streams, which are triggered by events with two muon or electron objects that pass the minimum transverse momentum thresholds. Some triggers do not record every event that satisfies the trigger requirements; these triggers are “prescaled”, usually because the trigger threshold is too loose and the event rate would be too high to record.

CHAPTER 4

Analysis

The following chapters describe the search for both the Higgs boson and a generic high mass resonance in the $Z\gamma \rightarrow \ell\ell\gamma$ decay channels. These searches are similar to one another in approach and execution, and will therefore be presented in parallel. When the two analyses diverge, special care will be given to emphasise the differences in analysis techniques. Both analyses are performed on data collected at the CMS detector at the LHC, select events in which there are well isolated and identified photon and dilepton pairs, perform data-driven background estimation techniques, and set upper limits on the production and decay of their respective parent particles. Unless specifically stated otherwise, analysis details will be relevant for both the SM Higgs search and the high mass resonance search.

Section 5 describes the data and simulation used in the analyses. The $Z \rightarrow \ell\ell$ decay requirement leads to an obvious trigger and datastream choice. Dimuon and dielectron streams are chosen, as they have the lowest transverse momenta requirements on the lepton pairs, and no requirement on photons. This prevents unnecessary efficiency loss during event selection by taking full advantage of the low momenta particle reconstruction available at the LHC. Simulated signal distributions are generated to model the shape and kinematic features that arise during the $Z\gamma$ decay process. Simulated background is used for selection optimization purposes, but not for background yield estimation.

The identification, isolation, and calibration of the dilepton and photon objects are described in Section 6.1. Electrons and muons are required to be well separated and well isolated from each other and from the photon. The $Z\gamma$ production should arise directly from the decay of a single, massive parent particle, and therefore small separation distance between particles is more indicative of background processes. Additionally, the default reconstruction of particle kinematics is imperfect. Corrections to the energy and momenta of all the final state particles are applied to improve the resolution of the reconstructed resonances and to reduce systematic uncertainties that arise from suboptimal reconstruction.

After all three final state particles are selected, further cuts are placed on surviving events to reduce background contamination while preserving signal acceptance. Section 6.2 describes these analysis requirements. Background contamination tends to come from either true SM processes (final and initial state photon radiation during Z production and decay) or particle misreconstruction (hadronic jets that are reconstructed as photons). The event selection process also takes care to prevent unwanted shaping of the $m_{\ell\ell\gamma}$ invariant mass distribution, which could hinder parametric background estimation.

Parametric modeling of the background and signal distributions are described in section 7. The background model is derived directly from the data distribution. The event selection requirements, background contamination, and detector effects render the use of a theoretically motivated parametric function impractical. Instead, a large selection of functional families are tested and selected based on a series of fit-bias studies. These studies are similar in nature to parametric bootstrapping, and make use of bias-variance

trade-offs to minimize uncertainties in background estimation without artificially enhancing signal yield in any given region. The signal modeling is simpler, and makes use of theoretical resonance shapes convoluted with error terms to account for detector-based resolution effects. To improve the granularity of the searches, more signal models are produced through linear interpolation of the existing samples.

Sources of systematic uncertainty are discussed in section 8. The sources include the estimation of reconstructed particle efficiency, luminosity measurements, and model dependent parameters. There are no systematic uncertainties associated with background estimation; the background estimation is chosen such that the statistical uncertainty dwarfs any potential bias that may be introduced by the choice of parameterization. While some sources of uncertainty are conservative, the sensitivity of these analyses are mainly dependent on the statistical uncertainty that arises from the total amount of collected data.

Section 9 describes the results and interpretations of the analyses. Confidence intervals are determined in order to place limits on the maximum production and decay rates for the aforementioned resonances.

CHAPTER 5

Data and Simulation

5.1. Data Samples

The data sets used in the $H \rightarrow Z\gamma$ and $A \rightarrow Z\gamma$ analyses were collected at the CMS detector during the 2011 ($H \rightarrow Z\gamma$ only) and 2012 (both $H \rightarrow Z\gamma$ and $A \rightarrow Z\gamma$) run periods. As it is impossible to record all collision events that occur during any given run period, certain hardware and software triggers must activate during a collision event in order for that event to be recorded. The analyses use the lowest threshold double lepton trigger available for a given run period. A double lepton trigger requires that the event has at least two leptons that meet minimum momenta requirements and pass basic identification criteria. The double muon and double electron triggers are the most relevant, as two visible, opposite sign, same flavor leptons are integral parts of the final states of the analyses.

The primary 2011 and 2012 datasets are summarized in Table 5.1. The $H \rightarrow Z\gamma$ and $A \rightarrow Z\gamma$ analyses use slightly different versions of the 2012 data set because the former was performed before the latest version of the 2012 data was released. The differences are minor, and include slight improvements in calibration and the recovery of roughly 0.5% more events in both data streams.

Table 5.1. Summary of 2011 and 2012 data samples.

Dataset Description	Used by	Integrated Luminosity (fb^{-1})
Double Electron, 2011 Run	$H \rightarrow Z\gamma \rightarrow \ell\ell\gamma$	4.98
Double Muon , 2011 Run	$H \rightarrow Z\gamma \rightarrow \ell\ell\gamma$	5.05
Double Electron, 2012 Run (v1)	$H \rightarrow Z\gamma \rightarrow \ell\ell\gamma$	19.6
Double Muon , 2012 Run (v1)	$H \rightarrow Z\gamma \rightarrow \ell\ell\gamma$	19.6
Double Electron, 2012 Run (v2)	$A \rightarrow Z\gamma \rightarrow \ell\ell\gamma$	19.7
Double Muon , 2012 Run (v2)	$A \rightarrow Z\gamma \rightarrow \ell\ell\gamma$	19.7

5.2. Simulation Samples

Simulated data samples are needed for determining the expected distributions of the signals that are searched for in these analyses. The simulations are created in multiple steps in order to mimic the underlying physical processes that occur during collision and decay, the interaction between the detector material and high energy particles, and the electrical outputs of the relevant subdetectors. The samples are generated via Monte Carlo (MC) methods, starting with a leading order (LO) or next-to-leading order (NLO) generator, then a hadronic and electromagnetic showering program, which is then fed into a detector simulation program.

Both background and signal samples are generated for these analyses. In principle, background MC could be used to estimate the total background contribution in data. However, the region of interest is poorly modeled by MC, and would require specially generated, high statistics samples, or large systematic uncertainties, or both. To avoid those outcomes, MC background is only used as a sanity check for data distributions and for cut optimization; background yield estimates are determined via a completely data-driven approach 7.1.

Signals samples for $H \rightarrow Z\gamma$ were generated with POWHEG [9] at NLO for the gluon-gluon fusion and vector boson fusion Higgs production process. Associated production samples and the subsequent $Z\gamma$ decay for all samples were handled by PYTHIA6.4 [10]. Signal was generated from $120 < m_H < 160$ GeV in 5 GeV steps. The $A \rightarrow Z\gamma$ samples were generated at LO with PYTHIA8.175 [11] for the gluon-gluon production mode only, for the range $200 < m_A < 1200$ GeV in 50 GeV steps.

All signals are produced using a spin-0 Higgs Boson with a subsequent decay to a Z-boson and a photon. The Z is then allowed to decay to a charged lepton pair (e^+e^- , $\mu^+\mu^-$, $\tau^+\tau^-$). The narrow width signals for the $A \rightarrow Z\gamma$ analysis are produced with the same production and decay particles, but the Higgs Boson is given a Breit-Wigner width of 1% of the Higgs mass. Because one of the goals of the $A \rightarrow Z\gamma$ analysis was to maximize model independence, it is unnecessary to generate signals at NLO, as only the final shape of the signal distribution is used to determine total signal yield, and there is no categorization based upon particle kinematics.

The background samples were generated with MADGRAPH [12] at NNLO to model the SM $Z\gamma$ contribution, while POWHEG at NLO was used to model the Z + Jets contribution. Special care was taken to remove QED photon events from the jet sample to prevent double-counting when used in conjunction with the SM $Z\gamma$ sample.

The Monte Carlo signal and background samples used in this analysis are given in Table 5.2. The cross-sections and branching fractions are obtained from the LHC Cross Section Working Group recommendations [13]. For the $H \rightarrow Z\gamma$ analysis, the number of expected events for each production process is given in Table 5.3

Table 5.2. Summary of MC signal and BG samples.

Simulation Description	Used by	Cross Section (pb)
Higgs signal (ggf) (120-160 GeV)	$H \rightarrow Z\gamma$	4.98
Higgs signal (vbf) (120-160 GeV)	$H \rightarrow Z\gamma$	4.98
Higgs signal (whzh) (120-160 GeV)	$H \rightarrow Z\gamma$	4.98
Higgs signal (tth) (120-160 GeV)	$H \rightarrow Z\gamma$	4.98
Scalar signal (broad) (200-1200 GeV)	$A \rightarrow Z\gamma$	4.98
Scalar signal (narrow) (200-1200 GeV)	$A \rightarrow Z\gamma$	4.98
SM $Z\gamma$ (MADGRAPH)	$H \rightarrow Z\gamma$ and $A \rightarrow Z\gamma$	100
$Z + \text{Jet}$ (POWHEG)	$H \rightarrow Z\gamma$ and $A \rightarrow Z\gamma$	100

Table 5.3. Expected signal yields for a 125 GeV SM Higgs boson for each production process.

Sample	Luminosity (fb^{-1})	num. of GF events	num. of VBF events	num. of VH events	num. of ttH events
2011 ee	4.98	1.1	0.09	0.07	0.005
2011 $\mu\mu$	5.05	1.3	0.1	0.07	0.005
2012 ee	19.62	5.5	0.5	0.3	0.03
2012 $\mu\mu$	19.62	6.1	0.5	0.4	0.03

5.2.1. Pileup Reweighting

All simulations include accurate distributions of the number of interactions taking place in each bunch crossing. On average, 10 to 20 proton-proton collisions occur for each recorded event, but only one of those collisions tend to produce the desired final state particles. The rest of the interactions only help to obfuscate the interesting physics by contaminating the detector with extra particles that negatively impact the reconstruction and resolution of the primary interaction. These extra collisions are known as pileup (PU), and all simulation must account for their effects in order to produce reliable results.

Although the Deterministic Annealing primary vertex reconstruction [14] has been shown to be efficient and well-behaved up to the levels of pileup in the 2011 and 2012 data,

the final distribution for the number of reconstructed primary vertices is still sensitive to the details of the primary vertex reconstruction and to the underlying events in data compared to MC. Additionally, there is a potentially larger effect where the distribution for the number of reconstructed vertices can be biased by the offline event selection criteria and even by the trigger. In order to factorize these effects, instead of reweighting the MC by the number of reconstructed Primary Vertices, the events are reweighted to the number of pileup interactions from the simulated observed interactions. The target pileup distribution for data is derived by using the per bunch-crossing, per luminosity-section instantaneous luminosity, together with the total pp inelastic cross-section (69.3 mb for 8 TeV) to generate an expected pileup distribution, correctly weighted by the per-bunch-crossing-per-lumi section integrated luminosity over the relevant data-taking period. Of all the available pileup simulation options, two run-independent versions are used, which corresponds to the expected amount of pileup produced during the entire 2011 and 2012 run periods, respectively. As shown in Fig. 5.1, using this pileup description results in a reasonable agreement between data and simulated events.

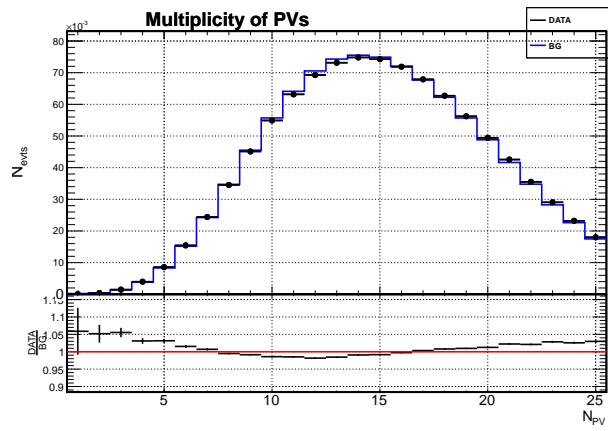


Figure 5.1. Distribution of the number of vertices in the 2012 data sample and simulation.

CHAPTER 6

Object and Event Selection

6.1. Object Selection

6.1.1. Triggers

Entirely too much data is produced at the LHC to record each collision. In order to determine which event is interesting enough to save to disk, a series of software and hardware triggers are employed by CMS, as described in 3.2.6. Analyses rely on High Level Triggers (HLTs), which combine the outputs of the hardware level triggers with some basic particle reconstruction algorithms. If the thresholds for a given HLT are met, that event is recorded and routed to the relevant data stream. The data streams used in these analyses are either Double Muon or Double Electron.

The analyses cover two lepton channels, corresponding to the $e e \gamma$ and $\mu \mu \gamma$ final states. Both channels use the lowest momentum threshold, un-prescaled double lepton triggers available for the given run ranges. These trigger requirements are needed in order to properly calculate the total integrated luminosity and correct for potential differences in data acquisition efficiency between data and MC.

Double lepton trigger efficiencies and scale factors are calculated via the tag-and-probe (TnP) method [15]. In general, the tag-and-probe method uses $Z \rightarrow \ell\ell$ in order to measure single-lepton efficiencies. A tight, high-purity lepton is selected to *tag* the event, and the selection criteria in question is placed on the other *probe* lepton. The ratio of

passing probes (given a tagged lepton) to total tagged events within a Z peak is used to determine the efficiency of that probe. A single lepton trigger is used to tag events for double lepton trigger leg efficiencies.

In order to determine the total efficiency of an event that passes a double lepton trigger, the overall passing probability must take into account the individual efficiencies of each lepton leg (6.1):

$$\begin{aligned}
 \epsilon_{DoubleTrig} &= 1 - P(fail) \\
 &= 1 - P(single\ leg\ fails) - P(both\ legs\ fail) \\
 (6.1) \quad &= 1 - \{\epsilon_{\ell_1,leg_1} \cdot (1 - \epsilon_{\ell_2,leg_2}) + \epsilon_{\ell_2,leg_1} \cdot (1 - \epsilon_{\ell_1,leg_2})\} \\
 &\quad - \{(1 - \epsilon_{\ell_1,leg_1}) \cdot (1 - \epsilon_{\ell_2,leg_1})\} \\
 &= \epsilon_{\ell_1,leg_1} \cdot \epsilon_{\ell_2,leg_2} + \epsilon_{\ell_2,leg_1} \cdot \epsilon_{\ell_1,leg_2} - \epsilon_{\ell_1,leg_1} \cdot \epsilon_{\ell_2,leg_1}.
 \end{aligned}$$

6.1.1.1. Electron Triggers. For the $Z\gamma \rightarrow ee\gamma$ final states, the HLT_Ele17_CaloIdT_CaloIsoVL_TrkIdVL_TrkIsoVL_Ele8_CaloIdT_CaloIsoVL_TrkIdVL_TrkIsoVL trigger is used in the Double Electron data stream and related MC. Efficiencies for the electron trigger are measured via the TnP method, where the electron candidates are required to pass the ID and isolation requirements given in section 6.1.3. Additionally, the tag electron is required to match with an HLT_Ele27_WP80 trigger object. The efficiencies for the trailing and leading legs are calculated separately, and the total scale factors are calculated from Eq. 6.1. Probe electrons are broken into bins of p_T and η , and the number of Z boson candidates is determined by a simple counting method.

Trigger efficiencies for the 2011 run are shown in Fig 6.1, and for the 2012 run are shown in Fig 6.2-6.3.

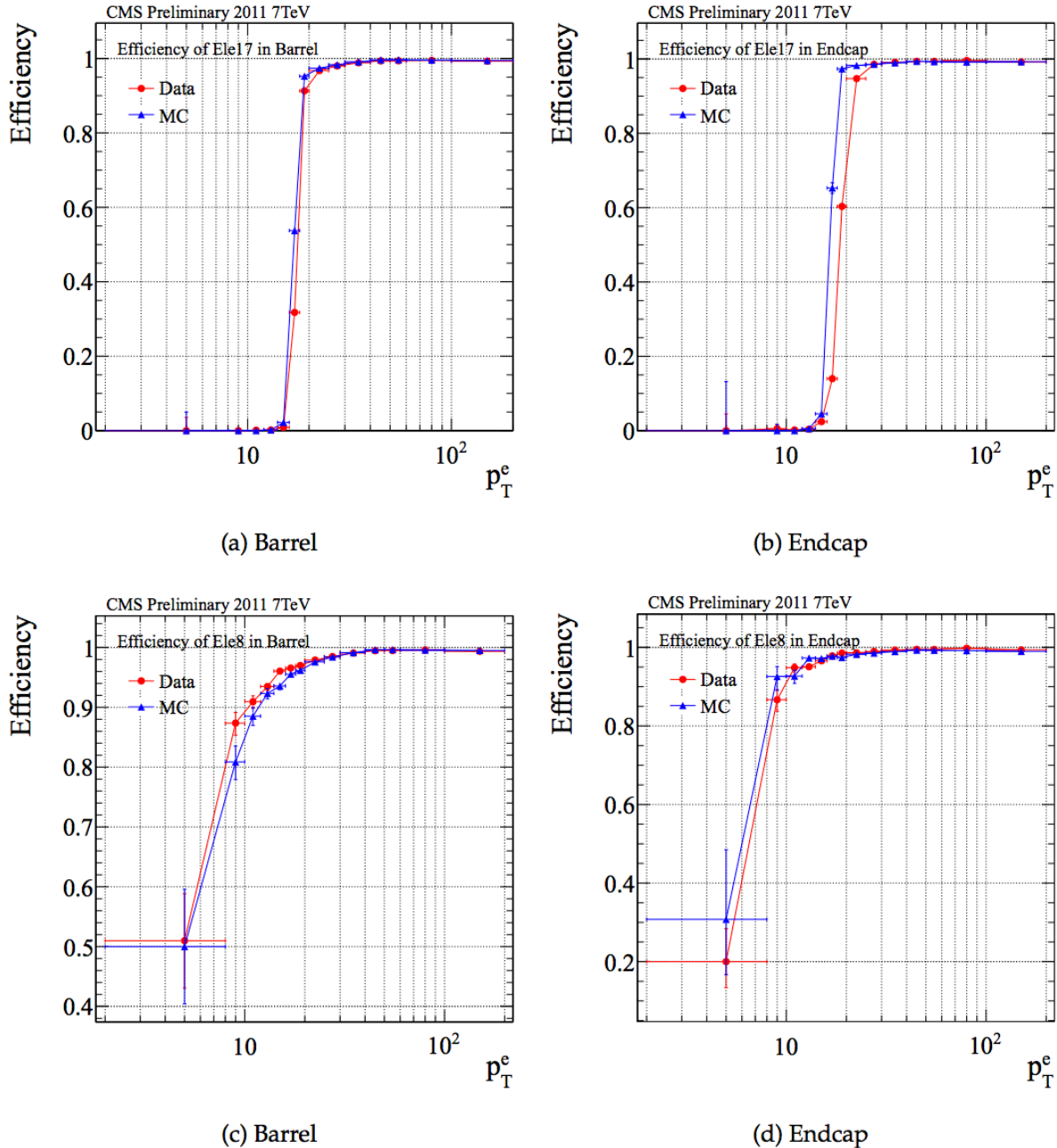


Figure 6.1. Plots of electron trigger efficiencies for the 2011 run.

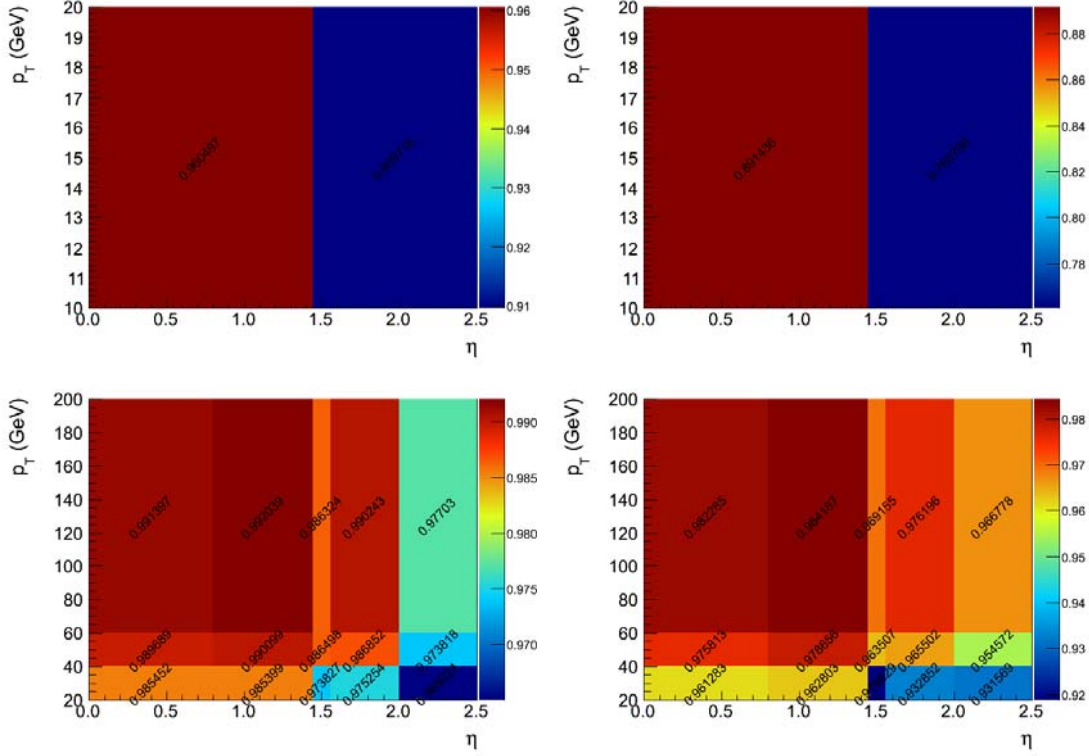


Figure 6.2. Plots of electron trigger efficiencies, binned in p_T and η . Top: Trailing trigger leg (10-20 GeV). Bottom: Trailing trigger leg (20+ GeV). Left: Data. Right: MC.

6.1.1.2. Muon Triggers. For the $Z\gamma \rightarrow \mu\mu\gamma$ final states, the HLT_Mu17_Mu8 trigger is used in the Double Muon data stream and related MC. Muon trigger leg efficiencies are calculated by the Muon Physics Object Group via the TnP method, using a cone of radius 0.3 for matching to trigger objects. For a discussion of systematic uncertainties, see Chapter 8. Trigger efficiencies are shown in Fig 6.4.

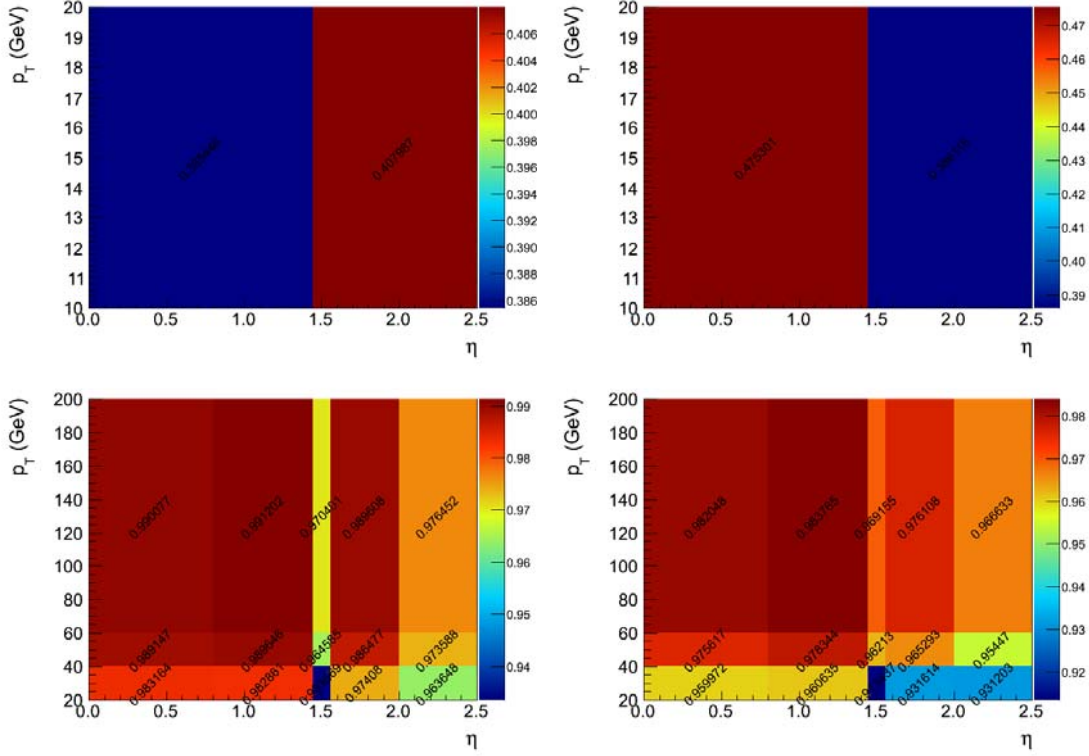


Figure 6.3. Plots of electron trigger efficiencies, binned in p_T and η . Top: Leading trigger leg (10-20 GeV). Bottom: Leading trigger leg ($20+$ GeV). Left: Data. Right: MC.

6.1.2. Event Vertex

The primary vertex (PV) of the hard scattering process is reconstructed using the Deterministic Annealing clustering algorithm (DA) [14]. Additionally, the PV is required to be within 24 cm of the interaction point longitudinally, and within 2 cm of the interaction point in the transverse plane. The number of degrees of freedom in the vertex fit is required to be greater than 4. Out of the vertices that pass the aforementioned selection, the vertex that has the largest sum squared of the momentum of the associated tracks is

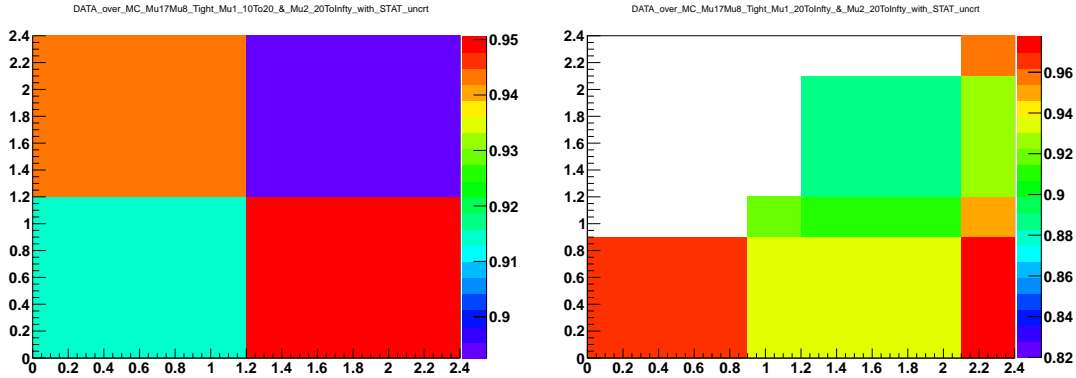


Figure 6.4. Scale factors for 2012 muon trigger, $|\eta|$ of Muon 1 vs $|\eta|$ of Muon 2. Left: Muon1 has $10 < pT < 20$ GeV, Muon2 has $pT > 20$ GeV. Right: Muon1 and Muon2 have $pT > 20$ GeV.

chosen as the PV of the hard scattering process. This PV is then used during the selection of lepton objects as detailed later in this section.

6.1.3. Electron Selection

The 2011 and 2012 electron selections use a simple cut-based and a more complex multivariate analysis-based identification, respectively. The multivariate analysis (MVA) selection is superior in signal efficiency and background rejection to that of the simple cut selection, but the MVA selection was not available for the 2011 data when the $H \rightarrow Z\gamma$ analysis was underway. The following sections will describe both the cut-based and MVA-based selections, as well as their calculated efficiencies for MC and data.

6.1.3.1. Cut-Based Electron Identification and Isolation for 2011. The offline electron selection used for the 2011 data and MC is detailed in Table 6.1. The identification requirements are essentially those of the recommended Loose cut-based identification scheme defined in [16]. This selection has an overall efficiency of roughly 80-90%, and because the electron pair is required to fall within the Z boson mass window and be sufficiently far from the photon, there is little contamination from non-electron sources. In addition to the aforementioned criteria, the leading (trailing) electron is required to have a p_T greater than 20 (10) GeV, and each electron is required to reside in a fiducial area of $|\eta| < 1.4442$ or $1.566 < |\eta| < 2.5$. The region of η between 1.4442 and 1.566 is vetoed because it is the transition region between the EB and the EE, and there is little ECAL coverage and thus unreliable electron reconstruction.

In addition to the identification criteria, an isolation parameter is constructed to minimize contamination from hadronic jets and pileup events. The transverse momenta of all particle-flow charged hadrons, neutral hadrons, and photons are summated in a ΔR cone of 0.4, centered around the electron. The contribution from the electron candidate is subtracted from this sum. Neutral hadrons and photons are corrected for pile-up contamination by using an estimate from the total jet contribution in the event, and the η of the electron. The energy in this sum, divided by the momentum of the electron, is required to be less than 0.4.

Efficiencies are calculated via the TnP method, which is covered in more detail in section 6.1.3.3.

Table 6.1. 2011 Election Selection Criteria.

Observable	Cut Value
Identification	
$\Delta(\eta)$	< 0.007
$\Delta(\phi)$	< 0.15
$\sigma_{inj\eta}$	< 0.01
H/E	< 0.12
$ d_0 $	< 0.02
$ d_Z $	< 0.2
$ 1/E - 1/p $	< 0.05
Conversion Veto: fit prob	< $1e^{-6}$
Conversion Veto: miss hits	< 2
Isolation	
Combined $PFIso/p_T$	< 0.4
Kinematics	
$ \eta_e $	< 1.4442 or (> 1.566 and < 2.5)
leading e p_T	> 20 GeV
trailing e p_T	> 10 GeV

6.1.3.2. MVA-Based Electron Identification and Isolation for 2012. The electron objects in 2012 data and MC are selected through use of an MVA-based electron ID [17–19] that combines the discrimination power of many ID and isolation variables into a single, more optimal discriminator. This discriminator leads to a better background rejection rate and higher signal efficiency, and has the additional benefit of allowing the analysis to recover electron objects that fall in the barrel-endcap transition region ($1.4442 < |\eta| < 1.566$). The cut-based IDs ignore this region because of poor ECAL coverage and thus poor ID efficiency.

The MVA selection only uses identification variables from the ECAL and tracker. Isolation variables are not added to the training, so isolation is still handled via the cut-based combined relative isolation sum as detailed in the previous section.

Figure 6.5 shows the performances of the electron MVA-based ID with a -0.50 cut compared to the cut-based working points used in [20] for electron $p_T > 20$ GeV and in three different η bins: $|\eta| < 0.8$, $|\eta| < 1.479$ and $|\eta| > 1.479$. A significant increase in performances for $|\eta| > 1.479$ can be observed. Similarly, as shown in Figure 6.6, there is better performance for $10 < p_T < 20$ GeV with a -0.90 cut on the MVA discriminant.

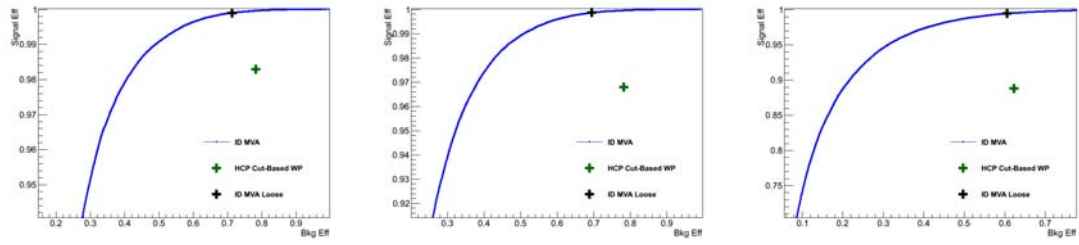


Figure 6.5. Performances of electron MVA-based ID in three different η bins: $|\eta| < 0.8$ (left), $|\eta| < 1.479$ (middle) and $|\eta| > 1.479$ (right) $p_T > 20$ GeV.

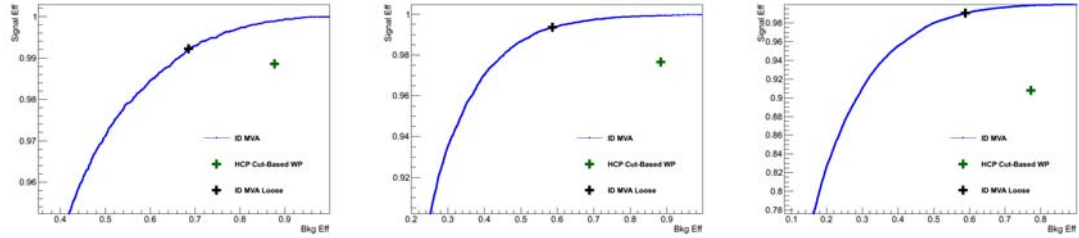


Figure 6.6. Performances of electron MVA-based ID in three different η bins: $|\eta| < 0.8$ (left), $|\eta| < 1.479$ (middle) and $|\eta| > 1.479$ (right) for $10 < p_T < 20$ GeV.

6.1.3.3. Electron Efficiency Calculation. The efficiencies for the ID and isolation are calculated via the TnP technique, binned by p_T and η . The tag electron is required to match the trailing leg of the analysis trigger, and pass the ID and isolation requirements. The probe electron has no analysis cut requirements for the ID efficiency, and must

pass the above ID for the isolation efficiency. The method of extracting the efficiency consists of counting the number of good Z candidates given a passing probe, divided by the total number of Z candidates from passing and failing probes. The number of Z candidates in MC is determined through a simple counting method, while the number of Z candidates for data is determined through fitting. For almost all eta and pt bins, the signal region is modeled with a template function derived from MC, convoluted with a Gaussian distribution. In the case of failing probes in the ECAL gap region, the signal region is modeled by a Crystal Ball convoluted with a Breit Wigner distribution, as the signal templates have too few entries and were subject to large statistical fluctuations. The background for passing probes was modeled as a linear function multiplied with an exponential. The background for the failing probes was modeled as an error function multiplied by an exponential. See Fig. 6.7-6.8 for example fits for tag and probe. The calculated efficiencies for ID and isolation are shown in Figs. 6.9-6.10. The full set of tag and probe fits for all bins can be found in Appendix A.

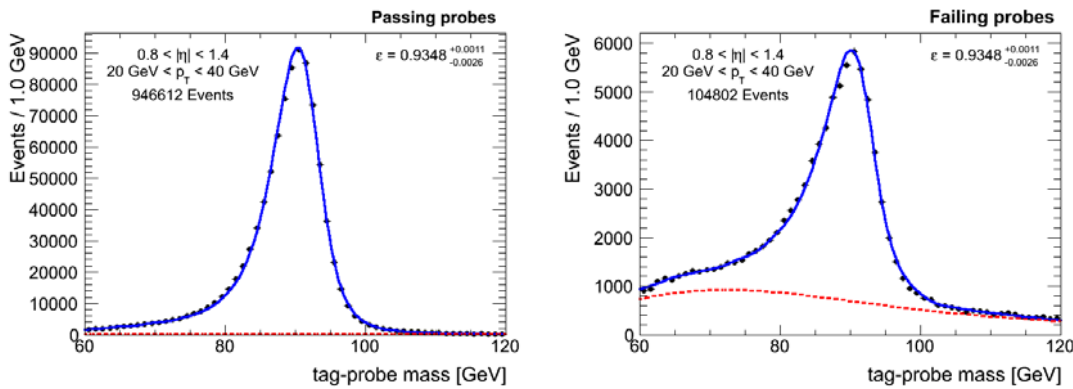


Figure 6.7. Tag and probe example fits to data for electron ID. Left: Passing probes, Right: Failing probes.

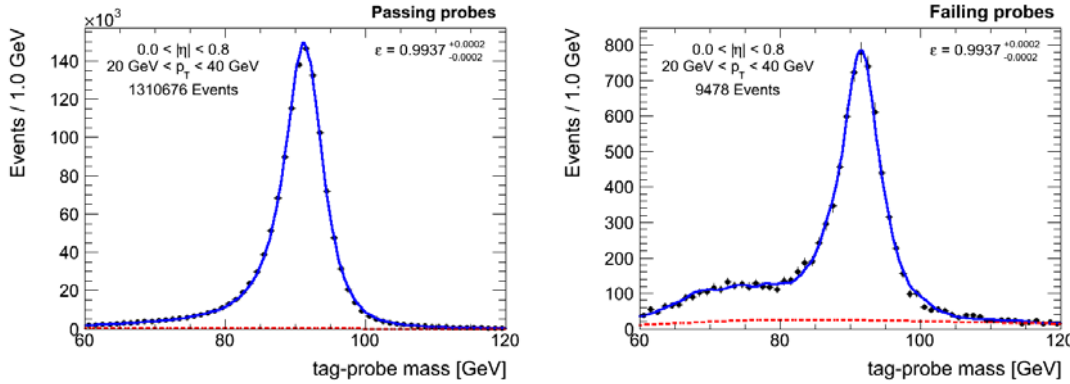


Figure 6.8. Tag and probe example fits to data for electron isolation. Left: Passing probes, Right: Failing probes.

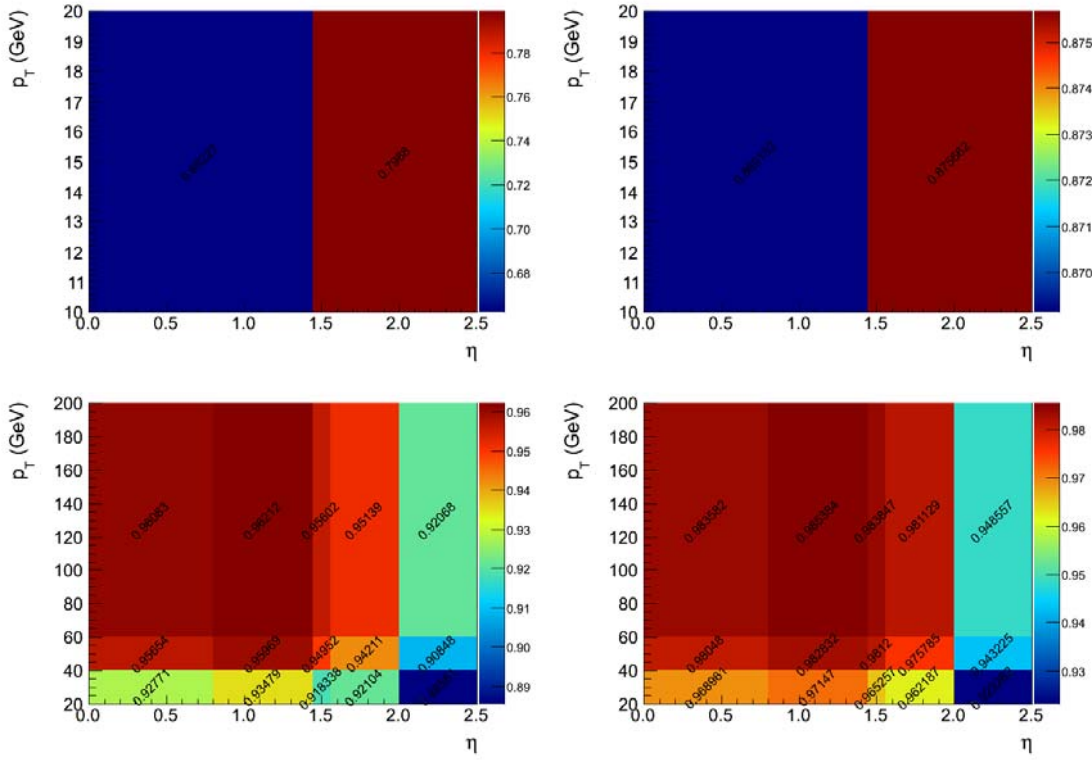


Figure 6.9. Plots of electron ID efficiencies, binned in p_T and η . Top: ID (10-20 GeV). Bottom: ID (20+ GeV). Left: Data. Right: MC.

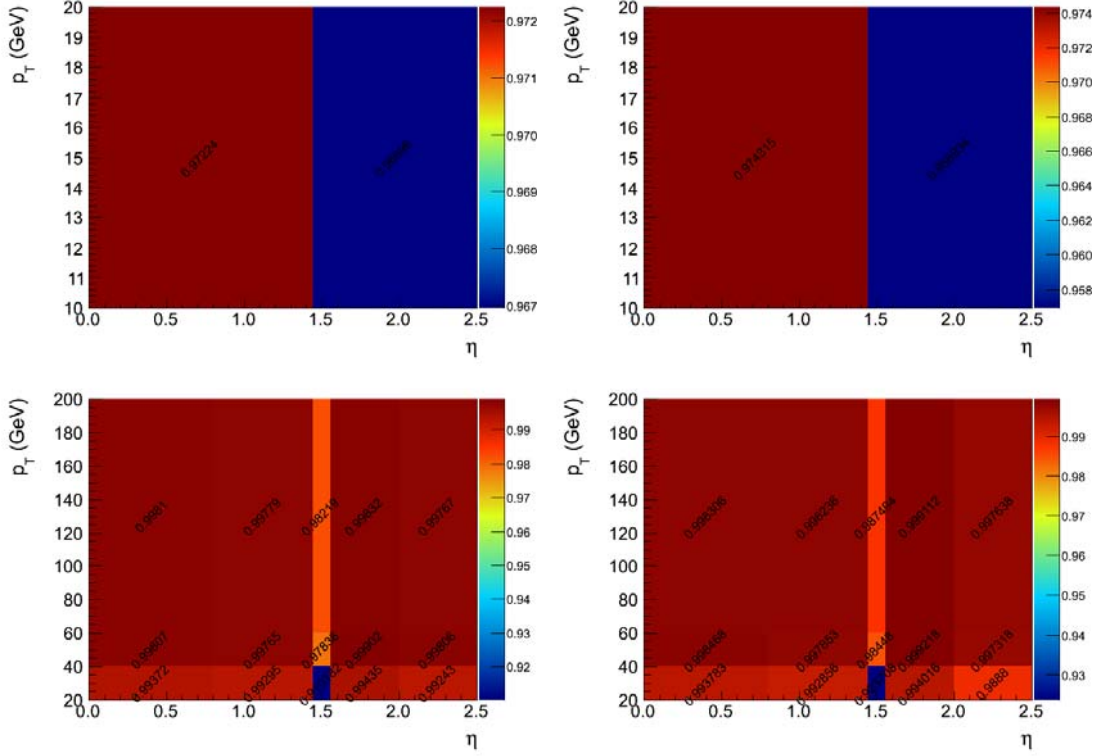


Figure 6.10. Plots of electron isolation efficiencies, binned in p_T and η . Top: Iso (10-20 GeV). Bottom: Iso (20+ GeV). Left: Data. Right: MC.

6.1.3.4. Electron Energy Regression and Corrections. The energy resolution of the reconstructed electrons is improved through use of an energy regression technique. The regression is trained much like the MVA ID, where ECAL-only information is fed into a multivariate training algorithm. The training compares the reconstructed energy with the true energy of a simulated electron in Drell-Yan MC, and determines a correction factor. This regression technique produces scale and smearing corrections to both data and MC, see [21].

6.1.4. Muon Selection

6.1.4.1. Muon Identification and Isolation. There are only minor differences between the muon selection used in the 2011 and 2012 data and MC sets. Muons in these analyses are initially reconstructed as hits in the muon chambers, which are matched to segments, which in turn are used to generate “standalone muon” tracks. Those standalone muon tracks are then matched to inner tracks from the silicon and pixel detectors to form “global muons” [22]. After an event passes the required double muon trigger, any final state muon must satisfy the following identification requirements:

- Each muon must lie within pseudo-rapidity $|\eta| < 2.4$.
- Muons must be reconstructed as global muons.
- Muons must be identified by the particle flow algorithm [23].
- The quality of the global muon fit must satisfy $\chi^2/ndof < 10$.
- There must be at least one good muon chamber hit.
- Muon segments in at least two muon stations must be matched to a tracker track.
- There must be at least one valid pixel hit.
- At least five tracker layers must have hits.
- The impact parameter in the transverse plane ($|d_0|$) must be less than 0.2 cm with respect to the primary vertex.
- The impact parameter in the longitudinal direction ($|d_Z|$) must be less than 0.5 cm with respect to the primary vertex.

After the muons pass the identification requirements, a further quality cut on isolation is performed to reduce contamination from muons that originate from hadronic processes.

The transverse momenta of all particle-flow charged hadrons, neutral hadrons, and photons are summated in a cone of size $\Delta R = \sqrt{(\Delta\eta)^2 + (\Delta\phi)^2} = 0.4$, centered around the muon. The energy of the neutral hadrons and photons are corrected for pile-up contamination by using an estimate of the total contribution of PU tracks ($\Delta\beta$). The energy in this sum, divided by the momentum of the muon, is required to be less than 0.4.

After two muons are selected, the transverse momentum of the leading (trailing) muon must be greater than 20 (10) GeV so that both muons are above the trigger leg thresholds. The full muon selection is summarized in Table 6.2.

Table 6.2. Muon selection criteria

Observable	Cut Value	
	2011	2012
Identification		
GlobalMuon	Yes	Yes
PFMuon	-	Yes
$\chi^2/ndof$	< 10	< 10
# muon chamber hits	> 0	> 0
# matched stations	> 1	> 1
# valid pixel hits	> 0	> 0
# tracker layers	> 8	> 5
$ d_0 $	< 0.2	< 0.2
$ d_Z $	-	< 0.5
Isolation		
Combined $PFIso/p_T$	< 0.12	< 0.4
Kinematics		
$ \eta_\mu $	< 2.4	< 2.4
leading μp_T	> 20 GeV	> 20 GeV
trailing μp_T	> 10 GeV	> 10 GeV

The efficiencies of the muon ID and isolation are measured via the tag-and-probe method, where the tags are tight, well isolated muons. The total number of passing and failing probes are measured via a line-fitting procedure. The systematic errors are

estimated by varying the isolation requirements on the probe muons or matching the probe to a generator-level object (further discussion in Chapter 8). The efficiencies are calculated per muon, binned into four eta regions, with four or five momentum bins. The scale factor weights are derived by dividing the data efficiencies by the MC efficiencies, which is then applied to the MC. The scale factors are applied to each muon individually, and are assumed to be independent. All scale factors and systematic uncertainties are derived by the muon POG, as the muon ID and isolation requirements are recommended defaults and not customized for this analysis. The impact of the scale factors is shown in Fig. 6.11 and Fig. 6.12

6.1.5. Photon Selection

Like the electron selection, two different photon selections are used: a cut-based selection and an MVA-based selection. The latter is superior to the former in both signal efficiency and background rejection, but the MVA selection was not finalized when the $H \rightarrow Z\gamma$ analysis was being performed. Both selections are described in the following section.

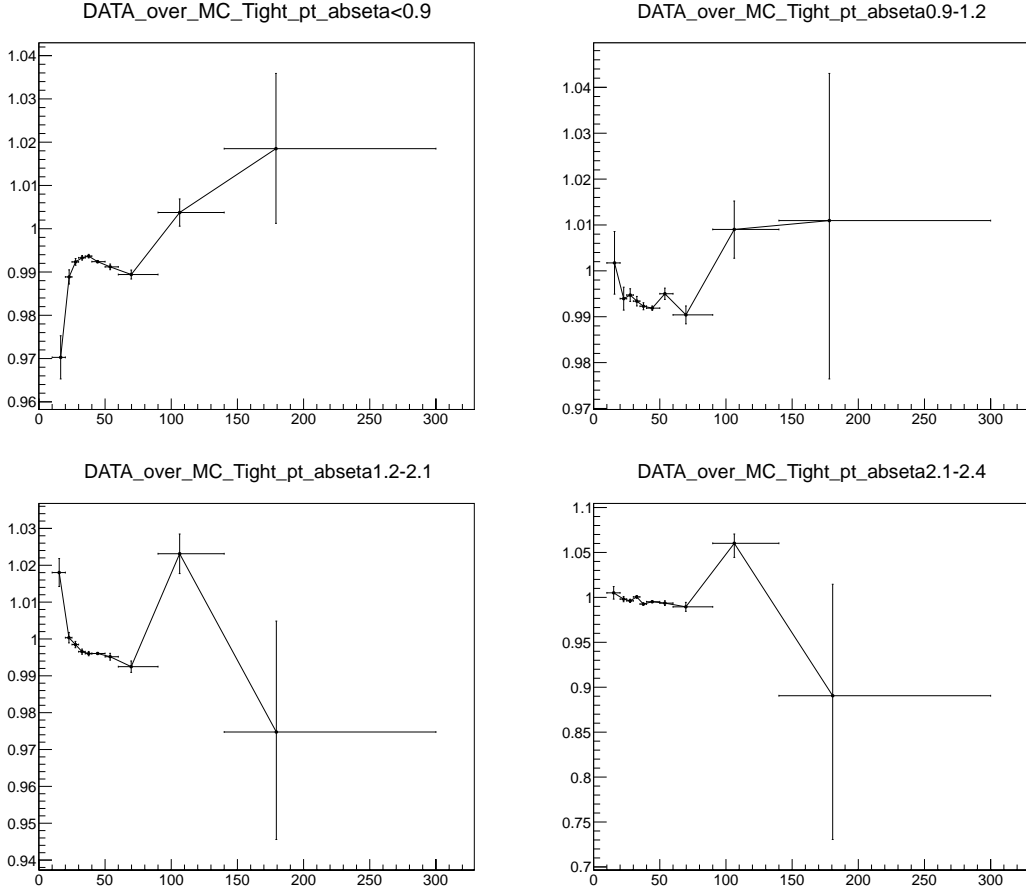


Figure 6.11. Muon ID scale factors per leg, broken into four eta bins.

6.1.5.1. Photon Cut-based Selection. Like the electrons, photon candidates are reconstructed as SuperClusters in the fiducial volume of the ECAL detector: barrel (EB) with $|\eta| < 1.4442$ and endcap (EE) with $1.566 < |\eta| < 2.5$. The efficiency of identification of photons as SuperClusters is measured in MC simulation. As shown in Fig. 6.13 there are four working points (WP) with efficiencies ranging between 65% and 94%. The Medium WP was chosen as a compromise between reconstruction efficiency and photon purity. For example, studies show that the photon fake background is reduced from 45%

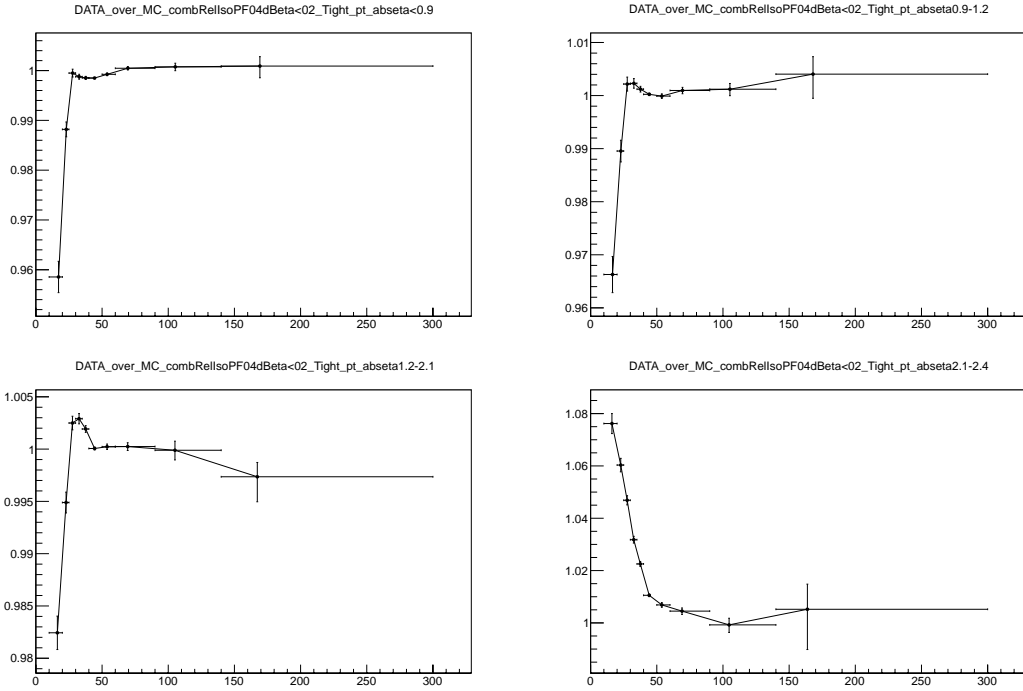


Figure 6.12. Muon Iso scale factors per leg, broken into four eta bins.

to 30% by using the Medium WP instead of the Loose WP. This is at the expense of about 10% in signal, but with a modest increase of about 5% in sensitivity ($\frac{S}{\sqrt{S+B}}$).

To reduce copious amount of contamination from jets misidentified as photons, the identification and isolation criteria are applied, which are based on the following cuts:

- Conversion safe Electron veto: A veto that separates out photons that begin to shower in the tracker from electrons.
- $\sigma i\eta i\eta$: The cluster shape in the η direction.
- Single tower H/E: The hadronic activity behind the photon ECAL supercluster within a ΔR cone of 0.15. Only the closest HCAL tower to the SC position is used.

- PF charged hadron isolation (PF IsoCH): The sum of the charged hadrons in a ΔR cone of 0.3. The charged hadrons should be associated to the first primary vertex, $|d_Z| < 0.2$ cm, and $|d_0| < 0.1$ cm. In addition, a veto ΔR cone of 0.02 is used as well, to reject the contribution from the photon.
- PF neutral hadron isolation (PF IsoNH): The sum of the neutral hadrons in a ΔR cone of 0.3.
- PF photon isolation (PF IsoPh): The sum of the photons in a ΔR cone of 0.3. In the barrel, an eta-strip veto of 0.015 is used. In the endcap a crystal-size cone is used. The definition of the crystal-size cone is $4 \times 0.00864 \times |\sinh(\eta_{SC}^\gamma)|$.

The isolation calculations are also corrected for pile-up activity, such that the average pileup of each event is calculated and reweighted depending on the pseudorapidity of the photon object. This procedure greatly reduces the isolation dependence on changing pileup conditions.

Table 6.3. Photon Selection Criteria for $H \rightarrow Z\gamma$ Analysis.

Observable	Cut Value	
	Barrel	Endcap
Conversion-Safe Electron Veto	Yes	Yes
$\sigma i\eta i\eta$	< 0.011	< 0.033
H/E	< 0.05	< 0.05
$PF Iso_{CH}$	< 1.5	< 1.2
$PF Iso_{NH}$	$< 1.0 + 0.04 \times E_T^\gamma$	$< 1.5 + 0.04 \times E_T^\gamma$
$PF Iso_\gamma$	$< 0.7 + 0.005 \times E_T^\gamma$	$< 1.0 + 0.005 \times E_T^\gamma$

The $e\gamma$ -POG blessed scale factors needed for the 2011 and full 2012 ABCD data samples are given in Tables 6.4 and 6.5 for the photon selection and 6.6 and 6.7 for the electron veto efficiencies. The tag-and-probe distributions used to estimate the selection

efficiency are shown in Fig. 6.14. The raw electron veto efficiencies for data and MC are shown in Fig. 6.15.

Table 6.4. The scale factors for photon selection without electron veto for 2011.

2011		
SC η	E_T (GeV)	Scale factor
0.0 - 1.4442	15-20	$1.0022 \pm 0.0064(stat.) \pm 0.0041(syst.)$
1.566 - 2.5	15-20	$1.0189 \pm 0.0081(stat.) \pm 0.0047(syst.)$
0.0 - 0.8	20-30	$0.9854 \pm 0.0026(stat.) \pm 0.0011(syst.)$
	30-40	$0.9834 \pm 0.0013(stat.) \pm 0.0000(syst.)$
	40-50	$0.9853 \pm 0.0011(stat.) \pm 0.0006(syst.)$
	50-Inf	$0.9847 \pm 0.0019(stat.) \pm 0.0001(syst.)$
	20-30	$0.9876 \pm 0.0031(stat.) \pm 0.0022(syst.)$
0.8 - 1.4442	30-40	$0.9932 \pm 0.0016(stat.) \pm 0.0006(syst.)$
	40-50	$0.9914 \pm 0.0012(stat.) \pm 0.0003(syst.)$
	50-Inf	$0.9941 \pm 0.0022(stat.) \pm 0.0001(syst.)$
	20-30	$1.0115 \pm 0.0039(stat.) \pm 0.0001(syst.)$
1.566 - 2.0	30-40	$1.0048 \pm 0.0022(stat.) \pm 0.0001(syst.)$
	40-50	$1.0013 \pm 0.0017(stat.) \pm 0.0015(syst.)$
	50-Inf	$1.0033 \pm 0.0030(stat.) \pm 0.0024(syst.)$
	20-30	$1.0056 \pm 0.0042(stat.) \pm 0.0001(syst.)$
2.0 - 2.5	30-40	$1.0108 \pm 0.0024(stat.) \pm 0.0014(syst.)$
	40-50	$1.0057 \pm 0.0017(stat.) \pm 0.0015(syst.)$
	50-Inf	$1.0106 \pm 0.0106(stat.) \pm 0.0005(syst.)$

The scale factors for the photon selection are obtained using $Z \rightarrow e^+e^-$ candidates and the tag-and-probe method, but without applying the electron veto requirement. The scale factor for the electron veto selection is obtained using $Z\gamma \rightarrow \mu\mu\gamma$. A simple-counting method is used to measure the efficiency and corresponding scale factor, because the photon purity is close to 100% after the full selection is applied.

Table 6.5. The scale factors for photon selection without electron veto for 2012.

2012		
SC η	E_T (GeV)	Scale factor
0.0 - 1.4442	15-20	0.9776 ± 0.0100
1.566 - 2.5	15-20	1.0143 ± 0.0116
0.0 - 0.8	20-30	0.9776 ± 0.0025
	30-40	0.9711 ± 0.0020
	40-50	0.9778 ± 0.0024
	50-Inf	0.9718 ± 0.0014
0.8 - 1.4442	20-30	0.9795 ± 0.0046
	30-40	0.9823 ± 0.0052
	40-50	0.9805 ± 0.0024
	50-Inf	0.9768 ± 0.0016
1.566 - 2.0	20-30	0.9804 ± 0.0042
	30-40	0.9964 ± 0.0017
	40-50	0.9947 ± 0.0022
	50-Inf	0.9990 ± 0.0025
2.0 - 2.5	20-30	1.0167 ± 0.0035
	30-40	1.0138 ± 0.0042
	40-50	1.0129 ± 0.0038
	50-Inf	1.0098 ± 0.0025

Table 6.6. The scale factors for electron veto selection. The efficiencies are around 99% in the barrel and 97-98% in the endcap.

Region	Scale factor 2011
Barrel	0.9971 ± 0.0015
Endcap	0.9983 ± 0.0043

6.1.5.2. Photon MVA Selection. The $A \rightarrow Z\gamma$ analysis uses an MVA-based identification and isolation selection. This selection was finalized after the publication of the $H \rightarrow Z\gamma$ analysis, after it was shown to be promising during post-publication improvements. As with all selections that transition from cut-based to MVA, the motivation was to use a higher efficiency, higher purity ID that takes advantage of correlated discriminators that contain information that cannot be exploited with simple 1D and 2D cuts.

Table 6.7. The scale factors for electron veto selection. The efficiencies are around 99% in the barrel and 97-98% in the endcap.

E_T (GeV)	Scale factor 2012
Barrel	
15 20	0.9961 ± 0.0033
20 30	0.9940 ± 0.0027
30 40	0.9958 ± 0.0043
40 Inf	0.9999 ± 0.0067
Endcap	
15 20	0.9941 ± 0.0133
20 30	0.9961 ± 0.0063
30 40	0.9924 ± 0.0079
40 Inf	0.9850 ± 0.0120

The ID is trained on EM-enriched photon+jet and QCD samples. All reconstructed photon objects must pass a loose pre-selection, shown in Table 6.8. Reconstructed photon objects are matched to generator-level photons with $\Delta R < 0.2$ and $\Delta p_T < 0.2$, where objects that fail to match are considered fakes. The matched photons undergo a 2D reweighting in η and p_T such that they agree with the η and p_T of the fakes. The R9 variable is rescaled to match data for the 2012 run.

Table 6.8. Photon MVA Pre-Selection.

Observable	R9 ≤ 0.9	R9 > 0.9
Barrel		
HoE	< 0.075	< 0.082
$\sigma i\eta i\eta$	< 0.014	< 0.014
EtCorr HcalIso	< 4 GeV	< 50 GeV
EtCorr TrackIso	< 4 GeV	< 50 GeV
ChargedPFIso	< 4 GeV	< 4 GeV
Endcap		
HoE	< 0.075	< 0.075
$\sigma i\eta i\eta$	< 0.034	< 0.034
EtCorr HcalIso	< 4 GeV	< 50 GeV
EtCorr TrackIso	< 4 GeV	< 50 GeV
ChargedPFIso	< 4 GeV	< 4 GeV

The variables considered in the MVA training were the following:

- Photon Kinematics
 - ϕ
 - SuperCluster η
 - SuperCluster Raw Energy
- Isolation
 - PFChargedIso (cone 0.3)
 - PFPhotonIso (cone 0.3)
 - $\max(\text{PFChargedIso}(\text{cone 0.3}) \text{ w.r.t. vertex_i}, \text{vertex_i} \in \text{All Event Vertices})$
- Shower Shape
 - R9 (reweighted)
 - $\sigma i\eta i\eta$
 - $\sigma i\eta i\phi$
 - E2x2/E5x5
 - E1x3/E5x5
 - E2x5max/E5x5
 - $\sigma\eta$
 - $\sigma\phi$
 - ES σ RR (endcap only)
 - ESEnergy/SCRaw Energy (endcap only)
- ρ (for pile up)

After training, the purity and efficiency were found to be superior to the cut-based ID, see Fig. 6.16. The MVA ID cuts were optimized for a Z + photon selection and

the scale factors were generated accordingly. All scale factors were very close to one, see Table 6.9. Similarly to the muon and electron, the efficiencies, scale factors and systematic uncertainties on the photon ID are calculated via the TnP method. For photons, the $Z \rightarrow e^+e^-$ distribution is used for tag and probe, where the tag electron passes a tight electron ID and Iso, and the probe electron matches to a photon that passes the MVA ID for the given probe bin. After calculation, the scale factors are further validated against the invariant mass of $Z \rightarrow \mu\mu\gamma$, where one of the muons has a radiated a photon (Fig. 6.17).

Table 6.9. Photon MVA Scale Factors.

γ pT	EB	EE
$40 < pT < 45$	0.9877	0.9941
$45 < pT < 50$	1.0124	0.9913
$50 < pT < 55$	1.0259	0.9850
$55 < pT < 60$	1.0262	0.9883
$60 < pT < 70$	1.0217	0.9870
$70 < pT < 80$	1.0181	0.9708
$80 < pT$	1.0258	1.0059

6.1.6. Photon Energy Corrections

The photon energy scale and resolution corrections (Phosphor Corrections) are given in Table 6.10. The details on how the central values and its uncertainties are obtained can be found in [24]. These corrections were produced using $Z \rightarrow \mu\mu$ candidates from the 2012 ABC data periods. The scale and resolution numbers were also re-derived for the 2012 AB and 2012 CD run periods as crosschecks. There was good agreement between the two data sets within the errors quoted, as can be seen in Figures 6.18 and 6.19.

The systematic uncertainty of the photon energy corrections is dominated by the uncertainty in the line shape model which is derived from MC. These uncertainties have been derived from closure tests on the MC.

Barrel Scale, $R9 > 0.94$	$P_T[10, 12]$ (%)	$P_T[12, 15]$ (%)	$P_T[15, 20]$ (%)	$P_T[20, 999]$ (%)
MC 2011	0.8 ± 0	0.79 ± 0.1	0.45 ± 0.07	0.45 ± 0.04
MC 2012	0.46 ± 0.1	0.29 ± 0.08	0.28 ± 0.06	0.11 ± 0.04
DATA 2011	-0.89 ± 0.45	-0.06 ± 0.36	-0.06 ± 0.28	1.1 ± 0.12
DATA 2012	2.18 ± 0.46	0.64 ± 0.37	1.78 ± 0.22	1.15 ± 0.13
Barrel Scale, $R9 < 0.94$	$P_T[10, 12]$ (%)	$P_T[12, 15]$ (%)	$P_T[15, 20]$ (%)	$P_T[20, 999]$ (%)
MC 2011	2.15 ± 0.27	1.81 ± 0.21	1.48 ± 0.16	0.8 ± 0.09
MC 2012	1.32 ± 0.21	0.81 ± 0.16	0.64 ± 0.12	0.62 ± 0.07
DATA 2011	-0.25 ± 0.43	0.28 ± 0.33	0.24 ± 0.25	-0.36 ± 0.16
DATA 2012	0.95 ± 0.42	1.15 ± 0.32	0.28 ± 0.25	0.39 ± 0.15
Endcap Scale	$P_T[10, 12]$ (%)	$P_T[12, 15]$ (%)	$P_T[15, 20]$ (%)	$P_T[20, 999]$ (%)
MC 2011	3 ± 0.32	2.33 ± 0.24	1.64 ± 0.18	0.96 ± 0.11
MC 2012	1.82 ± 0.36	1.3 ± 0.25	1.14 ± 0.19	0.62 ± 0.12
DATA 2011	1.41 ± 0.58	0.07 ± 0.48	0.58 ± 0.37	0.45 ± 0.22
DATA 2012	0.9 ± 0.73	-0.66 ± 0.51	1.14 ± 0	1.24 ± 0.24
Barrel Resolution, $R9 > 0.94$	$P_T[10, 12]$ (%)	$P_T[12, 15]$ (%)	$P_T[15, 20]$ (%)	$P_T[20, 999]$ (%)
MC 2011	2.69 ± 0	2.56 ± 0.03	2.1 ± 0.02	1.47 ± 0.01
MC 2012	1.93 ± 0.03	1.8 ± 0.02	1.51 ± 0.01	1.12 ± 0.01
DATA 2011	5.03 ± 0.61	3.75 ± 0.53	3.59 ± 0.38	2.18 ± 0.16
DATA 2012	3.01 ± 0.69	3.95 ± 0.61	1.91 ± 0.26	2.29 ± 0.22
Barrel Resolution, $R9 < 0.94$	$P_T[10, 12]$ (%)	$P_T[12, 15]$ (%)	$P_T[15, 20]$ (%)	$P_T[20, 999]$ (%)
MC 2011	8.2 ± 0.08	7.31 ± 0.06	5.82 ± 0.05	3.94 ± 0.03
MC 2012	6.16 ± 0.07	5.92 ± 0.54	4.7 ± 0.05	2.77 ± 0.02
DATA 2011	15.69 ± 0.29	11.13 ± 0.54	7.54 ± 0.34	5.36 ± 0.23
DATA 2012	9.24 ± 0.59	8.87 ± 0.5	7.58 ± 0.31	3.58 ± 0.24
Endcap Resolution	$P_T[10, 12]$ (%)	$P_T[12, 15]$ (%)	$P_T[15, 20]$ (%)	$P_T[20, 999]$ (%)
MC 2011	7.48 ± 0.1	6.05 ± 0.07	4.93 ± 0.06	3.39 ± 0.03
MC 2012	6.17 ± 0.1	5.2 ± 0.08	4.28 ± 0.05	2.93 ± 0.03
DATA 2011	15.16 ± 0.48	13.46 ± 0.73	10.68 ± 0.5	6.21 ± 0.4
DATA 2012	10.65 ± 0.93	8.86 ± 0.66	4.28 ± 0	5.62 ± 0.43

Table 6.10. A summary of the measured photon energy scale and resolution for the data and MC. Values are given for 2011 and 2012 separately as well as in two categories of R_9 in EB.

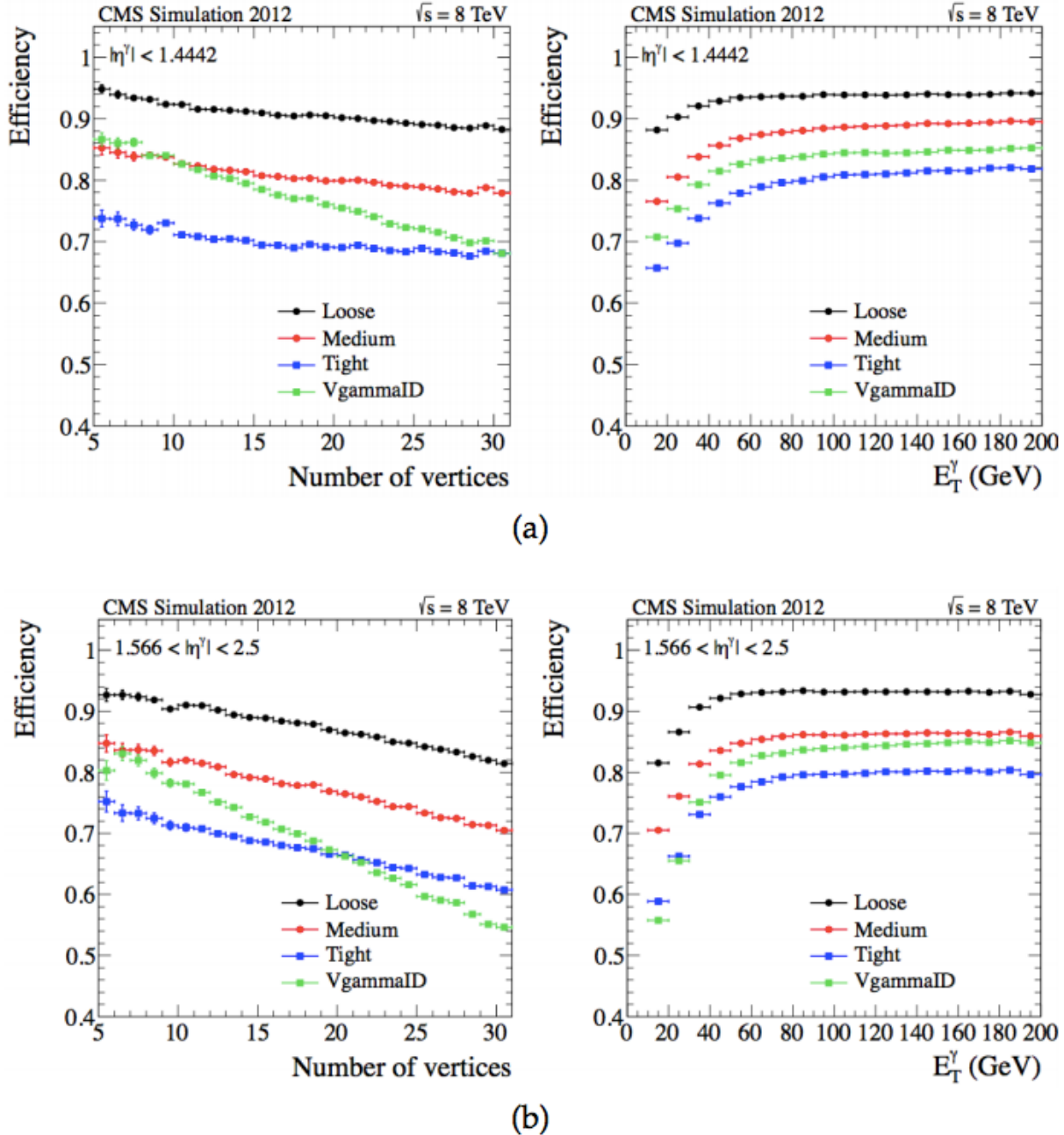


Figure 6.13. Photon identification efficiency at 8 TeV (A+B) for (a) the barrel and the (b) the endcap. The "Medium" working point is used in this analysis. Similar performance in observed in 7 TeV data.

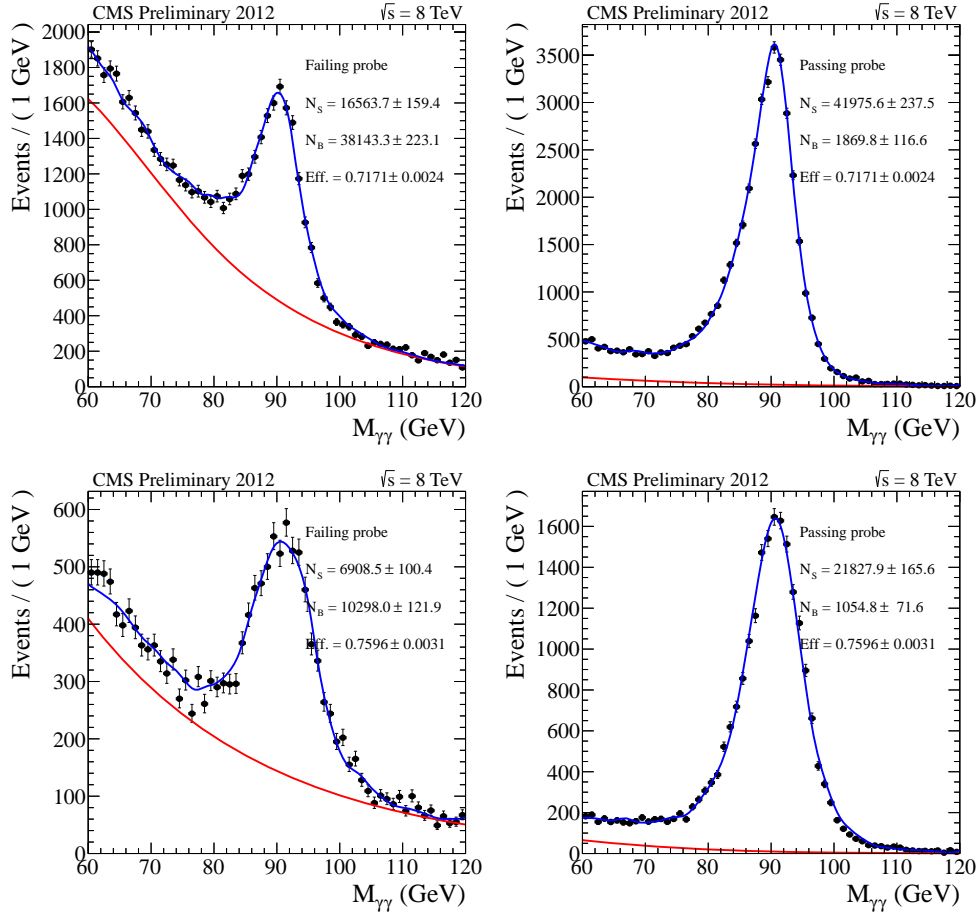


Figure 6.14. Tag-and-probe distributions used in the estimation of the photon efficiencies.

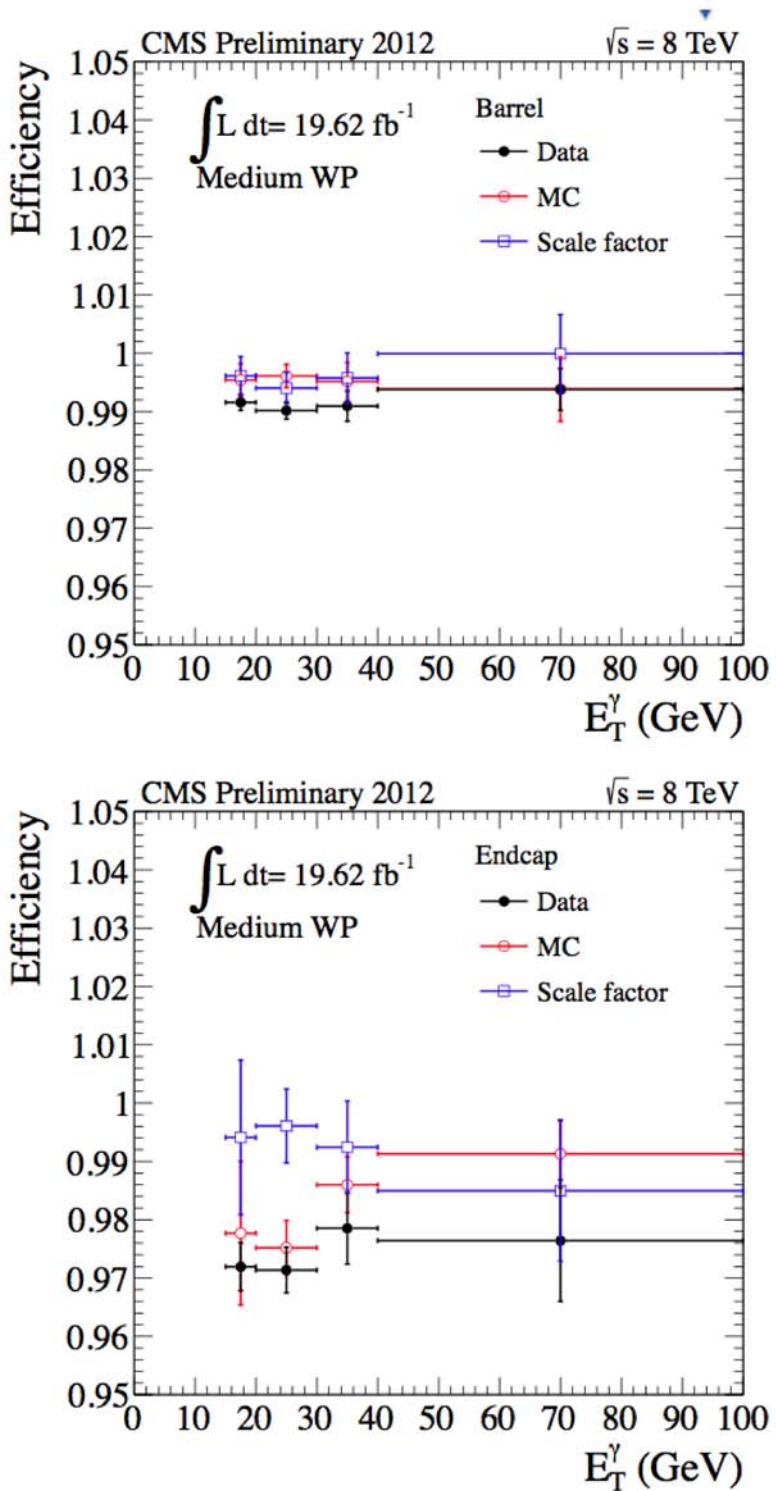


Figure 6.15. Electron veto efficiency for data and MC.

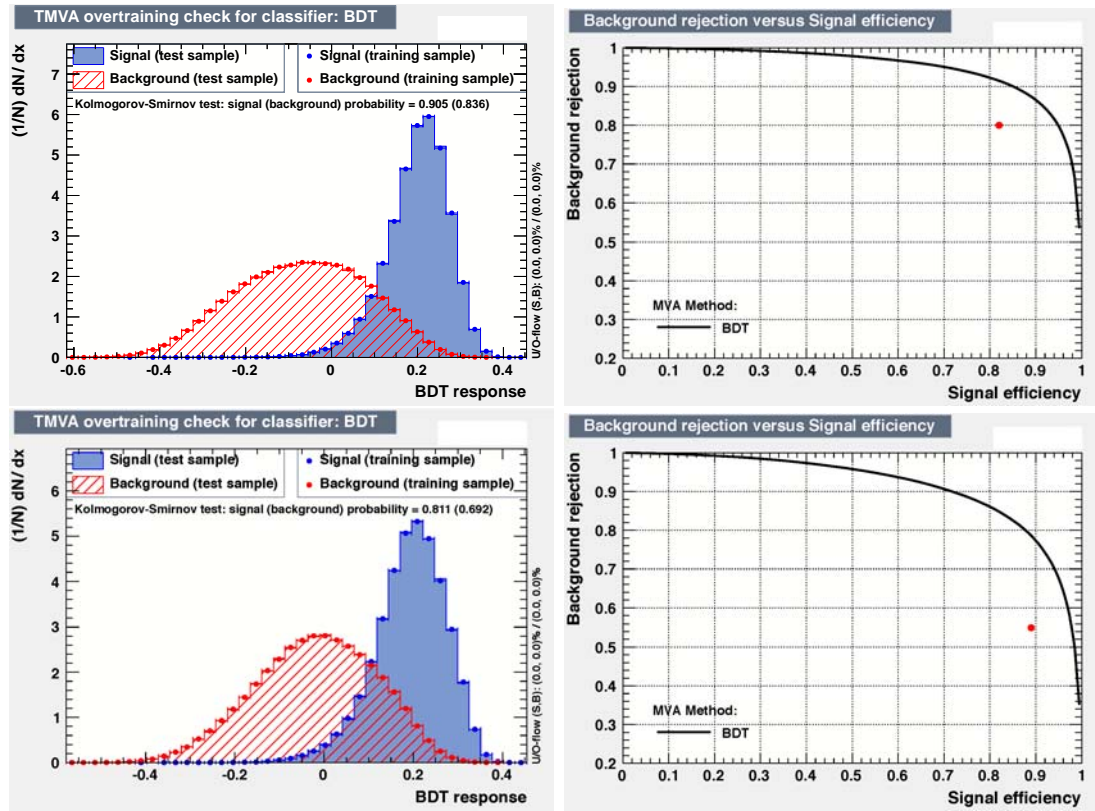


Figure 6.16. Training output and performances of the photon MVA ID. Red point on right plots represents medium WP cut-based photon ID. Top: Barrel, Bottom: Endcap.

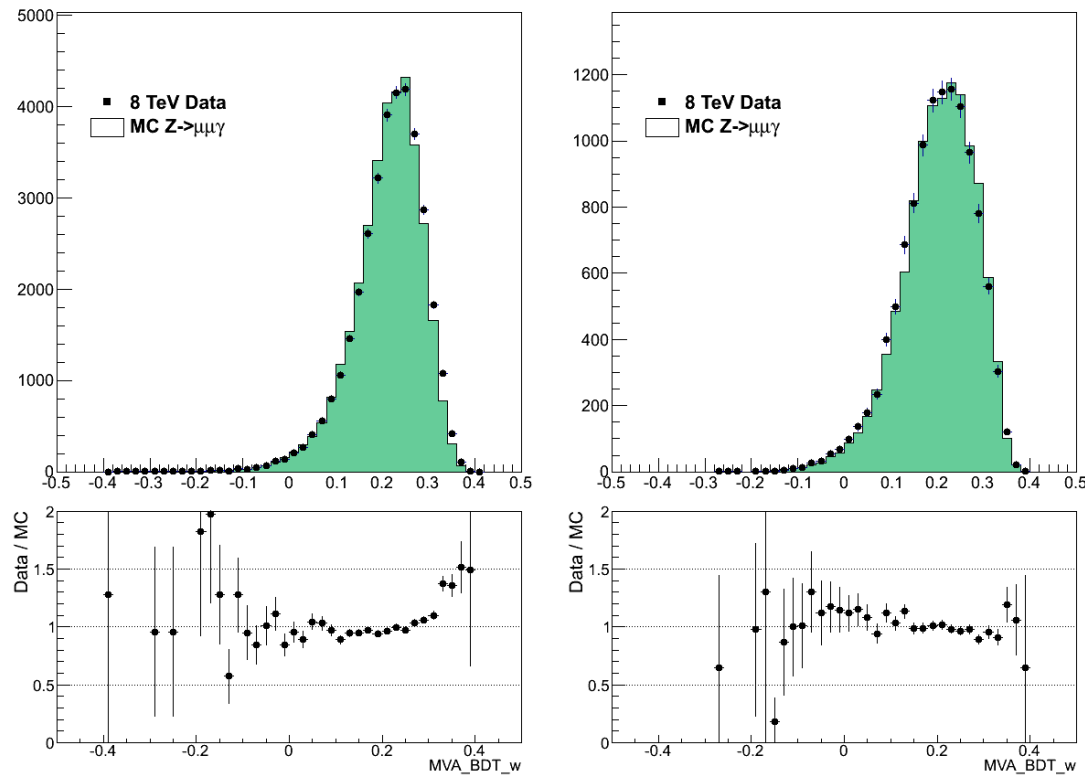


Figure 6.17. Validation plots of Photon MVA ID with $Z \rightarrow \mu\mu\gamma$ MC. Left: Barrel. Right: Endcap.

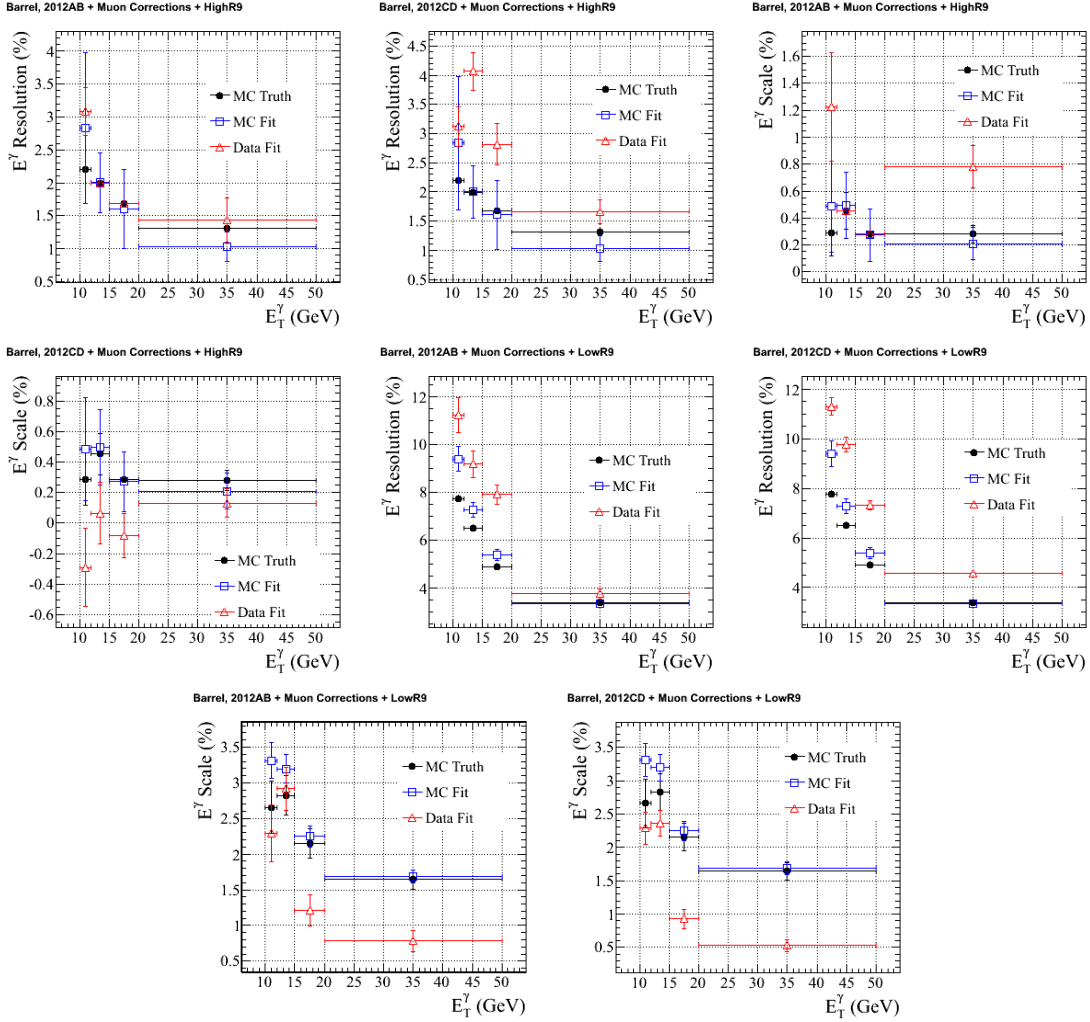


Figure 6.18. Comparison of the fits on the $Z \rightarrow \mu\mu\gamma$ invariant mass distribution for data for 2012 AB and 2012 CD. Results for the barrel as well as for high and low R_9 are shown separately. Only the corrections at high E_T are relevant as the photon is required to have $p_T > 15$ GeV.

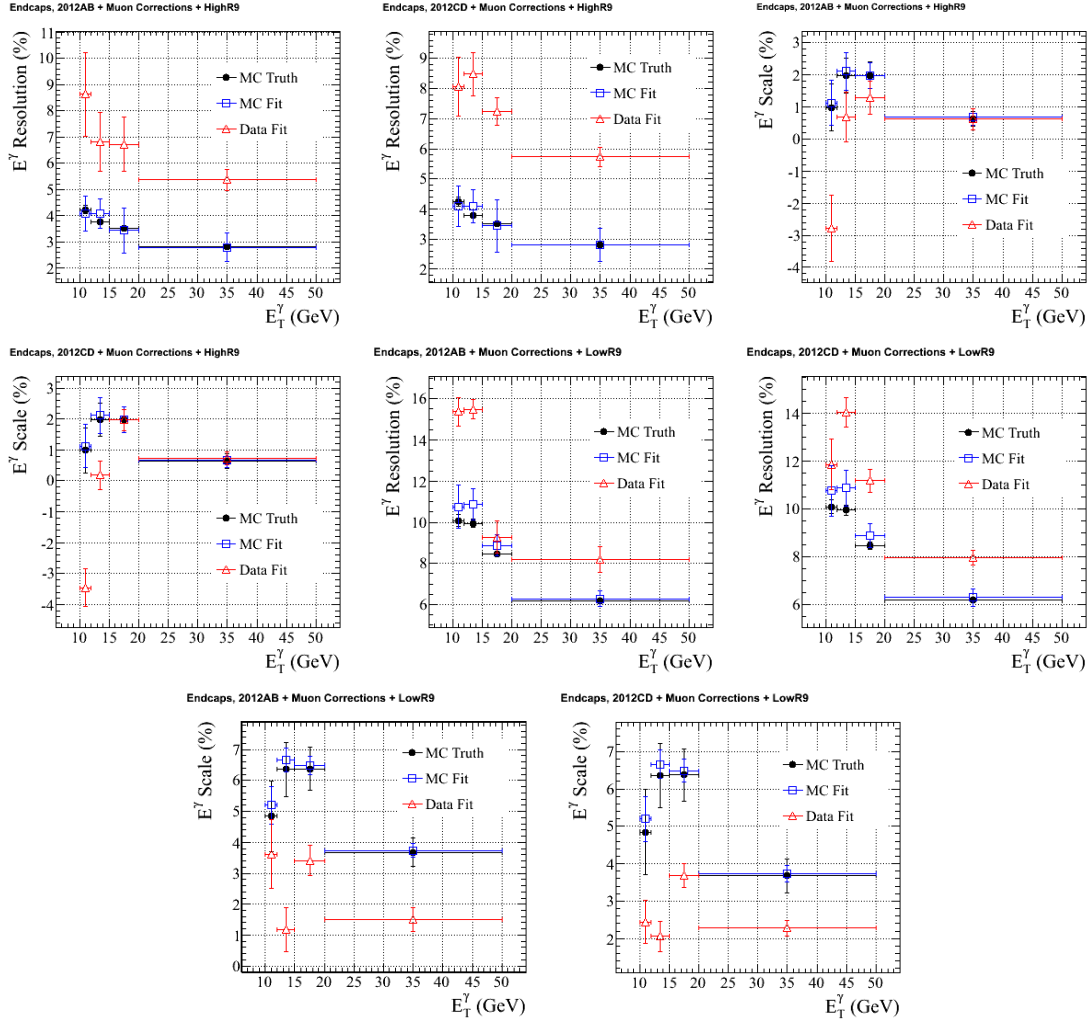


Figure 6.19. Comparison of the fits on the $Z \rightarrow \mu\mu\gamma$ invariant mass distribution for data for 2012 AB and 2012 CD. Results for the barrel as well as for high and low R_9 are shown separately. Only the corrections at high E_T are relevant as the photon is required to have $p_T > 15$ GeV.

6.1.7. Dijet Selection

The hadronic jet selection is used for the dijet tagged event class for the $H \rightarrow Z\gamma$ analysis. The VBF production channel tends to include high energy forward jets as part of the signal topology. Using this signature greatly reduces the background, making this class very sensitive, even with potentially large jet-related systematic uncertainties.

Jets used in this analysis are built by clustering the Particle Flow (PF) candidates with the anti-kT [25] clustering algorithm with distance parameter ΔR of 0.5. The jets must pass a standard jet identification and isolation selection that reduced pileup-related contamination. The energy and momenta of the reconstructed PF Jets are rescaled using correction factors derived and validated with 2012 dijet $Z\gamma +$ jet MC samples. Four energy corrections (pile-up, relative, absolute and residual calibration) are applied. The standard CMS pile-up subtraction method is used. The jet energy and resolution uncertainties are evaluated on a jet-by-jet basis, and are used to evaluate related systematic effects (see Chapter 8).

The two highest transverse energy (E_T), jets are used. Jets within a cone of $\Delta R < 0.5$ with respect to either of the two leptons or the photon are rejected. All jets must have E_T greater than 30 GeV and be within $|\eta| < 4.7$. The difference in pseudorapidity between the two jets has to be greater than 3.5 and the Zeppenfeld variable $Z_{\text{epp}} = \eta_{Z\gamma} - (\eta_{j_1} + \eta_{j_2})/2$ must be less than 2.5. The dijet mass is required to be greater than 500 GeV. Finally, the difference in azimuthal angle between the dijet system and the $Z\gamma$ system has to be greater than 2.4.

Based on MC studies, this selection is optimized to give the best signal-to-background ratio. The impact of each of the cuts in the dijet selection is shown in Figs. 6.20 to 6.24.

After weighting MC with all relevant scale factors, a difference of $(15 \pm 2.5)\%$ between data and simulated events was observed with the dijet selection, as opposed to a difference was only 5% before requiring the jets. This difference is most likely due to the $Z\gamma$ MC samples, which only simulate up to 2 jets. As the background yield is estimated via data driven methods, this discrepancy does not effect the systematic uncertainties of the analysis, but may lead to a sub-optimal event selection that could be refined in the future for even greater sensitivity.

In the 8 TeV sample, we expect ≈ 1 event in the fiducial volume for a 125 GeV Higgs that originates from the VBF process. After the dijet selection, about 0.2 VBF events remain. The ggF contribution in the final dijet tagged class is 18.3%, while the VH contribution is only 0.3%.

The data yield for the dijet tag sample at 8 TeV is 21 (19) events for the muon (electron) channel for $m_{\ell\ell\gamma}$ between 100 and 190 GeV, while at 7 TeV is only 9 events after combining the muon and electron channels.

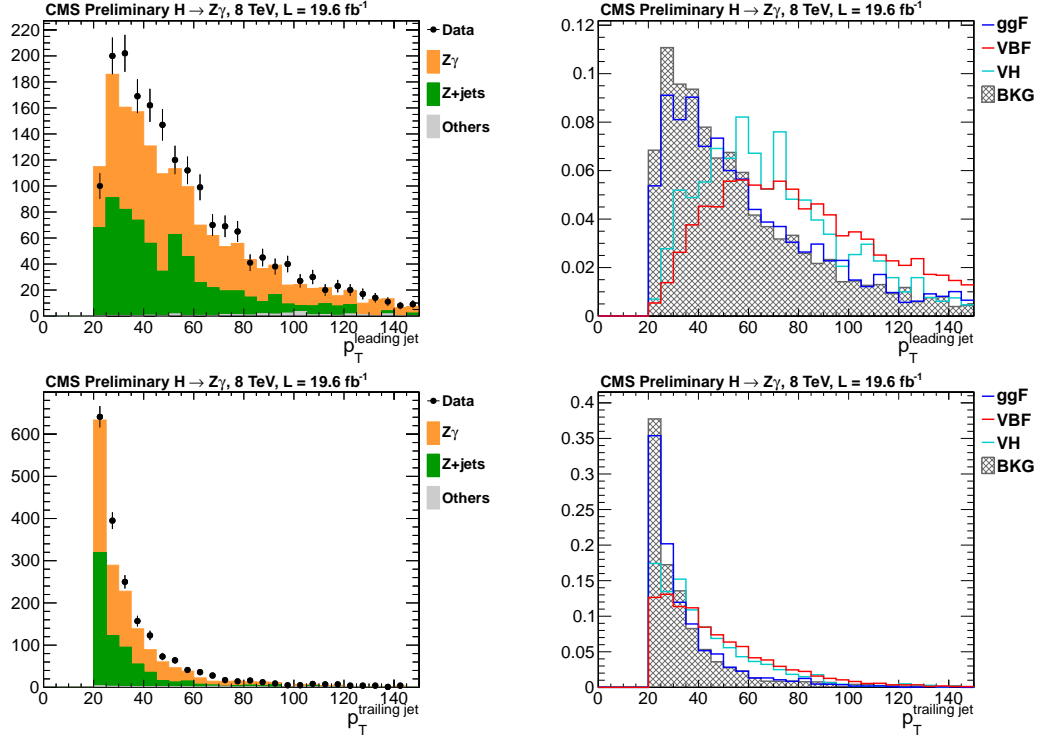


Figure 6.20. Raw jet transverse momentum distribution for data and simulated signal events.

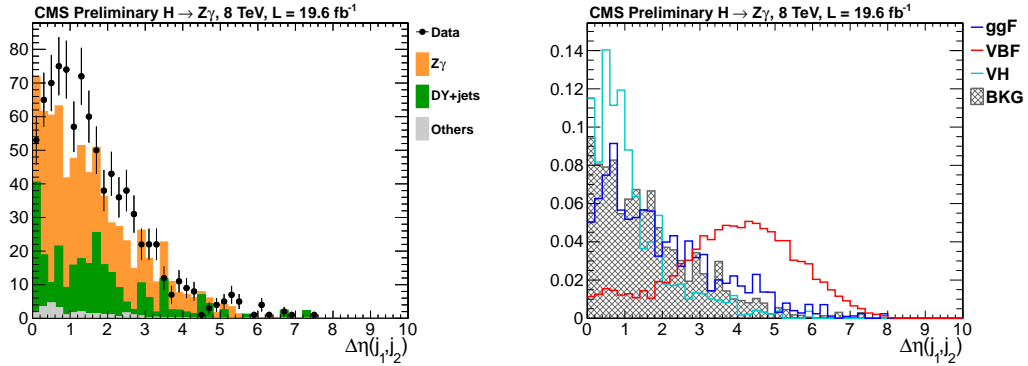


Figure 6.21. Jet rapidity gap distribution for data and signal events after the minimum transverse momentum on the jets is required.

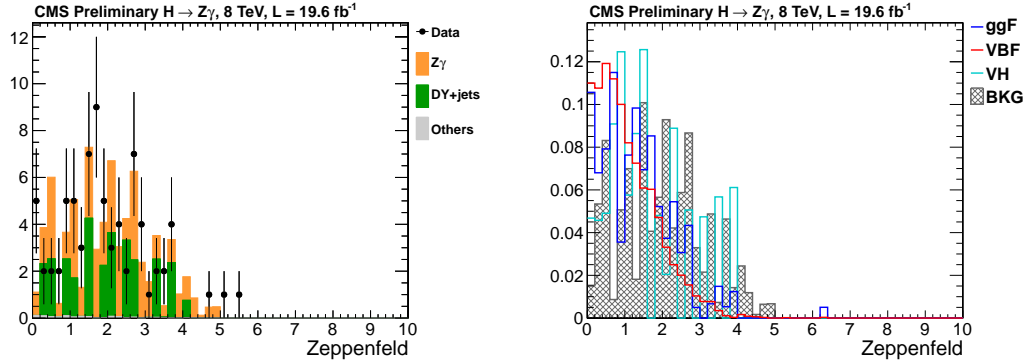


Figure 6.22. Zeppenfeld distribution for data and signal events after requiring a minimum transverse momentum on the jets and the jet rapidity gap are required.

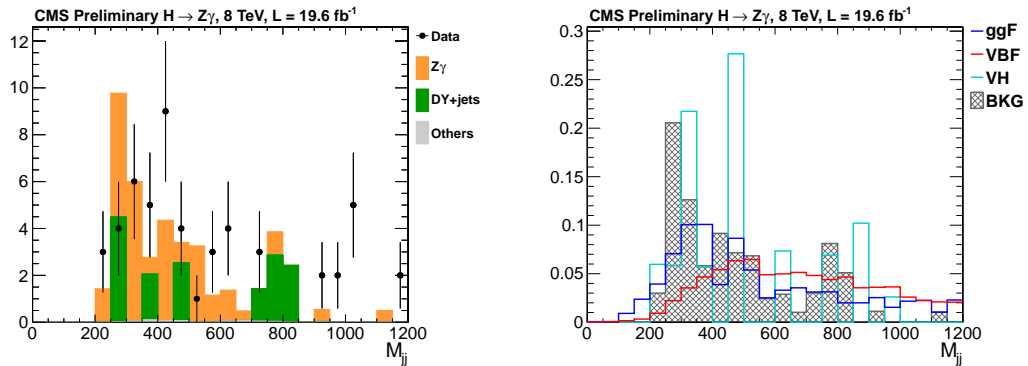


Figure 6.23. Dijet invariant mass for data and signal events after requiring a minimum transverse momentum on the jets, a jet rapidity gap and a maximum value on the Zeppenfeld variable.

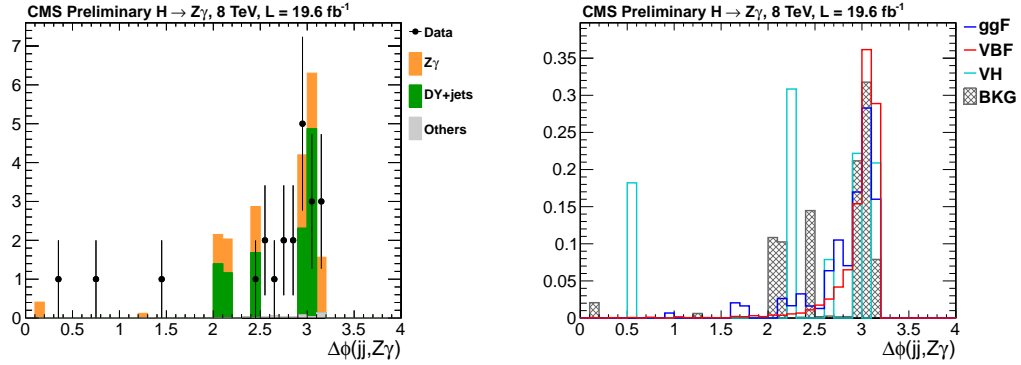


Figure 6.24. Difference in azimuthal angle for data and signal events after requiring a minimum transverse momentum on the jets, a jet rapidity gap, a maximum value on the Zeppenfeld variable and the minimum value in the dijet invariant mass.

6.2. Event Selection and Categorization

The $H \rightarrow Z\gamma$ and $A \rightarrow Z\gamma$ analyses share very similar event selections, as they both require the same final states and have the same background components. However, the $H \rightarrow Z\gamma$ analysis also splits the final events into categories, which improve the sensitivity of the final result. These categories are chosen based on the kinematics and the resolution of the final state particles; the $H \rightarrow Z\gamma$ decays tend to be more barrel centric, and the barrel tends to lead to better object resolution. There is no categorization for the $A \rightarrow Z\gamma$ analysis, as one of its aims it to be model independent.

6.2.1. Basic Selection

All events selected must pass the following criteria:

- There must be at least one good primary vertex, Section 6.1.2.
- A di-lepton trigger must have fired, Section 6.1.1.
- At least two opposite sign, same flavor leptons must be present, Section 6.1.3 and Section 6.1.4.
- At least one good photon, Section 6.1.5. Additionally, the photon must satisfy $\Delta R(\ell, \gamma) > 0.4$.
- If there are additional leptons, the two selected leptons satisfy the above selection and have an invariant mass closest to the nominal Z boson mass.
- The di-lepton invariant mass must be larger than 50 GeV.
- The sum of the $m_{\ell\ell}$ and $m_{\ell\ell\gamma}$ distributions must be greater than 185 GeV ($H \rightarrow Z\gamma$ analysis only).

- The photon transverse momentum divided by the three-body mass for the $H \rightarrow Z\gamma$ ($A \rightarrow Z\gamma$) analysis must be greater than 15/110 (40/150).

The ΔR requirement between the photon and lepton reduces the final state radiation background, as the FSR photon tends to be collinear with its parent lepton. The Z boson mass requirement vetoes events from the $\gamma^*\gamma$ spectrum for both signal and background, as off-shell Z bosons are not the focus of this analysis.

The photon p_T over three-body mass cut reduces background without significant impact to signal strength, while maintaining the overall shape of the three-body mass distribution at low mass. This cut tightens the p_T requirement on the photon at higher three-body invariant mass. As the signal increases in mass, the photon increases in energy. Removing lower energy photons from the higher-mass signals prevents unnecessary contamination from background sources without sacrificing sensitivity at low mass. Fig 6.34 depicts the aforementioned cut variable before the cut is applied.

For the $H \rightarrow Z\gamma$ search, the low mass region is highly contaminated by final state radiation (FSR) in Z decays, see Figures 6.29 and 6.30. For this reason, the selected events are required to have $m_{\ell\ell} + m_{\ell\ell\gamma} > 185$ GeV – referred to later in the text as the mass-sum cut. The FSR events are significantly reduced, while the loss in signal events is at the percent level. After the introduction of this requirement, the turn-on region becomes more defined, making it easier to find a good parametric function for the background fitting procedure, see Fig. 6.27 and 6.28. Any further adjustment of this mass-sum cut will change the shape of the turn-on, but will not reduce the remaining backgrounds without adversely effecting the signal efficiency. Kinematic distributions of selected objects are shown in the following figures.

6.2.2. $H \rightarrow Z\gamma$ Kinematic Plots

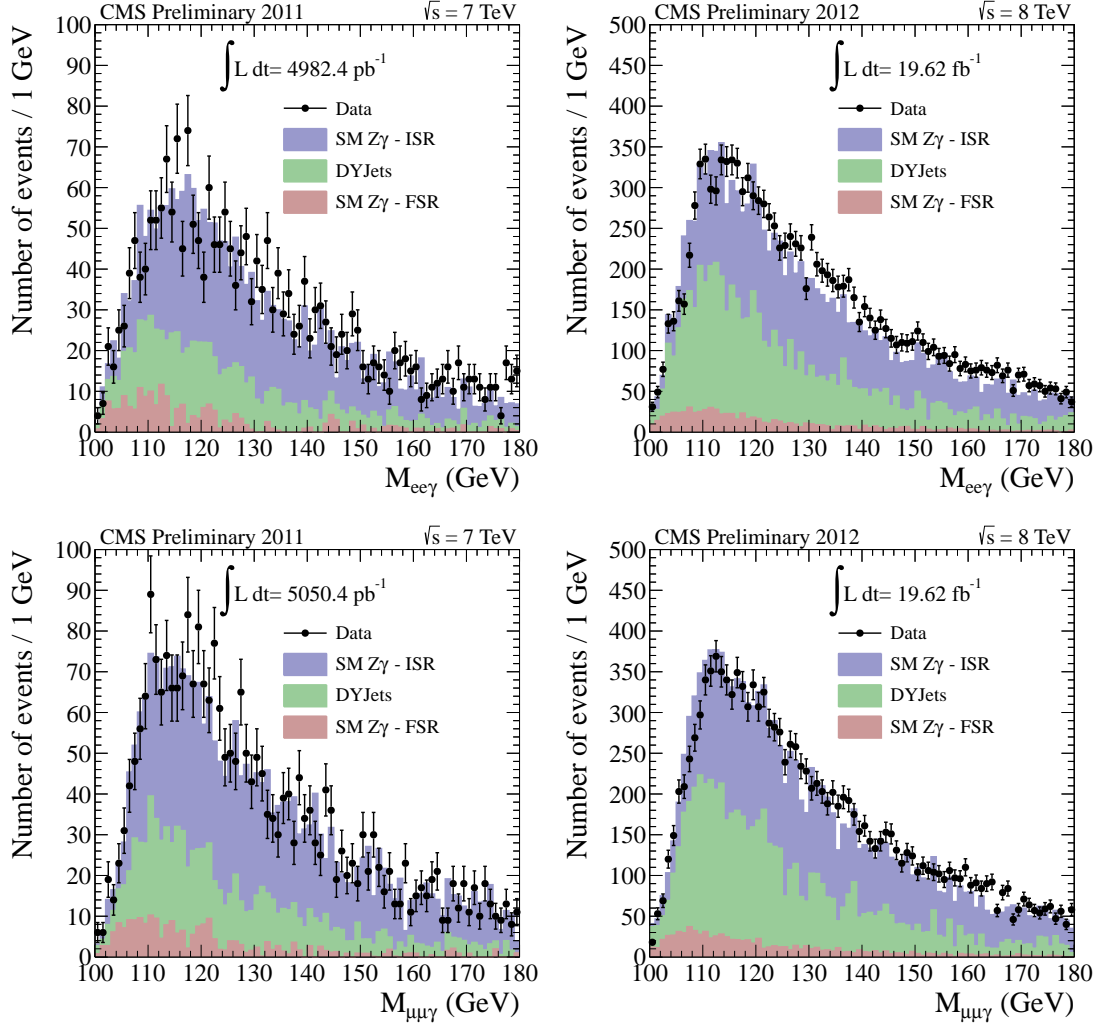


Figure 6.25. Final three-body mass distributions for the four datasets are reported for data and the main backgrounds (SM $Z\gamma$ and DYJets). Top plot is relative to 2011 $ee\gamma$, top right is for 2012 $ee\gamma$, bottom left is for 2011 $\mu\mu\gamma$ and bottom right is for 2012 $\mu\mu\gamma$.

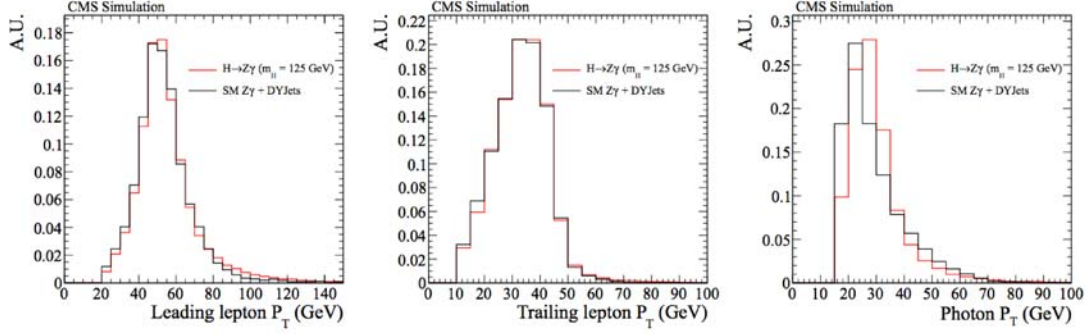


Figure 6.26. Transverse momenta of final state particles in the $H \rightarrow Z\gamma$ analysis.

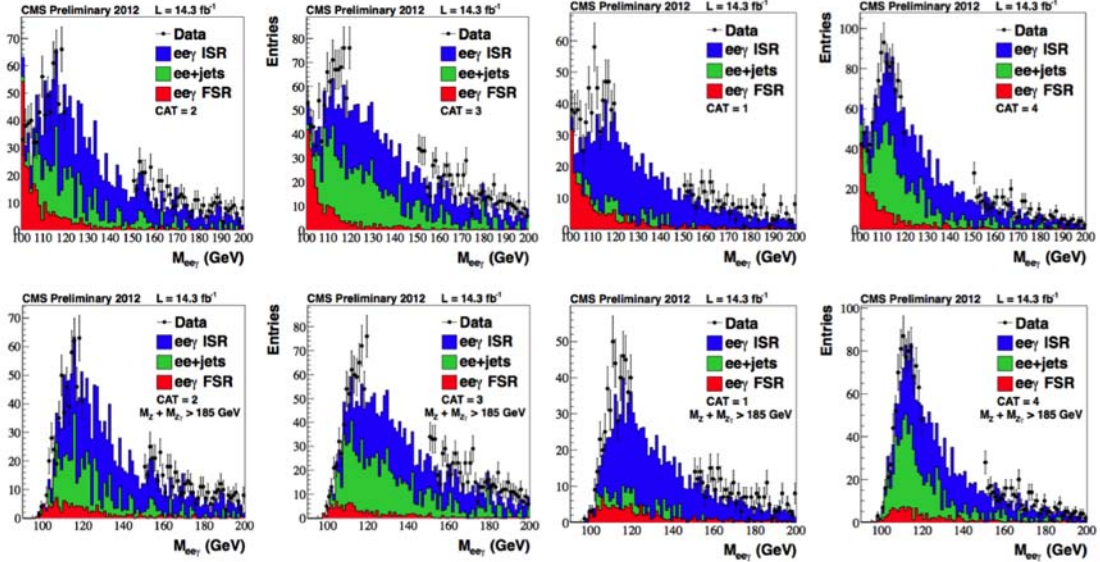


Figure 6.27. Mass distributions of $m_{e\bar{e}\gamma}$ events in the four categories, before and after the $m_{\ell\bar{\ell}} + m_{\ell\bar{\ell}\gamma} > 185$ GeV cut.

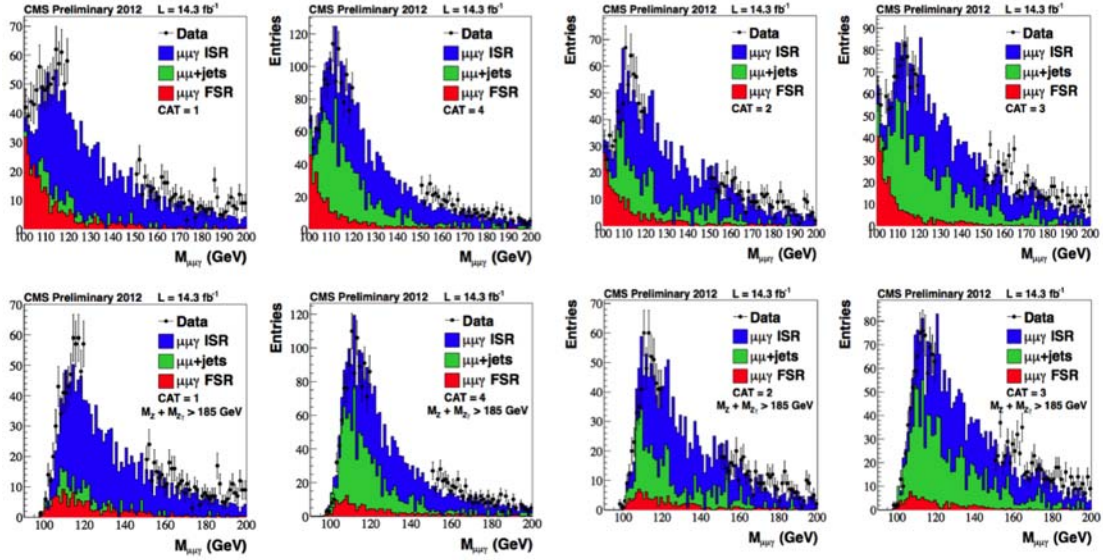


Figure 6.28. Mass distributions of $m_{\mu\mu\gamma}$ events in the four categories, before and after the $m_{\ell\ell} + m_{\ell\ell\gamma} > 185$ GeV cut.

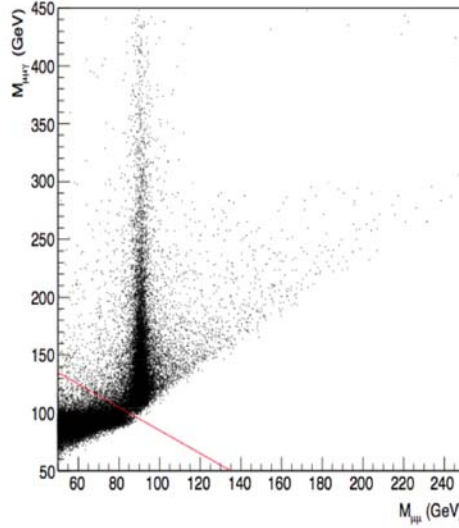


Figure 6.29. Mass distribution of $\mu\mu\gamma$ events vs. invariant mass distribution of $\mu\mu$ events from Z decay. The red line represents the mass-sum ($m_{\ell\ell} + m_{\ell\ell\gamma} > 185$) cut.

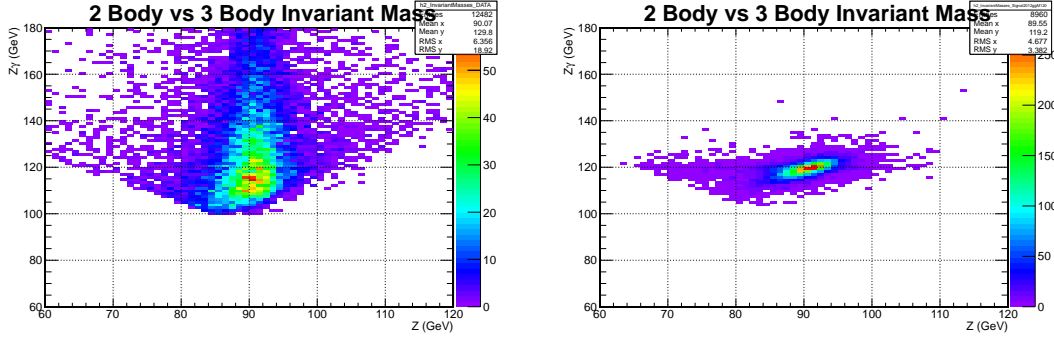


Figure 6.30. Mass distribution of $\mu\mu\gamma$ events vs. invariant mass distribution of $\mu\mu$ events from Z decay after applying the mass-sum requirement in data and simulated events for $m_H = 120$ GeV.

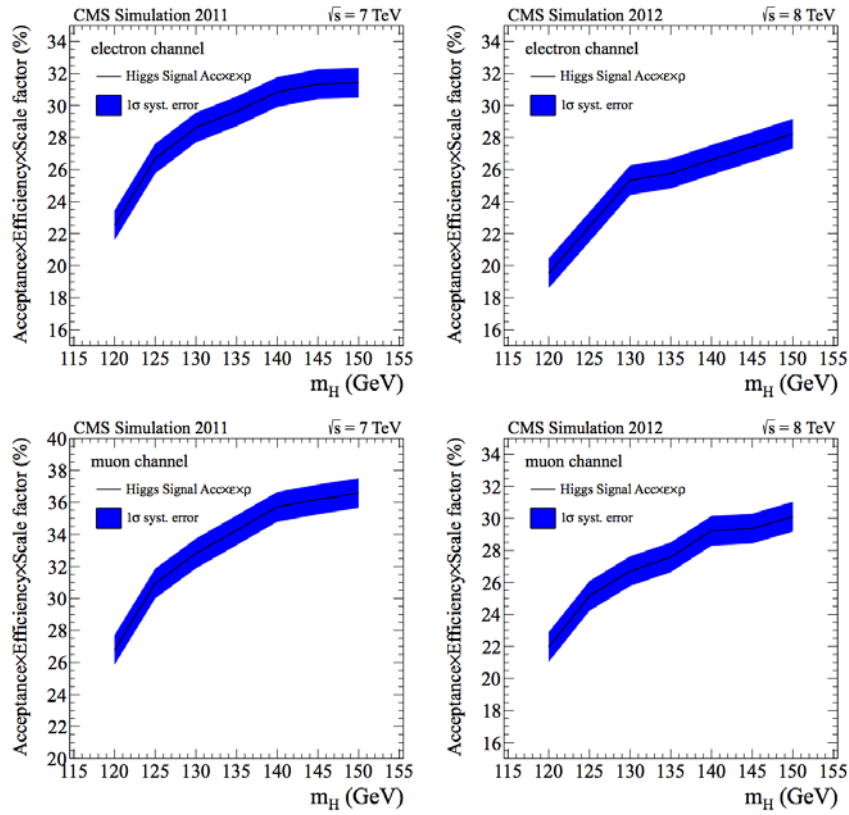


Figure 6.31. Acceptance X Efficiency as a function of signal mass for the $H \rightarrow Z\gamma$ analysis.

6.2.3. $A \rightarrow Z\gamma$ Kinematic Plots

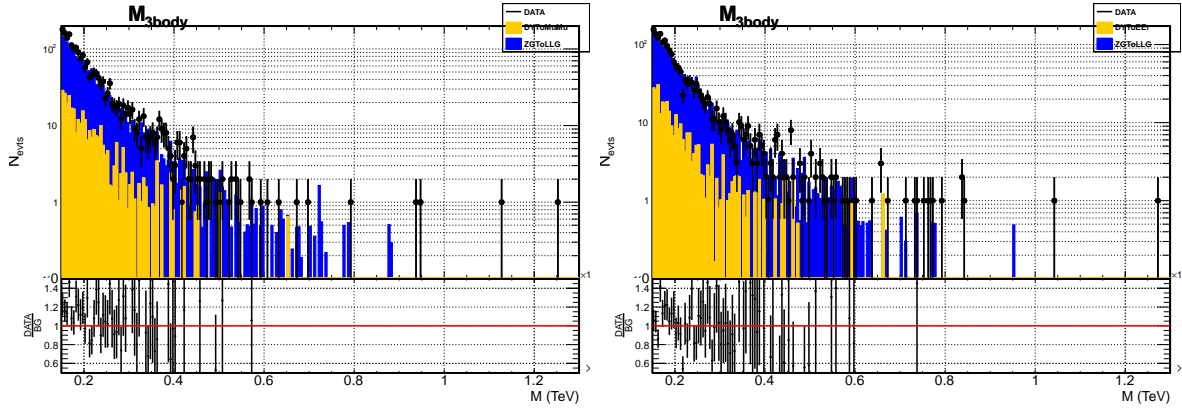


Figure 6.32. Three-body invariant mass for 2012 data for in $A \rightarrow Z\gamma$ analysis in the $\mu\mu\gamma$ (left) ee γ (right) channel after the full analysis selection. Errors on data distributions are poissonian.

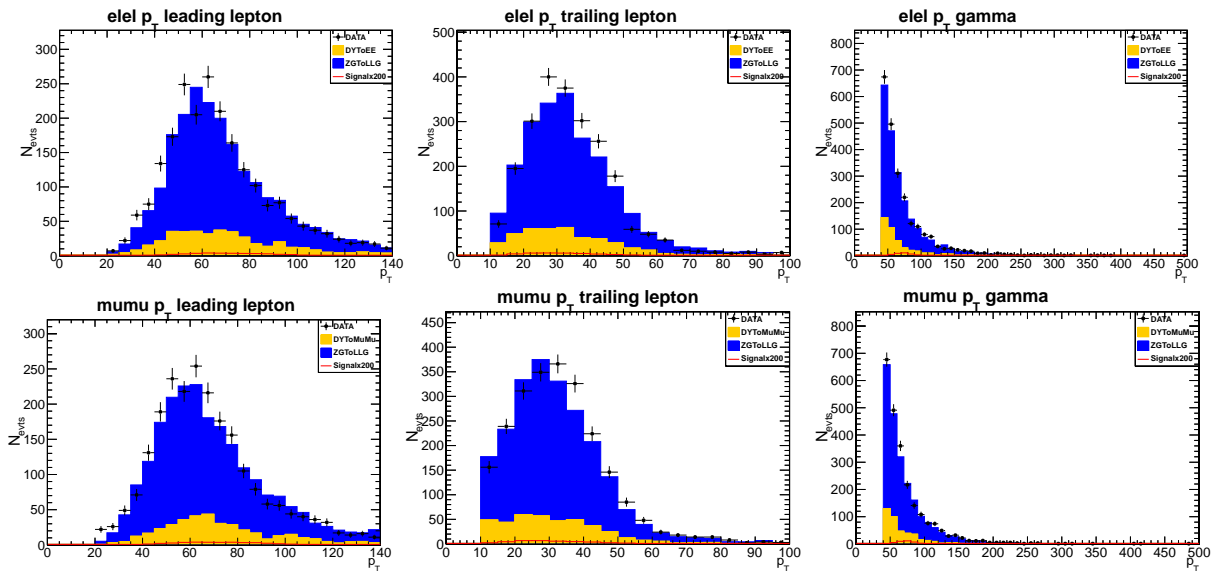


Figure 6.33. Transverse momentum distributions for the final state particles for the $A \rightarrow Z\gamma$ analysis. Top: dielectron channel. Bottom: dimuon channel.

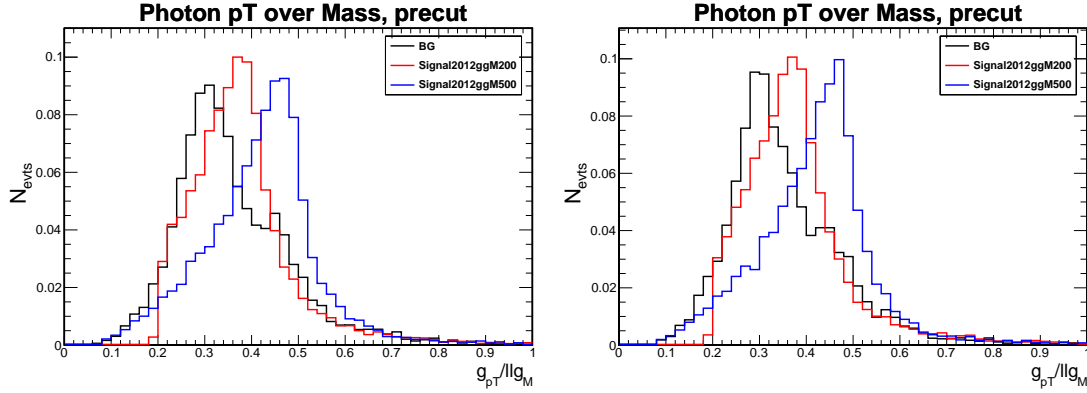


Figure 6.34. $\gamma_{pT}/\ell\ell\gamma_m$ for signal (M200 and M500) and background. Left: Muon, Right: Electron.

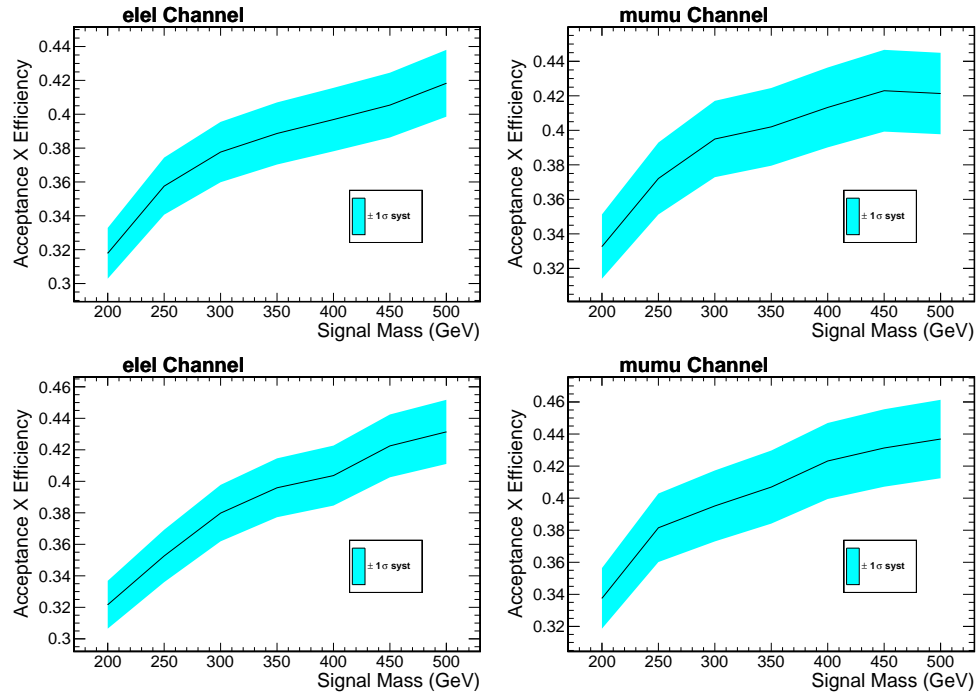


Figure 6.35. Acceptance \times Efficiency as a function of signal mass for the $A \rightarrow Z\gamma$ analysis. Top: wide width. Bottom: narrow width. Left: dielectron channel. Right: dimuon channel.

6.2.4. Event Categorization ($H \rightarrow Z\gamma$ Only)

The sensitivity of the $H \rightarrow Z\gamma$ search can be enhanced by subdividing the selected events into categories according to indicators of the expected mass resolution and the signal-to-background ratio, the results of which are combined during the limit calculation. As these categorizations are heavily determined by the kinematic distributions and production methods of the signal model, they are inappropriate for the model independent $A \rightarrow Z\gamma$ analysis. Therefore, this categorization section pertains only to the $H \rightarrow Z\gamma$ analysis.

A significant fraction of the signal events are expected to have both the leptons and the photon in the barrel, while at least one third of the background events have the photon in the endcap. In addition, events with unconverted photons have less background and higher resolution. For these reasons, the events are classified according to the pseudorapidity of the leptons, the pseudorapidity of the photon and the value for the R_9 shower shape variable of the photon. The R_9 variable is defined as the energy sum of 3×3 crystals centered on the most energetic crystal in the supercluster divided by the energy of the supercluster. A high R_9 value, i.e. greater than 0.94, is used to identify unconverted photons.

The sensitivity of the search is further increased by at least 10-20% by adding another event class defined by two forward jets with high pseudorapidity difference and large invariant mass. This class has a very high signal to background ratio, as the combined electron and muon channels have about 40 events in data, and 1 signal event is expected.

The exact definition of the five event classes is shown in Table 6.11. The definition for electrons and muons are not the same due to the differences in the geometry of the detector and resulting resolution. In order to have enough events for the background

fitting, only the event class with the two leptons in the barrel is subdivided according to the R_9 value of the photon ($R_9 > 0.94$ or $R_9 \geq 0.94$). The table includes the expected event fractions in each class for signal events for a Higgs boson with a mass of a 125 GeV (gg process at 8 TeV only) and the observed data in the full mass window. The expected mass resolution is also included.

Table 6.11. Definition of the four untagged event classes, the fraction of selected events for a signal with $m_H = 125$ GeV produced by gluon-gluon fusion at 8 TeV and data in a narrow bin centered at 125 GeV. The expected mass resolution on the signal is also shown.

Event class	$e^+e^-\gamma$				
	1	2	3	4	VBF
Photon	$0 < \eta < 1.4442$	$0 < \eta < 1.4442$	$0 < \eta < 1.4442$	$1.566 < \eta < 2.5$	$0 < \eta < 2.5$
Lepton 1	$0 < \eta < 1.4442$	$0 < \eta < 1.4442$	$0.0 < \eta < 2.5$	$0 < \eta < 2.5$	$0 < \eta < 2.5$
Lepton 2	$0 < \eta < 1.4442$	$0 < \eta < 1.4442$	$1.4442 < \eta < 2.5$	$0 < \eta < 2.5$	$0 < \eta < 2.5$
R_9	> 0.94	< 0.94	N/A	N/A	N/A
Data	17%	26%	26%	31%	0.1%
Signal	29%	27%	23%	19%	1.8%
σ_{eff} (GeV)	1.9	2.1	3.1	3.3	2.6
FWHM (GeV)	4.5	5.0	7.3	7.8	4.4
Event class	$\mu^+\mu^-\gamma$				
	1	2	3	4	VBF
Photon	$0 < \eta < 1.4442$	$0 < \eta < 1.4442$	$0 < \eta < 1.4442$	$1.566 < \eta < 2.5$	$0 < \eta < 2.5$
Lepton 1	$0 < \eta < 2.1$	$0 < \eta < 2.1$	$0 < \eta < 0.9$	$0 < \eta < 2.4$	$0 < \eta < 2.4$
Lepton 2	$0 < \eta < 0.9$	$0 < \eta < 0.9$	$0 < \eta < 2.4$	$0 < \eta < 2.4$	$0 < \eta < 2.4$
R_9	> 0.94	< 0.94	N/A	N/A	N/A
Data	20%	31%	20%	29%	0.2%
Signal	33%	30%	18%	17%	1.7%
σ_{eff} (GeV)	1.6	1.9	2.1	3.2	2.2
FWHM (GeV)	3.7	4.6	5.0	7.5	3.8

The dilepton pseudorapidity distributions for the topological component of the category definitions are shown in Fig. 6.36. Categories are combined in the aforementioned figure if they have the same pseudorapidity definition.

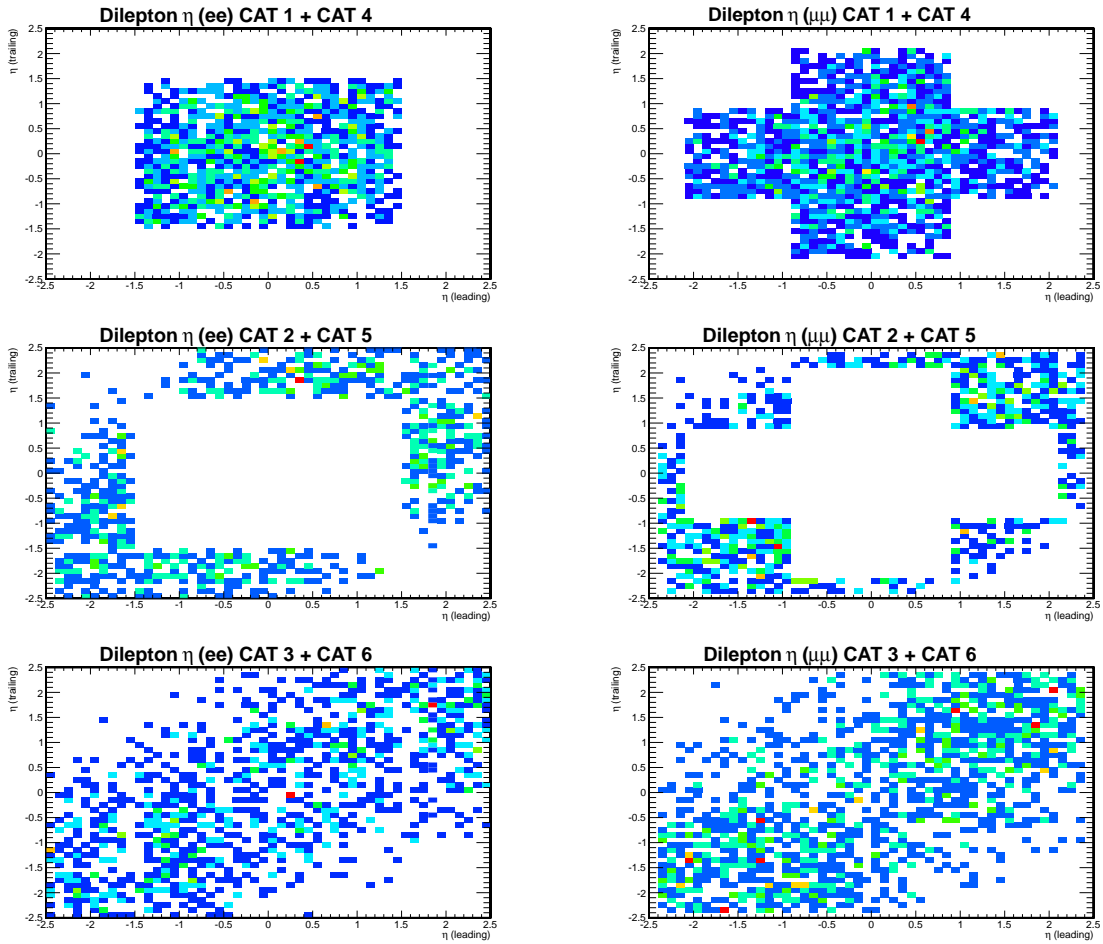


Figure 6.36. The 2D dilepton distributions for the topological categories.

CHAPTER 7

Parametric Modeling

7.1. Background Modeling

Background estimation is a necessity for any resonance search. The $m_{\ell\ell\gamma}$ spectrum in this analysis is sculpted by the kinematic cuts placed on the final state objects, thus deviating from easily calculable theoretical cross sections. If Monte-Carlo based background estimation was employed, the simulation of both QED initial state radiation and fake photon reconstructed would need to be improved, or large systematic uncertainties would be put in place.

Instead of relying on event simulation, a fit bias study is performed to estimate the overall background contribution in a given signal region. The bias study relies on “truth” functions (functional families with low degrees of freedom that model the data well with respect to a goodness-of-fit metric) that are used to generate thousands of toy datasets. These datasets are then fit with “test” functions (functional families with larger degrees of freedom that also satisfactorily fit the real data and toy data) combined with a freely floating signal template or function. In practice, the signal template or function will fluctuate in its allowed region, finding some positive or negative signal yield for any given toy. After all toys are fitted, an unbiased function is determined as one that, on average, has a statistical error that is substantially larger than the average signal deviation from null.

Any potential systematic error associated with the background function can safely be ignored, as the bias study is done in order to show that the systematic error is sufficiently smaller than the statistical error. “Sufficiently smaller” is defined such that the average deviation in the number of signal events is five times smaller than the statistical error on the yield of the background function in the signal region. This criterion is quantified as follows:

- A modified pull distribution as defined by $(\mu_{FIT} - t)/\sigma_{BG}$, where μ_{FIT} is average signal yield, t is the true signal yield, and σ_{BG} is the error on the background yield in the signal region (see Fig. 7.17). This metric must be less than 0.2 for the function to be considered as the actual background estimator.

Fit bias studies were performed using simulated events of background-only event samples for the analysis presented. Based on that work, a function consisting of the sum of three exponentials was used to model the background for both the $\mu\mu\gamma$ and $ee\gamma$ distributions, for all generated mass points. The overall bias was found to be smaller than the requirement listed above for all mass points, and no function with fewer degrees of freedom satisfied the criterion.

There are three distinct regions that were considered when choosing truth and test functions for the $H \rightarrow Z\gamma$ and $A \rightarrow Z\gamma$ analyses:

- The four kinematic event classes in the $H \rightarrow Z\gamma$ analysis.
- The dijet event class in the $H \rightarrow Z\gamma$ analysis.
- The high mass $A \rightarrow Z\gamma$ analysis.

The background considered in the $H \rightarrow Z\gamma$ analysis is in the range $120 < m_H < 160$ GeV, where the four kinematic event classes are parameterized with the same set

of functions, but the fifth class (dijet-tagged class) is parameterized with a different set of functions, as it is qualitatively different (less events, no discernible turn-on). The $A \rightarrow Z\gamma$ analysis considers the range $200 < m_A < 1200$ GeV, and uses a third set of functions. All function sets are the same between the electron and muon channels. The full ranges and estimated MC background components are shown in the previous section (Figs. 6.2.2 , 6.32). The MC samples shown in the plots are not used to estimate background in the actual limit calculations.

7.1.1. $H \rightarrow Z\gamma$ Background Modeling

The $m_{\ell\ell\gamma}$ distribution for the $H \rightarrow Z\gamma \rightarrow \ell\ell\gamma$ analysis is fit over the range from 100 to 180 GeV. For the four kinematic event classes, there is a prominent turn-on in the distribution from roughly 100 to 115 GeV, and then the distribution decreases monotonically from 115 to 180 GeV. It is necessary to fit the turn-on; the resonance search region starts at 120 GeV and the background estimation in that low mass region would be highly dependent on the statistical fluctuation around 115 GeV, necessitating a systematic uncertainty.

Two functional forms are being considered:

- Bernstein polynomials and a step function with value 0 in the region < 115 GeV convoluted with a gaussian.
- Bernstein polynomials and a step function with value 0 in the region < 115 GeV convoluted with a hyperbolic secant of the form:

$$(7.1) \quad F(m) = \frac{\exp^{\frac{-(m-p_1)}{p_2}}}{1 + \exp^{\frac{-2(m-p_1)}{p_2}}}.$$

The fits for all four data samples and each event class are shown in Figs. 7.1–7.4. The dijet-tagged class has less than 20 events per lepton channel. There is no prominent turn-on, and as a consequence, a different set of truth and test functions are employed. The truth functions were an exponential and a power law distribution, and the test functions were Bernstein polynomials of order 2, 3, and 4. The truth and test functions are shown in Fig. 7.5

After completing and evaluating all bias studies, the following functions were chosen represent the background components of the data: A fifth-order Bernstein polynomial convoluted with a gaussian for all kinematic (not dijet tagged) classes except class 1. The class 1 events were modeled by a forth-order Bernstein polynomial convoluted with a gaussian. The dijet classes were modeled with a third-order Bernstein polynomial. The final fits are shown in Figs 7.10–7.13.

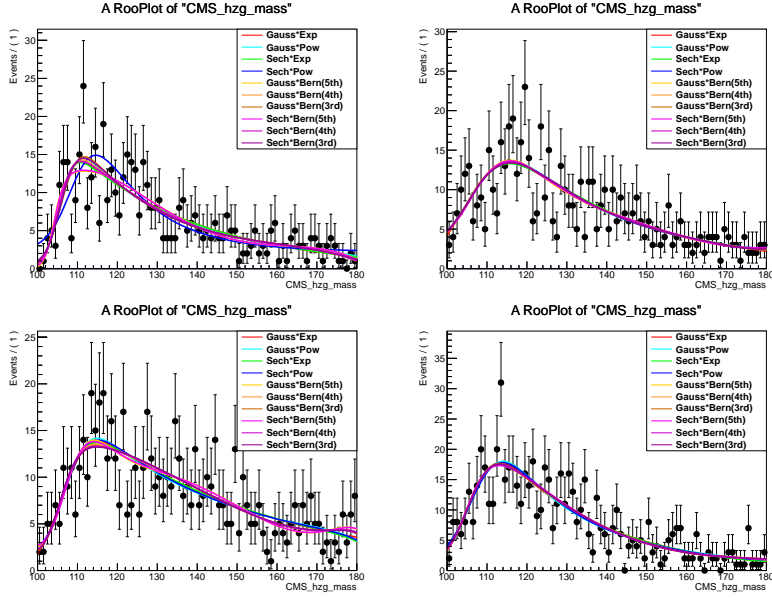


Figure 7.1. Three-body invariant mass for 2011 data in the $ee\gamma$ channel after the application of the $m_{\ell\ell} + m_{\ell\ell\gamma}$ cut. Errors on data distributions are poissonian.

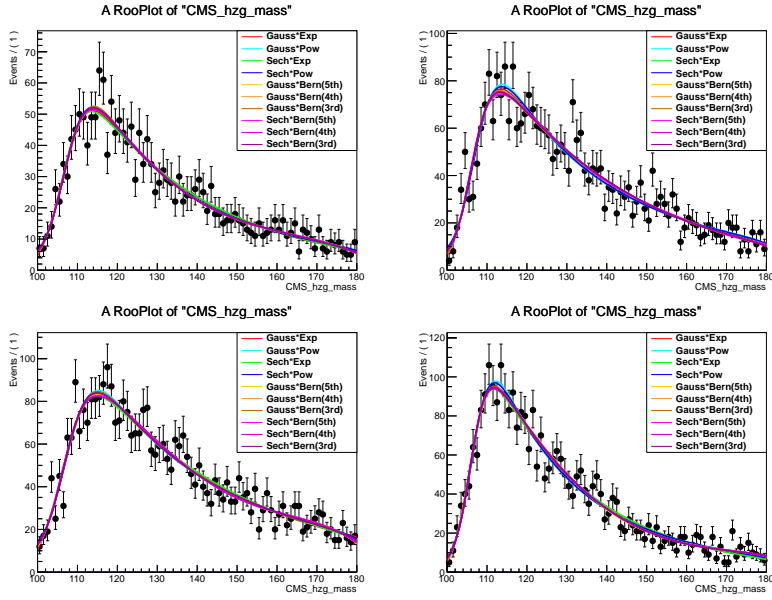


Figure 7.2. Three-body invariant mass for 2012 data in the $ee\gamma$ channel after the application of the $m_{\ell\ell} + m_{\ell\ell\gamma}$ cut. Errors on data distributions are poissonian.

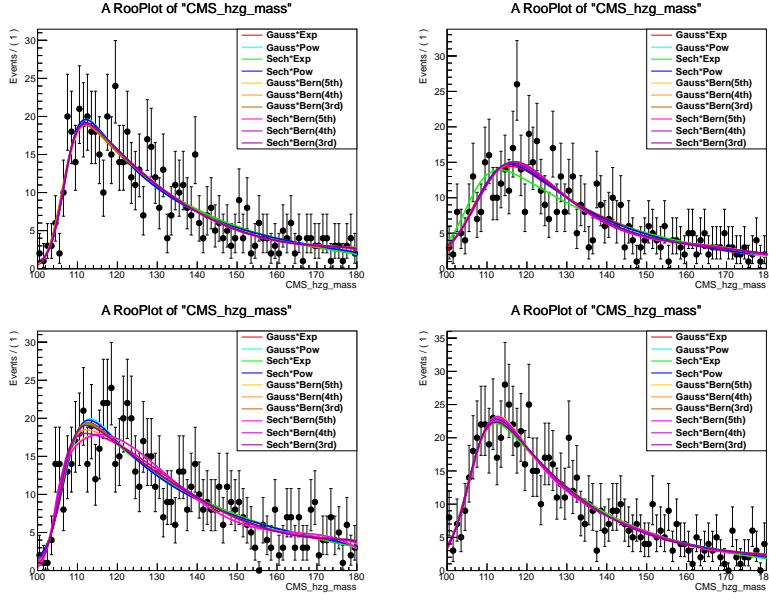


Figure 7.3. Three-body invariant mass for 2011 data in the $\mu\mu\gamma$ channel after the application of the $m_{\ell\ell} + m_{\ell\ell\gamma}$ cut. Errors on data distributions are poissonian.

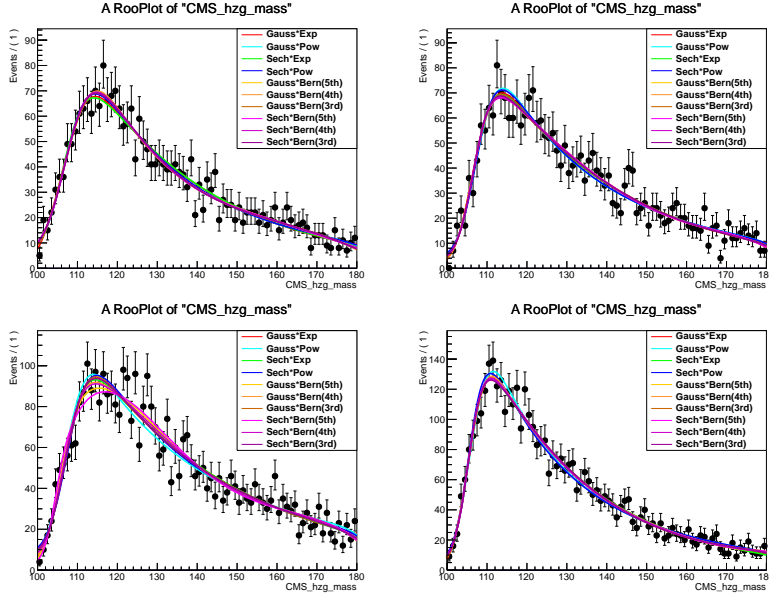


Figure 7.4. Three-body invariant mass for 2012 data in the $\mu\mu\gamma$ channel after the application of the $m_{\ell\ell} + m_{\ell\ell\gamma}$ cut. Errors on data distributions are poissonian.

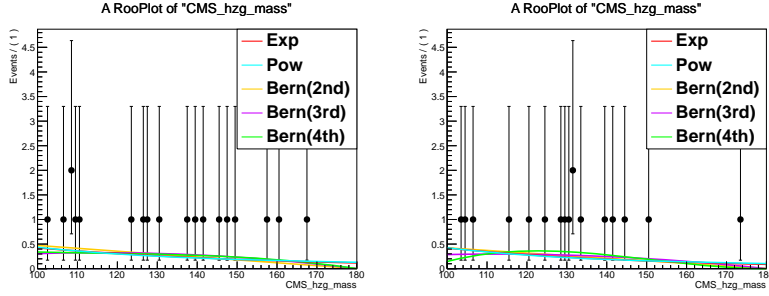


Figure 7.5. Three-body invariant mass for 2012 data in the $\mu\mu\gamma$ (right) and $ee\gamma$ (left) channel. Errors on data distributions are poissonian.

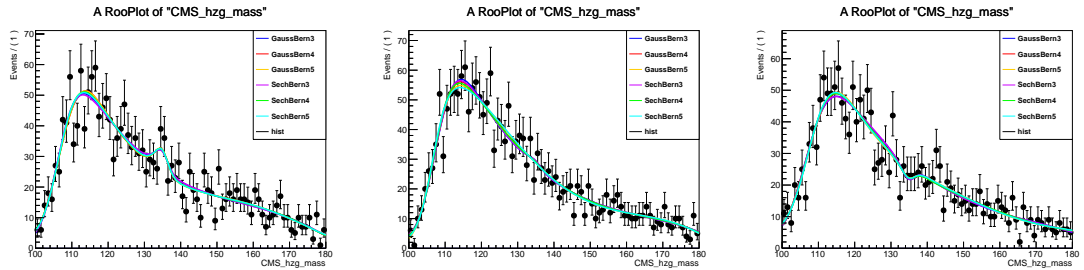


Figure 7.6. Sample toy distributions for events in the $ee\gamma$ channel. Truth model Gauss*pow shown, $mH = 135$ GeV, electron cat 4.

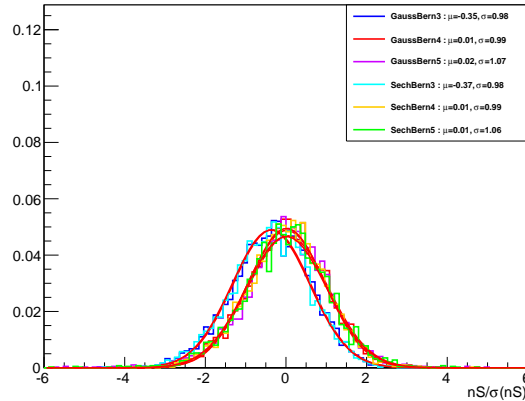


Figure 7.7. Example of mean bias (pull) distributions for events in the $ee\gamma$ channel. Truth model Gauss*pow shown, $mH = 135$ GeV, cat 4.

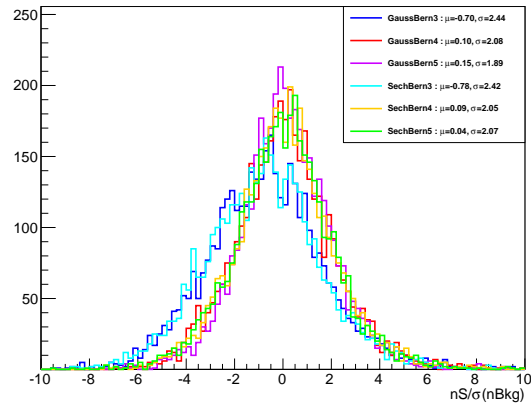


Figure 7.8. Example of mean bias (Type-A) distributions for events in the $e\bar{e}\gamma$ channel. Truth model Gauss^*pow shown, $mH = 135$ GeV, cat 4.

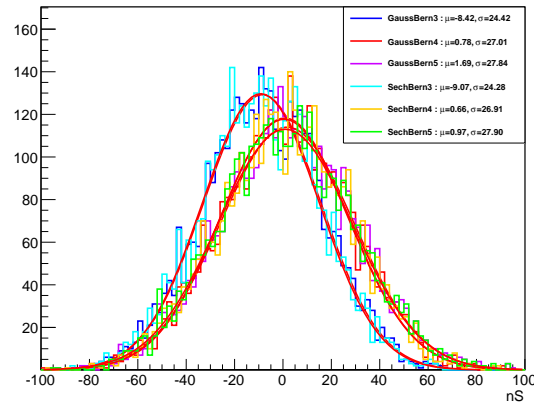


Figure 7.9. Mean signal yield for events in the $e\bar{e}\gamma$ channel. Truth model Gauss^*pow shown, $mH = 135$ GeV, cat 4.

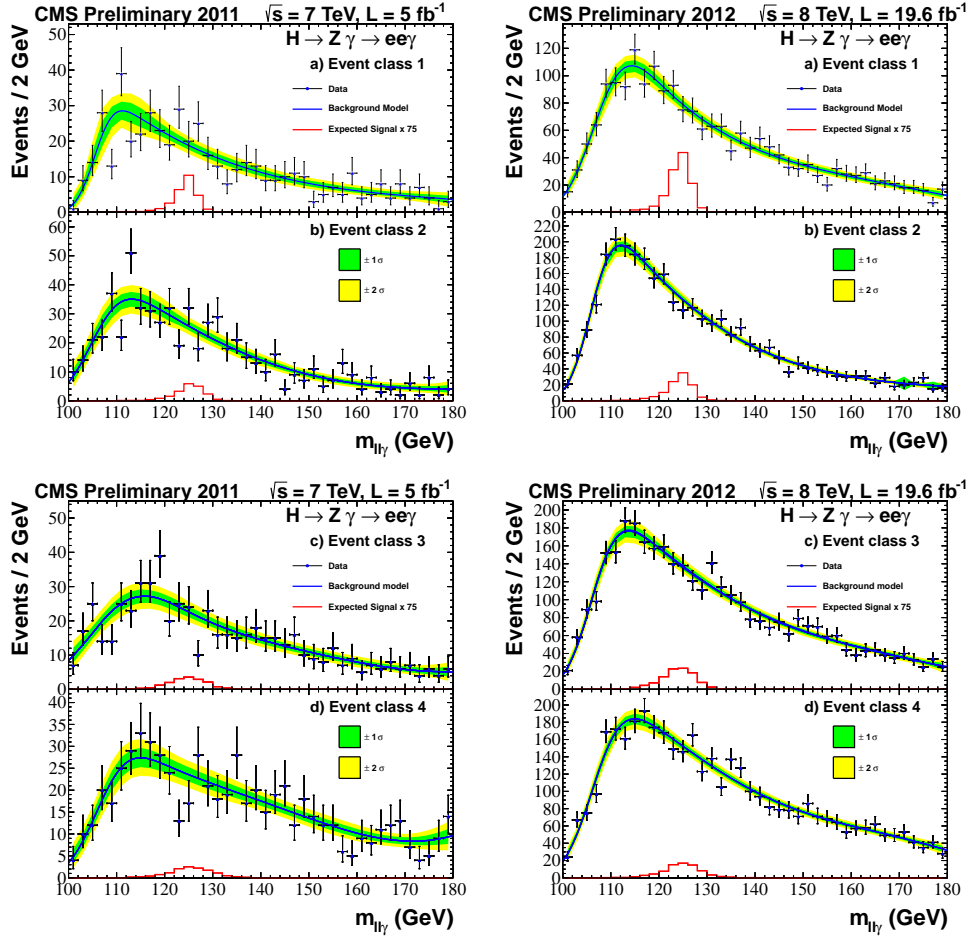


Figure 7.10. Background model fit to the $m_{ee\gamma}$ distribution for all event classes for the two data samples at 7 and 8 TeV. The statistical uncertainty bands shown are computed from the data fit.

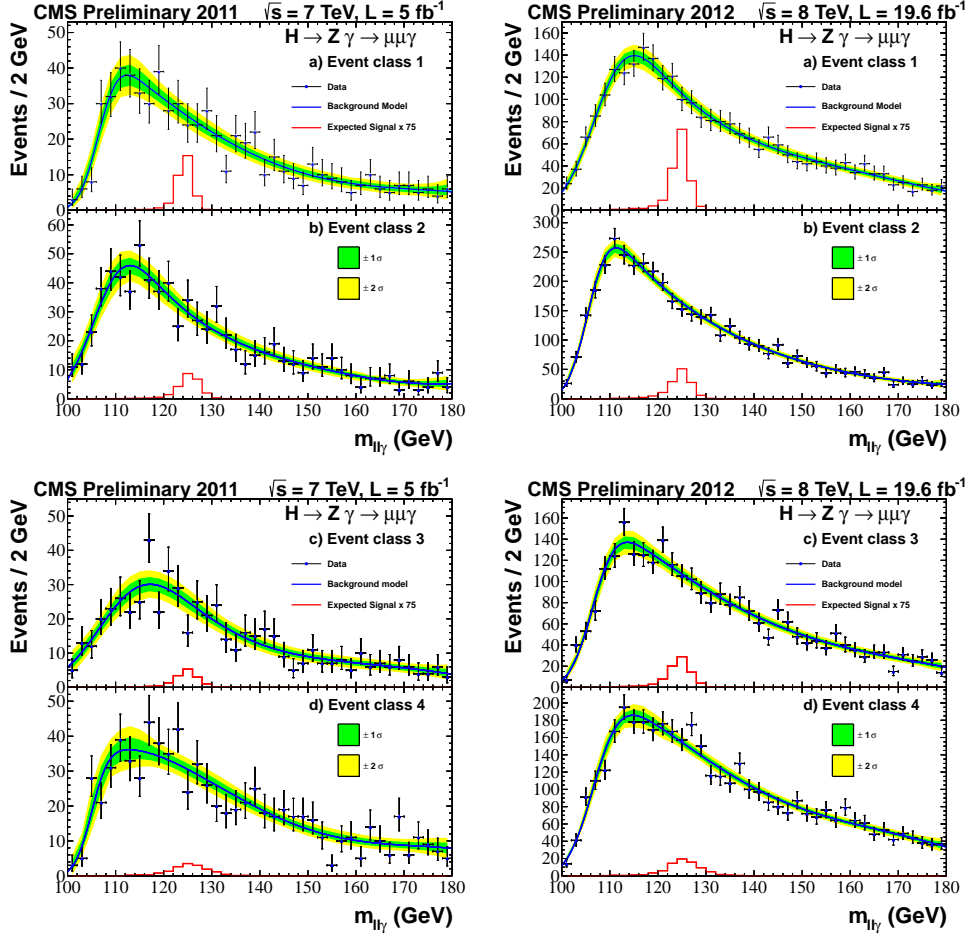


Figure 7.11. Background model fit to the $m_{\mu\mu\gamma}$ distribution for all event classes for the two data samples at 7 and 8 TeV. The statistical uncertainty bands shown are computed from the data fit.

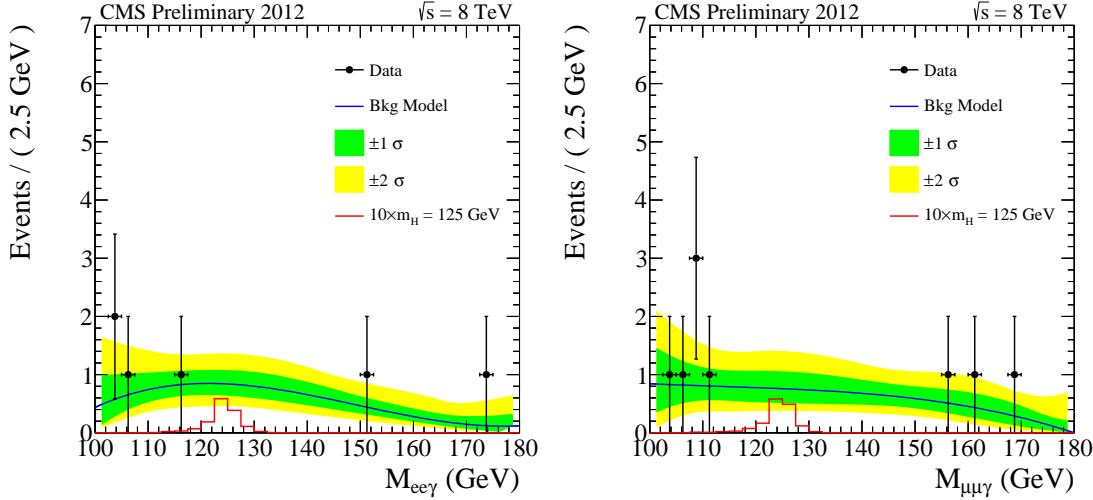


Figure 7.12. Mass distribution for the electron and the muon channels for the events in the dijet class at 8 TeV. The data is fitted to a polynomial of the third order.

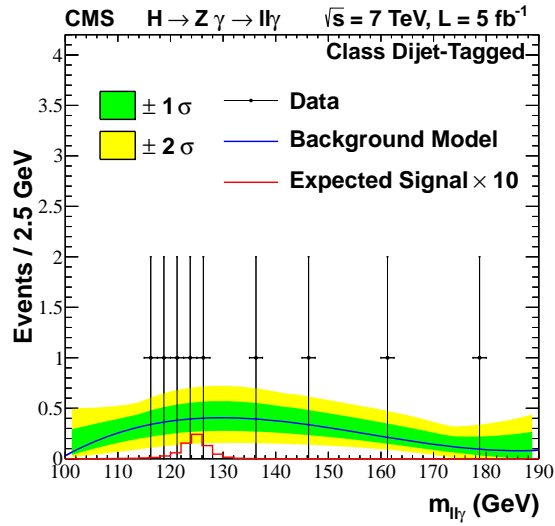


Figure 7.13. Mass distribution for the electron and the muon channels combined for the events in the dijet class at 7 TeV. The data is fitted to a polynomial of the third order.

7.1.2. $A \rightarrow Z\gamma$ Background Modeling

A new set of truth functions and test functions were used for this analysis, as compared to the SM HZG analysis [26]. Not only is the mass range and selection different, but the overall shape of the three-body mass distribution is different. There is no longer a turn-on at low mass; instead the entire spectrum is smooth and monotonically decreasing. Therefore the gaussian and sech functions that were convoluted with a decaying tail were no longer needed. Initially the distributions were fitted with Bernstein polynomials of varying degrees, but they all failed goodness-of-fit tests. New families of functions were chosen in their place.

The truth models considered were the following:

- A power function:

$$(7.2) \quad f_{Pow}(m) = m^{-p_1}.$$

- A simple Laurent polynomial expansion:

$$(7.3) \quad f_{Laurent}(m) = (1 - p_1) \cdot m^{-4} + p_1 \cdot m^{-5}.$$

- An exponential decay:

$$(7.4) \quad f_{Exp}(m) = e^{\frac{-m}{p_1 + p_2 \cdot m}}.$$

- A gamma distribution:

$$(7.5) \quad f_{Gamma}(m) = \frac{(m - \mu)^{\gamma-1} \cdot e^{-(m-\mu)/\beta}}{\Gamma(\gamma) \cdot \beta^\gamma}.$$

- A Hill function:

$$(7.6) \quad f_{Hill}(m) = \left(1 + \left(\frac{m}{\lambda}\right)^k\right)^{-1}.$$

- The Weibull distribution:

$$(7.7) \quad f_{Weibull}(m) = \frac{k}{\lambda} \left(\frac{m}{\lambda}\right)^{k-1} e^{-(m/\lambda)^k}.$$

The test models considered were the following:

- A power function times an exponential:

$$(7.8) \quad f_{PowDecay}(m) = m^{-p_1} \cdot e^{-m \cdot p_2}.$$

- A sum of a power function and an exponential function:

$$(7.9) \quad f_{PowExpSum}(m) = (1 - p_1) \cdot e^{-p_2 \cdot m} + p_1 \cdot m^{-p_3}.$$

- A sum of 2 exponentials:

$$(7.10) \quad f_{ExpSum}(m) = (1 - p_1) \cdot e^{-p_2 \cdot m} + p_1 \cdot e^{-p_3 \cdot m}.$$

- A sum of 3 exponentials:

$$(7.11) \quad f_{TripExpSum}(m) = (1 - p_1 - p_2) \cdot e^{-p_3 \cdot m} + p_1 \cdot e^{-p_4 \cdot m} + p_2 \cdot e^{-p_5 \cdot m}.$$

- A sum of 3 power functions :

$$(7.12) \quad f_{TripPowSum}(m) = (1 - p_1 - p_2) \cdot m^{-p_3} + p_1 \cdot m^{-p_4} + p_2 \cdot m^{-p_5}.$$

Fits to 2012 data for all truth and test functions are shown in Fig 7.14.

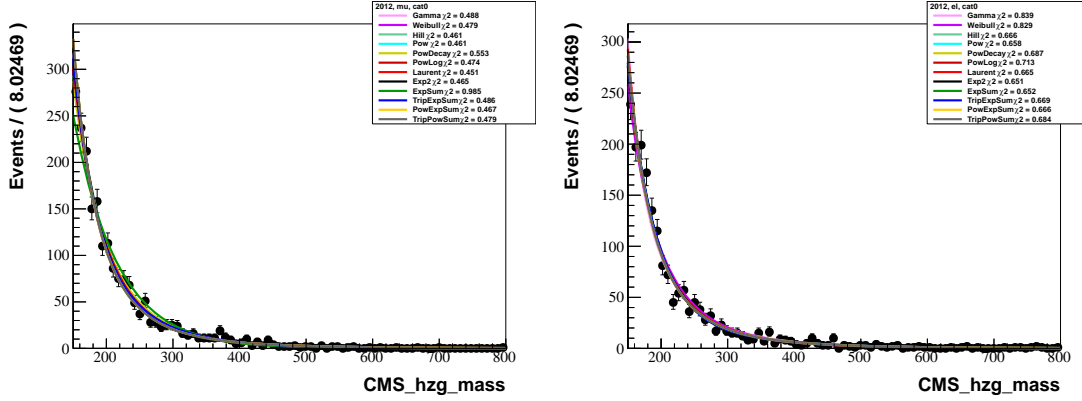


Figure 7.14. Three-body invariant mass for 2012 data in the $\mu\mu\gamma$ (left) ee γ (right) channel with initial truth and test function fits. Errors on data distributions are poissonian.

Examples of the bias-study output for a particular channel are shown below. Fig. 7.15 shows an example of a toy data distribution, generated by the exponential truth function. The truth function itself was initially fit to the data in order to produce the most accurate shape for this particular channel. The test functions are fit to the toy data, along with a signal template generated from the M200 signal MC. Fig. 7.16 (left) is an example of the average signal yield obtained after thousands of toys are generated and fit. As expected, the average signal yield is roughly centered on 0, as no actual signal was injected into the toys. Fig. 7.16 (right) shows the average error on the background yield parameter within the signal region for a given set of toys. Fig. 7.17 is an example of the final bias metric ($n\text{Sig}/\text{bg err}$). A test function with bias < 0.2 is considered satisfactory to model the background contribution in the data.

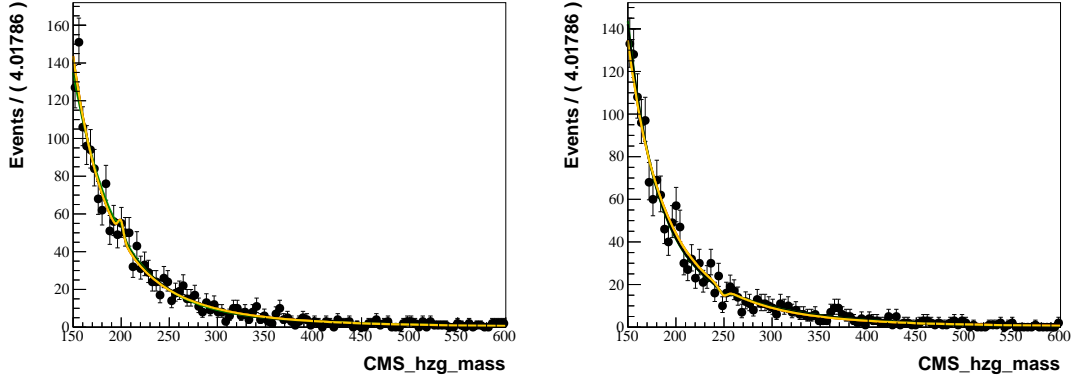


Figure 7.15. Sample fits to MC toys. Left: $\mu\mu\gamma$, exp truth function, 200 GeV signal. Right: $ee\gamma$, pow truth function, 250 GeV signal.

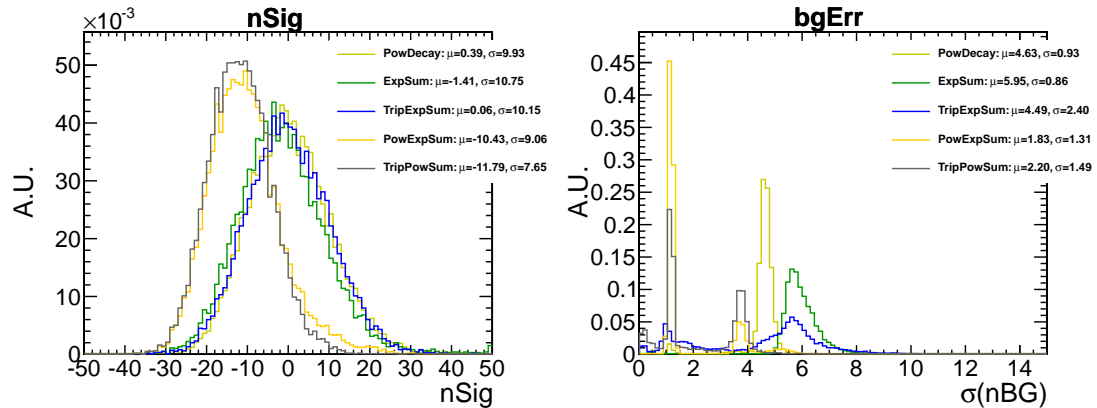


Figure 7.16. Example of average signal distribution (left) and background yield (right) after 10k toys. $\mu\mu\gamma$ channel, Hill truth function, 500 GeV signal.

The sum of three exponential functions (TripExpSum) was found to pass all bias criteria for all mass points and lepton channels. The results of all bias studies are located in Appendix B.

The background fits to the $m_{\ell\ell\gamma}$ distributions for the electron and muon channels based on the functional form indicated (TripExpSum) by the fit bias studies are shown in Figure 7.18.

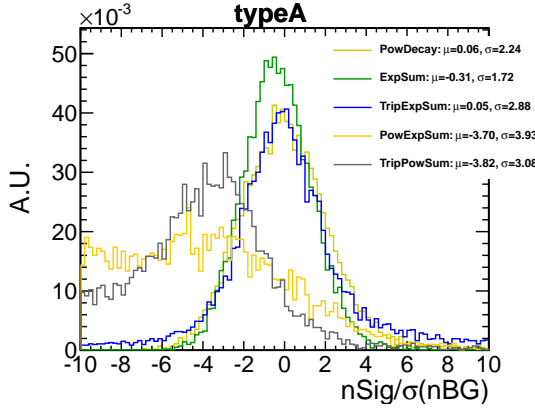


Figure 7.17. Example of bias metric distribution after 10k toys. $\mu\mu\gamma$ channel, Hill truth function, 500 GeV signal.

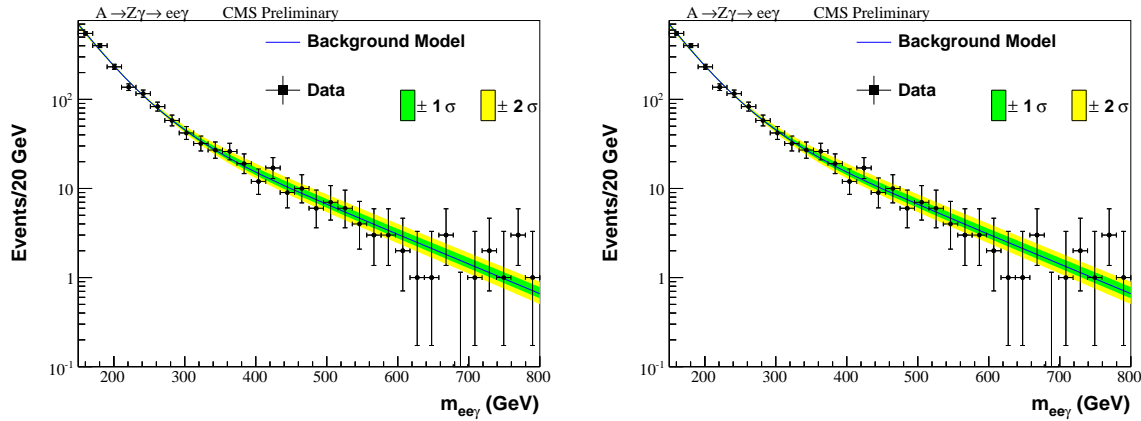


Figure 7.18. Background model fit to the $m_{e\ell\gamma}$ distribution for muon (left) and electron (right) channels at 8 TeV. The statistical uncertainty bands shown are computed from the data fit.

7.2. Signal Modeling

After the full analysis selection, application of weights based on selection efficiencies, and modification of the reconstructed dilepton and photon objects with their associated energy corrections, the three-body mass distribution was parametrically modeled. All five production methods (ggF, VBF, WH, ZH, ttH) in the $H \rightarrow Z\gamma$ analysis are fit

independently of one another. Both signal models (broad and narrow) in the $A \rightarrow Z\gamma$ analysis are fit independently of one another. For the $H \rightarrow Z\gamma$ signals and the $A \rightarrow Z\gamma$ narrow width signals, the model used was a Crystal Ball (CB) (Eq. 7.13) plus a Gaussian distribution (CBG), which has enough flexibility to accurately model the signal resonance and associated tail from lossy processes, along with additional resolution effects. For the broad-width $A \rightarrow Z\gamma$ signals, two crystal ball functions were added together, with opposite sign tail parameters (DCB). This combination was needed to model the pronounced tail-like features on both the low and high mass sides of the distributions:

$$(7.13) \quad f_{CB}(m; \bar{m}, \sigma, \alpha, n) = \begin{cases} \exp\left(-\frac{(m-\bar{m})^2}{2\sigma^2}\right) & : \frac{m-\bar{m}}{\sigma} > -\alpha \\ \left(\frac{n}{|\alpha|}\right)^n \cdot \exp\left(-\frac{|\alpha|^2}{2}\right) \cdot \left(\frac{n}{|\alpha|} - |\alpha| - \frac{m-\bar{m}}{\sigma}\right)^{-n} & : \frac{m-\bar{m}}{\sigma} \leq -\alpha \end{cases}.$$

For the CBG models, the mean of the Gaussian distribution was fixed to the mean of the Crystal Ball, so that only its width can vary freely. An additional free parameter is added to allow the total contribution of the Crystal Ball and Gaussian to fluctuate, leading to a grand total of six free parameters. For the DCB models, The mean and width of both CBs were set equal to each other, so that there were a total of seven free parameters. Examples of the broad and narrow signal fits are given in Fig. 7.19 and Fig. 7.20, and all fits for the 125 GeV mass point for the $H \rightarrow Z\gamma$ analysis can be found in Appendix C.

In order to search for possible resonances at masses located between the generated signals, new signal pdfs are derived from the existing fitted functions. All free parameters are linearly interpolated between existing adjacent mass points in 0.5 (5) GeV steps for

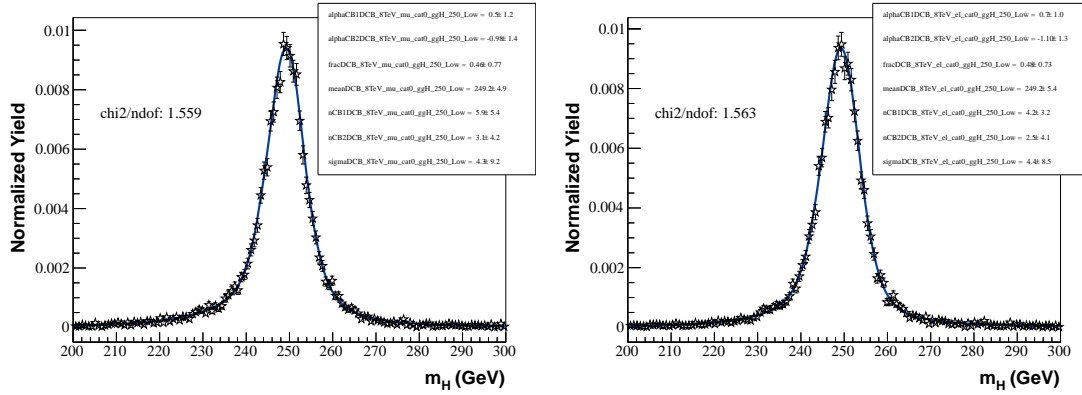


Figure 7.19. Crystal Ball + Crystal Ball fits in the $\mu\mu\gamma$ (left) $ee\gamma$ (right) channel for $m_H = 250$ GeV, wide signal width.

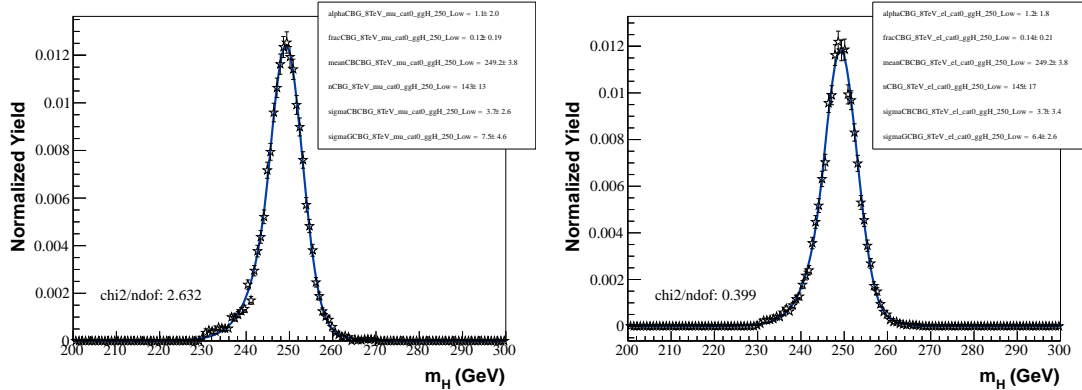


Figure 7.20. Crystal Ball + Gaussian fits in the $\mu\mu\gamma$ (left) $ee\gamma$ (right) channel for $m_H = 250$ GeV, narrow signal width.

the $H \rightarrow Z\gamma$ ($A \rightarrow Z\gamma$). The mean and widths vary smoothly and monotonically, while the tail parameters tend to remain flat over the full mass range. The full set of interpolated fits are shown in Figs 7.21-7.22.

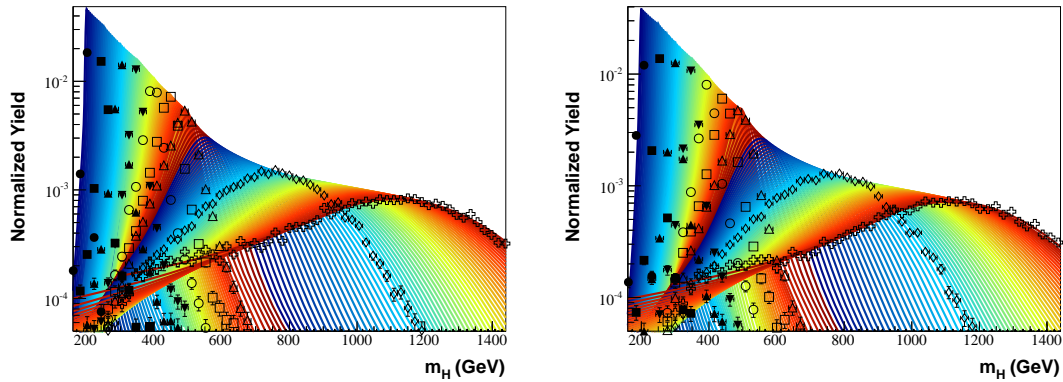


Figure 7.21. Interpolated signals for the broad resonance signal models. Muon channel (left) and electron channel (right).

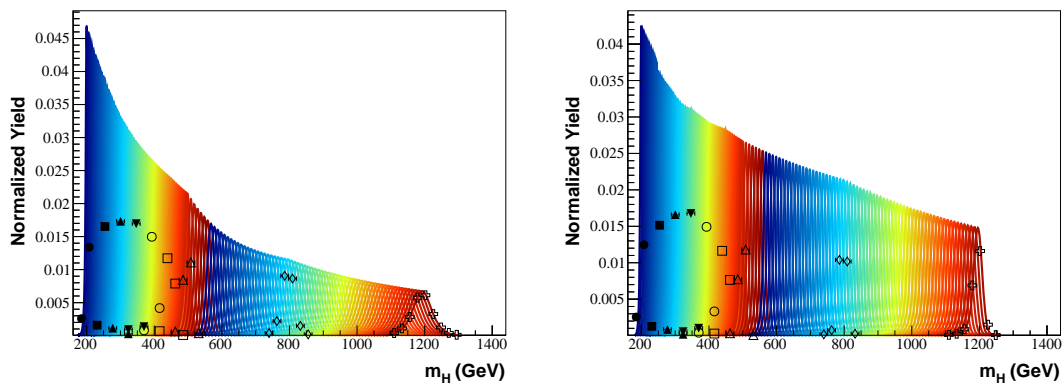


Figure 7.22. Interpolated signals for the narrow resonance signal models. Muon channel (left) and electron channel (right).

CHAPTER 8

Systematic Uncertainties

The sensitivities of the limits calculated in these analyses are, in part, dependent on the particular choices of modeling and the detection hardware itself. Systematic uncertainties arise from the quantitative differences in event features when complementary techniques are compared. They differ from statistical uncertainties, as they tend to not depend on the amount of data collected in the experiment. This section will detail their derivation for both the $H \rightarrow Z\gamma$ and $A \rightarrow Z\gamma$ analyses. As the $H \rightarrow Z\gamma$ is much more model-dependent, there are more sources of systematic uncertainties that arise from theoretical considerations and assumptions made when producing signal simulations.

The systematic uncertainties come from the uncertainty on the luminosity measurement [27], the trigger efficiency, the event pileup, the corrections applied to the simulation to reproduce the performance of the leptons and photon selections, and signal modeling. For the $H \rightarrow Z\gamma$ analysis, additional systematic uncertainties arise from the theoretical calculation of the Higgs production cross sections and branching ratios. The statistical and systematic uncertainties for the corrections are assumed to be uncorrelated. Based on the fit bias studies, the uncertainty on the background estimation due to the chosen functional form is assumed to be negligible.

8.1. Muon

The muon selection is essentially identical for the $H \rightarrow Z\gamma$ and $A \rightarrow Z\gamma$ analyses, and therefore the determination of systematic uncertainties are also identical. As the muon ID, isolation, and trigger cuts used are standard recommendations from the Muon POG, the systematic uncertainties are also calculated by the Muon POG [28]. The uncertainties are derived from variations of the TnP efficiency calculations, by means of MC closure tests, as well as varying signal and background parametric shapes. The overall uncertainty in the ID and Isolation SFs for a pair of muons in this analysis was found to be no greater than 2%.

The simulation available for the 2012 dimuon triggers, that is currently used in the centrally produced signal MC samples, corresponds to the conditions of the 2012 B data and to a small degree 2012 C. Run 2012 A and D data were taken at a substantially different configuration. The ΔZ requirement in the trigger varied from run to run during the 2012 data acquisition period, the exact trigger efficiency was difficult to calculate. However, the 3.5% uncertainty extracted from the RunB period covers all possible TnP systematic uncertainties from trigger efficiency calculations, and is sufficient for these analyses.

8.2. Electron

The electron systematic uncertainties, along with the SFs, were calculated for both analyses and approved by the EGM POG [29]. The ID, Isolation and trigger uncertainties were determined via the TnP procedure by varying the tag selection and the background and signal shapes. The differences in scale factor vary by p_T bin, with the lowest p_T

varying by roughly 10% while the higher pT bins vary by 1-2%. For the $H \rightarrow Z\gamma$ analysis, the per-electron systematic uncertainty was determined to be 0.8%. For $A \rightarrow Z\gamma$, the new scale factors are then propagated through the analysis and a new set of expected limits are calculated. The maximum discrepancy is within 5% for the dielectron selection. In both analyses, the uncertainties are within 2% for the trigger scale factors, see Fig. 8.1.

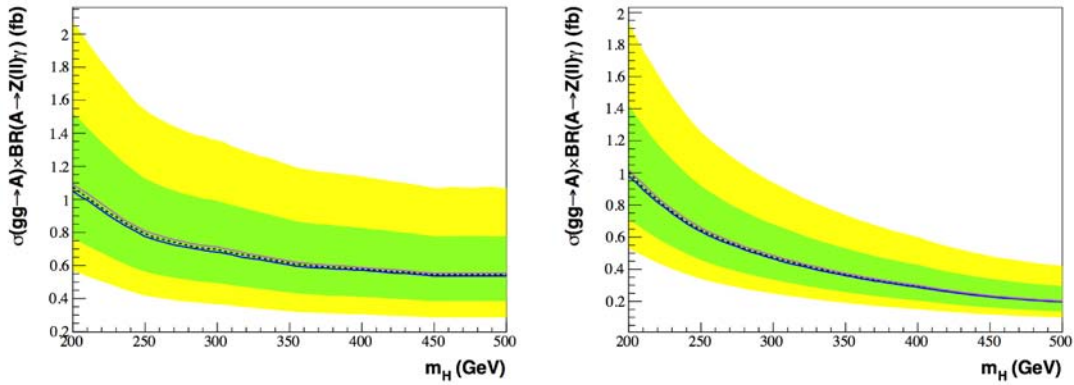


Figure 8.1. Effect of electron systematic uncertainties on expected limit for wide signal $A \rightarrow Z\gamma$ analysis. Left: Broad, Right: Narrow

8.3. Photon

Systematic errors on the photon scale factors are derived by the EGM POG. The main source of uncertainty arises from the parametric shape used to determine the background component of the TnP efficiency studies. Additional uncertainties are determined from both MC and Z FSR closure tests.

Two different tag selections (Medium and Tight working points) are used to remeasure the efficiency and scale factors. The difference between those two sets of corrections is treated as the uncertainty due to the tag dependence. The fitting error is also included in the total uncertainty.

To measure the uncertainty in the electron veto, MC is used to estimate the background from photons and treat it as part of the uncertainty. In addition to the MC-based background estimation, the scale factors are recalculated after varying the $\mu\mu\gamma$ mass window (70–110 GeV and 80–100 GeV). The difference is considered to be part of the photon background and added to the uncertainty.

The total uncertainty for the photon selection in the 2012 ABCD sample is 0.6% for the barrel and 1% for the endcap.

8.4. Jets

Systematic uncertainties for the jet selection only affect the dijet-tagged class in the $H \rightarrow Z\gamma$ analysis. The signal efficiency is affected both by the uncertainty on the jet energy scale (JES) and jet energy resolution (JER). The systematic uncertainty on the jet energy scale was estimated by changing the scale of the MC jet energies on a jet-by-jet basis by $\pm 1\sigma$, where σ is the jet energy scale uncertainty. Similarly, the systematic uncertainty on the jet energy resolution was estimated by varying the MC jet p_T resolution by $\pm 10\%$ [25]. The difference in the PU jet identification efficiency between data and Monte Carlo was evaluated as a function of the transverse momentum and pseudorapidity using $Z \rightarrow \mu^+\mu^-$ +jets events. Since the jet-related systematic uncertainties are assumed to be the same between the two lepton channels, the uncertainties are estimated by combining the two channels to improve statistical accuracy.

The effects on the kinematics of the selected jets due to theoretical uncertainties are also taken into account: Firstly, the impact of different parton distribution function (PDF) parametrizations on the jet kinematics was evaluated. The three PDF sets used

are: CT10, MSTW2008, and NNPDF21 [30]. In addition, the impact due to the variation of α_s was also considered. The systematics are estimated by evaluating the change on signal efficiency and acceptance and the final systematic uncertainty is the quadratic sum of the systematics due to the PDF and α_s . Secondly, the impact related to the presence of underlying events (UE) was estimated by comparing different UE tunes. The ggF and VBF Higgs production samples with $m_H = 125$ GeV was re-simulated with S10 PU scenarios and different UE tunes, including Pythia8 4C, Pythia6 D6T, Pythia6 P0, Pythia6 P11 and Pythia6 Z2star [31]. The systematic uncertainty is then estimated by taking the largest variation on signal efficiency among the different UE tunes with respect to the default tune, Z2star. To be useful for the analysis, the changes in PDF and UE tunes must be propagated through the $H \rightarrow Z\gamma$ event selection. Table 8.1 shows the impact of the tunes for the $H \rightarrow Z\gamma$ event selection, and Table 8.2 shows the impact of the tunes on the $H \rightarrow Z\gamma$ and dijet selection. These tables were used to determine the actual systematic uncertainty on just the dijet selection, see Table 8.3.

Table 8.1. Summary of the variation of the $Z\gamma$ selection efficiency w.r.t. the default UE tune, Z2star.

Higgs production process	UE tunes			
	Pythia8 4C	Pythia6 D6T	Pythia6 P0	Pythia6 P11
Electron channel				
gluon fusion	0.957 ± 0.013	0.985 ± 0.013	0.991 ± 0.013	0.974 ± 0.013
vector boson fusion	0.999 ± 0.013	0.967 ± 0.013	1.003 ± 0.013	1.004 ± 0.013
Muon channel				
gluon fusion	0.997 ± 0.013	1.002 ± 0.013	1.004 ± 0.013	1.001 ± 0.013
vector boson fusion	0.991 ± 0.013	0.984 ± 0.013	1.016 ± 0.013	1.020 ± 0.013

Table 8.4 summarizes the additional systematic uncertainties on dijet tagged event class.

Table 8.2. Summary of the variation of the $Z\gamma$ plus dijet selection efficiency w.r.t. to the default UE tune, Z2star.

Higgs production process	UE tunes			
	Pythia8 4C	Pythia6 D6T	Pythia6 P0	Pythia6 P11
Electron channel				
gluon fusion	1.060 ± 0.188	1.205 ± 0.208	1.120 ± 0.197	0.893 ± 0.166
vector boson fusion	1.066 ± 0.030	0.905 ± 0.027	1.019 ± 0.029	1.049 ± 0.030
Muon channel				
gluon fusion	1.372 ± 0.223	1.191 ± 0.199	1.005 ± 0.176	1.066 ± 0.184
vector boson fusion	1.008 ± 0.020	0.910 ± 0.025	1.021 ± 0.028	1.036 ± 0.028

Table 8.3. Summary of the variation of the dijet selection efficiency w.r.t. the default UE tune, Z2star.

Higgs production process	UE tunes			
	Pythia8 4C	Pythia6 D6T	Pythia6 P0	Pythia6 P11
Electron channel				
gluon fusion	1.108 ± 0.197	1.224 ± 0.216	1.130 ± 0.199	0.917 ± 0.171
vector boson fusion	1.067 ± 0.033	0.936 ± 0.030	1.016 ± 0.032	1.045 ± 0.033
Muon channel				
gluon fusion	1.375 ± 0.224	1.189 ± 0.200	1.002 ± 0.175	1.065 ± 0.184
vector boson fusion	1.017 ± 0.024	0.925 ± 0.029	1.005 ± 0.030	1.015 ± 0.030
Combined				
gluon fusion	1.249 ± 0.150	1.205 ± 0.145	1.063 ± 0.132	0.994 ± 0.126
vector boson fusion	1.041 ± 0.022	0.930 ± 0.020	1.010 ± 0.021	1.030 ± 0.022

Table 8.4. Summary of additional systematic uncertainties on the dijet tagged event class.

Source	Higgs production process	
	gluon fusion	vector boson fusion
JES	11.0%	4.6%
JER	6.0%	1.9%
Jet ID	1.7%	1.6%
UE tunes	24.9%	7.0%
PDF and α_s	2.1%	0.9%
Total	28.0%	8.8%

Finally, the event migration between dijet tagged and untagged event classes due to the jet energy scale, jet energy resolution and different UE tunes was also considered. The method of estimation is the similar to the aforementioned procedure, but in this case, the fraction of events migrating between tagged and untagged classes was measured. For signal events produced via gluon fusion, conservative estimations of 0.1% for each category due to jet energy scale, 0.1% due to jet energy resolution, and 0.2% due to different UE tunes. For signal events produced via vector boson fusion, the uncertainty of each untagged category due to event migration is shown in Table 8.5.

Table 8.5. Summary of the event migration systematic uncertainties on each untagged category for signal events produced via vector boson fusion.

Source	category 1	category 2	category 3	category 4
JES	2.8%	2.2%	2.2%	3.2%
JER	1.0%	1.1%	1.4%	1.1%
UE tunes	2.6%	1.8%	2.1%	3.5%

8.5. PU, Acceptance, Branching Ratios, Cross Sections

The signal shape and acceptance are influenced by the pileup reweighting and the choice of pdf when generating the signal. It was found that after recalculating the pileup distributions for MC by varying the underlying minimum bias cross section by 1 sigma from the nominal value [32], the maximum deviation in expected limit was under 1.3%.

For the $H \rightarrow Z\gamma$ analysis, the SM Higgs branching fractions and production cross section uncertainties are factored into the total systematic uncertainties. These values and their associated errors are derived from theory, as reported in [33–35]. The $A \rightarrow Z\gamma$ analysis accounts for uncertainty in production methods by reweighting the signal PDF set (CTEQ6L) with another (CT10). The total change in signal acceptance is within 3%.

8.6. Systematic Uncertainty Summary

Table 8.6 summarizes the systematic uncertainties for the $H \rightarrow Z\gamma$ analysis, and Table 8.7 summarizes the systematic uncertainties for the $A \rightarrow Z\gamma$ analysis.

Table 8.6. Separate sources of systematic uncertainties accounted for in the $H \rightarrow Z\gamma$ analysis of the 7 and 8 TeV data set. The magnitude of the variation of the source that has been applied to the signal model is shown. GGH stands for Gluon-gluon fusion cross section, VBF Vector boson fusion cross section, VH vector boson associate production and ttH top pair associate production.

Source	7 TeV	8 TeV	Source	7 TeV	8 TeV
Integrated luminosity	2.2%	4.4%	Selection		
Theory			- Photon Barrel	0.5%	0.6%
- GGF (scale)	+12.5% -8.2%	+7.6% -8.2%	- Photon Endcap	1.0%	1.0%
- GGF (PDF)	+7.9% -7.7%	+7.6% -7.0%	- Electron	0.8%	0.8%
- VBF (scale)	+0.5% -0.3%	+0.3% -0.8%	- Muon	0.7%	1.4%
- VBF (PDF)	+2.7% -2.1%	+2.8% -2.6%	Signal scale and resolution		
- WH (scale)	+0.7% -0.8%	+0.2% -0.7%	- Mean	1.0%	1.0%
- WH (PDF)	+3.5% -3.5%	+3.5% -3.5%	- Sigma	5.0%	5.0%
- ZH (scale)	+1.7% -1.6%	+1.9% -1.7%	Pileup		
- ZH (PDF)	+3.7% -3.7%	+3.9% -9.7%	- Electron	0.6%	0.8%
- ttH (scale)	+3.4% -9.4%	+3.9% -9.3%	- Muon	0.4%	0.4%
- ttH (PDF)	+8.5% -8.5%	+7.9% -7.9%	Dijet class		
Branching fraction	6.7%,9.4% -6.7%,-9.3%	6.7%,9.4% -6.7%,-9.3%	- Gluon fusion	27.9%	28.5%
Trigger			- Vector boson fusion	8.7%	8.8%
- Electron	0.5%	2.0%	Event migration		
- Muon	0.5%	3.5%	- Dijet selection	5.1%-9.8%	5.1%-9.8%
			- Photon shower shape	5.0	5.0%

Table 8.7. Separate sources of systematic uncertainties accounted for in the $A \rightarrow Z\gamma$ analysis. The magnitude of the variation of the source that has been applied to the signal model is shown.

Source	Value
Integrated luminosity	2.6%
PDF Acceptance	3.0%
Trigger	
- Electron	2%
- Muon	3.5%
Selection	
- Photon	1.0–2.6%
- Electron	5.0%
- Muon	2.0%
Signal	
- Mean	1.0%
- Sigma	10.0%
Pileup	1.3%

CHAPTER 9

Results and Interpretation

Identical statistical tests determining the significance of any potential signal-like excess were performed for both analyses. These tests were conducted in terms of the local p-value, the probability of observing an excess under the background-only hypothesis. The local p-value is expressed as a number of standard deviations using the onesided Gaussian tail convention, and is used to derive upper limits on the existence of the Higgs or a generic high mass resonance. The limits are evaluated using a modified frequentist approach taking the profile likelihood as a test statistic [36, 37]. An unbinned evaluation of the likelihood over the full mass range of data was used. The uncertainties on the limits are dominated by the size of the data sample and systematic uncertainties have a negligible impact.

9.1. $H \rightarrow Z\gamma \rightarrow \ell\ell\gamma$

A search was performed for a Higgs boson decaying into a Z boson and a photon. The analysis used a dataset from proton-proton collisions at a center-of-mass energy of 7 and 8 TeV, corresponding to an integrated luminosity of 5.0 and 19.6 fb^{-1} , respectively. No excess above standard model predictions has been found and the first limits on the Higgs boson production cross section times the $H \rightarrow Z\gamma$ branching fraction at the LHC have been derived. The expected exclusion limits at 95% confidence level are between 5 and 16 times the standard model cross section in the 120–160 GeV mass range and the

observed limit ranges between about 4 and 25 times the standard model cross section. The observed and expected limits for $m_{\ell\ell\gamma}$ at 125 GeV are within one order of magnitude of the standard model prediction. Models predicting $\sigma(pp \rightarrow H) \times \mathcal{B}(H \rightarrow Z\gamma)$ to be larger than one order of magnitude of the standard model prediction, for most of the 125–157 GeV mass range, are excluded.

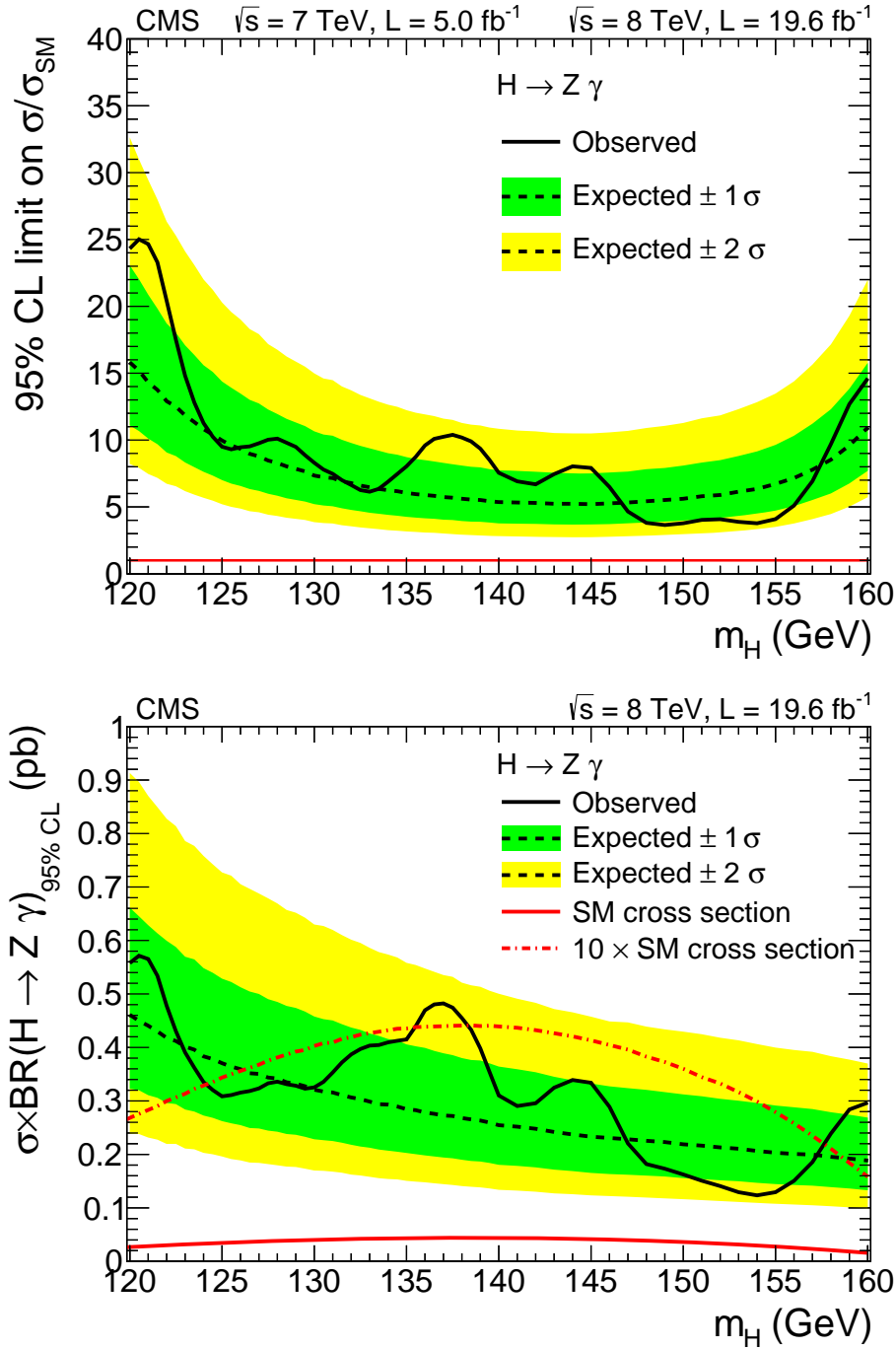


Figure 9.1. (a) The exclusion limit on the cross section times the branching fraction of a Higgs boson decaying into a Z boson and a photon divided by the SM value. (b) Exclusion limit on the inclusive cross section alone, where the theoretical uncertainties on the cross section have been excluded in the limit setting.

9.2. $A \rightarrow Z\gamma \rightarrow \ell\ell\gamma$

A search was performed for a Higgs-like boson decaying into a Z-boson and a photon between 200 and 1200 GeV. The analysis was conducted on a CMS dataset from proton-proton collisions at a centre-of-mass energy of 8 TeV, corresponding to an integrated luminosity of 19.6 fb^{-1} . Exclusion limits on the total production rate of potential resonances were determined through use of unbinned maximum likelihood fits to the $\ell\ell\gamma$ invariant mass distributions for double electron and double muon categories.

The results given are for two different signal models: A narrow generated width of approximately 2 GeV, and a wide width, assuming SM Higgs production at high mass. All signal models assume a gluon-gluon production mechanism. The signals are normalized to the acceptance, efficiency, and total luminosity, and thus are independent of theoretical cross section and branching ratio predictions. The limits are given on the cross-section times branching ratio in units of fb .

The expected limits on production for the broad (narrow) width signal model range from 1.1 fb (1.0 fb) at a mass of 200 GeV to 0.2 (0.06) fb at a mass of 1200 GeV. No significant excess was found in the observed limits of the broad or narrow width models.

The 95% CL exclusion limit for the broad (narrow) signal models is shown in Fig. 9.2 (Fig. 9.3).

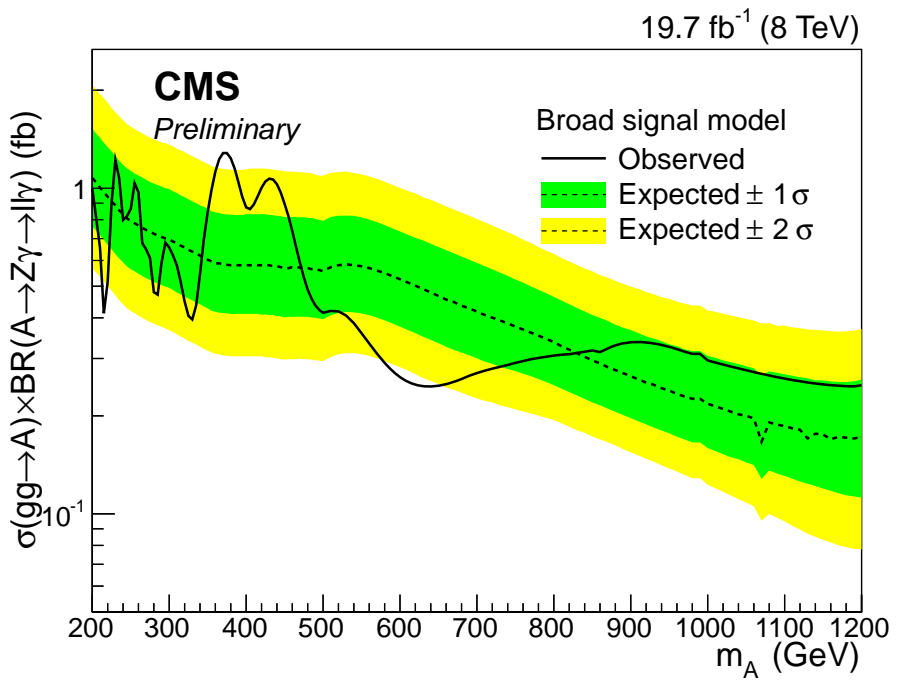


Figure 9.2. Expected exclusion limit at 95% CL on the cross section times branching ratio for broad generated signal widths.

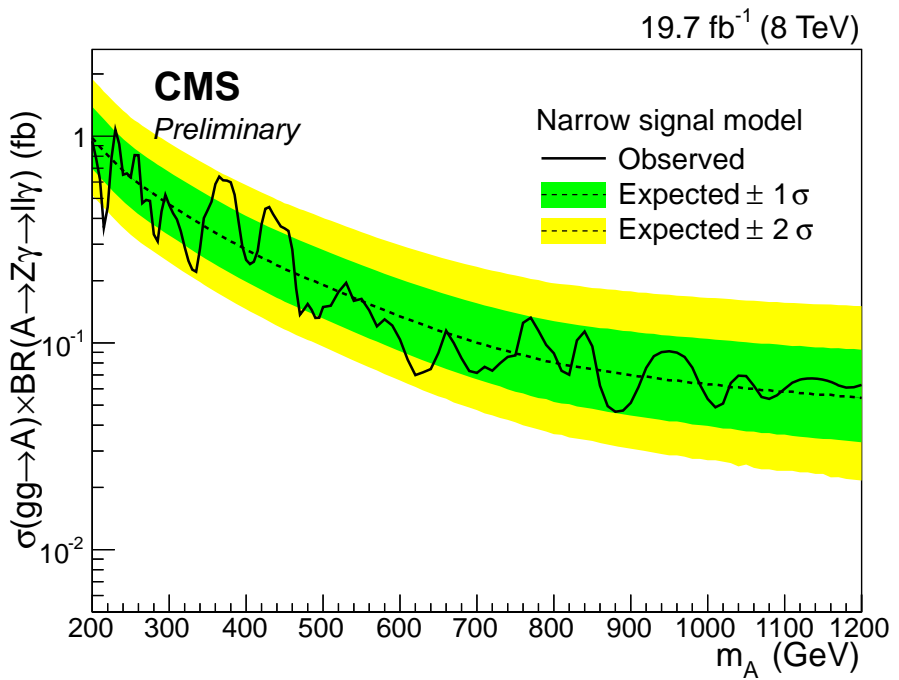


Figure 9.3. Expected exclusion limit at 95% CL on the cross section times branching ratio for narrow generated signal widths.

References

- [1] S. Dawson, “Introduction to electroweak symmetry breaking,” pp. 1–83, 1998.
- [2] G. Bhattacharyya, “A Pedagogical Review of Electroweak Symmetry Breaking Scenarios,” *Rept. Prog. Phys.*, vol. 74, p. 026201, 2011.
- [3] B. Bellazzini, C. Csaki, and J. Serra, “Composite Higgses,” *Eur. Phys. J.*, vol. C74, no. 5, p. 2766, 2014.
- [4] A. Arbey, G. Cacciapaglia, H. Cai, A. Deandrea, S. Le Corre, *et al.*, “Fundamental Composite Electroweak Dynamics: Status at the LHC,” 2015.
- [5] L. R. Evans and P. Bryant, “LHC Machine,” *J. Instrum.*, vol. 3, p. S08001. 164 p, 2008. This report is an abridged version of the LHC Design Report (CERN-2004-003).
- [6] S. Chatrchyan *et al.*, “The CMS experiment at the CERN LHC,” *JINST*, vol. 3, p. S08004, 2008.
- [7] P. Adzic, R. Alemany-Fernandez, C. Almeida, N. Almeida, G. Anagnostou, *et al.*, “Energy Resolution Performance of the CMS Electromagnetic Calorimeter,” 2006.
- [8] S. Chatrchyan *et al.*, “Energy calibration and resolution of the CMS electromagnetic calorimeter in pp collisions at $\sqrt{s} = 7$ TeV,” *JINST*, vol. 8, p. P09009, 2013.

- [9] S. Frixione, P. Nason, and C. Oleari, “Matching NLO QCD computations with Parton Shower simulations: the POWHEG method,” *JHEP*, vol. 11, p. 070, 2007.
- [10] T. Sjöstrand, S. Mrenna, and P. Skands, “PYTHIA 6.4 physics and manual,” *JHEP*, vol. 05, p. 026, 2006.
- [11] T. Sjostrand, S. Mrenna, and P. Z. Skands, “A Brief Introduction to PYTHIA 8.1,” *Comput.Phys.Commun.*, vol. 178, pp. 852–867, 2008.
- [12] J. Alwall, M. Herquet, F. Maltoni, O. Mattelaer, and T. Stelzer, “MadGraph 5 : Going Beyond,” *JHEP*, vol. 1106, p. 128, 2011.
- [13] P. Lenzi, S. Padhi, G. Retuerto, F. Wuerthwein, T. Seva, and H. Tong, “Standard model cross sections for cms at 8 tev,” cms twiki, 2014.
- [14] W. Erdmann, “Offline primary vertex reconstruction with deterministic annealing clustering,” *CMS Internal note*, vol. 2011/014, 2011.
- [15] S. Chatrchyan *et al.*, “Measurement of the inclusive W and Z production cross sections in pp collisions at $\sqrt{s} = 7 \text{ TeV}$ with the CMS experiment,” *JHEP*, vol. 10, p. 132, 2011.
- [16] CMS Collaboration, “Electron reconstruction and identification at $\sqrt{s} = 7 \text{ TeV}$,” *CMS Physics Analysis Summary*, vol. CMS-PAS-EGM-10-004, 2010.

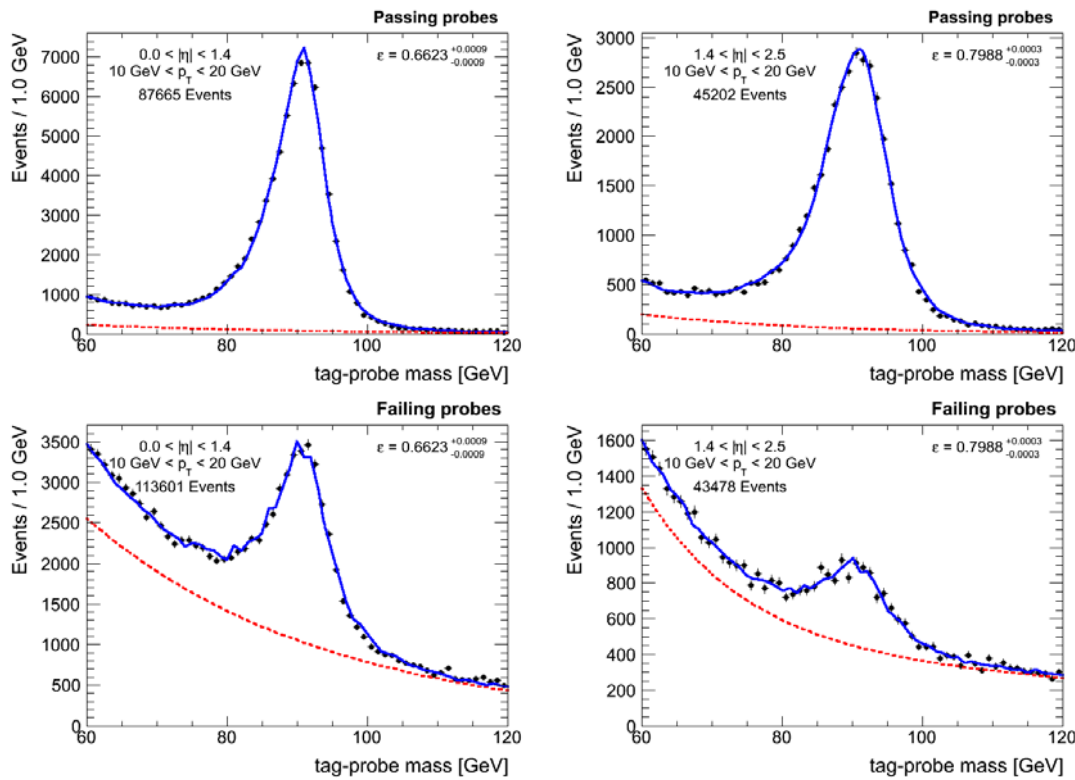
- [17] CMS Collaboration, “Evidence for a particle decaying to in the fully leptonic final state in a standard model higgs boson search in pp collisions at the lhc,” *CMS Physics Analysis Summary*, vol. CMS-PAS-HIG-12-042, 2012.
- [18] CMS Collaboration, “A higgs boson search in the fully leptonic w+w- final state,” *CMS Analysis Note*, vol. CMS-AN2012-228, 2012.
- [19] <https://twiki.cern.ch/twiki/bin/viewauth/CMS/MultivariateElectronIdentification>.
- [20] CMS Collaboration, “Search for a light higgs boson in the z boson plus a photon decay channel,” *CMS Physics Analysis Summary*, vol. CMS-PAS-HIG-12-049, 2012.
- [21] <https://twiki.cern.ch/twiki/bin/viewauth/CMS/ElectronMomentumRegression>.
- [22] S. Chatrchyan *et al.*, “Performance of CMS muon reconstruction in pp collision events at $\sqrt{s} = 7 \text{ TeV}$,” *JINST*, vol. 7, p. P10002, 2012.
- [23] CMS Collaboration, “Particle-flow event reconstruction in CMS and performance for jets, taus, and E_T^{miss} ,” CMS Physics Analysis Summary CMS-PAS-PFT-09-001, 2009.
- [24] J. Veverka, “Studies of Z production and constraints on anomalous triple gauge couplings in pp collisions at $s = 7 \text{ TeV}$,”
- [25] CMS Collaboration, “Jet performance in pp collisions at $\sqrt{s}=7 \text{ TeV}$,” CMS Physics Analysis Summary CMS-PAS-JME-10-003, 2010.

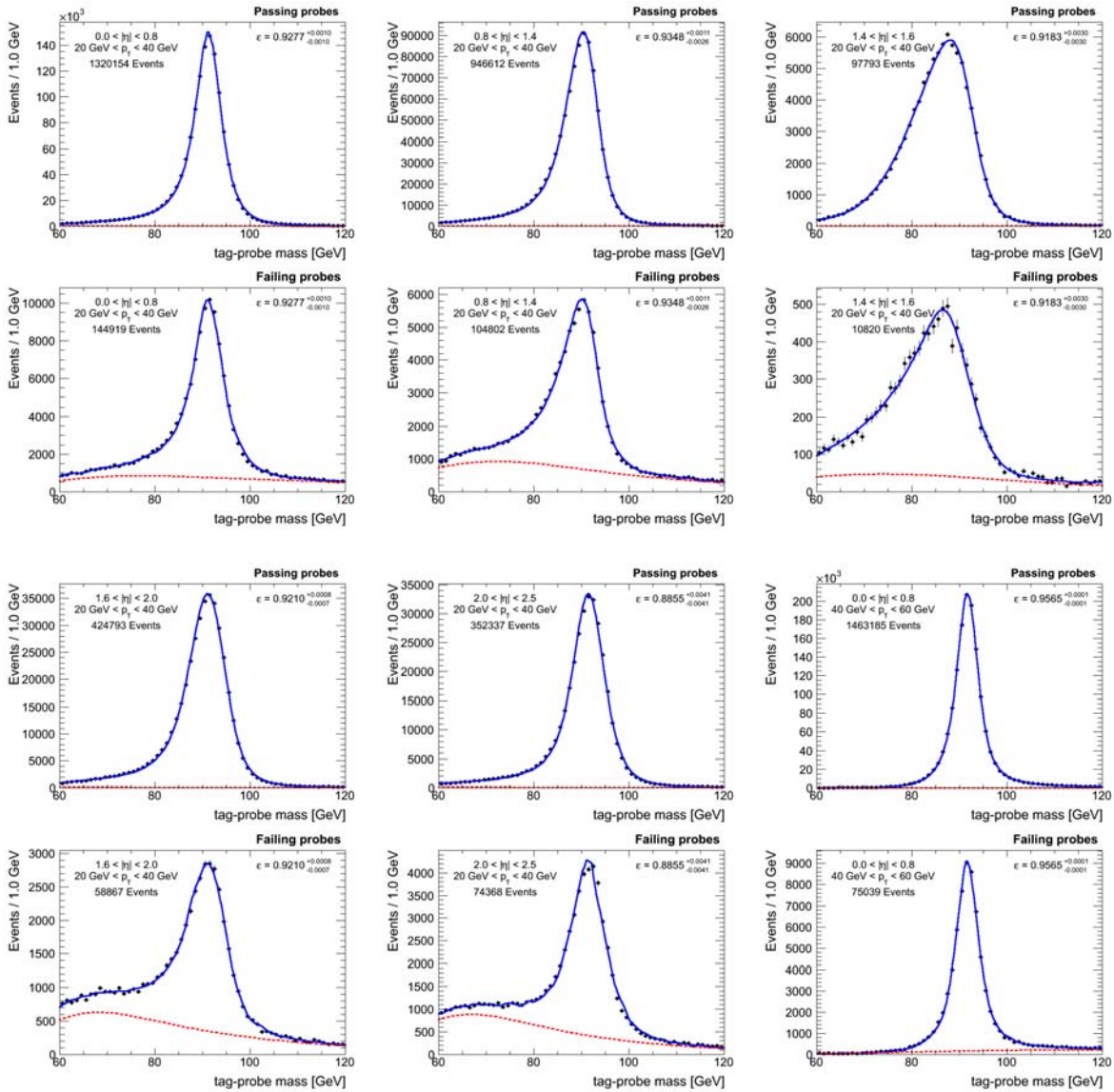
- [26] S. Chatrchyan *et al.*, “Search for a Higgs boson decaying into a Z and a photon in pp collisions at $\sqrt{s} = 7$ and 8 TeV,” *Phys. Lett. B*, vol. 726, pp. 587–609, 2013.
- [27] CMS Collaboration, “Cms luminosity based on pixel cluster counting - summer 2013 update,” CMS Physics Analysis Summary CMS-PAS-LUM-13-001, 2013.
- [28] <https://twiki.cern.ch/twiki/bin/viewauth/CMS/MuonPOG>.
- [29] <https://twiki.cern.ch/twiki/bin/viewauth/CMS/EgammaPOG>.
- [30] A. Martin, W. Stirling, R. Thorne, and G. Watt, “Parton distributions for the LHC,” *Eur.Phys.J.*, vol. C63, pp. 189–285, 2009.
- [31] R. Field, “Min-Bias and the Underlying Event at the LHC,” *Acta Phys.Polon.*, vol. B42, pp. 2631–2656, 2011.
- [32] <https://twiki.cern.ch/twiki/bin/viewauth/CMS/TWikiLUM>.
- [33] LHC Higgs Cross Section Working Group, S. Dittmaier, C. Mariotti, G. Passarino, and R. Tanaka (Eds.), “Handbook of LHC Higgs Cross Sections: 1. Inclusive Observables,” *CERN-2011-002*, CERN, Geneva, 2011.
- [34] LHC Higgs Cross Section Working Group, S. Dittmaier, C. Mariotti, G. Passarino, and R. Tanaka (Eds.), “Handbook of LHC Higgs Cross Sections: 2. Differential Distributions,” *CERN-2012-002*, CERN, Geneva, 2012.

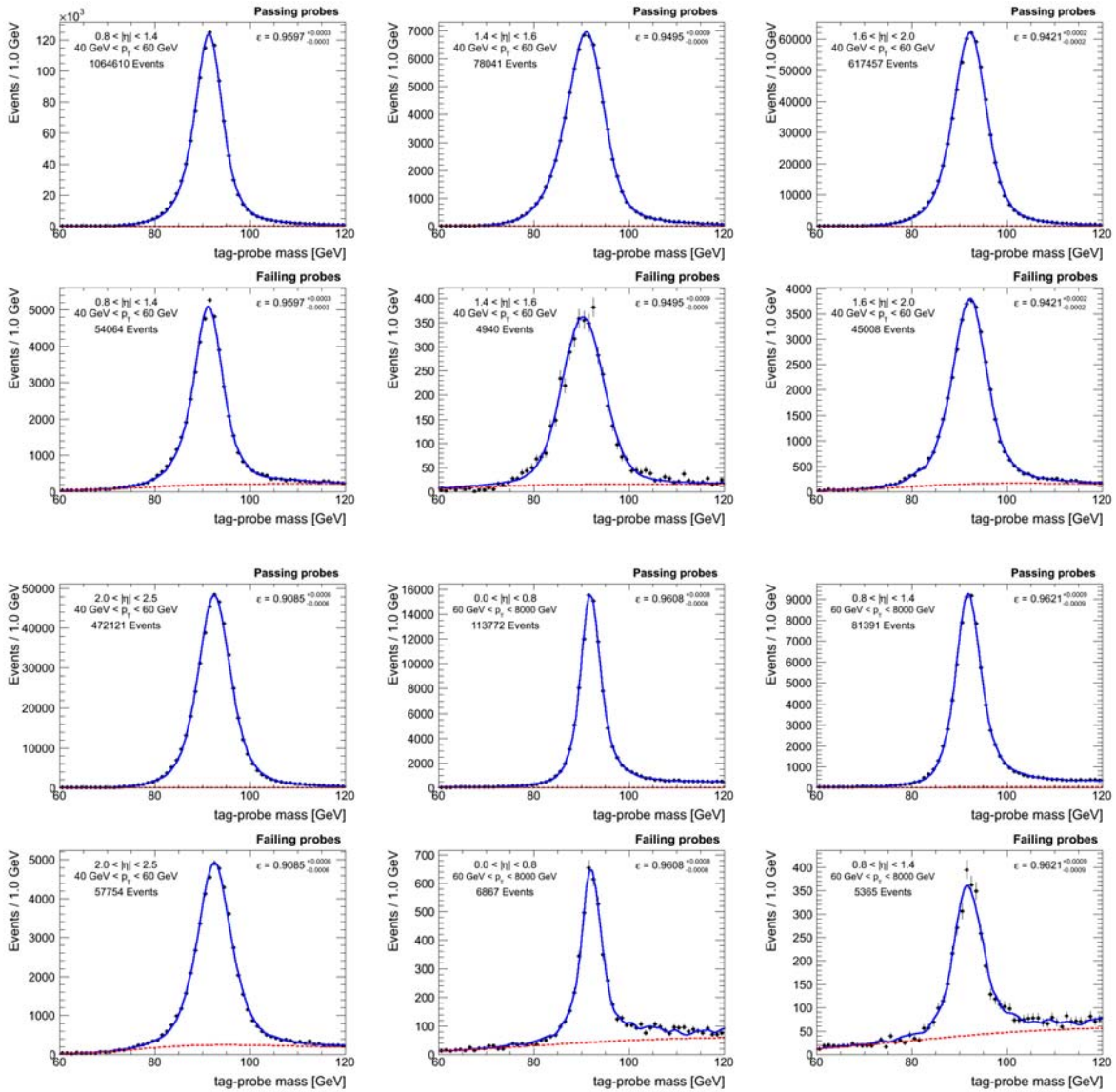
- [35] LHC Higgs Cross Section Working Group, S. Heinemeyer, C. Mariotti, G. Passarino, and R. Tanaka (Eds.), “Handbook of LHC Higgs Cross Sections: 3. Higgs Properties,” *CERN-2013-004*, CERN, Geneva, 2013.
- [36] A. L. Read, “Presentation of search results: the cl_s technique,” *Journal of Physics G: Nuclear and Particle Physics*, vol. 28, no. 10, p. 2693, 2002.
- [37] T. Junk, “Confidence level computation for combining searches with small statistics,” *Nuclear Instruments and Methods in Physics Research Section A: Accelerators, Spectrometers, Detectors and Associated Equipment*, vol. 434, no. 23, pp. 435 – 443, 1999.

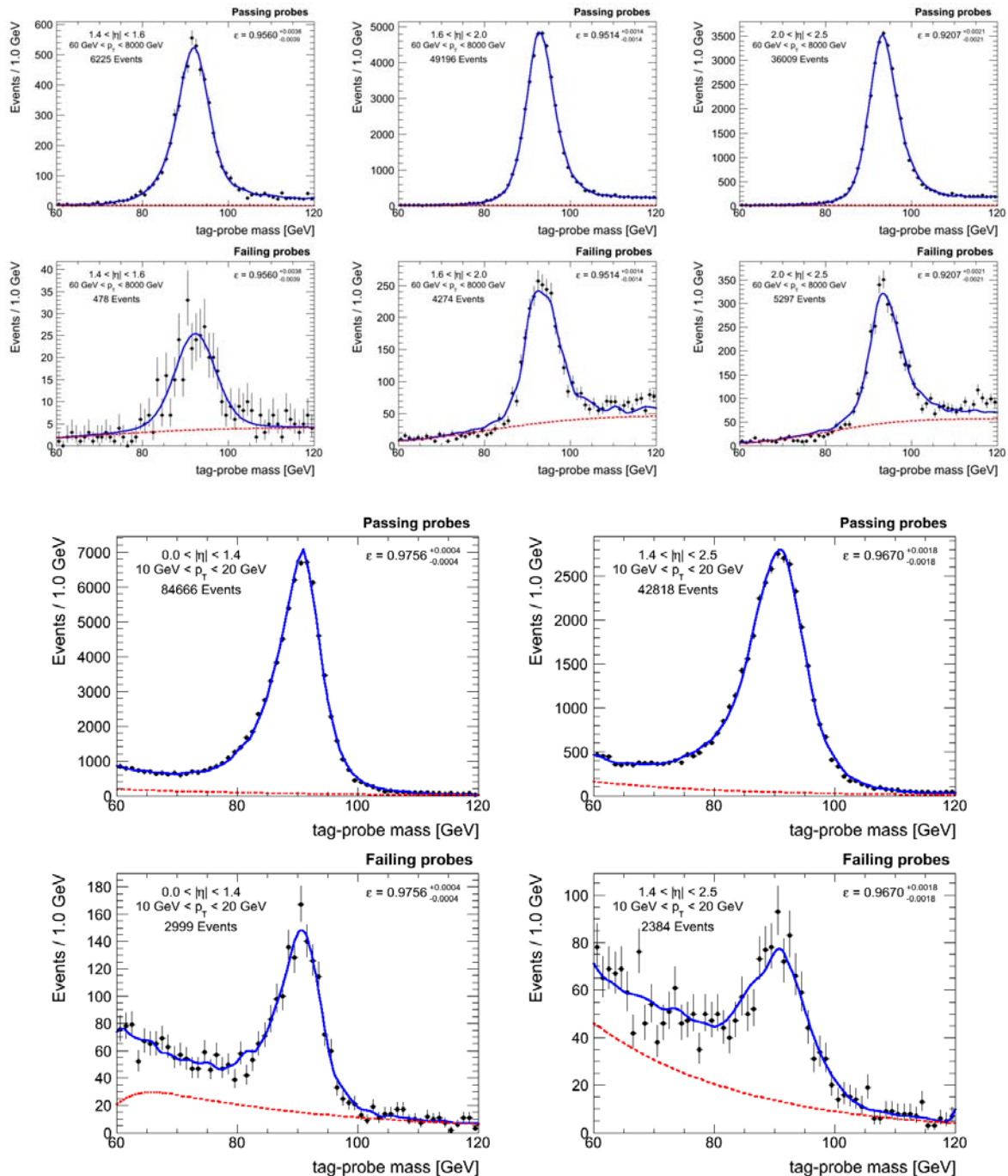
APPENDIX A

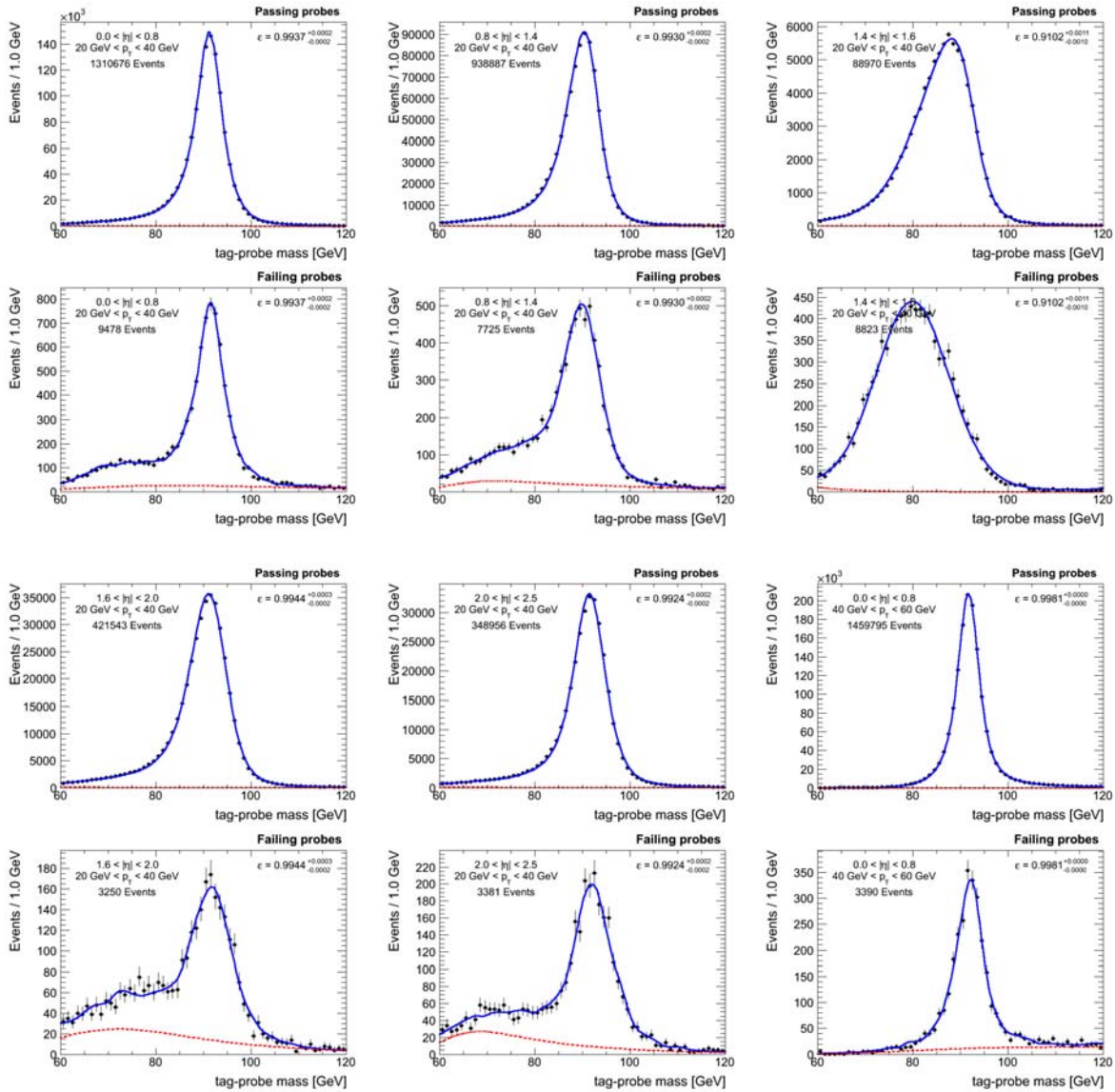
Electron ID and Iso Fits

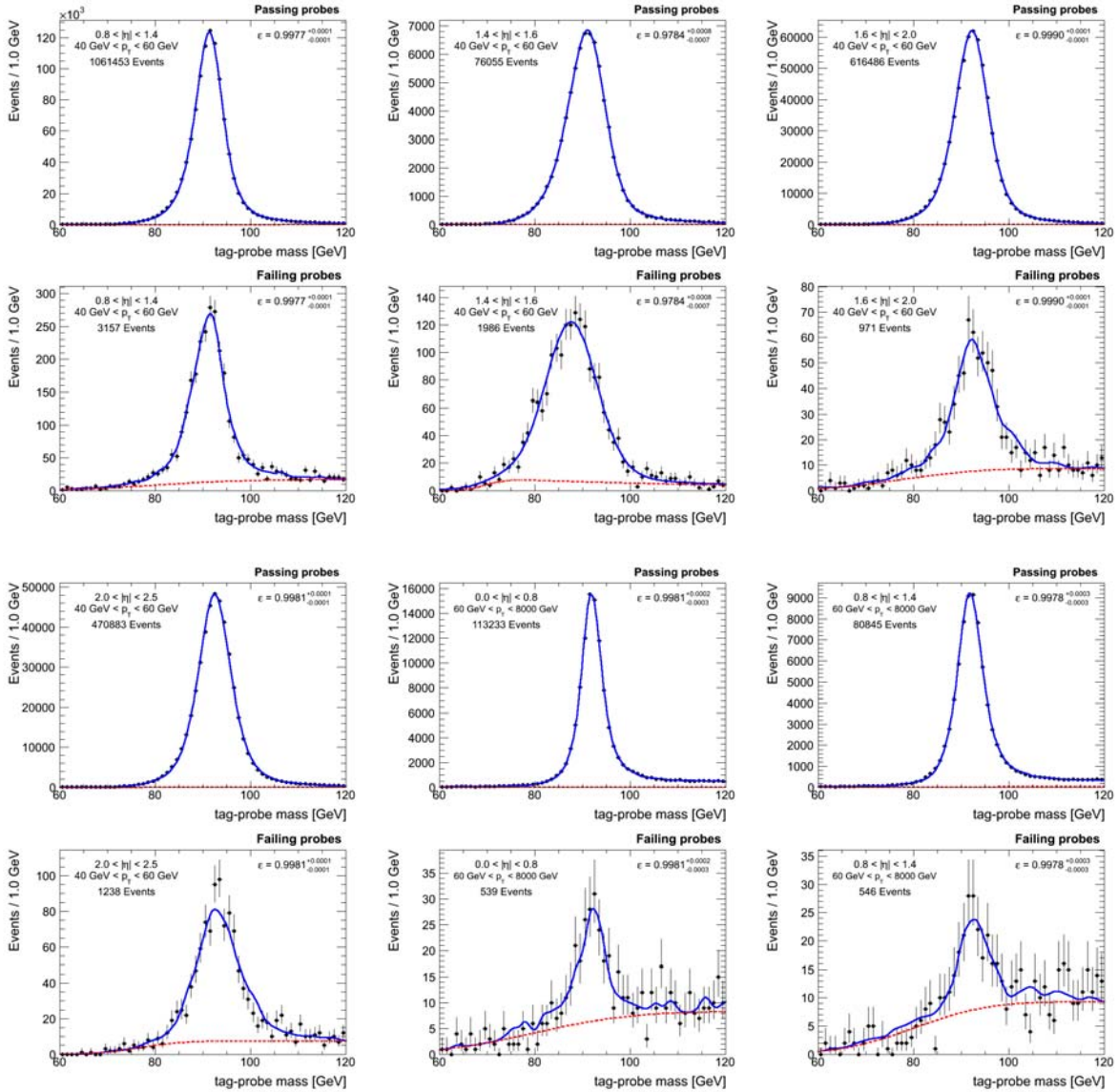


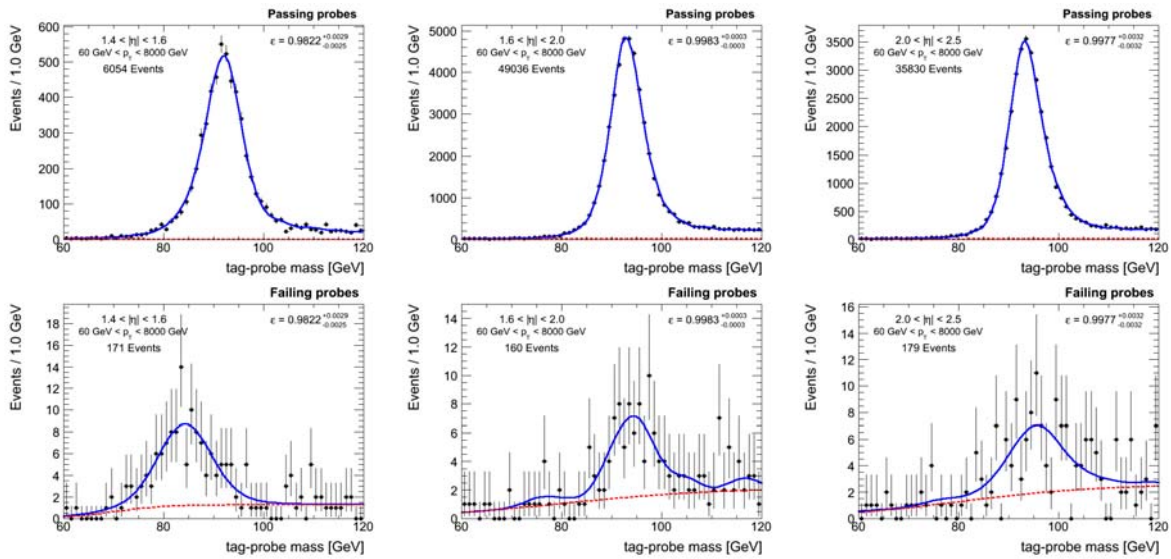












APPENDIX B

Bias Studies**B.1. $H \rightarrow Z\gamma$ Bias Studies**Signal Pulls, Gaussian turn-on $m_H=120$

2012 electrons				
cat.	GaussBern3(GE/GP/SE/SP)	GaussBern4(GE/GP/SE/SP)	GaussBern5(GE/GP/SE/SP)	GaussBern6(GE/GP/SE/SP)
1	0.10 /0.08 /-0.02 /-0.01	0.07 /-0.00 /-0.04 /-0.08	0.06 /-0.02 /-0.06 /-0.10	-0.01 /-0.02 /-0.11 /-0.11
2	0.20 /0.07 /-0.00 /0.02	0.16 /-0.03 /-0.04 /-0.07	0.12 /-0.07 /-0.07 /-0.12	0.01 /-0.25 /-0.19 /-0.29
3	0.29 /0.08 /-0.04 /-0.03	0.23 /0.02 /-0.10 /-0.09	0.18 /-0.09 /-0.12 /-0.17	0.09 /-0.09 /-0.16 /-0.19
4	0.03 /0.10 /-0.02 /0.07	0.02 /-0.03 /-0.01 /-0.03	0.09 /0.07 /0.05 /0.05	0.03 /0.06 /-0.01 /-0.00

Table B.1. 4-Category Signal Yield Pulls, $m_H=120$, Gaussian turn-on for fit. Columns show results for the various background models used in combined signal+background fits to background-only toys. The four numbers given for each background fit model correspond to toys generated from either an gauss×exponential, gauss×power-law, sech×exponential, or sech×power-law truth model. Boldface is used to indicate the lowest-order polynomial that satisfies the “low-bias” pull criteria: $|\mu(nS/\sigma(nS))| \leq 0.2$

Signal Pulls, Sech turn-on $m_H=120$

cat.	2012 electrons			
	SechBern3(GE/GP/SE/SP)	SechBern4(GE/GP/SE/SP)	SechBern5(GE/GP/SE/SP)	SechBern6(GE/GP/SE/SP)
1	0.13 / 0.14 / 0.01 / 0.04	0.09 / 0.08 / -0.01 / -0.03	0.09 / 0.05 / -0.03 / -0.03	0.07 / 0.08 / -0.03 / -0.03
2	0.22 / 0.13 / -0.00 / 0.06	0.18 / 0.07 / -0.01 / 0.00	0.16 / 0.05 / -0.04 / -0.02	-0.01 / -0.05 / -0.15 / -0.14
3	0.32 / 0.15 / -0.02 / 0.03	0.26 / 0.10 / -0.06 / -0.01	0.30 / 0.12 / -0.03 / 0.01	0.12 / 0.06 / -0.08 / -0.04
4	-0.00 / 0.10 / -0.05 / 0.06	-0.01 / -0.03 / -0.04 / -0.05	0.08 / 0.06 / 0.03 / 0.04	0.02 / 0.04 / 0.00 / 0.03

Table B.2. 4-Category Signal Yield Pulls, $m_H=120$, Sech turn-on. Columns show results for the various background models used in combined signal+background fits to background-only toys. The four numbers given for each background fit model correspond to toys generated from either an gauss×exponential, gauss×power-law, sech×exponential, or sech×power-law truth model. Boldface is used to indicate the lowest-order polynomial that satisfies the “low-bias” pull criteria: $|\mu(nS/\sigma(nS))| \leq 0.2$

Type-A Criterion, Gaussian turn-on, $m_H=120$

2012 electrons				
cat.	GaussBern3(GE/GP/SE/SP)	GaussBern4(GE/GP/SE/SP)	GaussBern5(GE/GP/SE/SP)	GaussBern6(GE/GP/SE/SP)
1	0.27 / 0.18 / 0.03 / 0.04	0.21 / 0.07 / 0.03 / -0.07	0.19 / 0.01 / -0.03 / -0.11	0.04 / 0.01 / -0.15 / -0.14
2	0.44 / 0.16 / 0.06 / 0.08	0.37 / 0.02 / 0.01 / -0.07	0.29 / -0.03 / -0.05 / -0.13	0.06 / -0.32 / -0.27 / -0.39
3	0.58 / 0.18 / -0.01 / -0.01	0.48 / 0.12 / -0.08 / -0.08	0.38 / -0.08 / -0.15 / -0.23	0.18 / -0.09 / -0.23 / -0.27
4	0.14 / 0.24 / 0.03 / 0.17	0.11 / 0.02 / 0.06 / 0.01	0.17 / 0.11 / 0.10 / 0.06	0.08 / 0.14 / 0.02 / 0.05

Table B.3. 4-Category Type-A Criteria, $m_H=120$, Gaussian turn-on.

Columns show results for the various background models used in combined signal+background fits to background-only toys. The four numbers given for each background fit model correspond to toys generated from either a gauss×exponential, gauss×power-law, sech×exponential, or sech×power-law truth model. Boldface is used to indicate the lowest-order polynomial that satisfies the “low-bias” type-A criteria: $|\mu(nS/\sigma(nB))| \leq 0.2$

Type-A Criterion, Sech turn-on, $m_H=120$

2012 electrons				
cat.	SechBern3(GE/GP/SE/SP)	SechBern4(GE/GP/SE/SP)	SechBern5(GE/GP/SE/SP)	SechBern6(GE/GP/SE/SP)
1	0.33 / 0.32 / 0.10 / 0.13	0.26 / 0.21 / 0.06 / 0.01	0.24 / 0.16 / 0.02 / 0.02	0.17 / 0.14 / -0.00 / -0.01
2	0.48 / 0.28 / 0.06 / 0.15	0.40 / 0.18 / 0.05 / 0.06	0.37 / 0.16 / 0.00 / 0.02	0.05 / -0.02 / -0.22 / -0.17
3	0.64 / 0.30 / 0.03 / 0.09	0.54 / 0.25 / -0.03 / 0.08	0.57 / 0.25 / 0.01 / 0.07	0.26 / 0.15 / -0.09 / -0.02
4	0.07 / 0.24 / -0.04 / 0.16	0.04 / 0.01 / -0.02 / -0.03	0.15 / 0.12 / 0.07 / 0.08	0.08 / 0.11 / 0.05 / 0.09

Table B.4. 4-Category Type-A Criteria, $m_H=120$, Sech turn-on. Columns

show results for the various background models used in combined signal+background fits to background-only toys. The four numbers given for each background fit model correspond to toys generated from either a gauss×exponential, gauss×power-law, sech×exponential, or sech×power-law truth model. Boldface is used to indicate the lowest-order polynomial that satisfies the “low-bias” type-A criteria: $|\mu(nS/\sigma(nB))| \leq 0.2$

Signal Pulls, Gaussian turn-on $m_H=125$

2012 electrons				
cat.	GaussBern3(GE/GP/SE/SP)	GaussBern4(GE/GP/SE/SP)	GaussBern5(GE/GP/SE/SP)	GaussBern6(GE/GP/SE/SP)
1	-0.07 / -0.16 / 0.01 / -0.10	-0.02 / -0.10 / 0.05 / -0.02	-0.04 / -0.09 / 0.05 / -0.01	-0.03 / -0.08 / 0.09 / 0.01
2	-0.03 / -0.20 / -0.03 / -0.09	0.04 / -0.09 / 0.04 / 0.01	-0.04 / -0.11 / 0.02 / -0.03	-0.30 / -0.39 / -0.10 / -0.26
3	0.03 / -0.12 / 0.03 / -0.07	-0.04 / -0.21 / -0.02 / -0.13	0.00 / -0.04 / 0.07 / 0.02	-0.11 / -0.08 / 0.07 / 0.02
4	-0.23 / -0.44 / -0.13 / -0.33	-0.06 / -0.17 / 0.02 / -0.06	0.03 / -0.04 / 0.10 / 0.06	0.10 / 0.02 / 0.22 / 0.15

Table B.5. 4-Category Signal Yield Pulls, $m_H=125$, Gaussian turn-on for fit. Columns show results for the various background models used in combined signal+background fits to background-only toys. The four numbers given for each background fit model correspond to toys generated from either an gauss×exponential, gauss×power-law, sech×exponential, or sech×power-law truth model. Boldface is used to indicate the lowest-order polynomial that satisfies the “low-bias” pull criteria: $|\mu(nS/\sigma(nS))| \leq 0.2$

Signal Pulls, Sech turn-on $m_H=125$

2012 electrons				
cat.	SechBern3(GE/GP/SE/SP)	SechBern4(GE/GP/SE/SP)	SechBern5(GE/GP/SE/SP)	SechBern6(GE/GP/SE/SP)
1	-0.12 / -0.21 / -0.04 / -0.15	-0.08 / -0.16 / 0.00 / -0.09	-0.10 / -0.15 / -0.00 / -0.07	-0.12 / -0.16 / 0.02 / -0.04
2	-0.11 / -0.28 / -0.10 / -0.17	-0.04 / -0.17 / -0.04 / -0.07	-0.14 / -0.21 / -0.05 / -0.10	-0.37 / -0.43 / -0.16 / -0.28
3	-0.04 / -0.19 / -0.05 / -0.14	-0.10 / -0.26 / -0.08 / -0.19	-0.08 / -0.12 / -0.01 / -0.03	-0.25 / -0.20 / -0.01 / -0.08
4	-0.30 / -0.52 / -0.21 / -0.42	-0.13 / -0.26 / -0.05 / -0.15	-0.04 / -0.13 / 0.04 / 0.01	-0.06 / -0.12 / 0.08 / 0.02

Table B.6. 4-Category Signal Yield Pulls, $m_H=125$, Sech turn-on. Columns show results for the various background models used in combined signal+background fits to background-only toys. The four numbers given for each background fit model correspond to toys generated from either an gauss×exponential, gauss×power-law, sech×exponential, or sech×power-law truth model. Boldface is used to indicate the lowest-order polynomial that satisfies the “low-bias” pull criteria: $|\mu(nS/\sigma(nS))| \leq 0.2$

Type-A Criterion, Gaussian turn-on, $m_H=125$

2012 electrons				
cat.	GaussBern3(GE/GP/SE/SP)	GaussBern4(GE/GP/SE/SP)	GaussBern5(GE/GP/SE/SP)	GaussBern6(GE/GP/SE/SP)
1	-0.05 / -0.24 / 0.12 / -0.13	0.02 / -0.12 / 0.18 / 0.04	-0.02 / -0.13 / 0.14 / 0.03	-0.06 / -0.13 / 0.19 / 0.07
2	-0.00 / -0.32 / 0.01 / -0.11	0.12 / -0.11 / 0.12 / 0.07	-0.04 / -0.16 / 0.06 / -0.01	-0.56 / -0.66 / -0.16 / -0.50
3	0.13 / -0.15 / 0.12 / -0.06	-0.02 / -0.29 / 0.01 / -0.16	0.01 / -0.04 / 0.13 / 0.05	-0.20 / -0.11 / 0.13 / 0.06
4	-0.46 / -0.92 / -0.23 / -0.68	-0.08 / -0.29 / 0.09 / -0.09	0.05 / -0.09 / 0.17 / 0.10	0.20 / 0.08 / 0.34 / 0.28

Table B.7. 4-Category Type-A Criteria, $m_H=125$, Gaussian turn-on.

Columns show results for the various background models used in combined signal+background fits to background-only toys. The four numbers given for each background fit model correspond to toys generated from either a gauss×exponential, gauss×power-law, sech×exponential, or sech×power-law truth model. Boldface is used to indicate the lowest-order polynomial that satisfies the “low-bias” type-A criteria: $|\mu(nS/\sigma(nB))| \leq 0.2$

Type-A Criterion, Sech turn-on, $m_H=125$

2012 electrons				
cat.	SechBern3(GE/GP/SE/SP)	SechBern4(GE/GP/SE/SP)	SechBern5(GE/GP/SE/SP)	SechBern6(GE/GP/SE/SP)
1	-0.19 / -0.36 / 0.00 / -0.24	-0.10 / -0.25 / 0.08 / -0.12	-0.15 / -0.25 / 0.02 / -0.09	-0.22 / -0.25 / 0.05 / -0.05
2	-0.16 / -0.49 / -0.15 / -0.28	-0.04 / -0.27 / -0.04 / -0.09	-0.23 / -0.32 / -0.08 / -0.15	-0.67 / -0.78 / -0.29 / -0.50
3	-0.02 / -0.29 / -0.03 / -0.21	-0.11 / -0.39 / -0.10 / -0.27	-0.15 / -0.18 / -0.01 / -0.04	-0.15 / -0.18 / -0.01 / -0.04
4	-0.61 / -1.07 / -0.39 / -0.86	-0.22 / -0.47 / -0.04 / -0.25	-0.08 / -0.23 / 0.06 / 0.00	-0.09 / -0.21 / 0.16 / 0.08

Table B.8. 4-Category Type-A Criteria, $m_H=125$, Sech turn-on. Columns

show results for the various background models used in combined signal+background fits to background-only toys. The four numbers given for each background fit model correspond to toys generated from either a gauss×exponential, gauss×power-law, sech×exponential, or sech×power-law truth model. Boldface is used to indicate the lowest-order polynomial that satisfies the “low-bias” type-A criteria: $|\mu(nS/\sigma(nB))| \leq 0.2$

Signal Pulls, Gaussian turn-on $m_H=130$

2012 electrons				
cat.	GaussBern3(GE/GP/SE/SP)	GaussBern4(GE/GP/SE/SP)	GaussBern5(GE/GP/SE/SP)	GaussBern6(GE/GP/SE/SP)
1	-0.08 / -0.19 / -0.06 / -0.14	-0.01 / -0.07 / -0.01 / -0.02	-0.02 / -0.06 / -0.00 / 0.01	0.03 / -0.01 / 0.03 / 0.04
2	-0.09 / -0.25 / -0.06 / -0.14	-0.01 / -0.07 / 0.01 / 0.03	-0.04 / -0.07 / 0.03 / 0.05	-0.05 / -0.07 / 0.04 / 0.05
3	-0.11 / -0.17 / -0.00 / -0.10	-0.16 / -0.32 / -0.05 / -0.20	-0.13 / -0.03 / 0.07 / 0.08	-0.10 / -0.00 / 0.09 / 0.12
4	-0.31 / -0.54 / -0.21 / -0.49	-0.10 / -0.13 / -0.03 / -0.09	-0.05 / -0.02 / 0.00 / 0.02	0.06 / 0.00 / 0.11 / 0.04

Table B.9. 4-Category Signal Yield Pulls, $m_H=130$, Gaussian turn-on for fit. Columns show results for the various background models used in combined signal+background fits to background-only toys. The four numbers given for each background fit model correspond to toys generated from either an gauss×exponential, gauss×power-law, sech×exponential, or sech×power-law truth model. Boldface is used to indicate the lowest-order polynomial that satisfies the “low-bias” pull criteria: $|\mu(nS/\sigma(nS))| \leq 0.2$

Signal Pulls, Sech turn-on $m_H=130$

2012 electrons				
cat.	SechBern3(GE/GP/SE/SP)	SechBern4(GE/GP/SE/SP)	SechBern5(GE/GP/SE/SP)	SechBern6(GE/GP/SE/SP)
1	-0.11 / -0.24 / -0.09 / -0.19	-0.05 / -0.13 / -0.04 / -0.06	-0.06 / -0.12 / -0.04 / -0.04	-0.04 / -0.10 / -0.03 / -0.02
2	-0.15 / -0.32 / -0.12 / -0.21	-0.08 / -0.17 / -0.05 / -0.05	-0.11 / -0.17 / -0.03 / -0.03	-0.13 / -0.14 / -0.04 / -0.02
3	-0.18 / -0.24 / -0.06 / -0.17	-0.27 / -0.38 / -0.09 / -0.23	-0.23 / -0.17 / -0.02 / -0.02	-0.19 / -0.13 / 0.04 / 0.03
4	-0.35 / -0.59 / -0.25 / -0.55	-0.12 / -0.18 / -0.06 / -0.14	-0.08 / -0.07 / -0.02 / -0.01	-0.05 / -0.09 / 0.01 / -0.02

Table B.10. 4-Category Signal Yield Pulls, $m_H=130$, Sech turn-on. Columns show results for the various background models used in combined signal+background fits to background-only toys. The four numbers given for each background fit model correspond to toys generated from either an gauss×exponential, gauss×power-law, sech×exponential, or sech×power-law truth model. Boldface is used to indicate the lowest-order polynomial that satisfies the “low-bias” pull criteria: $|\mu(nS/\sigma(nS))| \leq 0.2$

Type-A Criterion, Gaussian turn-on, $m_H=130$

cat.	2012 electrons			
	GaussBern3(GE/GP/SE/SP)	GaussBern4(GE/GP/SE/SP)	GaussBern5(GE/GP/SE/SP)	GaussBern6(GE/GP/SE/SP)
1	-0.09 / -0.35 / -0.06 / -0.25	0.04 / -0.10 / 0.03 / 0.00	-0.00 / -0.07 / 0.02 / 0.05	0.05 / 0.00 / 0.08 / 0.08
2	-0.16 / -0.50 / -0.10 / -0.25	-0.01 / -0.12 / 0.01 / 0.07	-0.04 / -0.11 / 0.05 / 0.09	-0.11 / -0.11 / 0.07 / 0.09
3	-0.21 / -0.32 / 0.02 / -0.18	-0.30 / -0.56 / -0.09 / -0.34	-0.25 / -0.05 / 0.14 / 0.14	-0.21 / -0.01 / 0.13 / 0.21
4	-0.68 / -1.18 / -0.44 / -1.07	-0.17 / -0.20 / -0.02 / -0.13	-0.07 / -0.00 / 0.02 / 0.04	0.10 / 0.04 / 0.18 / 0.08

Table B.11. 4-Category Type-A Criteria, $m_H=130$, Gaussian turn-on.

Columns show results for the various background models used in combined signal+background fits to background-only toys. The four numbers given for each background fit model correspond to toys generated from either a gauss×exponential, gauss×power-law, sech×exponential, or sech×power-law truth model. Boldface is used to indicate the lowest-order polynomial that satisfies the “low-bias” type-A criteria: $|\mu(nS/\sigma(nB))| \leq 0.2$

Type-A Criterion, Sech turn-on, $m_H=130$

cat.	2012 electrons			
	SechBern3(GE/GP/SE/SP)	SechBern4(GE/GP/SE/SP)	SechBern5(GE/GP/SE/SP)	SechBern6(GE/GP/SE/SP)
1	-0.17 / -0.48 / -0.14 / -0.36	-0.05 / -0.22 / -0.03 / -0.07	-0.05 / -0.20 / -0.05 / -0.03	-0.05 / -0.20 / -0.05 / -0.03
2	-0.29 / -0.66 / -0.23 / -0.41	-0.16 / -0.30 / -0.10 / -0.08	-0.19 / -0.31 / -0.05 / -0.05	-0.23 / -0.26 / -0.05 / -0.02
3	-0.34 / -0.46 / -0.09 / -0.31	-0.50 / -0.66 / -0.15 / -0.39	-0.43 / -0.28 / -0.02 / -0.04	-0.37 / -0.25 / 0.04 / 0.04
4	-0.76 / -1.32 / -0.52 / -1.23	-0.21 / -0.30 / -0.07 / -0.22	-0.12 / -0.09 / -0.01 / -0.02	-0.12 / -0.09 / -0.01 / -0.02

Table B.12. 4-Category Type-A Criteria, $m_H=130$, Sech turn-on. Columns

show results for the various background models used in combined signal+background fits to background-only toys. The four numbers given for each background fit model correspond to toys generated from either a gauss×exponential, gauss×power-law, sech×exponential, or sech×power-law truth model. Boldface is used to indicate the lowest-order polynomial that satisfies the “low-bias” type-A criteria: $|\mu(nS/\sigma(nB))| \leq 0.2$

Signal Pulls, Gaussian turn-on $m_H=135$

2012 electrons				
cat.	GaussBern3(GE/GP/SE/SP)	GaussBern4(GE/GP/SE/SP)	GaussBern5(GE/GP/SE/SP)	GaussBern6(GE/GP/SE/SP)
1	-0.13 / -0.12 / -0.11 / -0.13	-0.08 / -0.01 / -0.06 / -0.02	-0.08 / 0.00 / -0.07 / -0.01	-0.07 / -0.03 / -0.09 / -0.04
2	-0.13 / -0.14 / -0.05 / -0.11	-0.06 / -0.01 / -0.00 / 0.01	-0.03 / 0.03 / 0.01 / 0.04	0.13 / 0.21 / 0.15 / 0.23
3	-0.18 / -0.08 / -0.08 / -0.10	-0.20 / -0.16 / -0.09 / -0.16	-0.10 / 0.03 / -0.03 / 0.04	-0.08 / -0.02 / -0.08 / -0.00
4	-0.19 / -0.35 / -0.14 / -0.36	-0.02 / 0.01 / -0.01 / -0.02	-0.03 / 0.01 / -0.01 / -0.01	-0.01 / -0.08 / -0.01 / -0.09

Table B.13. 4-Category Signal Yield Pulls, $m_H=135$, Gaussian turn-on for fit. Columns show results for the various background models used in combined signal+background fits to background-only toys. The four numbers given for each background fit model correspond to toys generated from either an gauss×exponential, gauss×power-law, sech×exponential, or sech×power-law truth model. Boldface is used to indicate the lowest-order polynomial that satisfies the “low-bias” pull criteria: $|\mu(nS/\sigma(nS))| \leq 0.2$

Signal Pulls, Sech turn-on $m_H=135$

2012 electrons				
cat.	SechBern3(GE/GP/SE/SP)	SechBern4(GE/GP/SE/SP)	SechBern5(GE/GP/SE/SP)	SechBern6(GE/GP/SE/SP)
1	-0.14 / -0.14 / -0.11 / -0.15	-0.09 / -0.02 / -0.06 / -0.03	-0.09 / -0.02 / -0.06 / -0.02	-0.09 / -0.05 / -0.09 / -0.04
2	-0.13 / -0.16 / -0.04 / -0.12	-0.07 / -0.02 / 0.01 / 0.02	-0.05 / 0.02 / 0.02 / 0.04	0.09 / 0.17 / 0.11 / 0.20
3	-0.17 / -0.08 / -0.06 / -0.08	-0.19 / -0.12 / -0.05 / -0.10	-0.15 / -0.03 / -0.04 / 0.01	-0.05 / -0.01 / -0.06 / -0.01
4	-0.19 / -0.38 / -0.13 / -0.39	-0.02 / 0.00 / 0.01 / -0.02	-0.03 / 0.01 / -0.01 / 0.02	-0.06 / -0.09 / -0.06 / -0.11

Table B.14. 4-Category Signal Yield Pulls, $m_H=135$, Sech turn-on. Columns show results for the various background models used in combined signal+background fits to background-only toys. The four numbers given for each background fit model correspond to toys generated from either an gauss×exponential, gauss×power-law, sech×exponential, or sech×power-law truth model. Boldface is used to indicate the lowest-order polynomial that satisfies the “low-bias” pull criteria: $|\mu(nS/\sigma(nS))| \leq 0.2$

Type-A Criterion, Gaussian turn-on, $m_H=135$

2012 electrons				
cat.	GaussBern3(GE/GP/SE/SP)	GaussBern4(GE/GP/SE/SP)	GaussBern5(GE/GP/SE/SP)	GaussBern6(GE/GP/SE/SP)
1	-0.21 / -0.17 / -0.16 / -0.19	-0.10 / 0.05 / -0.07 / 0.02	-0.12 / 0.04 / -0.08 / 0.00	-0.10 / -0.03 / -0.14 / -0.04
2	-0.23 / -0.24 / -0.06 / -0.19	-0.09 / -0.01 / 0.01 / 0.05	-0.06 / 0.05 / 0.03 / 0.07	0.24 / 0.33 / 0.24 / 0.39
3	-0.32 / -0.11 / -0.13 / -0.15	-0.33 / -0.28 / -0.16 / -0.27	-0.17 / 0.06 / -0.06 / 0.06	-0.13 / -0.03 / -0.13 / -0.01
4	-0.36 / -0.73 / -0.23 / -0.72	-0.01 / 0.07 / 0.02 / 0.01	-0.03 / 0.05 / 0.01 / 0.04	-0.01 / -0.15 / -0.01 / -0.16

Table B.15. 4-Category Type-A Criteria, $m_H=135$, Gaussian turn-on.

Columns show results for the various background models used in combined signal+background fits to background-only toys. The four numbers given for each background fit model correspond to toys generated from either a gauss×exponential, gauss×power-law, sech×exponential, or sech×power-law truth model. Boldface is used to indicate the lowest-order polynomial that satisfies the “low-bias” type-A criteria: $|\mu(nS/\sigma(nB))| \leq 0.2$

Type-A Criterion, Sech turn-on, $m_H=135$

2012 electrons				
cat.	SechBern3(GE/GP/SE/SP)	SechBern4(GE/GP/SE/SP)	SechBern5(GE/GP/SE/SP)	SechBern6(GE/GP/SE/SP)
1	-0.24 / -0.21 / -0.18 / -0.22	-0.12 / 0.04 / -0.06 / 0.02	-0.13 / -0.01 / -0.07 / -0.01	-0.13 / -0.07 / -0.14 / -0.04
2	-0.22 / -0.27 / -0.06 / -0.19	-0.11 / -0.00 / 0.04 / 0.06	-0.08 / 0.03 / 0.05 / 0.07	0.17 / 0.32 / 0.23 / 0.36
3	-0.31 / -0.10 / -0.10 / -0.12	-0.32 / -0.20 / -0.10 / -0.17	-0.27 / -0.05 / -0.08 / 0.02	-0.10 / -0.01 / -0.10 / -0.02
4	-0.36 / -0.81 / -0.23 / -0.81	0.01 / 0.07 / 0.06 / 0.02	-0.03 / 0.05 / 0.02 / 0.07	-0.08 / -0.19 / -0.08 / -0.18

Table B.16. 4-Category Type-A Criteria, $m_H=135$, Sech turn-on. Columns

show results for the various background models used in combined signal+background fits to background-only toys. The four numbers given for each background fit model correspond to toys generated from either a gauss×exponential, gauss×power-law, sech×exponential, or sech×power-law truth model. Boldface is used to indicate the lowest-order polynomial that satisfies the “low-bias” type-A criteria: $|\mu(nS/\sigma(nB))| \leq 0.2$

Signal Pulls, Gaussian turn-on $m_H=140$

2012 electrons				
cat.	GaussBern3(GE/GP/SE/SP)	GaussBern4(GE/GP/SE/SP)	GaussBern5(GE/GP/SE/SP)	GaussBern6(GE/GP/SE/SP)
1	-0.08 / -0.02 / -0.07 / -0.03	-0.07 / 0.04 / -0.05 / 0.01	-0.09 / 0.02 / -0.07 / -0.02	-0.09 / -0.02 / -0.11 / -0.04
2	-0.11 / 0.02 / -0.01 / -0.06	-0.09 / 0.06 / 0.01 / -0.02	-0.06 / 0.05 / -0.01 / -0.03	0.14 / 0.27 / 0.14 / 0.21
3	-0.12 / 0.00 / -0.07 / -0.05	-0.06 / 0.10 / -0.02 / 0.06	-0.10 / -0.02 / -0.09 / -0.08	-0.01 / -0.04 / -0.09 / -0.12
4	-0.04 / -0.14 / -0.06 / -0.15	0.00 / 0.05 / -0.02 / 0.01	-0.07 / -0.09 / -0.10 / -0.12	-0.12 / -0.14 / -0.16 / -0.17

Table B.17. 4-Category Signal Yield Pulls, $m_H=140$, Gaussian turn-on for fit. Columns show results for the various background models used in combined signal+background fits to background-only toys. The four numbers given for each background fit model correspond to toys generated from either an gauss×exponential, gauss×power-law, sech×exponential, or sech×power-law truth model. Boldface is used to indicate the lowest-order polynomial that satisfies the “low-bias” pull criteria: $|\mu(nS/\sigma(nS))| \leq 0.2$

Signal Pulls, Sech turn-on $m_H=140$

2012 electrons				
cat.	SechBern3(GE/GP/SE/SP)	SechBern4(GE/GP/SE/SP)	SechBern5(GE/GP/SE/SP)	SechBern6(GE/GP/SE/SP)
1	-0.07 / -0.01 / -0.05 / -0.02	-0.05 / 0.07 / -0.02 / 0.04	-0.06 / 0.05 / -0.05 / 0.01	-0.06 / 0.02 / -0.08 / -0.02
2	-0.07 / 0.07 / 0.04 / -0.00	-0.04 / 0.11 / 0.05 / 0.03	-0.03 / 0.09 / 0.03 / 0.02	0.13 / 0.27 / 0.13 / 0.21
3	-0.08 / 0.06 / -0.00 / 0.01	-0.02 / 0.17 / 0.03 / 0.11	-0.07 / -0.01 / -0.08 / -0.06	0.06 / 0.02 / -0.06 / -0.05
4	-0.02 / -0.15 / -0.04 / -0.16	0.04 / 0.07 / 0.01 / 0.04	-0.06 / -0.07 / -0.09 / -0.12	-0.08 / -0.11 / -0.13 / -0.14

Table B.18. 4-Category Signal Yield Pulls, $m_H=140$, Sech turn-on. Columns show results for the various background models used in combined signal+background fits to background-only toys. The four numbers given for each background fit model correspond to toys generated from either an gauss×exponential, gauss×power-law, sech×exponential, or sech×power-law truth model. Boldface is used to indicate the lowest-order polynomial that satisfies the “low-bias” pull criteria: $|\mu(nS/\sigma(nS))| \leq 0.2$

Type-A Criterion, Gaussian turn-on, $m_H=140$

cat.	2012 electrons			
	GaussBern3(GE/GP/SE/SP)	GaussBern4(GE/GP/SE/SP)	GaussBern5(GE/GP/SE/SP)	GaussBern6(GE/GP/SE/SP)
1	-0.08 / 0.08 / -0.06 / 0.04	-0.08 / 0.12 / -0.05 / 0.06	-0.12 / 0.07 / -0.09 / 0.01	-0.08 / 0.06 / -0.11 / 0.00
2	-0.19 / 0.11 / 0.01 / -0.05	-0.14 / 0.12 / 0.03 / -0.03	-0.10 / 0.07 / -0.03 / -0.06	0.28 / 0.48 / 0.26 / 0.37
3	-0.20 / 0.05 / -0.11 / -0.07	-0.10 / 0.14 / -0.03 / 0.08	-0.18 / -0.04 / -0.16 / -0.13	0.01 / -0.07 / -0.14 / -0.20
4	-0.01 / -0.17 / -0.04 / -0.19	0.04 / 0.14 / -0.00 / 0.06	-0.10 / -0.12 / -0.17 / -0.18	-0.14 / -0.17 / -0.23 / -0.20

Table B.19. 4-Category Type-A Criteria, $m_H=140$, Gaussian turn-on.

Columns show results for the various background models used in combined signal+background fits to background-only toys. The four numbers given for each background fit model correspond to toys generated from either a gauss×exponential, gauss×power-law, sech×exponential, or sech×power-law truth model. Boldface is used to indicate the lowest-order polynomial that satisfies the “low-bias” type-A criteria: $|\mu(nS/\sigma(nB))| \leq 0.2$

Type-A Criterion, Sech turn-on, $m_H=140$

cat.	2012 electrons			
	SechBern3(GE/GP/SE/SP)	SechBern4(GE/GP/SE/SP)	SechBern5(GE/GP/SE/SP)	SechBern6(GE/GP/SE/SP)
1	-0.06 / 0.12 / -0.03 / 0.07	-0.05 / 0.17 / 0.01 / 0.13	-0.05 / 0.14 / -0.05 / 0.07	-0.03 / 0.11 / -0.04 / 0.06
2	-0.11 / 0.21 / 0.09 / 0.07	-0.06 / 0.20 / 0.11 / 0.06	-0.04 / 0.14 / 0.06 / 0.01	0.30 / 0.52 / 0.27 / 0.41
3	-0.11 / 0.19 / 0.01 / 0.06	-0.04 / 0.28 / 0.06 / 0.17	-0.11 / -0.03 / -0.14 / -0.10	0.10 / 0.06 / -0.09 / -0.09
4	0.04 / -0.20 / 0.03 / -0.20	0.12 / 0.17 / 0.06 / 0.12	-0.10 / -0.12 / -0.15 / -0.20	-0.04 / -0.09 / -0.12 / -0.13

Table B.20. 4-Category Type-A Criteria, $m_H=140$, Sech turn-on. Columns

show results for the various background models used in combined signal+background fits to background-only toys. The four numbers given for each background fit model correspond to toys generated from either a gauss×exponential, gauss×power-law, sech×exponential, or sech×power-law truth model. Boldface is used to indicate the lowest-order polynomial that satisfies the “low-bias” type-A criteria: $|\mu(nS/\sigma(nB))| \leq 0.2$

Signal Pulls, Sech turn-on $m_H=145$

cat.	2012 electrons			
	SechBern3(GE/GP/SE/SP)	SechBern4(GE/GP/SE/SP)	SechBern5(GE/GP/SE/SP)	SechBern6(GE/GP/SE/SP)
1	0.03 / 0.03 / 0.03 / 0.00	0.00 / 0.04 / 0.01 / -0.02	-0.01 / 0.01 / -0.01 / -0.06	0.01 / 0.00 / -0.00 / -0.07
2	0.01 / 0.21 / 0.06 / 0.12	-0.04 / 0.12 / 0.01 / 0.03	-0.03 / 0.10 / -0.04 / 0.01	0.03 / 0.19 / 0.01 / 0.11
3	0.05 / 0.17 / 0.04 / 0.10	0.16 / 0.41 / 0.13 / 0.33	0.01 / 0.05 / -0.04 / -0.05	0.11 / 0.09 / 0.00 / -0.02
4	0.12 / 0.11 / 0.09 / 0.11	0.04 / 0.11 / 0.01 / 0.09	-0.08 / -0.06 / -0.09 / -0.08	-0.05 / -0.01 / -0.07 / -0.02

Table B.21. 4-Category Signal Yield Pulls, $m_H=145$, Sech turn-on.

Columns show results for the various background models used in combined signal+background fits to background-only toys. The four numbers given for each background fit model correspond to toys generated from either an gauss×exponential, gauss×power-law, sech×exponential, or sech×power-law truth model. Boldface is used to indicate the lowest-order polynomial that satisfies the “low-bias” pull criteria: $|\mu(nS/\sigma(nS))| \leq 0.2$

Type-A Criterion, Gaussian turn-on, $m_H=145$

2012 electrons				
cat.	GaussBern3(GE/GP/SE/SP)	GaussBern4(GE/GP/SE/SP)	GaussBern5(GE/GP/SE/SP)	GaussBern6(GE/GP/SE/SP)
1	0.10 / 0.16 / 0.10 / 0.07	-0.01 / 0.05 / 0.01 / -0.06	-0.03 / -0.03 / -0.03 / -0.14	0.06 / 0.02 / 0.04 / -0.07
2	-0.05 / 0.34 / 0.03 / 0.16	-0.15 / 0.13 / -0.09 / -0.04	-0.16 / 0.03 / -0.14 / -0.10	0.14 / 0.33 / 0.09 / 0.20
3	0.01 / 0.22 / -0.02 / 0.08	0.17 / 0.53 / 0.13 / 0.37	-0.06 / -0.04 / -0.13 / -0.17	0.12 / 0.06 / -0.01 / -0.09
4	0.24 / 0.36 / 0.15 / 0.35	0.06 / 0.16 / 0.01 / 0.12	-0.06 / -0.04 / -0.07 / -0.05	-0.09 / -0.06 / -0.12 / -0.05

Table B.22. 4-Category Type-A Criteria, $m_H=145$, Gaussian turn-on.

Columns show results for the various background models used in combined signal+background fits to background-only toys. The four numbers given for each background fit model correspond to toys generated from either a gauss×exponential, gauss×power-law, sech×exponential, or sech×power-law truth model. Boldface is used to indicate the lowest-order polynomial that satisfies the “low-bias” type-A criteria: $|\mu(nS/\sigma(nB))| \leq 0.2$

Type-A Criterion, Sech turn-on, $m_H=145$

2012 electrons				
cat.	SechBern3(GE/GP/SE/SP)	SechBern4(GE/GP/SE/SP)	SechBern5(GE/GP/SE/SP)	SechBern6(GE/GP/SE/SP)
1	0.15 / 0.18 / 0.16 / 0.11	0.06 / 0.13 / 0.07 / 0.00	0.06 / 0.10 / 0.06 / -0.04	0.14 / 0.12 / 0.10 / -0.02
2	0.04 / 0.45 / 0.13 / 0.27	-0.05 / 0.23 / 0.03 / 0.07	-0.07 / 0.15 / -0.08 / -0.00	-0.07 / 0.15 / -0.08 / -0.00
3	0.10 / 0.33 / 0.08 / 0.20	0.24 / 0.62 / 0.20 / 0.49	0.04 / 0.08 / -0.04 / -0.07	0.04 / 0.08 / -0.04 / -0.07
4	0.33 / 0.37 / 0.25 / 0.38	0.11 / 0.23 / 0.07 / 0.20	-0.03 / 0.01 / -0.05 / -0.02	-0.03 / 0.01 / -0.05 / -0.02

Table B.23. 4-Category Type-A Criteria, $m_H=145$, Sech turn-on. Columns

show results for the various background models used in combined signal+background fits to background-only toys. The four numbers given for each background fit model correspond to toys generated from either a gauss×exponential, gauss×power-law, sech×exponential, or sech×power-law truth model. Boldface is used to indicate the lowest-order polynomial that satisfies the “low-bias” type-A criteria: $|\mu(nS/\sigma(nB))| \leq 0.2$

Signal Pulls, Gaussian turn-on $m_H=150$

2012 electrons				
cat.	GaussBern3(GE/GP/SE/SP)	GaussBern4(GE/GP/SE/SP)	GaussBern5(GE/GP/SE/SP)	GaussBern6(GE/GP/SE/SP)
1	0.05 / 0.07 / 0.04 / 0.09	-0.02 / -0.02 / -0.02 / -0.02	-0.02 / -0.03 / -0.02 / -0.03	-0.00 / -0.02 / -0.00 / -0.00
2	0.08 / 0.18 / 0.02 / 0.10	-0.02 / 0.00 / -0.08 / -0.07	-0.03 / 0.00 / -0.09 / -0.08	-0.10 / -0.11 / -0.17 / -0.16
3	0.09 / 0.13 / 0.02 / 0.11	0.28 / 0.43 / 0.15 / 0.40	0.01 / -0.01 / -0.04 / -0.05	0.01 / 0.05 / 0.01 / 0.00
4	0.14 / 0.27 / 0.13 / 0.25	-0.05 / 0.04 / -0.02 / 0.01	-0.12 / -0.07 / -0.06 / -0.09	-0.09 / 0.01 / -0.02 / -0.01

Table B.24. 4-Category Signal Yield Pulls, $m_H=150$, Gaussian turn-on for fit. Columns show results for the various background models used in combined signal+background fits to background-only toys. The four numbers given for each background fit model correspond to toys generated from either an gauss×exponential, gauss×power-law, sech×exponential, or sech×power-law truth model. Boldface is used to indicate the lowest-order polynomial that satisfies the “low-bias” pull criteria: $|\mu(nS/\sigma(nS))| \leq 0.2$

Signal Pulls, Sech turn-on $m_H=150$

2012 electrons				
cat.	SechBern3(GE/GP/SE/SP)	SechBern4(GE/GP/SE/SP)	SechBern5(GE/GP/SE/SP)	SechBern6(GE/GP/SE/SP)
1	0.06 / 0.07 / 0.04 / 0.10	0.00 / 0.01 / -0.01 / 0.00	0.00 / 0.00 / -0.00 / -0.01	0.02 / 0.02 / 0.02 / 0.02
2	0.10 / 0.21 / 0.05 / 0.13	0.01 / 0.04 / -0.05 / -0.03	0.02 / 0.04 / -0.06 / -0.04	-0.06 / -0.04 / -0.14 / -0.13
3	0.11 / 0.14 / 0.04 / 0.13	0.28 / 0.41 / 0.15 / 0.39	0.08 / 0.07 / 0.01 / 0.02	0.03 / 0.08 / 0.02 / 0.03
4	0.17 / 0.27 / 0.16 / 0.26	-0.03 / 0.06 / 0.01 / 0.04	-0.10 / -0.03 / -0.05 / -0.06	-0.05 / 0.05 / -0.00 / 0.02

Table B.25. 4-Category Signal Yield Pulls, $m_H=150$, Sech turn-on. Columns show results for the various background models used in combined signal+background fits to background-only toys. The four numbers given for each background fit model correspond to toys generated from either an gauss×exponential, gauss×power-law, sech×exponential, or sech×power-law truth model. Boldface is used to indicate the lowest-order polynomial that satisfies the “low-bias” pull criteria: $|\mu(nS/\sigma(nS))| \leq 0.2$

Type-A Criterion, Gaussian turn-on, $m_H=150$

2012 electrons				
cat.	GaussBern3(GE/GP/SE/SP)	GaussBern4(GE/GP/SE/SP)	GaussBern5(GE/GP/SE/SP)	GaussBern6(GE/GP/SE/SP)
1	0.19 / 0.24 / 0.16 / 0.28	0.02 / 0.04 / 0.04 / 0.04	0.03 / 0.00 / 0.05 / 0.02	0.11 / 0.11 / 0.10 / 0.12
2	0.19 / 0.40 / 0.07 / 0.24	-0.01 / 0.03 / -0.12 / -0.09	-0.03 / -0.00 / -0.16 / -0.15	-0.11 / -0.09 / -0.20 / -0.22
3	0.19 / 0.26 / 0.07 / 0.23	0.44 / 0.62 / 0.29 / 0.57	0.04 / 0.00 / -0.05 / -0.06	0.06 / 0.12 / 0.05 / 0.04
4	0.32 / 0.60 / 0.32 / 0.56	-0.03 / 0.11 / 0.02 / 0.06	-0.08 / 0.05 / 0.02 / -0.00	-0.09 / 0.10 / 0.02 / 0.06

Table B.26. 4-Category Type-A Criteria, $m_H=150$, Gaussian turn-on.

Columns show results for the various background models used in combined signal+background fits to background-only toys. The four numbers given for each background fit model correspond to toys generated from either a gauss×exponential, gauss×power-law, sech×exponential, or sech×power-law truth model. Boldface is used to indicate the lowest-order polynomial that satisfies the “low-bias” type-A criteria: $|\mu(nS/\sigma(nB))| \leq 0.2$

Type-A Criterion, Sech turn-on, $m_H=150$

2012 electrons				
cat.	SechBern3(GE/GP/SE/SP)	SechBern4(GE/GP/SE/SP)	SechBern5(GE/GP/SE/SP)	SechBern6(GE/GP/SE/SP)
1	0.21 / 0.24 / 0.16 / 0.30	0.07 / 0.09 / 0.07 / 0.08	0.09 / 0.08 / 0.08 / 0.04	0.16 / 0.17 / 0.15 / 0.15
2	0.25 / 0.45 / 0.13 / 0.31	0.04 / 0.12 / -0.07 / -0.01	0.06 / 0.08 / -0.09 / -0.06	-0.01 / 0.03 / -0.13 / -0.14
3	0.22 / 0.29 / 0.10 / 0.27	0.45 / 0.63 / 0.26 / 0.57	0.14 / 0.12 / 0.03 / 0.03	0.14 / 0.12 / 0.03 / 0.03
4	0.37 / 0.61 / 0.38 / 0.58	0.00 / 0.16 / 0.06 / 0.12	-0.04 / 0.10 / 0.03 / 0.04	-0.03 / 0.13 / 0.06 / 0.09

Table B.27. 4-Category Type-A Criteria, $m_H=150$, Sech turn-on. Columns

show results for the various background models used in combined signal+background fits to background-only toys. The four numbers given for each background fit model correspond to toys generated from either a gauss×exponential, gauss×power-law, sech×exponential, or sech×power-law truth model. Boldface is used to indicate the lowest-order polynomial that satisfies the “low-bias” type-A criteria: $|\mu(nS/\sigma(nB))| \leq 0.2$

BG Pulls $m_H=120$

2012 muon			
cat.	Bern2(Exp/Pow)	Bern3(Exp/Pow)	Bern4(Exp/Pow)
VBF	-0.28 /-0.31	-0.09 /-0.17	0.06 /0.01

2012 electron			
cat.	Bern2(Exp/Pow)	Bern3(Exp/Pow)	Bern4(Exp/Pow)
VBF	-0.27 /-0.43	-0.01 /0.11	0.15 /0.19

Table B.28. VBF BG Yield Pulls, $m_H=120$ for fit models. Columns show results for the various background models used in combined signal+background fits to background-only toys. The two numbers given for each background fit model correspond to toys generated from either an exponential or a power-law. Boldface is used to indicate the lowest-order polynomial that satisfies the “low-bias” pull criteria: $|\mu(nBG)/\sigma(nBG))| \leq 0.2$

BG Pulls $m_H=125$

2012 muon			
cat.	Bern2(Exp/Pow)	Bern3(Exp/Pow)	Bern4(Exp/Pow)
VBF	-0.18 /-0.11	-0.12 /-0.10	0.07 /0.07

2012 electron			
cat.	Bern2(Exp/Pow)	Bern3(Exp/Pow)	Bern4(Exp/Pow)
VBF	-0.31 /-0.21	0.06 /-0.10	0.13 /0.00

Table B.29. VBF BG Yield Pulls, $m_H=125$ for fit models. Columns show results for the various background models used in combined signal+background fits to background-only toys. The two numbers given for each background fit model correspond to toys generated from either an exponential or a power-law. Boldface is used to indicate the lowest-order polynomial that satisfies the “low-bias” pull criteria: $|\mu(nBG)/\sigma(nBG))| \leq 0.2$

BG Pulls $m_H=130$

2012 muon			
cat.	Bern2(Exp/Pow)	Bern3(Exp/Pow)	Bern4(Exp/Pow)
VBF	-0.15 /-0.12	-0.04 /-0.06	0.10 /0.13

2012 electron			
cat.	Bern2(Exp/Pow)	Bern3(Exp/Pow)	Bern4(Exp/Pow)
VBF	-0.18 /-0.01	0.13 /0.02	0.10 /0.03

Table B.30. VBF BG Yield Pulls, $m_H=130$ for fit models. Columns show results for the various background models used in combined signal+background fits to background-only toys. The two numbers given for each background fit model correspond to toys generated from either an exponential or a power-law. Boldface is used to indicate the lowest-order polynomial that satisfies the “low-bias” pull criteria: $|\mu(nBG)/\sigma(nBG))| \leq 0.2$

BG Pulls $m_H=135$

2012 muon			
cat.	Bern2(Exp/Pow)	Bern3(Exp/Pow)	Bern4(Exp/Pow)
VBF	0.06 /0.14	0.03 /0.10	0.20 /0.20

2012 electron			
cat.	Bern2(Exp/Pow)	Bern3(Exp/Pow)	Bern4(Exp/Pow)
VBF	0.14 /0.19	0.19 /0.14	0.13 /0.07

Table B.31. VBF BG Yield Pulls, $m_H=135$ for fit models. Columns show results for the various background models used in combined signal+background fits to background-only toys. The two numbers given for each background fit model correspond to toys generated from either an exponential or a power-law. Boldface is used to indicate the lowest-order polynomial that satisfies the “low-bias” pull criteria: $|\mu(nBG)/\sigma(nBG))| \leq 0.2$

BG Pulls $m_H=140$

2012 muon			
cat.	Bern2(Exp/Pow)	Bern3(Exp/Pow)	Bern4(Exp/Pow)
VBF	0.22 /0.29	0.14 /0.13	0.17 /0.16

2012 electron			
cat.	Bern2(Exp/Pow)	Bern3(Exp/Pow)	Bern4(Exp/Pow)
VBF	0.37 /0.40	0.17 /0.20	0.07 /0.11

Table B.32. VBF BG Yield Pulls, $m_H=140$ for fit models. Columns show results for the various background models used in combined signal+background fits to background-only toys. The two numbers given for each background fit model correspond to toys generated from either an exponential or a power-law. Boldface is used to indicate the lowest-order polynomial that satisfies the “low-bias” pull criteria: $|\mu(nBG)/\sigma(nBG))| \leq 0.2$

BG Pulls $m_H=145$

2012 muon			
cat.	Bern2(Exp/Pow)	Bern3(Exp/Pow)	Bern4(Exp/Pow)
VBF	0.28 /0.27	0.07 /-0.01	0.03 /-0.02

2012 electron			
cat.	Bern2(Exp/Pow)	Bern3(Exp/Pow)	Bern4(Exp/Pow)
VBF	0.31 /0.32	0.12 /0.13	-0.02 /-0.05

Table B.33. VBF BG Yield Pulls, $m_H=145$ for fit models. Columns show results for the various background models used in combined signal+background fits to background-only toys. The two numbers given for each background fit model correspond to toys generated from either an exponential or a power-law. Boldface is used to indicate the lowest-order polynomial that satisfies the “low-bias” pull criteria: $|\mu(nBG)/\sigma(nBG))| \leq 0.2$

BG Pulls $m_H=150$

2012 muon			
cat.	Bern2(Exp/Pow)	Bern3(Exp/Pow)	Bern4(Exp/Pow)
VBF	0.00 /0.16	-0.03 /-0.02	-0.20 /0.10

2012 electron			
cat.	Bern2(Exp/Pow)	Bern3(Exp/Pow)	Bern4(Exp/Pow)
VBF	0.09 /0.14	0.02 /0.03	-0.07 /0.02

Table B.34. VBF BG Yield Pulls, $m_H=150$ for fit models. Columns show results for the various background models used in combined signal+background fits to background-only toys. The two numbers given for each background fit model correspond to toys generated from either an exponential or a power-law. Boldface is used to indicate the lowest-order polynomial that satisfies the “low-bias” pull criteria: $|\mu(nBG)/\sigma(nBG)| \leq 0.2$

B.2. $A \rightarrow Z\gamma$ Bias Studies

Type-A Bias, $m_H=200$

8TeV mu					
cat.	PowDecay(P/L/E/G/W/H)	ExpSum(P/L/E/G/W/H)	PowExpSum(P/L/E/G/W/H)	TripExpSum(P/L/E/G/W/H)	TripPowSum(P/L/E/G/W/H)
0	-0.19 /-0.17 /0.59 /-1.09 /-0.01 /1.29	-0.64 /-0.64 /-0.59 /-0.10 /-0.28 /-0.07	-0.03 /-0.02 /1.09 /0.81 /1.90 /2.39	-0.03 /-0.02 /-0.01 /0.02 /0.02 /0.19	0.18 /0.16 /1.27 /1.04 /2.19 /2.86
8TeV el					
cat.	PowDecay(P/L/E/G/W/H)	ExpSum(P/L/E/G/W/H)	PowExpSum(P/L/E/G/W/H)	TripExpSum(P/L/E/G/W/H)	TripPowSum(P/L/E/G/W/H)
0	-0.22 /-0.24 /0.45 /-1.96 /0.02 /0.29	-0.02 /-0.02 /-0.02 /-0.00 /-0.01 /-0.01	-0.00 /-0.00 /0.02 /-0.05 /0.03 /-0.00	-0.00 /-0.01 /-0.01 /0.00 /0.00 /0.00	0.02 /0.03 /0.10 /-0.10 /0.26 /0.11

Table B.35. typeA Bias, 200. Columns show results for the various background models used in combined signal+background fits to background-only toys. The three numbers given for each background fit model correspond to toys generated from either a power law, Laurent polynomial, or exponential-like truth model. Boldface and yellow highlight is used to indicate the lowest-order functional form that satisfies the “low-bias” criterion: $|\mu(nS/\sigma(nBG))| \leq 0.2$

Type-A Bias, $m_H=250$

8TeV mu					
cat.	PowDecay(P/L/E/G/W/H)	ExpSum(P/L/E/G/W/H)	PowExpSum(P/L/E/G/W/H)	TripExpSum(P/L/E/G/W/H)	TripPowSum(P/L/E/G/W/H)
0	-0.47 /-0.47 /-0.25 /-0.46 /-0.37 /-0.26	0.30 /0.27 /0.13 /0.15 /0.06 /-0.13	-0.13 /-0.13 /0.56 /2.16 /2.31 /1.60	0.04 /0.01 /-0.02 /0.01 /-0.03 /-0.16	-0.09 /-0.12 /0.59 /2.65 /2.80 /1.86
8TeV el					
cat.	PowDecay(P/L/E/G/W/H)	ExpSum(P/L/E/G/W/H)	PowExpSum(P/L/E/G/W/H)	TripExpSum(P/L/E/G/W/H)	TripPowSum(P/L/E/G/W/H)
0	-0.40 /-0.41 /-0.21 /-0.43 /-0.27 /-0.32	0.01 /0.01 /0.01 /0.01 /0.00 /0.01	-0.01 /-0.01 /0.01 /0.04 /0.07 /0.01	0.00 /0.00 /-0.00 /0.00 /-0.01 /-0.00	0.00 /0.01 /0.04 /0.13 /0.39 /0.05

Table B.36. typeA Bias, 250. Columns show results for the various background models used in combined signal+background fits to background-only toys. The three numbers given for each background fit model correspond to toys generated from either a power law, Laurent polynomial, or exponential-like truth model. Boldface and yellow highlight is used to indicate the lowest-order functional form that satisfies the “low-bias” criterion: $|\mu(nS/\sigma(nBG))| \leq 0.2$

Type-A Bias, $m_H=300$

8TeV mm					
cat.	PowDecay(P/L/E/G/W/H)	ExpSum(P/L/E/G/W/H)	PowExpSum(P/L/E/G/W/H)	TripExpSum(P/L/E/G/W/H)	TripPowSum(P/L/E/G/W/H)
0	-0.48 /-0.44 /-0.69 /0.07 /-0.46 /-0.93	0.55 /0.58 /0.51 /0.02 /0.17 /0.15	-0.10 /-0.10 /-0.09 /2.62 /1.83 /0.45	0.09 /0.12 /0.09 /-0.03 /0.01 /-0.03	-0.20 /-0.18 /-0.20 /2.50 /1.79 /0.31
8TeV el					
cat.	PowDecay(P/L/E/G/W/H)	ExpSum(P/L/E/G/W/H)	PowExpSum(P/L/E/G/W/H)	TripExpSum(P/L/E/G/W/H)	TripPowSum(P/L/E/G/W/H)
0	-0.40 /-0.44 /-0.66 /0.40 /-0.36 /-0.53	0.03 /0.03 /0.02 /0.00 /0.01 /0.02	-0.00 /-0.01 /-0.01 /0.11 /0.08 /-0.00	0.01 /0.00 /-0.00 /-0.01 /-0.00 /0.00	-0.01 /-0.01 /-0.04 /0.35 /0.29 /0.01

Table B.37. typeA Bias, 300. Columns show results for the various background models used in combined signal+background fits to background-only toys. The three numbers given for each background fit model correspond to toys generated from either a power law, Laurent polynomial, or exponential-like truth model. Boldface and yellow highlight is used to indicate the lowest-order functional form that satisfies the “low-bias” criterion: $|\mu(nS/\sigma(nBG))| \leq 0.2$

Type-A Bias, $m_H=350$

8TeV mm					
cat.	PowDecay(P/L/E/G/W/H)	ExpSum(P/L/E/G/W/H)	PowExpSum(P/L/E/G/W/H)	TripExpSum(P/L/E/G/W/H)	TripPowSum(P/L/E/G/W/H)
0	-0.45 /-0.45 /-1.11 /0.56 /-0.45 /-1.41	0.16 /0.18 /0.34 /-0.22 /0.11 /0.31	-0.30 /-0.28 /-1.06 /1.80 /0.58 /-1.06	0.03 /0.04 /0.03 /-0.01 /0.05 /0.10	-0.29 /-0.31 /-0.95 /1.40 /0.30 /-0.98
8TeV el					
cat.	PowDecay(P/L/E/G/W/H)	ExpSum(P/L/E/G/W/H)	PowExpSum(P/L/E/G/W/H)	TripExpSum(P/L/E/G/W/H)	TripPowSum(P/L/E/G/W/H)
0	-0.41 /-0.42 /-0.89 /1.11 /-0.39 /-0.63	0.01 /0.01 /0.02 /-0.02 /0.01 /0.01	-0.00 /-0.01 /-0.03 /0.15 /0.04 /-0.03	-0.00 /0.00 /0.01 /-0.02 /-0.00 /0.01	-0.04 /-0.05 /-0.11 /0.43 /0.10 /-0.05

Table B.38. typeA Bias, 350. Columns show results for the various background models used in combined signal+background fits to background-only toys. The three numbers given for each background fit model correspond to toys generated from either a power law, Laurent polynomial, or exponential-like truth model. Boldface and yellow highlight is used to indicate the lowest-order functional form that satisfies the “low-bias” criterion: $|\mu(nS/\sigma(nBG))| \leq 0.2$

Type-A Bias, $m_H=400$

8TeV mm					
cat.	PowDecay(P/L/E/G/W/H)	ExpSum(P/L/E/G/W/H)	PowExpSum(P/L/E/G/W/H)	TripExpSum(P/L/E/G/W/H)	TripPowSum(P/L/E/G/W/H)
0	-0.31 /-0.35 /-1.13 /0.91 /-0.29 /-1.31	-0.59 /-0.60 /-0.20 /-0.32 /-0.16 /0.23	-0.43 /-0.59 /-1.41 /-0.20 /-1.37 /-1.89	-0.04 /-0.06 /0.07 /0.08 /0.03 /0.18	-0.48 /-0.52 /-1.44 /-0.41 /-1.55 /-2.00
8TeV el					
cat.	PowDecay(P/L/E/G/W/H)	ExpSum(P/L/E/G/W/H)	PowExpSum(P/L/E/G/W/H)	TripExpSum(P/L/E/G/W/H)	TripPowSum(P/L/E/G/W/H)
0	-0.27 /-0.32 /-1.01 /1.43 /-0.30 /-0.57	-0.04 /-0.05 /-0.03 /-0.05 /-0.02 /-0.03	-0.02 /-0.03 /-0.09 /0.12 /-0.06 /-0.05	-0.01 /-0.02 /-0.01 /-0.01 /-0.00 /-0.01	-0.06 /-0.08 /-0.21 /0.28 /-0.18 /-0.13

Table B.39. typeA Bias, 400. Columns show results for the various background models used in combined signal+background fits to background-only toys. The three numbers given for each background fit model correspond to toys generated from either a power law, Laurent polynomial, or exponential-like truth model. Boldface and yellow highlight is used to indicate the lowest-order functional form that satisfies the “low-bias” criterion: $|\mu(nS/\sigma(nBG))| \leq 0.2$

Type-A Bias, $m_H=450$

8TeV mu					
cat.	PowDecay(P/L/E/G/W/H)	ExpSum(P/L/E/G/W/H)	PowExpSum(P/L/E/G/W/H)	TripExpSum(P/L/E/G/W/H)	TripPowSum(P/L/E/G/W/H)
0	0.01 /-0.02 /-0.71 /1.12 /0.27 /-0.69	-1.04 /-1.02 /-0.70 /-0.25 /-0.29 /-0.08	-0.52 /-0.58 /-1.77 /-2.24 /-2.77 /-2.76	-0.05 /-0.04 /0.05 /0.17 /0.04 /0.10	-0.62 /-0.64 /-1.69 /-2.39 /-3.10 /-2.72
8TeV el					
cat.	PowDecay(P/L/E/G/W/H)	ExpSum(P/L/E/G/W/H)	PowExpSum(P/L/E/G/W/H)	TripExpSum(P/L/E/G/W/H)	TripPowSum(P/L/E/G/W/H)
0	-0.04 /0.01 /-0.69 /1.15 /0.00 /-0.29	-0.09 /-0.09 /-0.08 /-0.05 /-0.04 /-0.07	-0.04 /-0.04 /-0.12 /-0.01 /-0.24 /-0.10	-0.02 /-0.02 /-0.02 /-0.00 /0.00 /-0.01	-0.09 /-0.08 /-0.24 /0.02 /-0.46 /-0.21

Table B.40. typeA Bias, 450. Columns show results for the various background models used in combined signal+background fits to background-only toys. The three numbers given for each background fit model correspond to toys generated from either a power law, Laurent polynomial, or exponential-like truth model. Boldface and yellow highlight is used to indicate the lowest-order functional form that satisfies the “low-bias” criterion:
 $|\mu(nS/\sigma(nBG))| \leq 0.2$

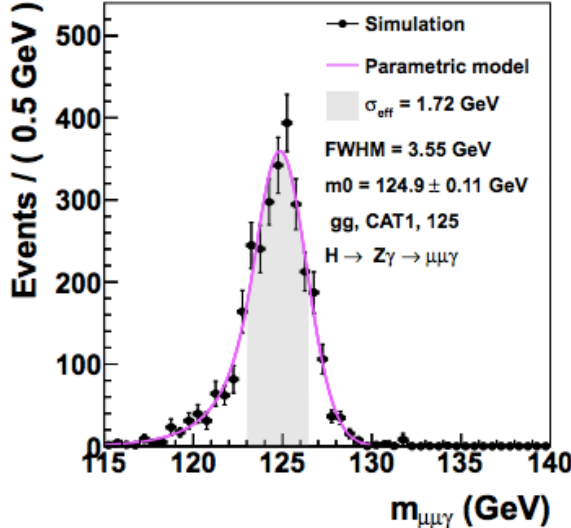
Type-A Bias, $m_H=500$

8TeV mu					
cat.	PowDecay(P/L/E/G/W/H)	ExpSum(P/L/E/G/W/H)	PowExpSum(P/L/E/G/W/H)	TripExpSum(P/L/E/G/W/H)	TripPowSum(P/L/E/G/W/H)
0	0.34 /0.27 /-0.24 /0.98 /0.76 /0.06	-1.08 /-1.12 /-0.96 /-0.06 /-0.30 /-0.31	-0.78 /-0.92 /-2.49 /-4.24 /-3.43 /-3.70	-0.05 /-0.11 /-0.12 /0.09 /0.06 /0.05	-0.76 /-0.80 /-2.28 /-4.46 /-4.62 /-3.82
8TeV el					
cat.	PowDecay(P/L/E/G/W/H)	ExpSum(P/L/E/G/W/H)	PowExpSum(P/L/E/G/W/H)	TripExpSum(P/L/E/G/W/H)	TripPowSum(P/L/E/G/W/H)
0	0.19 /0.21 /-0.30 /0.67 /0.58 /0.03	-0.12 /-0.12 /-0.12 /-0.04 /-0.06 /-0.10	-0.05 /-0.06 /-0.14 /-0.19 /-0.52 /-0.15	-0.02 /-0.02 /-0.03 /0.01 /0.01 /-0.01	-0.13 /-0.12 /-0.28 /-0.28 /-0.84 /-0.26

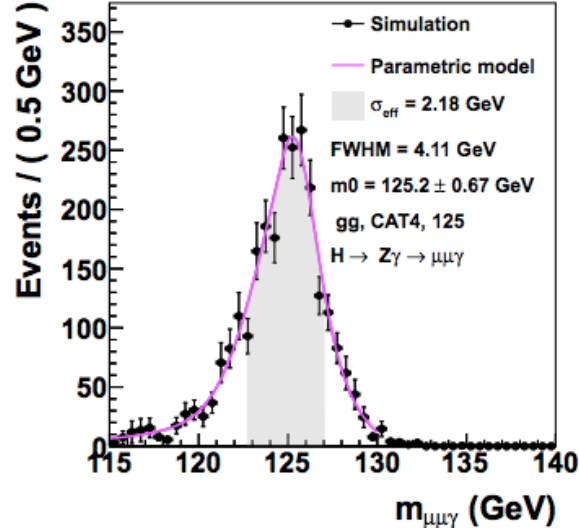
Table B.41. typeA Bias, 500. Columns show results for the various background models used in combined signal+background fits to background-only toys. The three numbers given for each background fit model correspond to toys generated from either a power law, Laurent polynomial, or exponential-like truth model. Boldface and yellow highlight is used to indicate the lowest-order functional form that satisfies the “low-bias” criterion:
 $|\mu(nS/\sigma(nBG))| \leq 0.2$

APPENDIX C

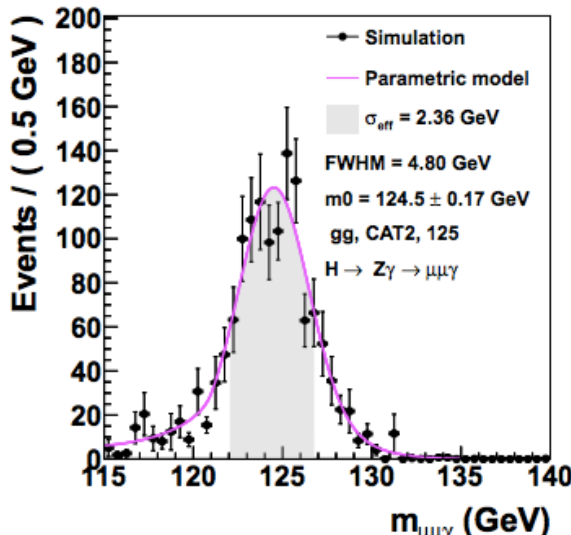
 $H \rightarrow Z\gamma$ Signal Fits

CMS Preliminary 2012 $\sqrt{s} = 8 \text{ TeV}, L = 5.2 \text{ fb}^{-1}$ 

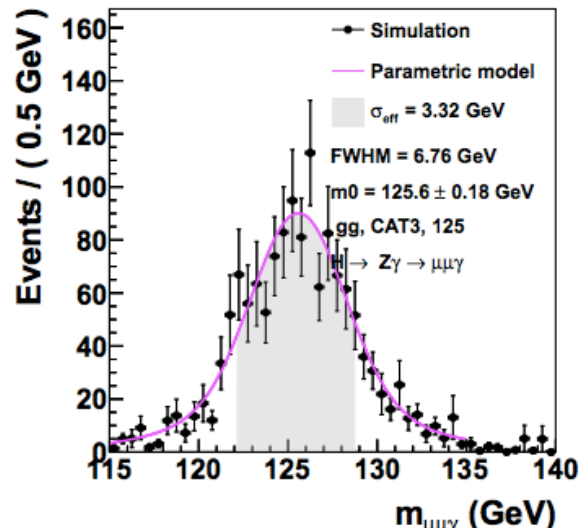
(a) CAT 1 High R9

CMS Preliminary 2012 $\sqrt{s} = 8 \text{ TeV}, L = 5.2 \text{ fb}^{-1}$ 

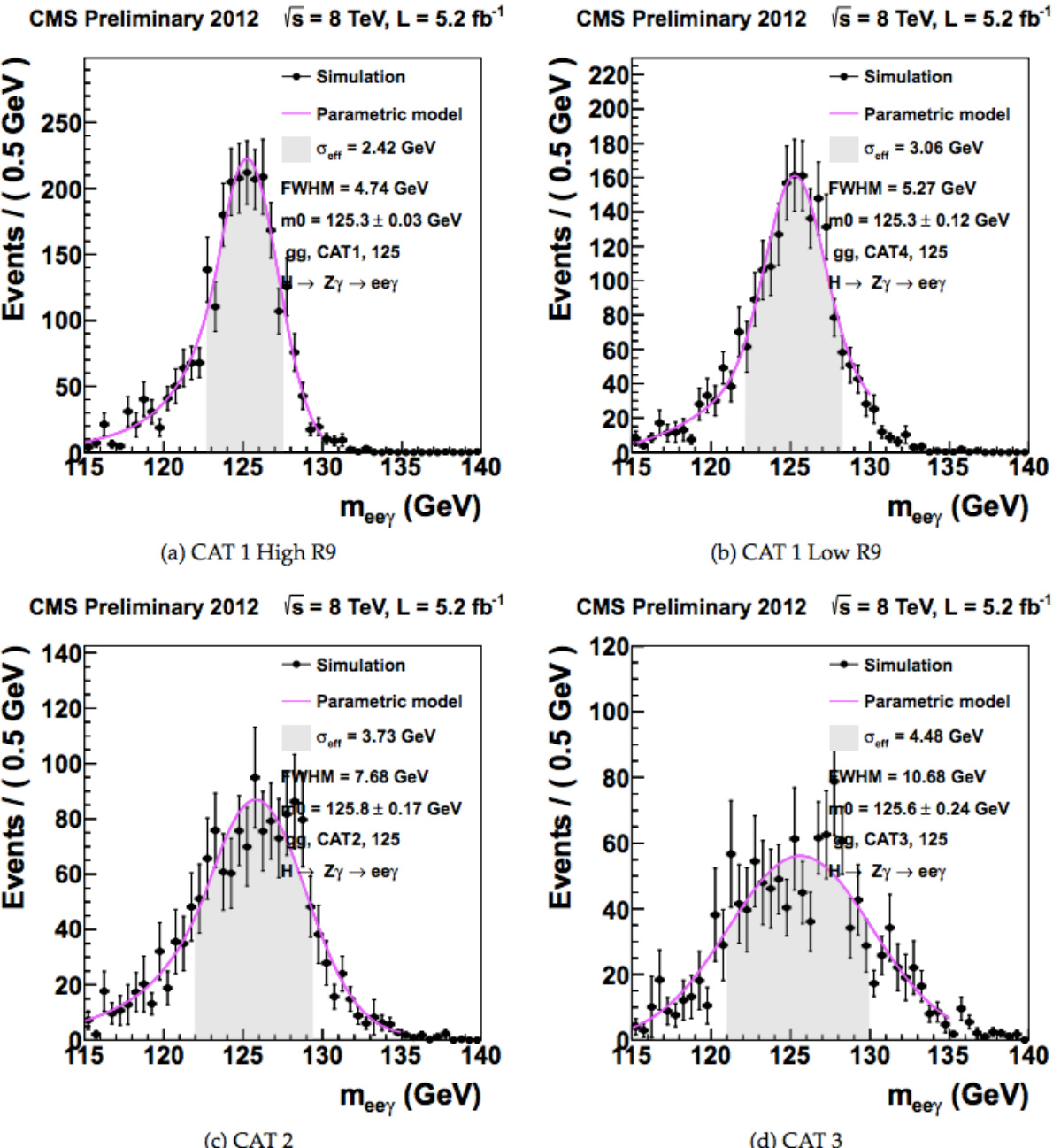
(b) CAT 1 Low R9

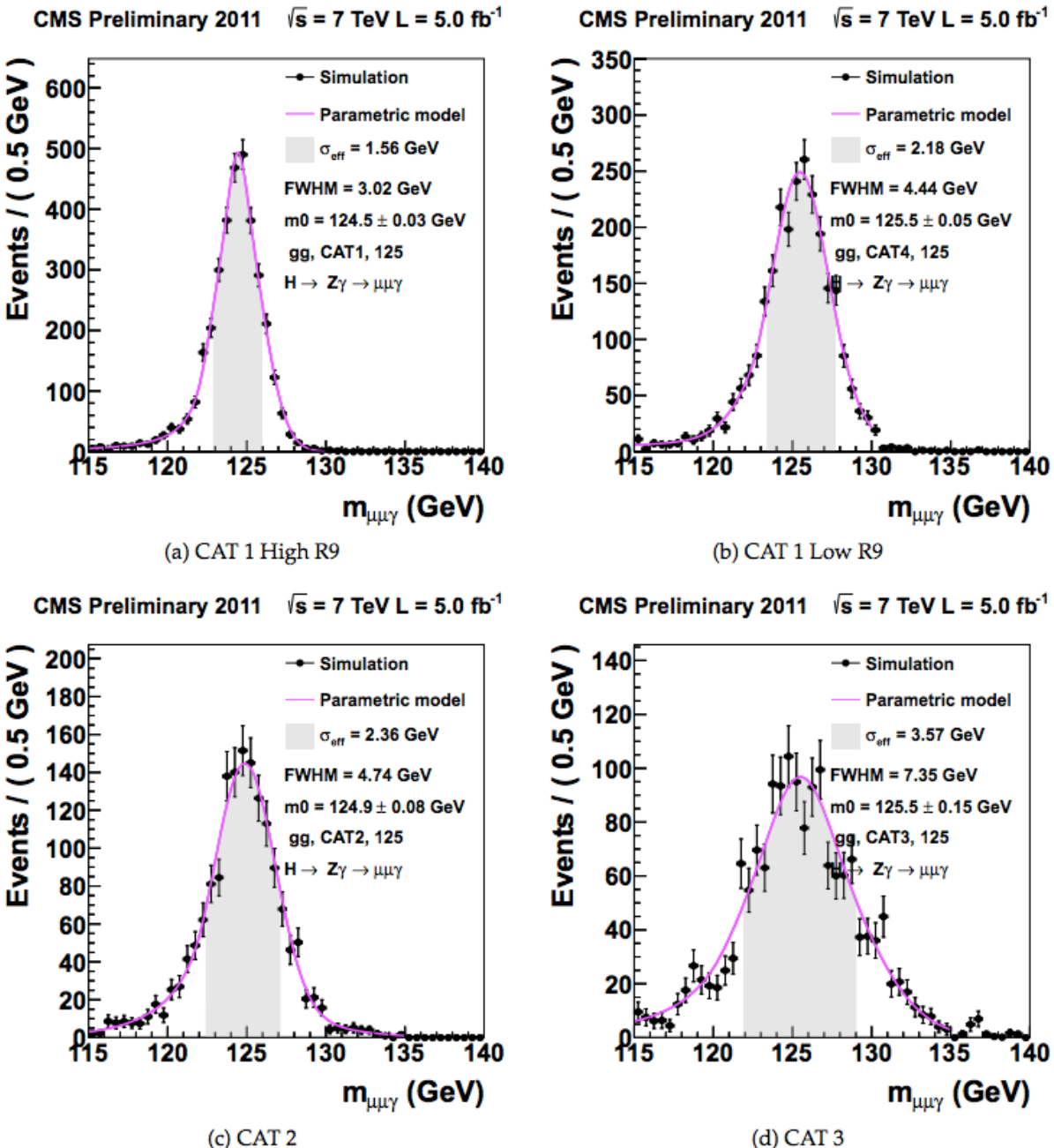
CMS Preliminary 2012 $\sqrt{s} = 8 \text{ TeV}, L = 5.2 \text{ fb}^{-1}$ 

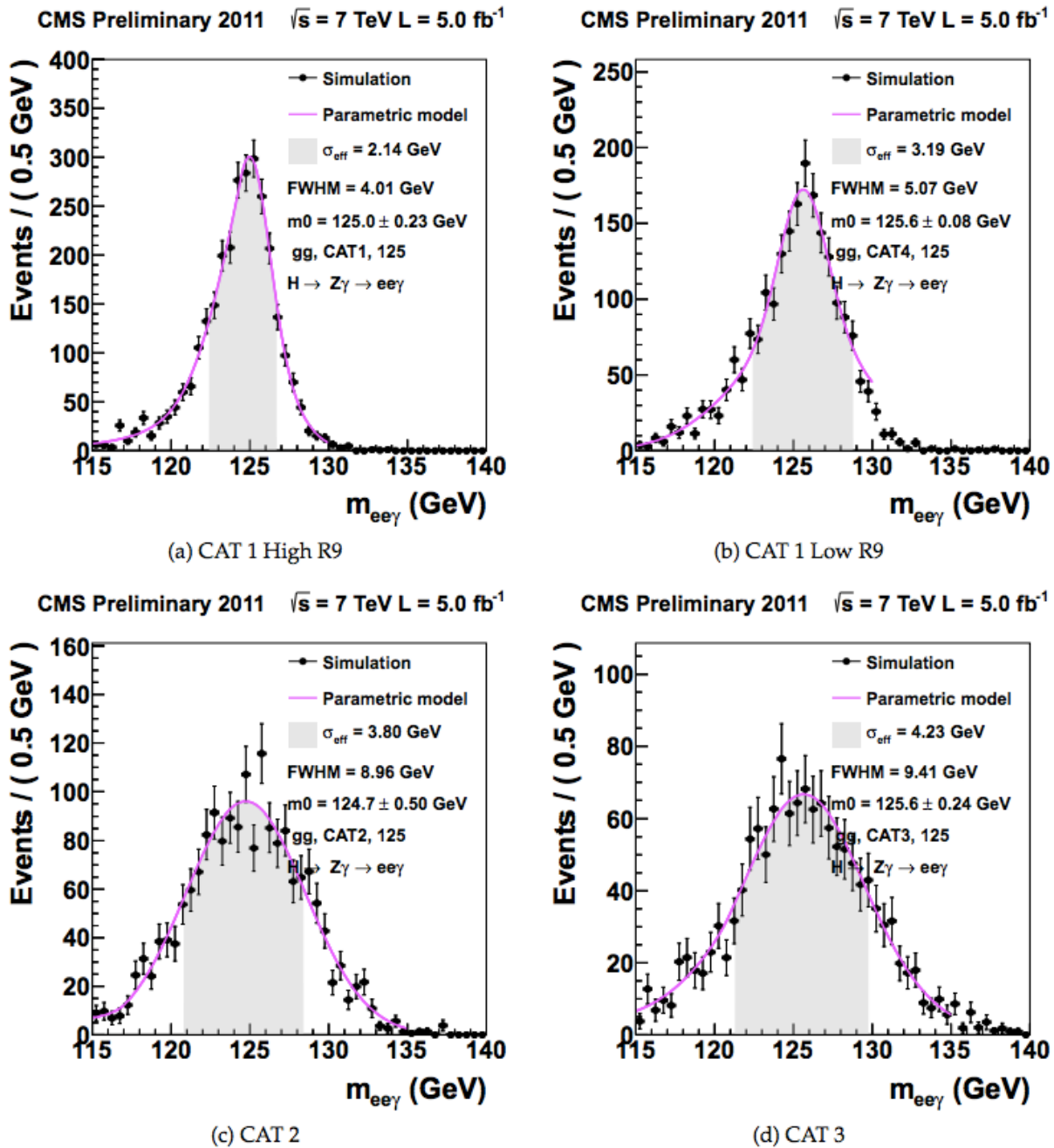
(c) CAT 2

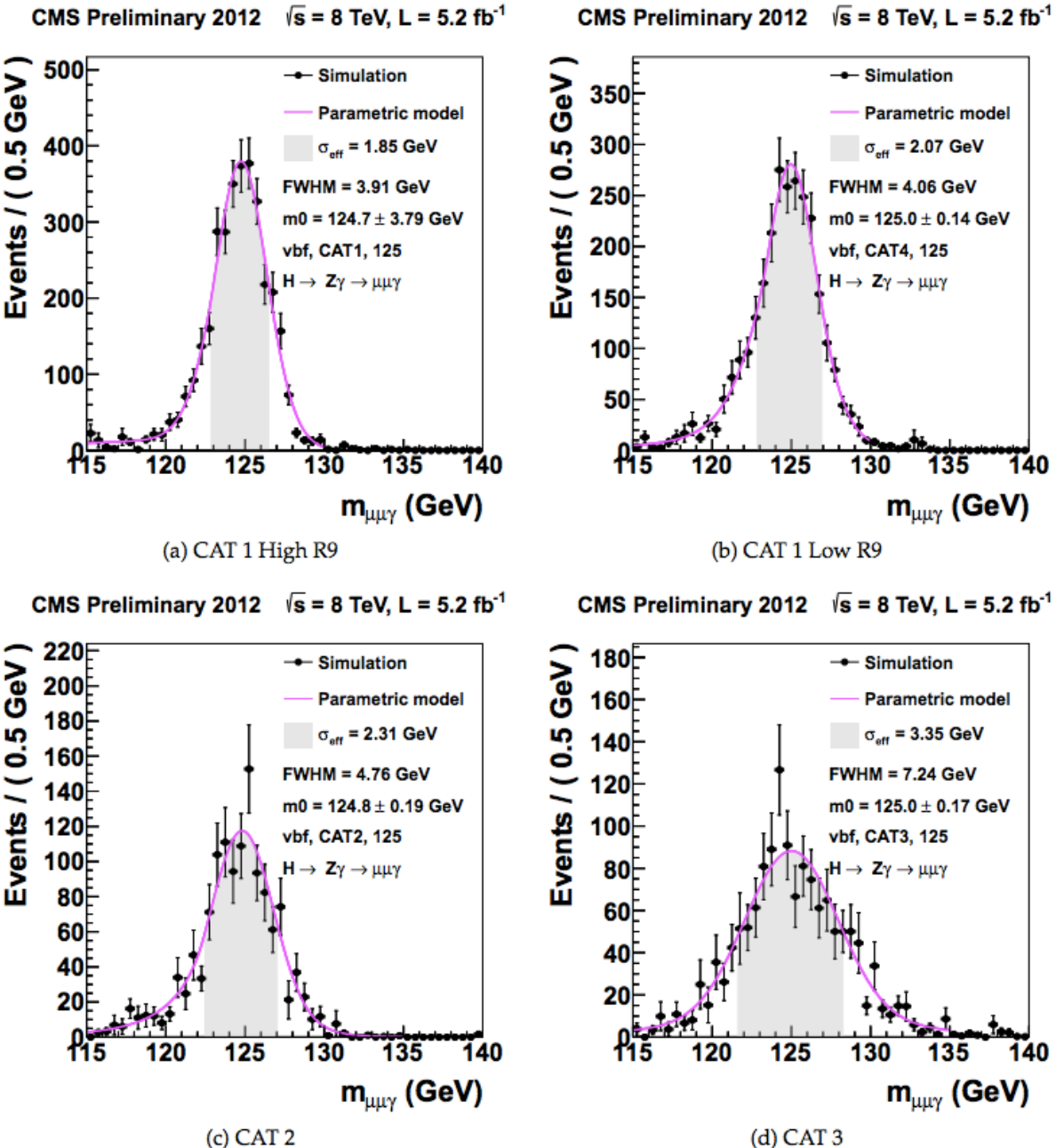
CMS Preliminary 2012 $\sqrt{s} = 8 \text{ TeV}, L = 5.2 \text{ fb}^{-1}$ 

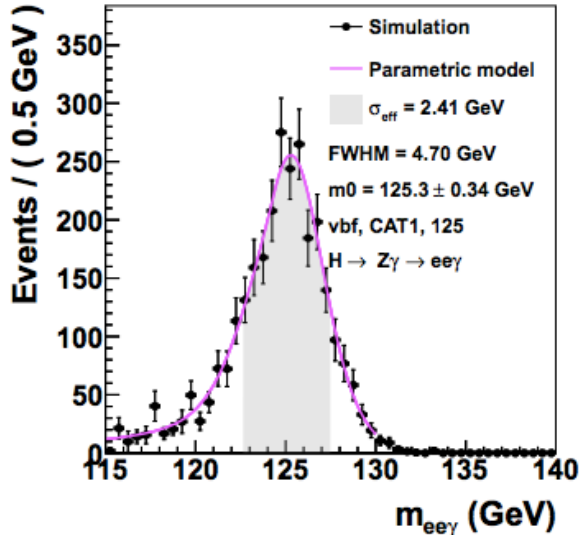
(d) CAT 3



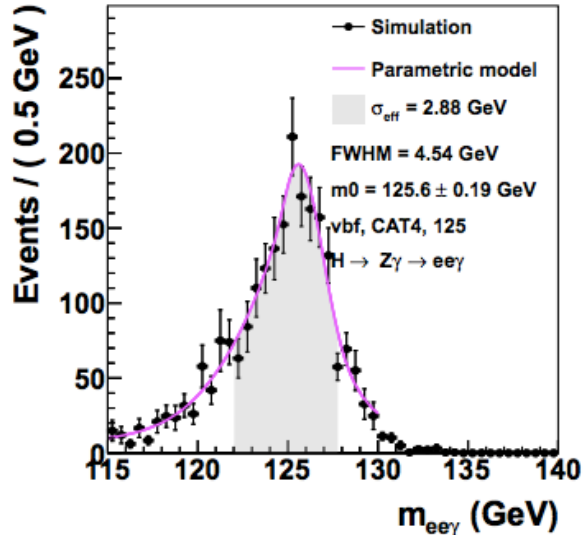




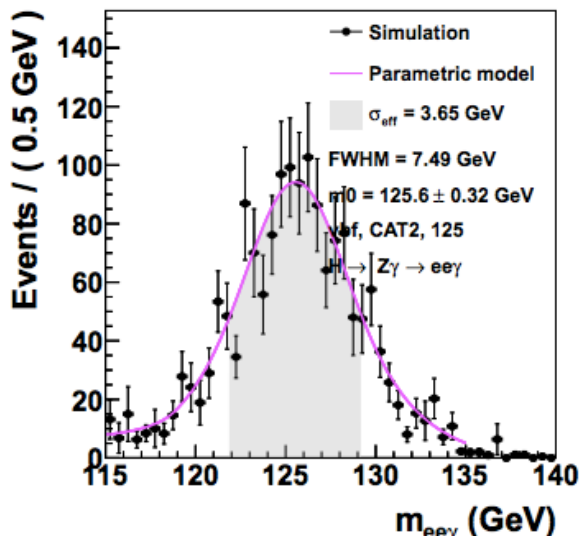


CMS Preliminary 2012 $\sqrt{s} = 8 \text{ TeV}, L = 5.2 \text{ fb}^{-1}$ 

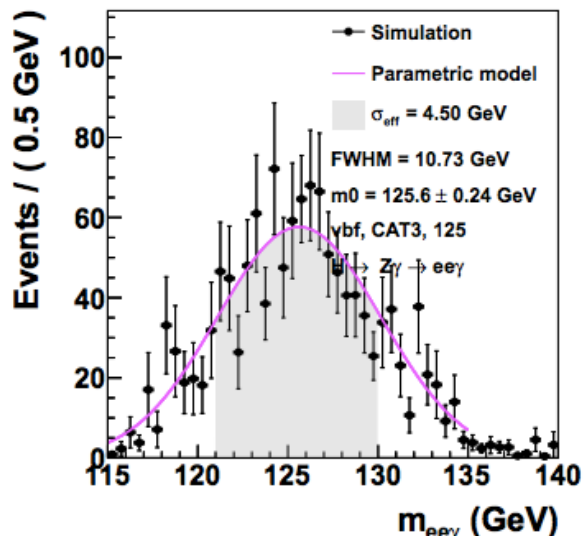
(a) CAT 1 High R9

CMS Preliminary 2012 $\sqrt{s} = 8 \text{ TeV}, L = 5.2 \text{ fb}^{-1}$ 

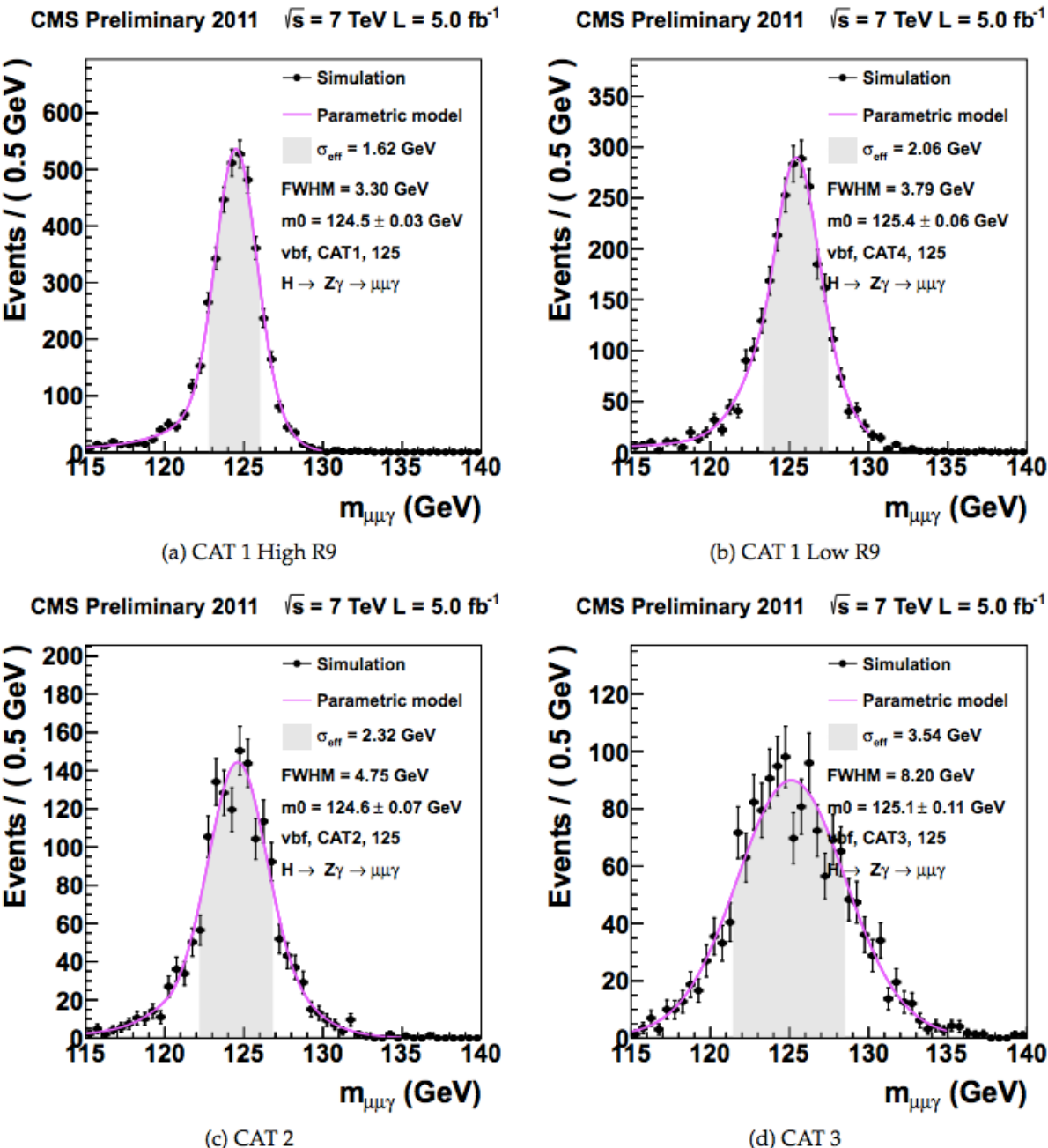
(b) CAT 1 Low R9

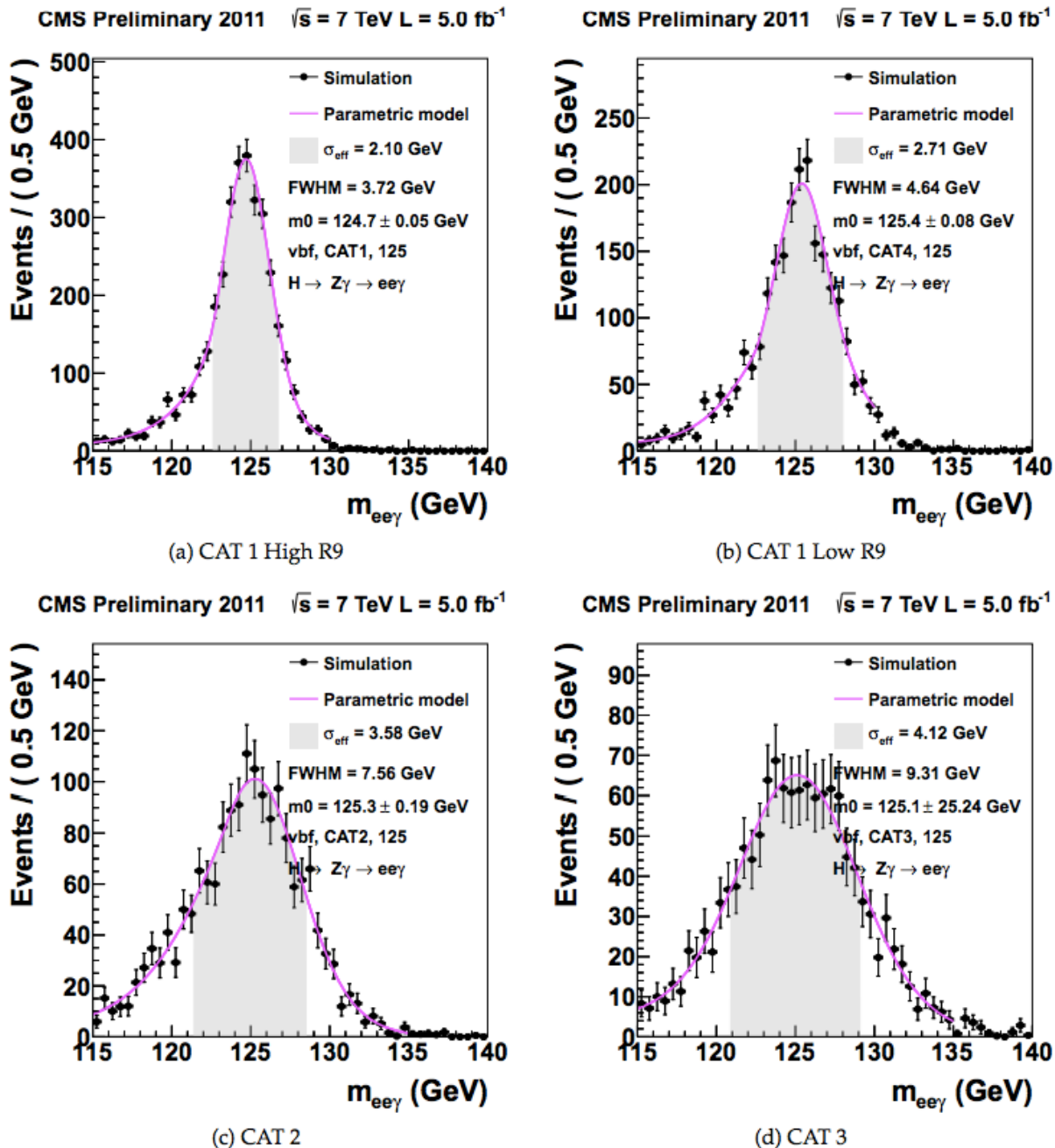
CMS Preliminary 2012 $\sqrt{s} = 8 \text{ TeV}, L = 5.2 \text{ fb}^{-1}$ 

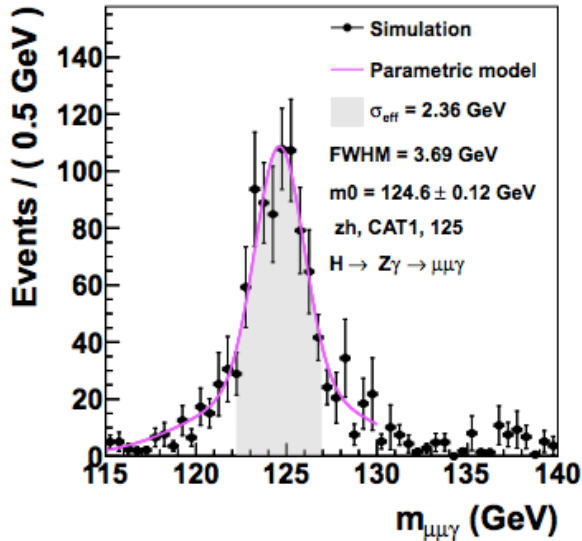
(c) CAT 2

CMS Preliminary 2012 $\sqrt{s} = 8 \text{ TeV}, L = 5.2 \text{ fb}^{-1}$ 

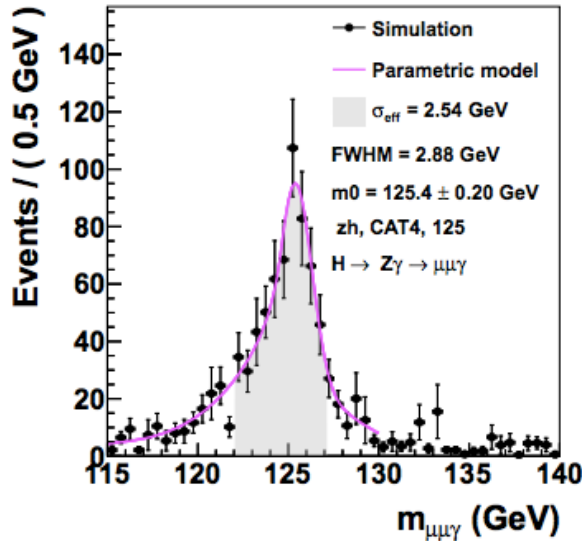
(d) CAT 3



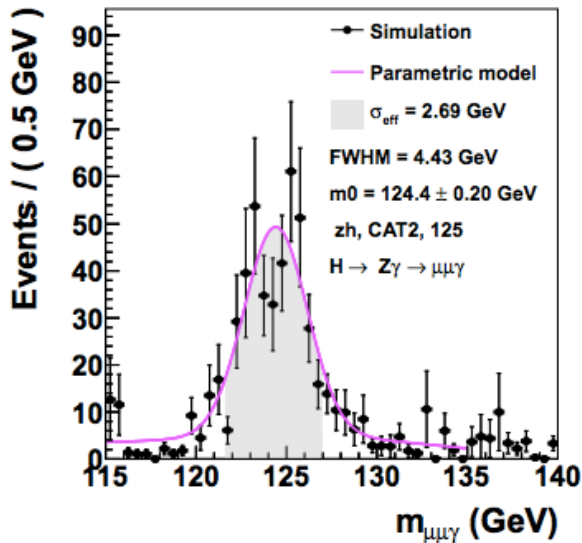


CMS Preliminary 2012 $\sqrt{s} = 8 \text{ TeV}, L = 5.2 \text{ fb}^{-1}$ 

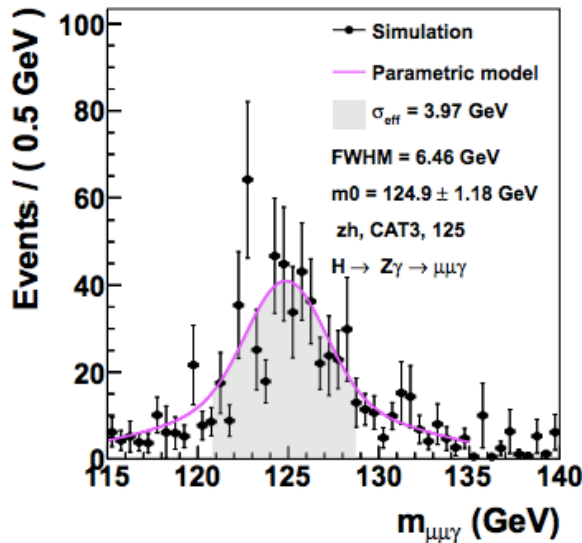
(a) CAT 1 High R9

CMS Preliminary 2012 $\sqrt{s} = 8 \text{ TeV}, L = 5.2 \text{ fb}^{-1}$ 

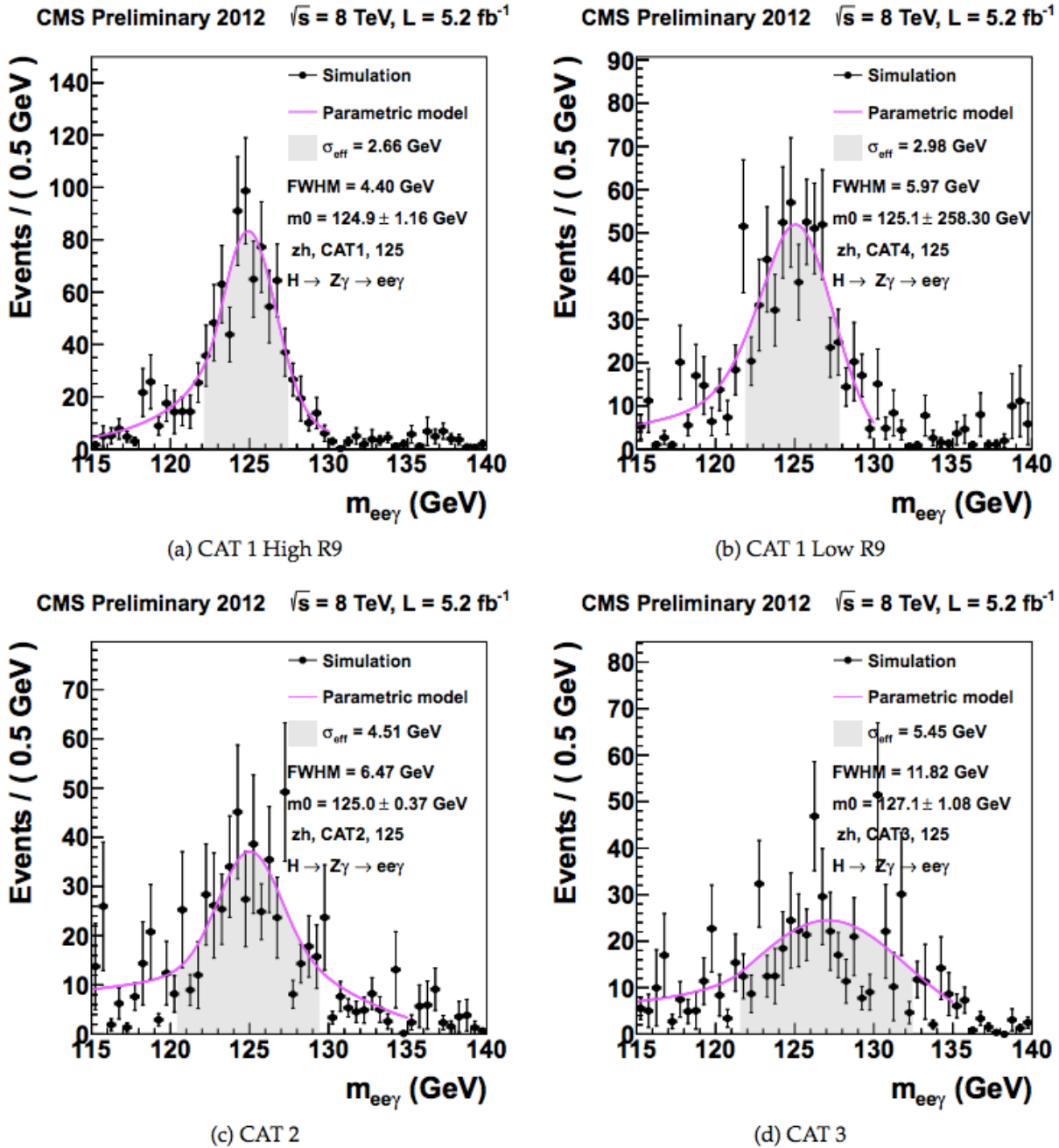
(b) CAT 1 Low R9

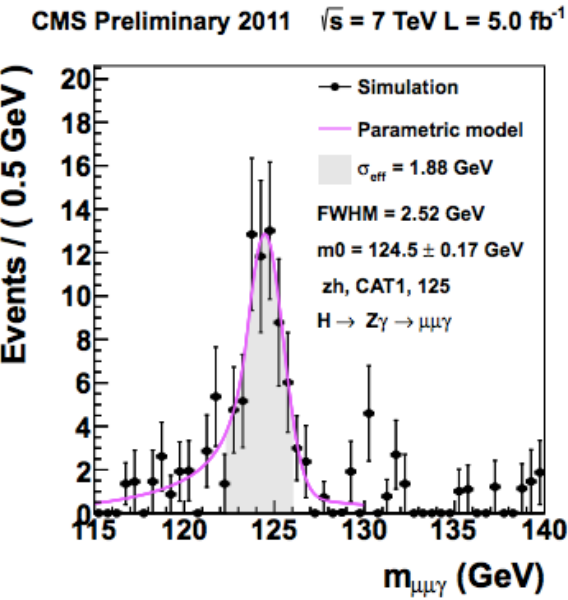
CMS Preliminary 2012 $\sqrt{s} = 8 \text{ TeV}, L = 5.2 \text{ fb}^{-1}$ 

(c) CAT 2

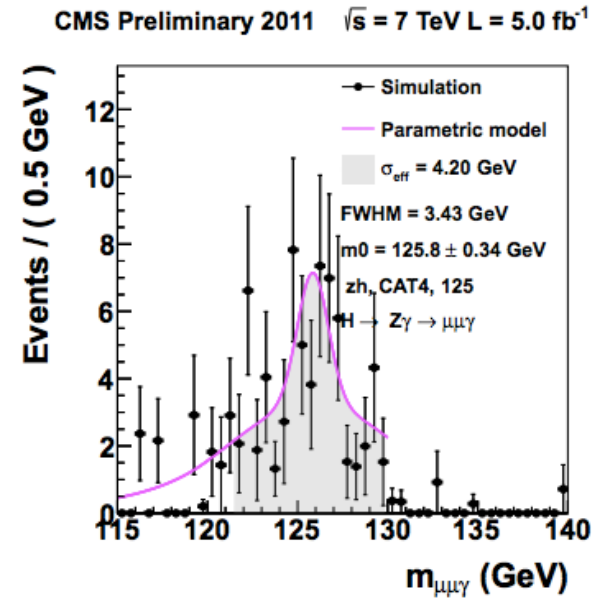
CMS Preliminary 2012 $\sqrt{s} = 8 \text{ TeV}, L = 5.2 \text{ fb}^{-1}$ 

(d) CAT 3

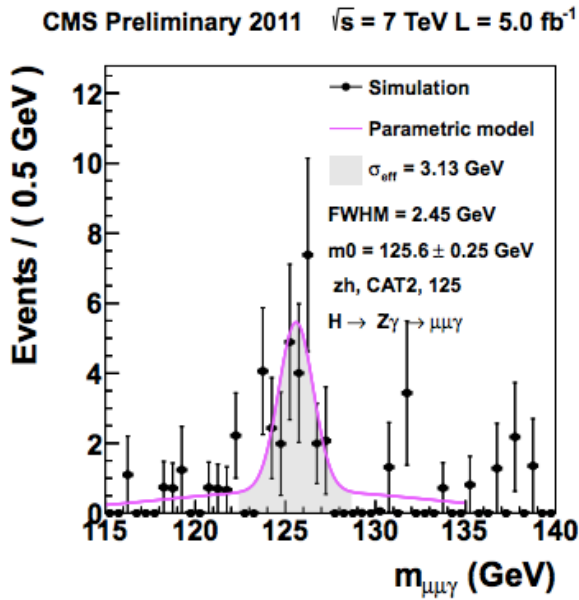




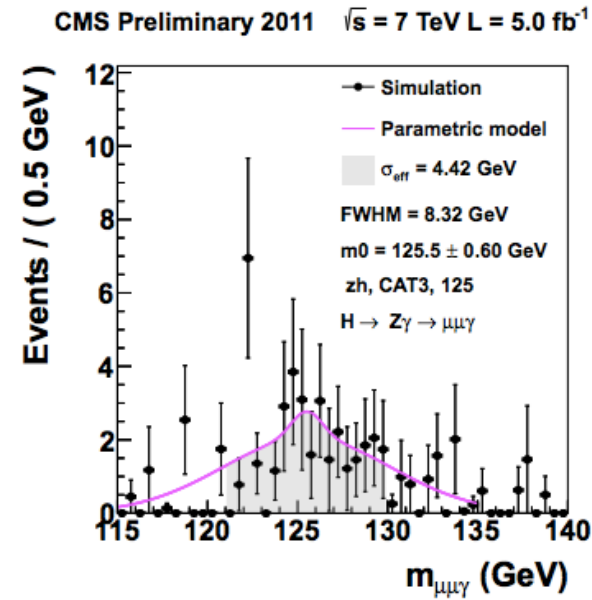
(a) CAT 1 High R9



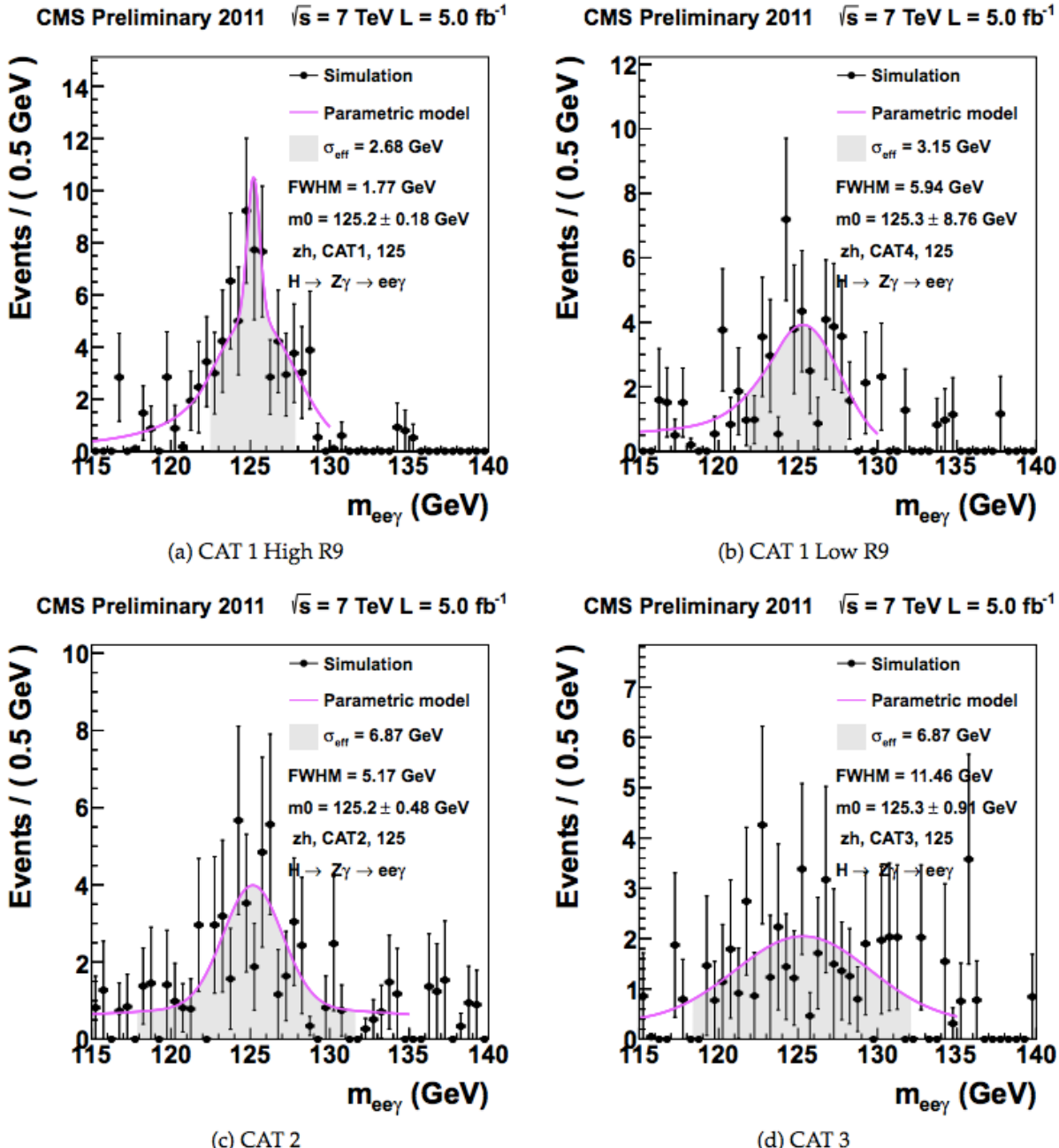
(b) CAT 1 Low R9

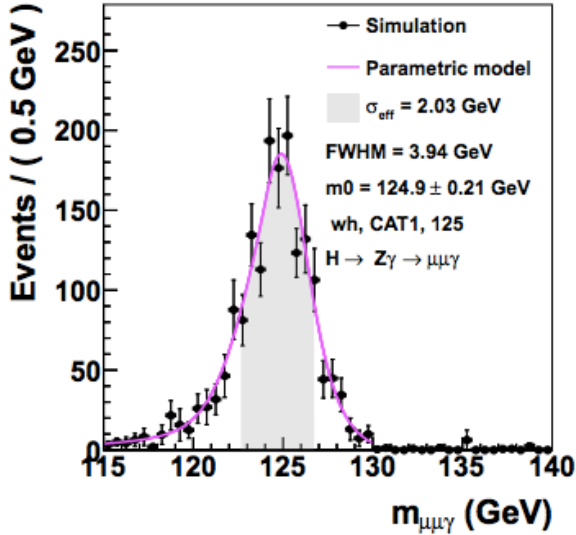


(c) CAT 2

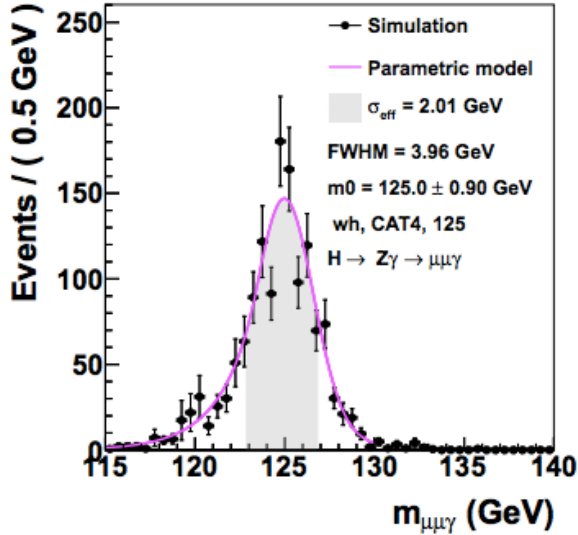


(d) CAT 3

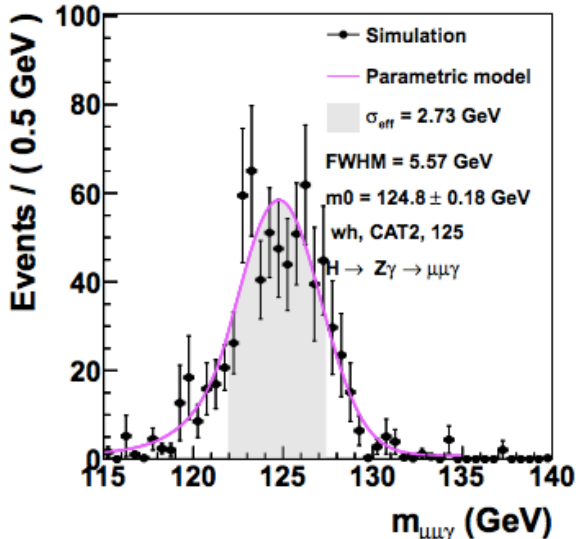


CMS Preliminary 2012 $\sqrt{s} = 8 \text{ TeV}, L = 5.2 \text{ fb}^{-1}$ 

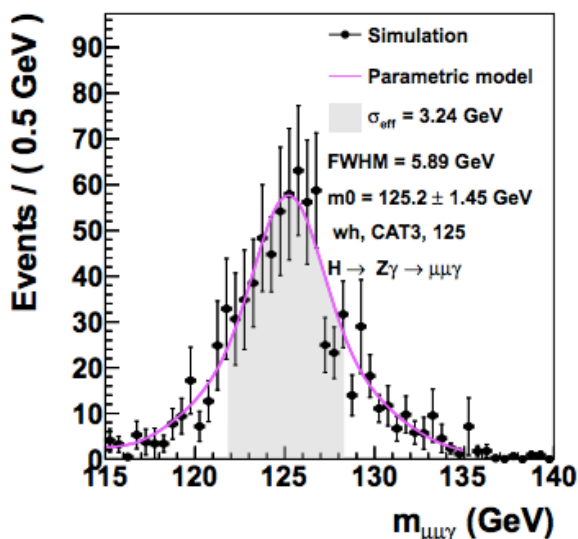
(a) CAT 1 High R9

CMS Preliminary 2012 $\sqrt{s} = 8 \text{ TeV}, L = 5.2 \text{ fb}^{-1}$ 

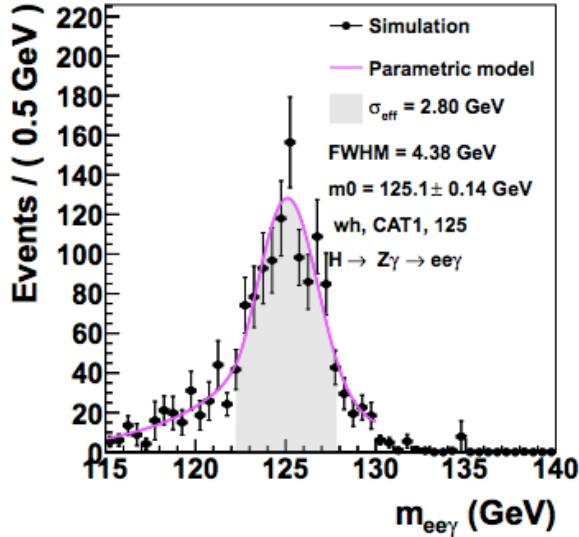
(b) CAT 1 Low R9

CMS Preliminary 2012 $\sqrt{s} = 8 \text{ TeV}, L = 5.2 \text{ fb}^{-1}$ 

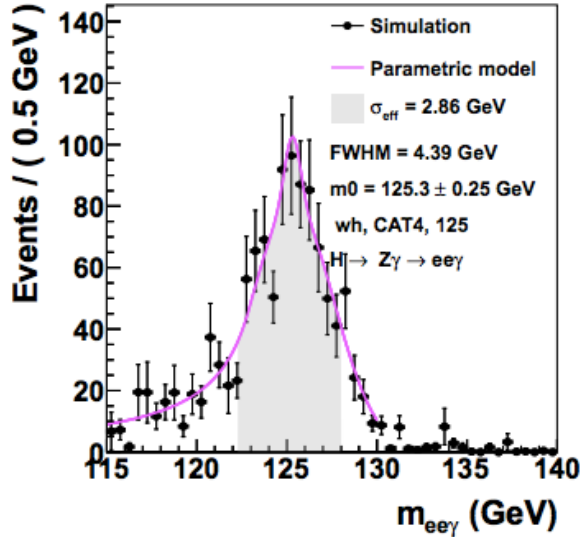
(c) CAT 2

CMS Preliminary 2012 $\sqrt{s} = 8 \text{ TeV}, L = 5.2 \text{ fb}^{-1}$ 

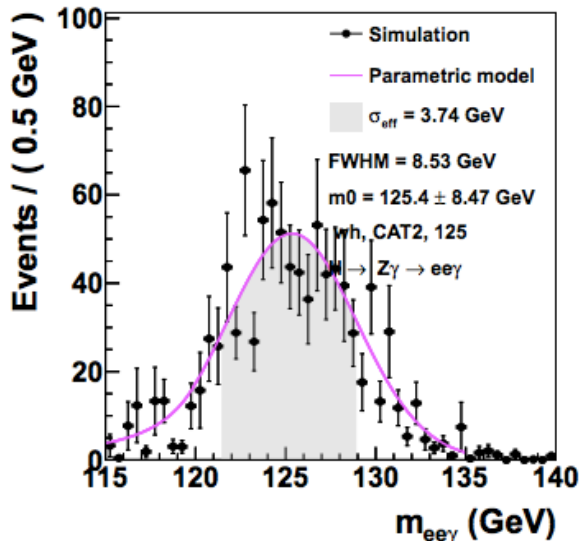
(d) CAT 3

CMS Preliminary 2012 $\sqrt{s} = 8 \text{ TeV}, L = 5.2 \text{ fb}^{-1}$ 

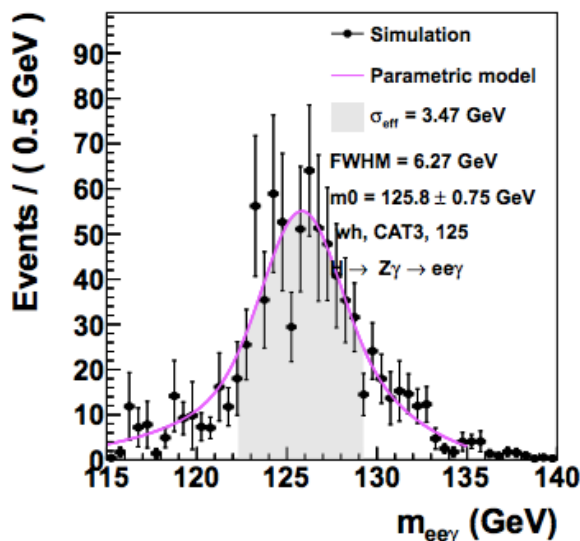
(a) CAT 1 High R9

CMS Preliminary 2012 $\sqrt{s} = 8 \text{ TeV}, L = 5.2 \text{ fb}^{-1}$ 

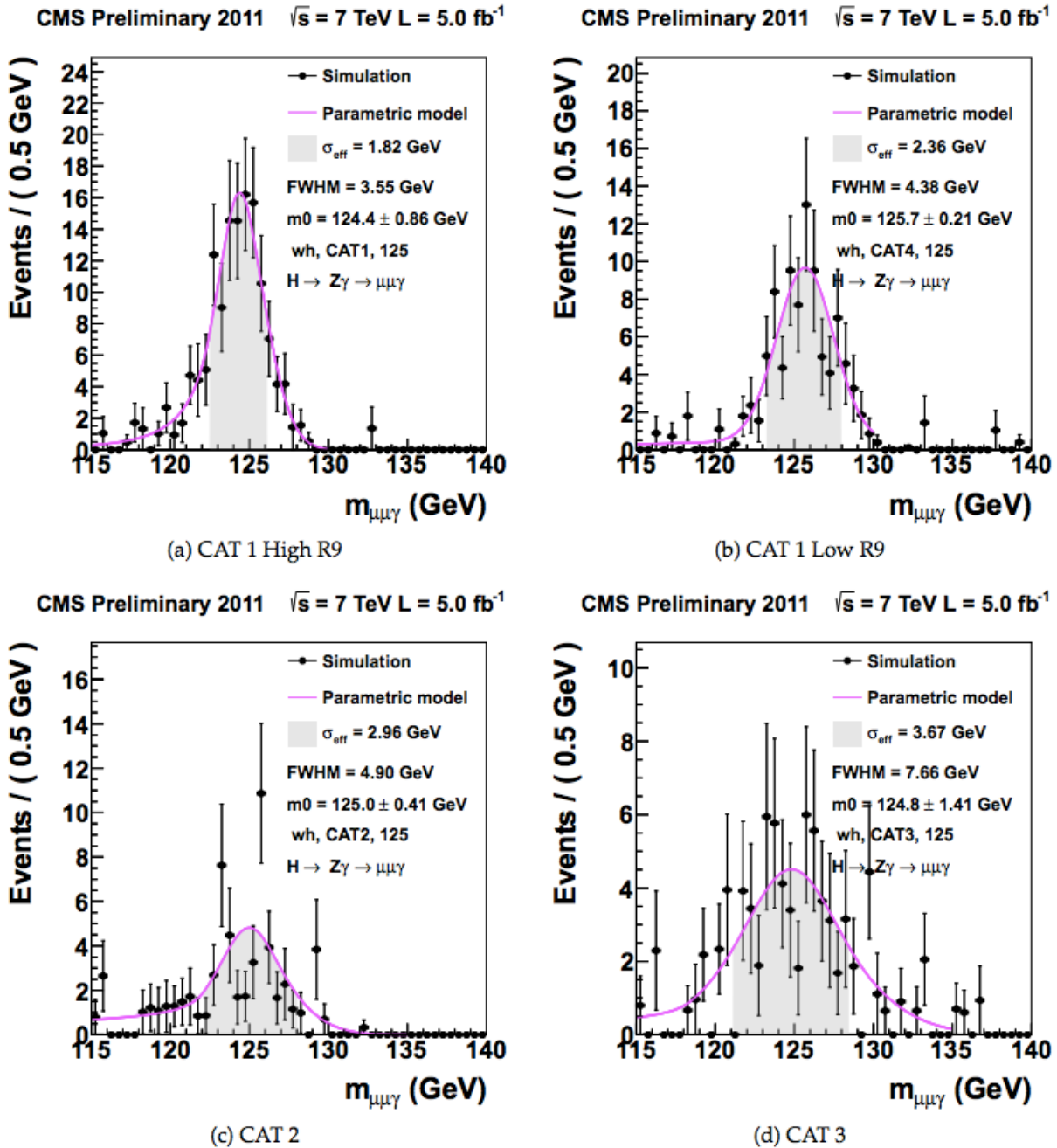
(b) CAT 1 Low R9

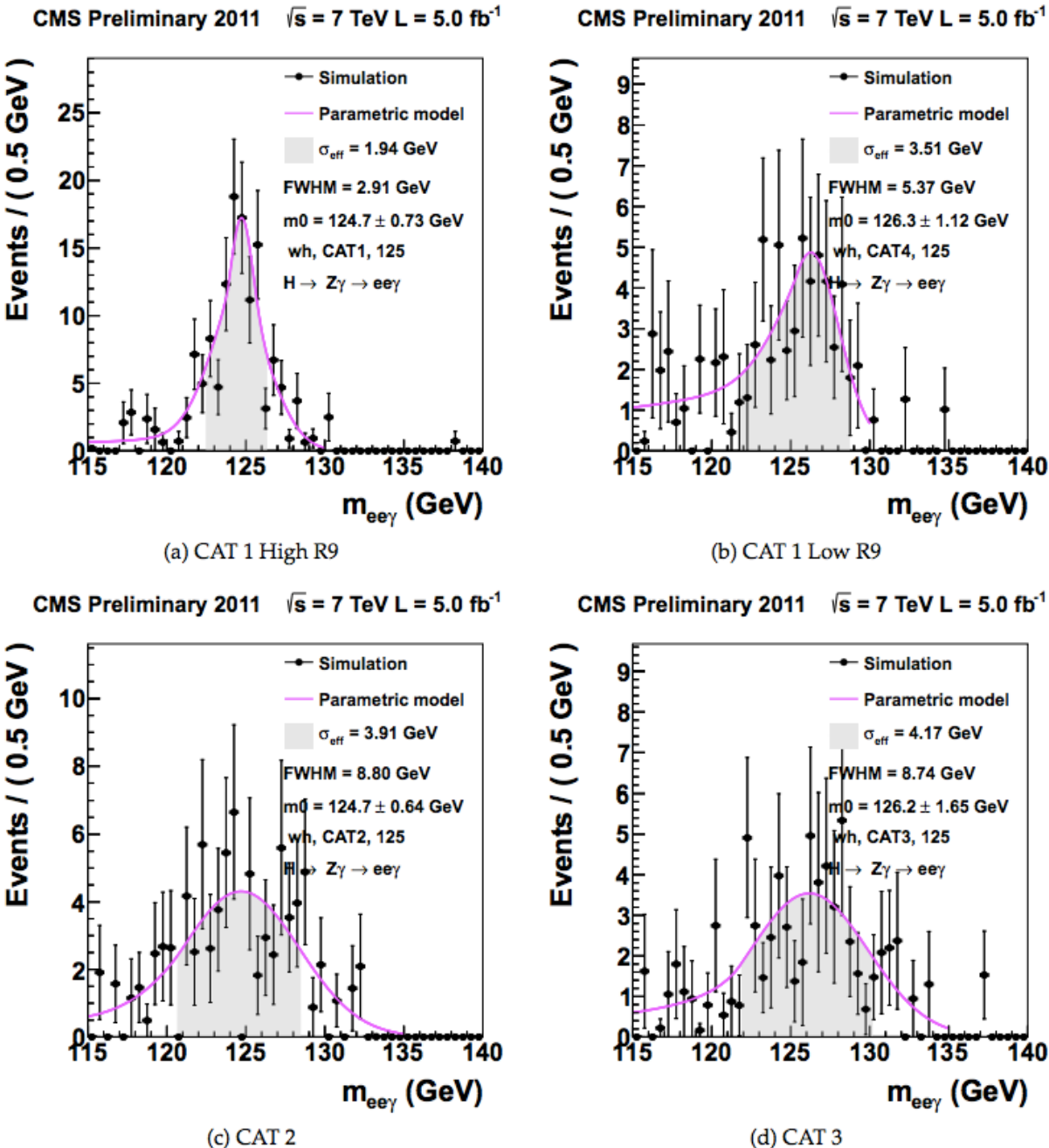
CMS Preliminary 2012 $\sqrt{s} = 8 \text{ TeV}, L = 5.2 \text{ fb}^{-1}$ 

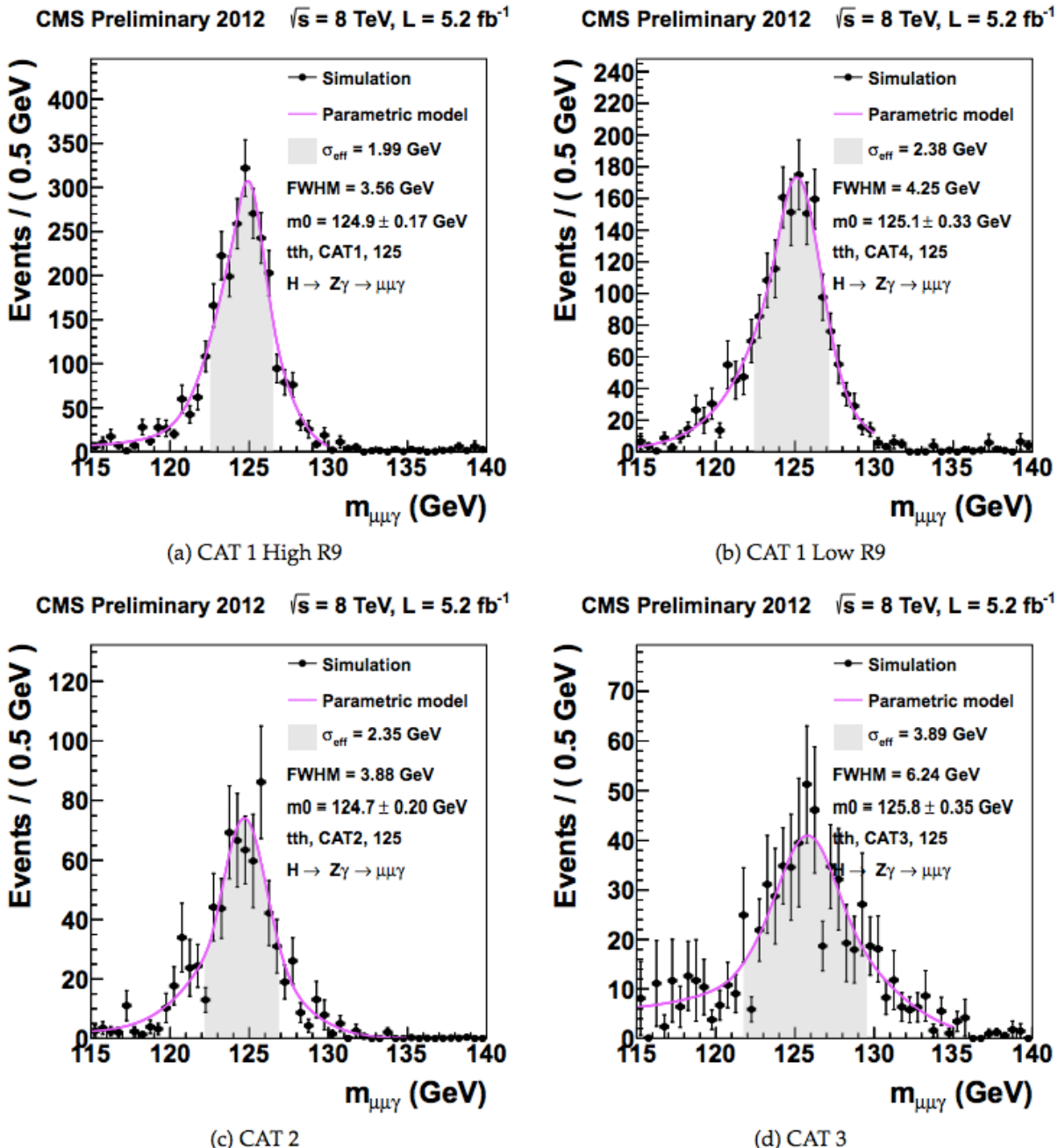
(c) CAT 2

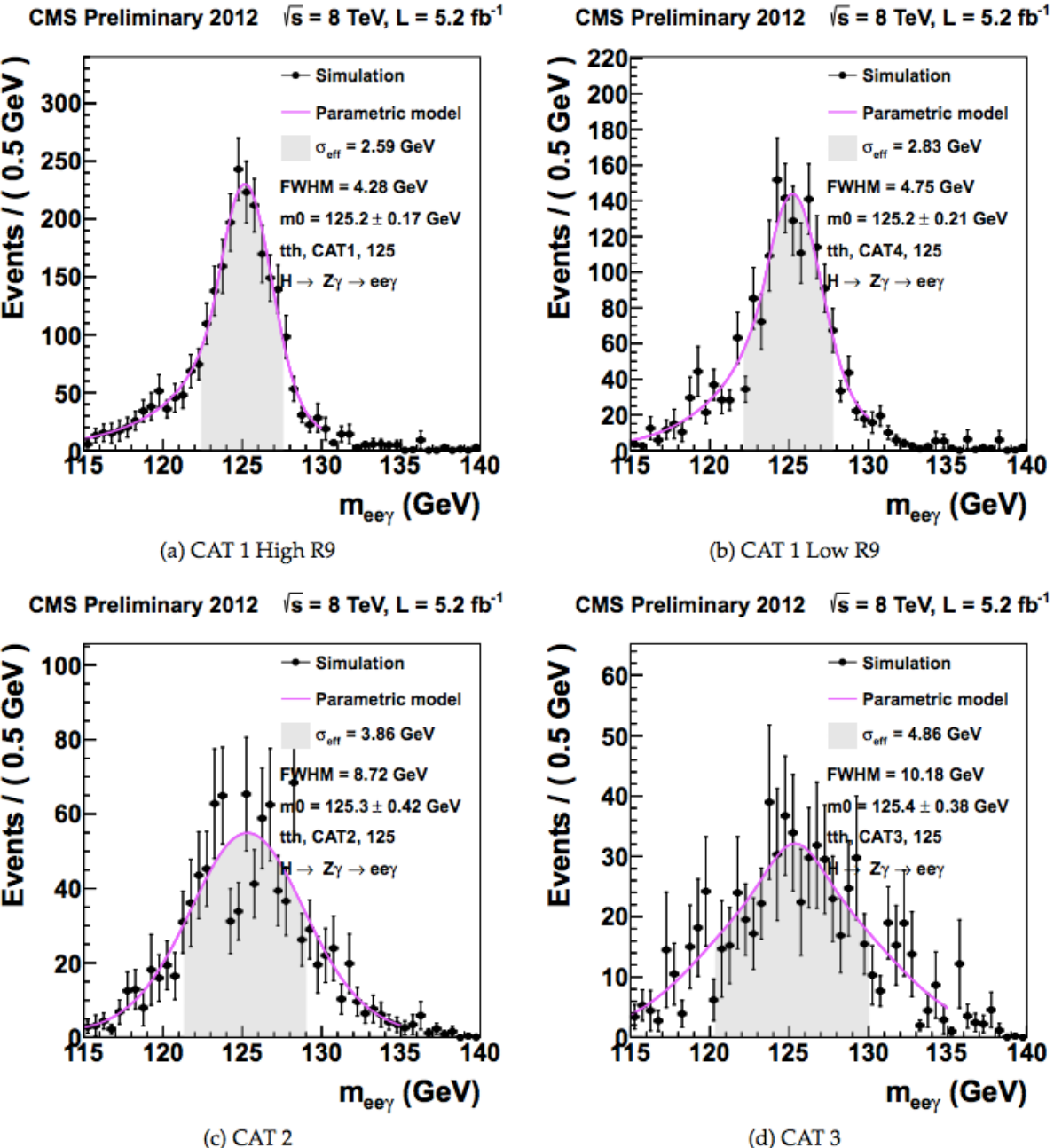
CMS Preliminary 2012 $\sqrt{s} = 8 \text{ TeV}, L = 5.2 \text{ fb}^{-1}$ 

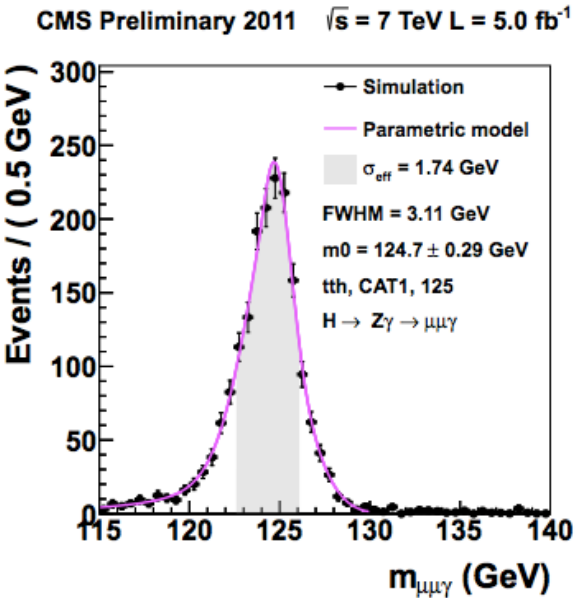
(d) CAT 3



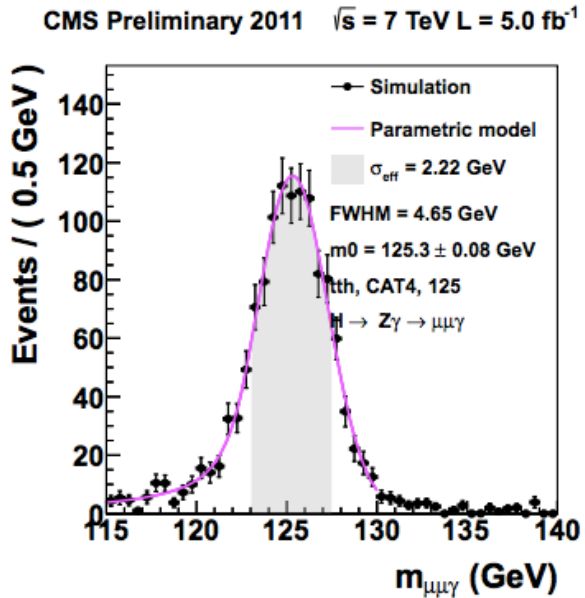




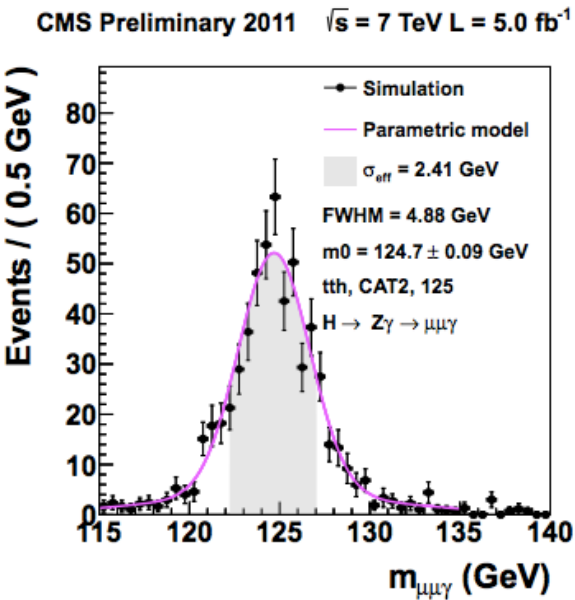




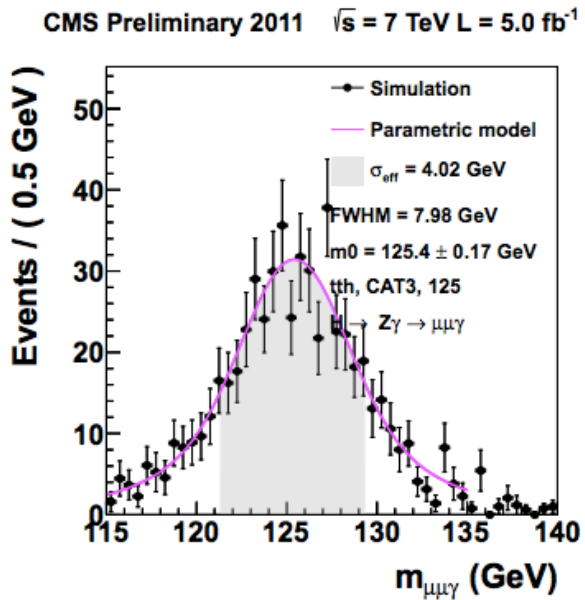
(a) CAT 1 High R9



(b) CAT 1 Low R9



(c) CAT 2



(d) CAT 3

